University of Strathclyde

Electronic and Electrical Engineering
Department

Current Source DC/DC Converter Based Multi-terminal DC Wind Energy Conversion System

by

Shixiong Fan

A thesis presented in fulfilment of the requirements for the degree of
Doctor of Philosophy

April 2012

Dedication

To my family

Abstract

Wind power energy conversion is growing rapidly in the world. There are two main wind farm types, namely ac grid-based and dc grid-based wind farms. The dc grid-based approach reduces the size and weight of the magnetic components and cables. In the dc system, the step-up dc/dc converter is the key component when interfacing the wind turbine to the ac grid, via its low/medium voltage generator. This thesis focuses on the control and design of a wind energy conversion system based on dc/dc current source converters. An optimized One-Power-Point method for maximum power tracking is proposed. It incorporates One-Power-Point control and Maximum Power Differential Voltage control to allow the wind turbine to extract more energy during rapid wind speed changes. A current output hard-switched full bridge converter and serial-parallel resonant converter with an intermediate high frequency transformer are investigated for interfacing wind turbines to a local dc grid. These converters are assessed and compared in terms of semiconductor stresses and losses. A new modified One-Power-Point control method is proposed for the dc/dc converter, which tracks the maximum power during wind speed changes. A design procedure for the serial-parallel resonant converter is presented, based on its characteristics specific to a wind energy conversion system (WECS). A current source dc/dc converter based multi-terminal dc WECS is presented, investigated, and simulated. A practical multi-terminal dc WECS verifies its feasibility and stability, using two dc current output wind turbine units. Furthermore, a coordinated de-loading control scheme for the current sourcing based WECS is proposed, to cater for ac grid demand changes. It combines pitch control, dc dumping chopper control, and dc/dc converter control, to safely and quickly establish de-loading control. Both simulation and experimental results verify the de-loading scheme.

Acknowledgements

I would like to express my deepest gratitude to my supervisors Prof. B. W. Williams, Dr. T. C. Lim and Dr. J. E. Fletcher for their continuous guidance, encouragement, helpful comments, kind advice and capable supervision during my PhD study.

I also wish sincerely to thank Dr. Huibin Zhang and Dr. Jin Yang for their help and support, not only in research aspects but also in my daily life.

A gracious acknowledgement is made to members of staff and technicians at the Department of Electronic and Electrical Engineering in Strathclyde University who provided their assistance and technical support during the years of research, especially Mr. Charles Croser.

Both the China Scholarship Council and the EPSRC are acknowledged for providing financial support for this research.

Finally, I would like to thank my family and Weiwei Ma for their love, support and encouragement throughout.

List of Symbols

A	ratio of parallel and series capacitances
B	flux density
C_c	inverter output filters capacitance (F)
C_p	wind turbine power coefficient
D_k	duty cycle values at iterations k
F	generator combined viscous friction of rotor and load
G_r	overall gain of LCC resonant converter
G_t	resonant tank gain of LCC resonant converter
i_d, i_q	generator d and q axis current (A)
i_{ga}, i_{gb}, i_{gc}	3-phase grid input currents (A)
i_{gd}, i_{gq}	d and q axis grid input current (A)
i_i	input current of DC/DC converter (A)
i_{iv}	3-phase inverter output currents (A)
J	generator combined inertia of rotor and load
L_d, L_q	generator d and q axis inductance (H)
m_{ivd}, m_{ivq}	modulation indices
N	transformer turns ratio
p	number of pole pairs
P_m	wind turbine mechanical power (W)
P_e	electrical power (W)
Q	loaded quality factor
R_{ac}	equivalent ac load resistance (Ω)
S	swept area (m^2)
T_e	electromagnetic torque (Nm)

T_m	input mechanical torque of torque (Nm)
u_{iv}	3-phase voltages of the inverter output filter (V)
U_{di}	inverter side dc link voltage (V)
V_{dc}	DC link voltage (V)
v_i	input voltage and current of DC/DC converter (V)
V	wind speed (m/s)
ΔE	energy captured by the wind turbine (J)
β	pitch angle (°)
θ	generator rotor angular position
λ	tip speed ratio
μ_r	core permeability
ρ	air density (kg/m^3)
ω	angular velocity of the generator rotor (rad/s)
ω_s	switching angular frequency
ω_g	angular frequency of the grid voltage
ω_0	undamped natural frequency of the resonant tank
ω_{lim}	limited rotor speed

List of Abbreviations

AC	Alternating Current
CSC	Current Source Converter
CSI	Current Source Inverter
DC	Direct Current
DFIG	Doubly Fed Induction Generator
EMI	Electro Magnetic Interference
ERCC	Energy Recovery Clamp Circuit
EU	European Union
FB	Full Bridge
FMA	Fundamental Mode Approximation
GTO	Gate Turn-Off
HF	High Frequency
HSFB	Hard Switched Full Bridge
HVAC	High Voltage Alternative Current
HVDC	High Voltage Direct Current
IGBT	Insulated Gate Bipolar Transistor
IGCT	Integrated Gate-Commutated Thyristor
LCC[*]	Line-Commutated Converter
MPDV	Maximum Power Differential Voltage
MPPT	Maximum Power Point Tracking
MPP	Maximum Power Point
OPP	One-Power-Point

---

[*] LCC is also used in the context of a resonant converter to reflect a resonant tank consisting of an inductor and two capacitors

PMSG	Permanent Magnet Synchronous Generator
P&O	Perturbation & Observation
PSF	Power Signal Feedback
PWM	Pulse Width Modulation
RCD	Resistor Capacitor Diode
SAB	Single Active Bridge
SCIG	Squirrel Cage Induction Generator
TSR	Tip Speed Ratio
VSC	Voltage Source Converter
WECS	Wind Energy Conversion System
WG	Wind Generator
WRIG	Wound Rotor Inductor Generator
WT	Wind Turbine
ZVS	Zero Voltage Switching
ZCS	Zero Current Switching

Preface

Wind energy conversion system (WECS) technology has been developing fast in many countries around the world. But there are challenges in terms of efficiency, stability and system cost. The goal of this thesis is to investigate a possible solution for the wind farm collection and transmission system.

Chapter one presents the characteristics of wind power, which involves its variability, intermittency and economics. The different collection and transmission technologies for wind farms are investigated.

Chapter two investigates each component used in a wind energy conversion system. Different types of wind turbine generators, power converters and inverters are compared in terms of their advantages and disadvantages.

Chapter three introduces an optimization scheme based on One-Power-Point control for a boost converter based wind energy conversion system, which improves energy conversion efficiency without additional mechanical sensors and measurements.

Chapter four investigates a wind energy conversion system, which uses a current source full bridge dc/dc converter with an intermediate high frequency transformer. The boost and H-Bridge converters are compared in terms of switch stresses. New modified One-Power-Point control is presented. The test rig with a constructed wind turbine emulator verifies the performance of the proposed system and control method.

Chapter five proposes a series-parallel resonant converter for interfacing the wind energy electrical source to the grid. The design procedures and analysis of the series-parallel converter are presented based on the Fundamental Mode Approximation. It compares the hard-switch full-bridge converter in terms of switch stress and efficiency. Simulation and experimental results demonstrate the feasibility of utilizing an LCC resonant converter for wind energy conversion systems.

Chapter six introduce a current source dc/dc converter based multi-terminal DC wind energy conversion system. The proposed WECS is based on a star connected system. The simulation and experimental results demonstrate the stability of the proposed WECS with three different operation cases.

Chapter seven proposes a coordinated de-loading control scheme for the proposed WECS under ac grid power demand changes. The proposed control scheme combines dc/dc converter control, dc dumping chopper control, and turbine pitch control. Simulation and experimental results are analysed and confirm the validity of the propose control scheme.

Finally, chapter eight presents the thesis general conclusions, the author's contribution, and suggestions for future research.

Table of Contents

Abstract i

Acknowledgements ii

List of Symbols iii

List of Abbreviations v

Preface vii

Table of Contents ix

Chapter 1 1

- 1.1 Wind Energy 2
  - 1.1.1 Variability and Intermittency 3
  - 1.1.2 Penetration 3
  - 1.1.3 Economics 4
- 1.2 Wind energy in the UK 5
- 1.3 Wind power collection and transmission technologies 7
  - 1.3.1 Wind farm collection systems 7
  - 1.3.2 Wind power transmission systems 8
- References 13

Chapter 2 17

- 2.1 Wind turbine generator concepts 18
  - 2.1.1 Fixed speed WECS 18
  - 2.1.2 Limited speed system 19
  - 2.1.3 Variable speed WECS 20
- 2.2 Permanent magnet synchronous generator 23

2.3 Power converter system ... 25
  2.3.1 Diode bridge rectifier ... 27
  2.3.2 Boost converter ... 28
  2.3.3 Full-bridge converter ... 29
  2.3.4 Resonant converter ... 29
2.4 Grid-side inverter ... 30
  2.4.1 Voltage source inverter ... 30
  2.4.2 Current source inverter ... 32
2.5 Summary ... 35
References ... 36
Chapter 3 ... 39
3.1 Background ... 40
3.2 Wind turbine aerodynamic characteristics ... 40
3.3 Existing MPPT schemes ... 41
  3.3.1 TSR and PSF control ... 41
  3.3.2 Perturbation & observation (P&O) ... 42
  3.3.3 One-Power-Point MPPT tracking ... 44
3.4 Proposed optimized MPPT algorithm ... 45
3.5 Simulation results ... 48
  3.5.1 Simulation results with linear wind speed changes ... 51
  3.5.2 Simulation results with a Realistic Wind Profile ... 54
3.6 Summary ... 56
References ... 58
Chapter 4 ... 60
4.1 Background ... 61
4.2 Three-phase PMSG based wind turbine emulator system ... 63

4.3 Analysis of the H-Bridge converter 68

4.3.1 H-bridge converter modelling 68

4.3.2 Comparative study of the boost converter and the H bridge converter 69

4.4 Control of the HSFB 76

4.5 Simulation and experimental results 77

4.6 Summary 80

References 82

Chapter 5 85

5.1 Background 86

5.2 A five phase PMSG based wind turbine emulator system 86

5.3 Resonant converter 87

5.3.1 Series resonant converter 88

5.3.2 Parallel resonant converter 91

5.3.3 Series-parallel resonant converter 94

5.4 Comparative study between the HSFB converter and the LCC resonant converter 97

5.5 Control and design method 101

5.5.1 MPPT tracking 101

5.5.2 LCC resonant converter design 103

5.6 System Simulink results and practical experiments 106

5.7 Passive component hardware specification 111

5.8 LCC resonant converter efficiency analysis 112

5.9 Summary 113

References 114

Chapter 6 117

6.1 Background 118

6.2 DC wind farm topology ... 118

6.3 Proposed WECS and control ... 120

6.3.1 System configuration description ... 120

6.3.2 Control of the proposed WECS ... 122

6.4 System simulink results and practical experimentation ... 123

6.4.1 Simulation results ... 126

6.4.2 Practical implementation of the proposed WECS ... 131

6.5 Summary ... 137

References ... 138

Chapter 7 ... 140

7.1 Background ... 141

7.2 The system configuration (current source converter) ... 143

7.3 Proposed De-loading Control Scheme ... 144

7.3.1 Pitch Control ... 146

7.3.2 DC/DC converter control ... 147

7.3.3 DC chopper control ... 148

7.4 Simulation and experiment results ... 149

7.4.1 Simulation results ... 149

7.4.2 Experimental results ... 156

7.5 Summary ... 163

References ... 164

Chapter 8 ... 166

8.1 General conclusion ... 166

8.2 Author’s contribution ... 168

8.3 Suggestions for future research ... 169

Appendices ... 171

Appendix A Passive component hardware design 172
- A.1 AC resonant inductor design 172
- A.2 DC filtering inductor design 178
- A.3 Power transformer design 181

Appendix B Test rig structure 185
- B.1 Test rig 185
- B.2 Test rig components 187

Appendix C Programme code 203
- C.1 LCC MPPT tracking and DC link voltage control 203
- C.2 LCC voltage control and DC chopper control 206
- C.3 Wind turbine control and pitch control 211

Appendix D List of tables and figures 213
- D.1 List of figures 213
- D.2 List of tables 218

Appendix E Summary of relevant published work by the author 219

Chapter 1

Introduction

Recently, wind energy has grown rapidly in the world since it is a free, clean, renewable fuel (wind), mature technology and because of the rising prices of fossil fuel. It is considered one of the promising alternative sources of electrical power. Wind power technology has also been rapidly developed in areas of power conversion, collection, and transmission technology, which make wind power more competitive than other energy sources.

1.1 Wind Energy

Nowadays, wind power as an alternative renewable energy source receives much more attention due to global warming and the energy crisis. It is known that fossil fuels such as coal, oil, and gas produce carbon dioxide which results in the greenhouse effect; also they are non-renewable and limited in supply. Windmills have been used for at least 3000 years [1.1], mainly for pumping water or grinding grain. The use of windmills (or wind turbines) to generate electricity can be traced back to the late nineteenth century. The 12 kW dc windmill generator was constructed by Brush in the USA, 1888, and the research was taken by LaCour in Denmark in the 1890’s. The development of wind energy was excited by the price of oil and concern about limited fossil fuel resources in 1973. The use of wind power is being promoted in many countries. In the European Union (EU), 32 GW of renewable power capacity was installed during 2011, which accounts for 71.3% of new power capacity installation (45 GW), while 9.6 GW of wind power capacity (worth some €12.6 billion) was installed in the EU in 2011. Wind power accounted for 21.4% of the total 2011 power capacity installation. A total of 94 GW wind power capacity is now installed in the EU, which is an increase of 11% on the previous year [1.2].

The total installed global wind energy capacity was 197 GW at the end of 2010, which increased by 24.1% during the year. China now has 44.7 GW of wind power, which is the largest installed wind power capacity country in the world. Figure 1.1 shows the top ten countries for installed wind power capacity up to December 2010 [1.3].

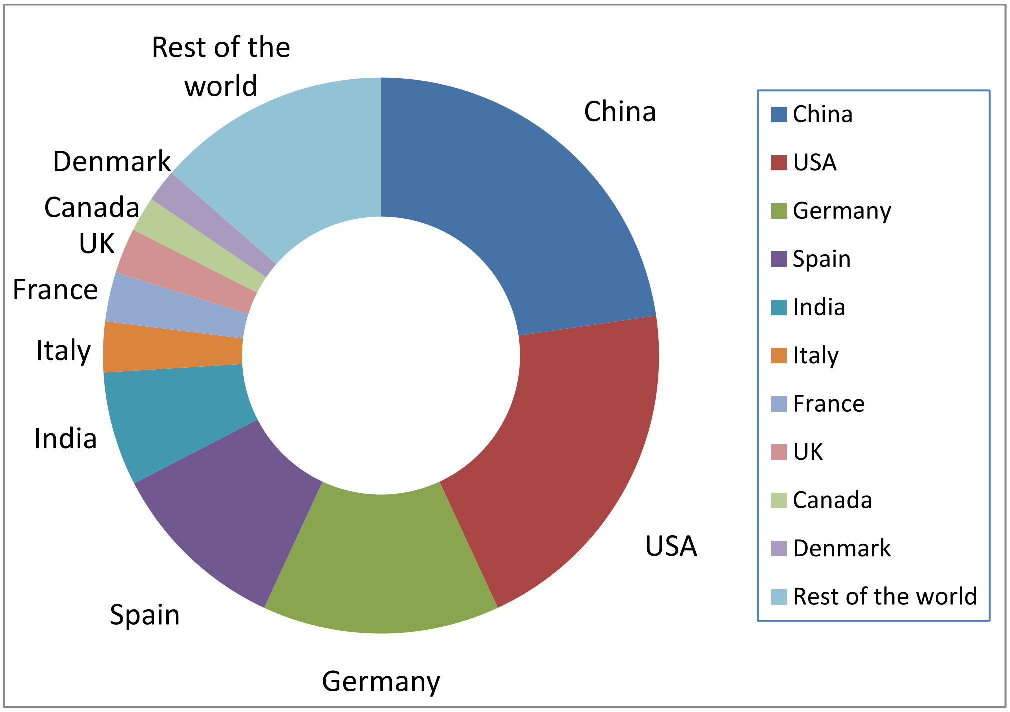

Figure 1.1 Top 10 cumulative installed wind capacity December 2010

1.1.1 Variability and Intermittency

The amount of wind power captured by a wind turbine depends on the wind speed. The wind speed is constantly varying. Sometimes the wind power plant stands idle when there is no wind. Thus wind power is variable and intermittent, which cannot be readily despatched. Because electrical generation and consumption must remain instantaneously in balance to maintain grid stability, it is a challenge to incorporate large amounts of wind power onto the grid due to its variability and intermittency. Also the intermittency and non-dispatchable nature of wind power increases costs for regulation and incremental operating reserve. An electricity system with large wind capacity requires more spinning reserve (plants operating at less than full-load) to regulate for variability of the wind power.

1.1.2 Penetration

Wind power penetration is the amount of energy produced by wind power as a percentage of the total available energy used. As the installed wind power capacity increases, large amounts of wind power can be incorporated onto the grid. There is no generally accepted maximum level of wind power penetration. The constraint on increasing wind power penetration is not inherently a technical problem with wind technology. It depends on the existing generating plants, pricing mechanisms, capacity for storage or demand management, and other factors [1.4].

Wind power penetration can be specified for different durations of time (years or days). A number of countries are beginning to achieve relatively high levels of wind power penetration in their electricity grids. On an annual basis, wind power is estimated to be capable of supplying the equivalent of approximately 26% of Denmark's electricity demand, Portugal-17%, Spain-15%, Ireland-14%, and Germany-9%. In the United States in 2011, wind power penetration was a small percentage, which was estimated at 2.9%. For shorter durations (days), the penetration levels can be much higher. Portugal has had a penetration level of 61% [1.5].

1.1.3 Economics

Wind power that is incorporated into the grid is economical. The cost of generating electricity comprises capital cost, running cost, and the cost of financing. Wind power has a moderate capital cost which accounts for 75% to 90% of the total cost for onshore projects. The capital cost consists of the cost of construction of the turbine and transmission facilities, etc. Figure 1.2 shows the capital cost breakdown of a typical 5 MW onshore project [1.6].

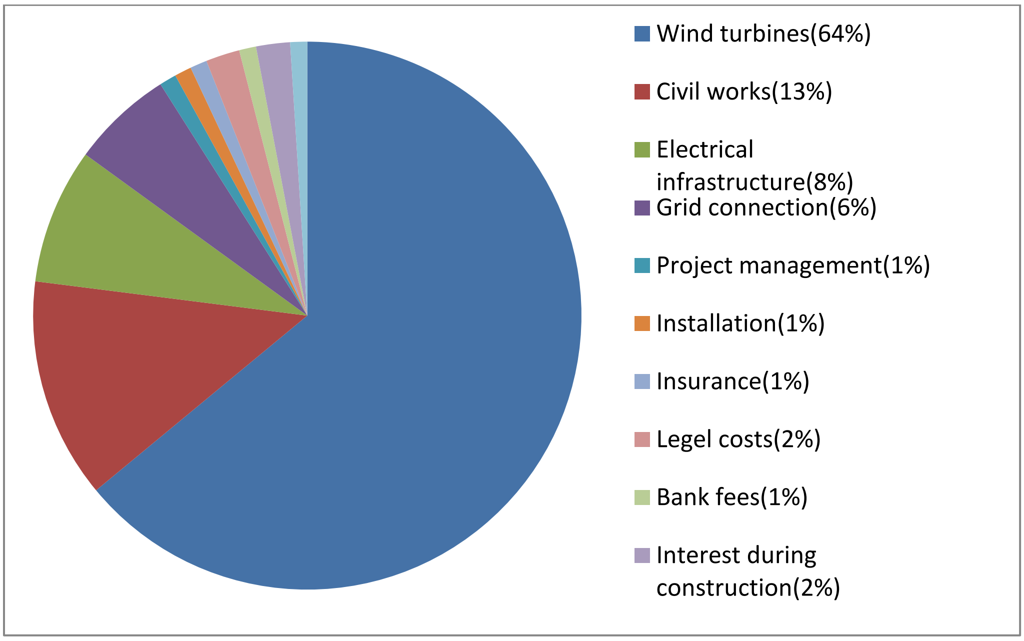

Figure 1.2 The capital cost breakdown of a typical 5 MW onshore project

While wind power has lower running costs than fossil fuels (such as coal, natural gas, and oil), since the wind is a free, clean and a renewable fuel, the price of fossil fuels has risen due to their non-renewability and limited supply.

Although wind power costs vary among the different countries, the cost trend is that wind energy is becoming cheaper as technology improves, which includes more economically made components and new designs. The cost of financing is also falling as lenders gain more confidence in wind technology. According to the 2011 report from the American Wind Energy Association, the cost of wind power has dropped to 5 to 6 cents per kilowatt-hour over the past two years, which is 2 cents cheaper than coal-fired electricity. In addition, wind power emits no air pollution unlike fossil fuel power plant. Considering the cost of pollution and rising fossil fuel prices, wind power is becoming more competitive than fossil fuel power.

1.2 Wind energy in the UK

Wind resources are rich in the UK which is estimated to have over a third of Europe's total offshore wind resource. The available offshore wind resource is equivalent to three times the electricity needs of the nation at current electricity consumption rates when the wind blows [1.7].

The first wind farm in the UK was built at Delabole in Cornwall in 1991. It consists of 10 turbines each with a 400kW maximum capacity. Renewable wind energy contributes 2.2% of the UK's electricity supply, which was the largest renewable generation source after hydropower in 2007 [1.8]. Currently, there are 311 operational onshore wind farms in the UK with a total capacity of 4.5 GW and 16 offshore wind farms with a total capacity of 1.8 GW. The detailed wind energy statistics regarding quantity and capacity of wind farm in the different UK countries are summarized in Table 1.1. A further 3.88 GW of capacity which involves 1.5 GW onshore and 2.36 GW offshore is being constructed, while 5.2 GW of projects (3.99 GW onshore plus 1.22 GW offshore) have consent and 11.47 GW (7.99 GW onshore plus 3.48 GW offshore) is in planning [1.9]. The installed capacity of wind power in the UK is increasing every year. Figure 1.3 shows the graph of UK installed wind power capacity from 1990-2011. The UK is ranked as the world's eighth largest producer of wind power [1.10]. The target is to generate 15% of all the UK's energy from renewable sources by 2020. Onshore and offshore wind together can deliver 30% of the UK's electricity supply by 2020 and be part of the radical decarbonisation economy by 2030 [1.11].

Table 1.1 Operational wind farms statistics in the UK

	Onshore	Capacity (MW)	Offshore	Capacity (MW)
England	117	926.96	13	1698.20
Northern Ireland	31	387.33	N/A	N/A
Scotland	127	2770.73	1	10.00
Wales	36	413.55	2	150.00
Total	311	4498.57	16	1858.2

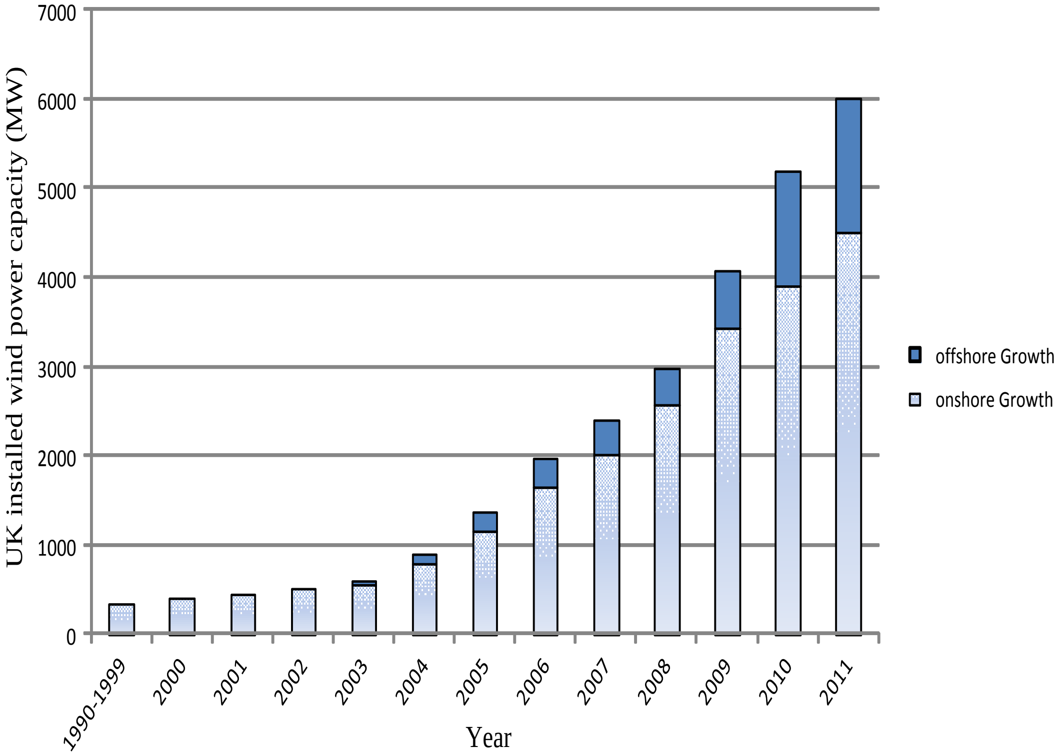

Figure 1.3 UK installed wind power capacity 1990-2011 (operational)

1.3 Wind power collection and transmission technologies

Electric power generated by wind turbine generators is required to be transmitted to the utility grid that services customers. The whole wind farm electrical system consists of a medium voltage electrical collection grid within the wind farm and a high voltage electrical transmission system to deliver the power to the grid. Different layouts exist for onshore and offshore wind farms.

1.3.1 Wind farm collection systems

From the collection system point of view, a wind farm can be divided into ac and dc wind farms. The choice of ac and dc depends on many factors such as wind turbine types (PMSG or DFIG), system control stability, system cost, etc.

i. AC wind farm system

Since wind turbine power is generated as an alternating current (ac) and the utility grid is ac, conventional wind farms use an ac system to facilitate connection. For ac systems, the collection grid begins with a transformer at each wind turbine, which is usually located in the base of the tower, to step up the generation voltage level (typically 690 volts) to a medium voltage, typically 25 to 40 kV. The collection grids are always medium voltage, because standardized equipment is available at competitive prices and higher voltage. 50Hz/60Hz transformers are too big to fit into the tower cross section. For wind farms, they are always located long distances from the transmission grid, thus the collection grid voltage is stepped up to a transmission voltage of 130-150 kV to improve transmission efficiency. An additional bulky 50Hz/60Hz transformer is used in the offshore substation to step up the voltage to the transmission voltage level.

ii. DC wind farm system

In a dc wind farm system the internal ac collection grid is replaced with a dc collection grid. For both the wind farm topologies, an ac/dc rectifier, which could either be an uncontrolled rectifier (diode rectifier) or a controlled rectifier (IGBT rectifier), is used to convert ac power to dc power. A three-phase inverter and a 50/60Hz transformer are needed to step up the generation voltage level to the collection grid level for the ac wind farm system, while a dc/dc converter is used to boost the generation voltage level for the dc wind farm system. A dc/dc converter is the key component to realize internal dc grid connection. Some of the dc/dc converter topologies used in dc wind farms are the boost converter, full bridge converter, and resonant converter. They readily step up voltage with an intermediate transformer. Compared to the three-phase inverter, the dc/dc converter has a simple topology and is easy to control. The traditional 50/60Hz bulky transformer used in the ac collection grid can be replaced with a medium or high frequency small volume transformer. For wind farms, especially offshore wind farms, component weight and volume are key issues. Higher component weight and volume increases the space, and tower and offshore platform costs. The dc wind farm topology may become the preferred wind farm configuration choice.

1.3.2 Wind power transmission systems

For the wind power transmission system, there are two available technology options: high-voltage ac (HVAC) and high-voltage dc (HVDC). The selection is related to the system cost, transmission distance, etc.

i. HVAC transmission system

HVAC transmission is preferable for large wind farms due to its mature operational and protection technologies [1.12-13]. HVAC systems are considered the most economical option for distances shorter than 50 km [1.10][1.14-16]. HVAC and HVDC have similar costs between 50 and 80 km. While unlike air insulated overhead lines and HVDC insulated cable, there are limits on HVAC cable lengths due to capacitance distributed along the entire cable length. The longer the cable, the larger the capacitance. Larger capacitance causes higher charging current to flow along the cable length. The charging current is given by the formula [1.17].

$$I_c = 2\pi fCE \tag{1.1}$$

where f is frequency, C is cable capacitance which is a function of cable geometry and insulation type (XLPE insulation has the lowest C of the most commonly used insulation alternatives in HVAC cables), and E is voltage.

From equation (1.1), the charging current is increased due to the larger cable capacitance and high voltage level. The charging current accounts for part of the cable rated capacity, which reduces the cable load carrying capability. The cable capacitance can also cause over-voltages, high harmonic currents and undesirable resonances, and may require special circuit breakers with high capacitance current switching capability which must be considered in the design of the terminal substation equipment. As the cable length increases (longer than 80 km), an HVAC system becomes more challenging and costly compared to an HVDC system. Thus HVDC is the preferred technology for longer distances.

ii. HVDC transmission system

Electric power transmission was originally developed with direct current. The first commercial electricity generated (by Thomas Alva Edison) was direct current electrical power in the 1880's [1.18]. The first electricity transmission systems were also direct current systems. A major problem was that dc power could not be transmitted over long distances at low voltage levels, thus ac transmission systems pioneered by Nikola Tesla were used due to the availability of ac transformers and the development and improvement of induction motors at the beginning of the 20th century. The transformer can readily step up ac voltage to a high-voltage level, which allows efficient long distant power transmission. Nevertheless, it was possible to transmit dc power at high voltages and over long distance when high voltage valve technology was developed. High-voltage direct current (HVDC) technology began. In 1950, a 116 km experimental HVDC transmission line was commissioned from Moscow to Kasira at 200 kV [1.19]. The first commercial HVDC line was built in 1954, which was a 98 km submarine cable with ground return between the island of Gotland and the Swedish mainland [1.20]. Subsequently, HVDC transmission system installations have increased rapidly around the world due to HVDC transmission system advantages. The advantages of HVDC compared to HVAC are summarised as:

1) DC power can be transmitted over long distances with lower capital costs and lower losses than HVAC transmission systems. From equation (1.1), the charging current I_c is zero in the steady state in dc circuits since frequency f = 0. This increases transmission capacity with the same conductor for long distance transmission.

2) For ac system connection, the two interconnected ac systems must operate synchronously, while dc transmission does not have such a limitation. It can be used to interconnect asynchronous systems. In Japan, half the country is a 60Hz network, the other is 50 Hz. With HVAC, it is impossible to connect two asynchronous systems directly. There are many back-to-back HVDC links built around the world [1.21-23].

3) In order to improve power system stability, HVDC links can be used within synchronous ac systems. Larger interconnected ac systems have increased system complexity from the operational point of view, which has consequences such as large blackouts. There have been large blackouts in the USA and Europe [1.24]. HVDC links can control power flow from one part of the system to another, thereby it has a ‘firewall’ function in preventing cascading ac system failures or even blackouts in the grid.

Currently, HVDC transmission technology can be classified into three types, depending on the converter configuration and power semiconductor type. For the first type, HVDC transmission using Line-Commutated Current-Source Converters (LCC) based on mercury arc valves, was introduced in the USSR in 1950 (Kashira to Moscow) and in Sweden in 1954 (Gotland). The first HVDC project based on thyristor valves was the Eel River scheme in New Brunswick, Canada [1.25]. The installed capacity of HVDC systems based on the thyristor has increased rapidly due to the superior reliability of thyristor technology. Thyristors can be rated up to 8.5kV, 4KA. LCC-HVDC is a mature technology that provides efficient, reliable and cost effective power transmission for many applications. Generally, most large wind farms especially offshore wind farms are located long distances from population centres. The wind power is collected locally and bulk transmitted to the ac grid. Two LCC-HVDC topologies have been proposed for doubly-fed induction generator (DFIG)-based wind farms [1.26-27]. However, LCC-HVDC technology suffers from several inherent weaknesses:

1) The active and reactive power control are coupled due to the thyristor-based converter which cannot be self-commutated, thereby independent reactive power support to the grid cannot be achieved. In addition, the converter station always consumes reactive power due to existing passive components, thus reactive power compensation such as with large ac capacitors at the converter station are required, which increases converter station system cost and space.

2) Commutation failure is possible due to ac system disturbance, especially with a weak ac system connection.

The second type of HVDC transmission uses force-commutated voltage-source converters and is attractive as a relatively new technology. The first commercial VSC-based HVDC transmission system for wind power was installed in 1999 (Gotland HVDC Light project, Sweden, ±80kV, 2*70km submarine cables) [1.28]. Subsequently, the installed VSC-HVDC system capacity has been increasing worldwide [1.29-31]. Compared to the natural commutated thyristor based converters, voltage source converters utilise forced commutated switches, such as gate turn-off thyristors (GTOs) or insulated-gate bipolar transistors (IGBTs), which have one more freedom of control. Thus VSC-based HVDC technology can provide flexible reactive power to the grid during normal and fault conditions [1.32]. As wind power penetration levels increase, HVDC with flexible reactive power control capability is appreciated by utility grid controllers [1.33]. It is especially attractive for the wind power transmission to ac systems. VSC-based HVDC for connecting wind farms to the grid is described in [1.32][1.34-37]. However, VSC-based HVDC has several inherent drawbacks regarding power loss, capacity, cost, and dc link short circuit recovery [1.38].

A new hybrid HVDC topology for large DFIG-based offshore wind farms is proposed in reference [1.39]. The rectifier is based on a line-commutated-converter with a static synchronous compensator (STATCOM), while the inverter is a current source inverter, which uses forced-commutated devices such as gate turn-off thyristors (GTOs) or integrated gate-commutated thyristors (IGCTs). It combines the advantages of the two mentioned HVDC technologies. The thyristor rectifier is expected to reduce costs and power losses. Compared with a VSC-HVDC scheme for high power rating, the rectifier a with STATCOM-LCC scheme is still likely to have lower costs and power losses [1.40]. Compared with a conventional LCC-HVDC scheme, the CSI using forced-commutated devices can provide flexible reactive power control to the utility grid. In addition, the proposed CSI scheme provides excellent short circuit protection, in contrast to the voltage source inverter.

In this chapter, wind power characteristics and collection and transmission technologies are investigated. Most wind farms (onshore and offshore) are located a long distance from an ac grid. It is important to collect energy locally and bulk transmit it to the ac grid. A conventional ac grid is used in most wind farms due to the mature ac grid operational and protection technologies. As transmission cable lengths increase, however, this approach is problematic in terms of system volume, cost and cable losses. A VSC-based dc transmission WECS is more attractive than a ac grid-based WECS due to its decoupled active and reactive power control. However the capacitor used on the high voltage side has disadvantages associated with lifetime, volume and cost. Further, during a dc link short circuit fault, capacitor current rating may be exceeded. Conventional ac breakers are not applicable due to the lack of a zero current crossing point and slow switching time. A dc breaker is more expensive and has a small capacity. The objective of research reported in this the thesis is to develop a current source dc/dc converter based multi-terminal dc WECS, which has advantages in terms of system volume, cost, losses, control and protection.

References

[1.1] T. Burton, D. Sharpe, N. Jenkins, and E. Bossanyi, *Wind Energy Handbook*: John Wiley & Sons, 2001.

[1.2] *European wind energy association*. Available: http://www.ewea.org/

[1.3] *Global wind energy council*. Available: http://www.gwec.net/

[1.4] J. P. Lamb, *The Greening of IT: How Companies Can Make a Difference for the Environment*: IBM Press/Pearson, 2009.

[1.5] *2010 wind technologies market report*. Available: www1.eere.energy.gov/wind/pdfs/51783.pdf

[1.6] *British wind energy association*. Available: http://www.bwea.com/ref/econ.html

[1.7] J. Oswald, M. Raine, and H. Ashraf-Ball, "Will British weather provide reliable electricity?," *Energy Policy*, vol. 36, No. 8, pp. 3212-3225, 2008.

[1.8] *British wind energy association. onshore wind.* Available: http://www.bwea.com/onshore/index.html.

[1.9] *British wind energy association.* Available: http://www.bwea.com/statistics/.

[1.10] T. Ackermann, *Wind power in power systems*: John Wiley, 2005.

[1.11] *The Committee on Climate Change. ' Building a Low Carbon Economy'.* Available: http://www.theccc.org.uk/reports/.

[1.12] H. Brakelmann, "Efficiency of HVAC power transmission from offshore-windmills to the grid," in *Power Tech Conference Proceedings, 2003 IEEE Bologna*, 2003, p. 6 pp. Vol.2.

[1.13] A. B. Morton, S. Cowdroy, J. R. A. Hill, M. Halliday, and G. D. Nicholson, "AC or DC? economics of grid connection design for offshore wind farms," in *AC and DC Power Transmission, 2006. ACDC 2006. The 8th IEE International Conference on*, 2006, pp. 236-240.

[1.14] T. Ackermann, "Technical/Economic Feasibility of Different Technologies for Transmission. System Between Offshore Wind Farm and the Shore," September, 2006.

[1.15] S. D. Wright, A.L. Rogers, J. F. Manwell, and A. Ellis, "Transmission Options for Offshore Wind Farms in the United States," in *Proceedings of the AWEA Annual Conference*, 2002, pp. 1-12.

[1.16] *Electrical collection and transmission systems for offshore wind power [electronic resource] : preprint / J. Green ... [et al.]*. Golden, CO :: National Renewable Energy Laboratory, 2007.

[1.17] *Transmission issues for offshore wind farms with specific application to siting of the proposed cape wind project*. Available: http://www.nae.usace.army.mil/projects/ma/ccwf/app3c.pdf

[1.18] R. Rudervall, "High Voltage Direct Current (HVDC) Transmission Systems Technology Review Paper," *Energy week* vol. 16, No. Ccc, pp. 7-8.

[1.19] M. W. Mustafa and A. F. A. Kadir, "A modified approach for load flow analysis of integrated AC-DC power systems," in *TENCON 2000. Proceedings*, 2000, pp. 108-113 vol.102.

[1.20] S. Lee Wei, A. Razani, and N. Prabhakaran, "Control of High Voltage Direct Current (HVDC) bridges for power transmission systems," in *Research and Development (SCOReD), 2010 IEEE Student Conference on*, 2010, pp. 430-435.

[1.21] J. Arrillaga, *High Voltage Direct Current Transmission*, 2nd Edition ed. London, 1998.

[1.22] M. P. Bahrman and B. K. Johnson, "The ABCs of HVDC transmission technologies," *Power and Energy Magazine, IEEE*, vol. 5, No. 2, pp. 32-44, 2007.

[1.23] V. K. Sood, *HVDC and FACTS controllers: applications of static converters in power systems*: Kluwer Academic, 2004.

[1.24] L. Zhang, "Modeling and control of VSC-HVDC Links connected to weak AC systems," Royal Institute of Technology, Stockholm, Sweden, 2010.

[1.25] *50 years of HVDC: 1954-2004*. Available: Http://www.abb.com

[1.26] X. Dawei, R. Li, J. R. Bumby, P. J. Tavner, and S. Yang, "Coordinated control of an HVDC link and doubly fed induction generators in a large offshore wind farm," *Power Delivery, IEEE Transactions on*, vol. 21, No. 1, pp. 463-471, 2006.

[1.27] S. V. Bozhko, R. Blasco-Gimenez, L. Risheng, J. C. Clare, and G. M. Asher, "Control of Offshore DFIG-Based Wind Farm Grid With Line-Commutated HVDC Connection," *Energy Conversion, IEEE Transactions on,* vol. 22, No. 1, pp. 71-78, 2007.

[1.28] N. Flourentzou, V. G. Agelidis, and G. D. Demetriades, "VSC-Based HVDC Power Transmission Systems: An Overview," *Power Electronics, IEEE Transactions on,* vol. 24, No. 3, pp. 592-602, 2009.

[1.29] K. Eriksson, "Operational experience of HVDC Light," in *AC-DC Power Transmission, 2001. Seventh International Conference on (Conf. Publ. No. 485)*, 2001, pp. 205-210.

[1.30] A. Petersson and A. Edris, "Dynamic performance of the Eagle Pass back-to-back HVDC Light tie," in *AC-DC Power Transmission, 2001. Seventh International Conference on (Conf. Publ. No. 485),* 2001, pp. 220-225.

[1.31] S. G. Johansson, L. Carlsson, and G. Russberg, "Explore the power of HVDC light® - a web based system interaction tutorial," in *Power Systems Conference and Exposition, 2004. IEEE PES*, 2004, pp. 839-842 vol.832.

[1.32] X. Lie, Y. Liangzhong, and C. Sasse, "Grid Integration of Large DFIG-Based Wind Farms Using VSC Transmission," *Power Systems, IEEE Transactions on,* vol. 22, No. 3, pp. 976-984, 2007.

[1.33] H. M. El-Helw and S. B. Tennakoon, "Evaluation of the suitability of a fixed speed wind turbine for large scale wind farms considering the new UK grid code," *Renewable Energy,* vol. 33, No. 1, pp. 1-12, 2008.

[1.34] P. Bresesti, W. L. Kling, R. L. Hendriks, and R. Vailati, "HVDC Connection of Offshore Wind Farms to the Transmission System," *Energy Conversion, IEEE Transactions on,* vol. 22, No. 1, pp. 37-43, 2007.

[1.35] S. M. Muyeen, R. Takahashi, and J. Tamura, "Operation and Control of HVDC-Connected Offshore Wind Farm," *Sustainable Energy, IEEE Transactions on,* vol. 1, No. 1, pp. 30-37, 2010.

[1.36] O. A. Giddani, G. P. Adam, O. Anaya-Lara, G. Burt, and K. L. Lo, "Control strategies of VSC-HVDC transmission system for wind power integration to meet GB grid code requirements," in *Power Electronics Electrical Drives*

Automation and Motion (SPEEDAM), 2010 International Symposium on, 2010, pp. 385-390.

[1.37] N. R. Chaudhuri and A. Yazdani, "An aggregation scheme for offshore wind farms with VSC-based HVDC collection system," in *Power and Energy Society General Meeting, 2011 IEEE*, 2011, pp. 1-8.

[1.38] I. Erlich and H. Brakelmann, "Integration of Wind Power into the German High Voltage Transmission Grid," in *Power Engineering Society General Meeting, 2007. IEEE*, 2007, pp. 1-8.

[1.39] Z. Honglin, Y. Geng, and G. Hua, "Grid integration of DFIG-based offshore wind farms with hybrid HVDC connection," in *Electrical Machines and Systems, 2008. ICEMS 2008. International Conference on*, 2008, pp. 2579-2584.

[1.40] B. R. Andersen and X. Lie, "Hybrid HVDC system for power transmission to island networks," *Power Delivery, IEEE Transactions on,* vol. 19, No. 4, pp. 1884-1890, 2004.

Chapter 2

Wind Energy Conversion Systems

This chapter introduces the electrical components of a wind energy conversion system, which include the wind turbine generator, dc/dc converter, and grid inverter. Three different wind turbine generator concepts are described. The topologies and control algorithms of the voltage source inverter (VSI) and current source inverter (CSI) are studied.

2.1 Wind turbine generator concepts

According to the rotation speed, the wind turbine generator concept can be classified as fixed speed, limited speed, and variable speed. The three have different topologies and generator types. A variable speed wind turbine generator can be classified into two types based on the rating of the power converter connected to the generator. One is a wind turbine generator with a partial-scale power converter (DFIG system). The other is a wind turbine generator with full-scale power converter (PMSG system and SCIG system).

2.1.1 Fixed speed WECS

A fixed speed wind turbine generator system consists of a wind turbine, multiple-stage gearbox and a squirrel cage induction generator (SCIG), which is directly connected to the ac grid through a transformer. The SCIG can only operate in a narrow range around synchronous speed. Figure 2.1 shows the wind energy conversion system (WECS) for a fixed speed scheme. Since the SCIG always absorbs reactive power from the grid, a capacitor bank is installed to provide reactive power compensation as shown in Figure 2.1. This conventional concept was applied by many Danish wind turbine manufacturers during the 1980s and 1990s [2.1], thus it is known as the ‘Danish concept’. This WECS concept has advantages of mechanical simplicity and cheap construction [2.2]. In addition, there is no need for synchronization devices. The power at higher wind speed can be limited through stall control, active stall control, and pitch control [2.3]. The disadvantages of the fixed speed WECS concept can be summarized as follows [2.4-6]:

- The rotation speed is not controllable from the electrical perspective. A SCIG can only operate over a narrow range, almost at constant speed. Thus wind speed fluctuations directly lead to electromechanical torque variations, which cause high mechanical and fatigue stresses on the mechanical system (turbine blades, gearbox, and generator).

- A three-stage gearbox in the drive train is necessary for the fixed-speed concept. The gearbox is one of the most expensive WECS components. The higher-than-expected failure rates add to the cost of wind energy.

- A stiff power grid is required to enable stable system operation.
- It cannot provide reactive power support without an additional parallel capacitor bank.

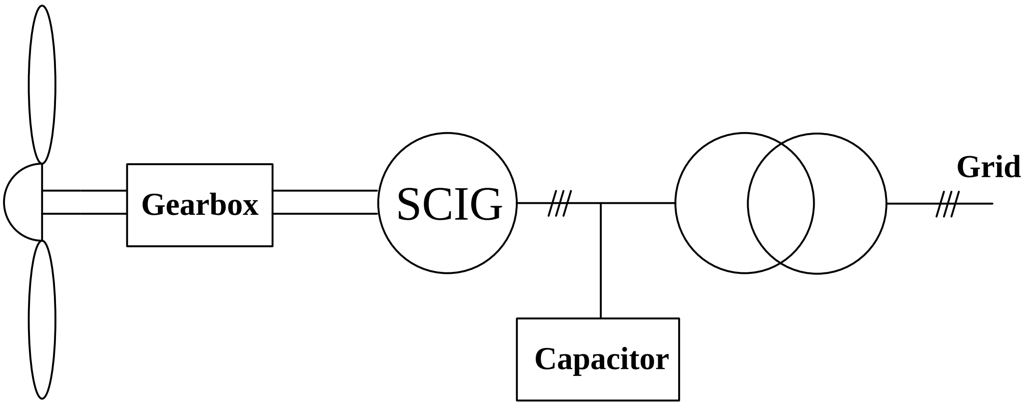

Figure 2.1 Scheme of fixed speed WECS.

2.1.2 Limited speed system

The limited speed system has been applied by the Danish manufacturer Vestas since the mid 1990's [2.7], and is known as the OptiSlip concept. Figure 2.2 shows the scheme of a WECS with a limited speed system.

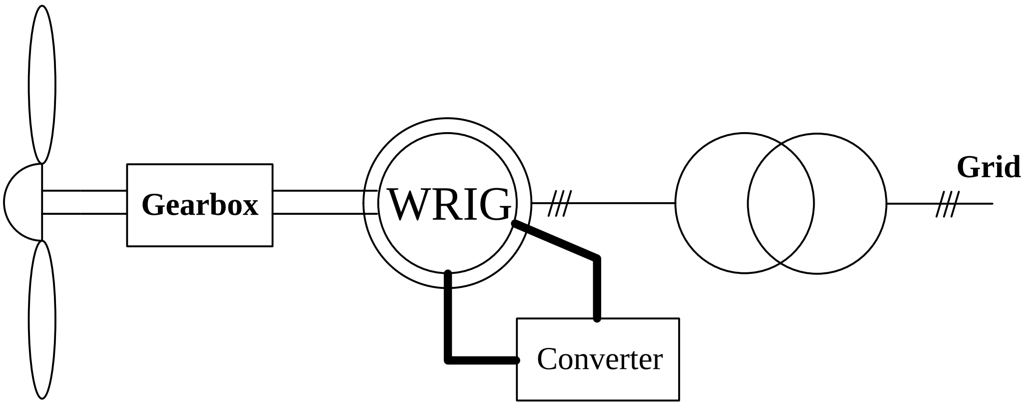

Figure 2.2 Scheme of limited speed WECS.

The system uses a wound rotor inductor generator (WRIG) with rotor resistors which are connected in series with the rotor winding through a power electronic converter mounted on the rotor shaft. The rotor resistance can be changed by controlling the power electronic converter, which allows the WRIG to operate with variable speed. A typical limited variable speed range is less than 10% above synchronous speed

[2.8]. A higher slip denotes more power is dissipated in the rotor resistor. The stator of the WRIG is directly connected to the ac grid, thus a reactive power compensation device and a soft-starter are also required.

2.1.3 Variable speed WECS

The variable speed wind generator concept has been applied to most wind turbines over 1.5 MW output power since the late 1990's. A fixed speed WG cannot be operated at its highest efficiency with a wide range of wind speeds, while a variable speed WG can achieve maximum power tracking with variable wind speeds [2.6][2.9]. In addition, low mechanical stress is imposed on the shaft and drive train due to variable speed operation during wind gusts.

Variable speed WGs can be divided into three types based on the type of generator, namely the SCIG system, DFIG system and PMSG system respectively.

i. Squirrel cage induction generator system

The variable speed SCIG system is shown in Figure 2.3. Compared to the fixed speed SCIG system, a full power converter replaces the capacitor bank and soft starter, which connects the generator to the grid. The advantage of the variable speed SCIG WECS is that the wind turbine is can operate with variable speed as a result of the full power converter. The capacity of the converter should be approximately 120% of the nominal generator power, which increases WECS cost. This disadvantage means high cost when compared to a fixed speed SCIG system.

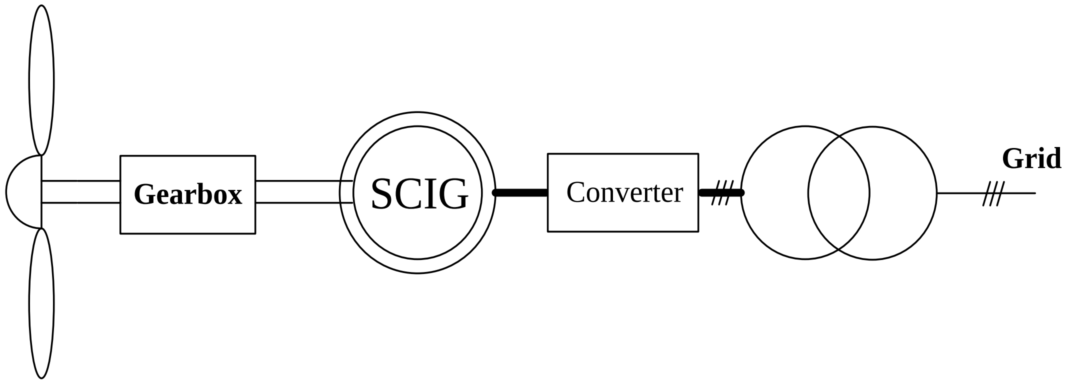

Figure 2.3 Variable SCIG WECS.

ii. Doubly fed induction generator system

The doubly-fed induction generator (DFIG) is widely used for the large wind turbines, which is an important generator for WECS [2.10-11]. This topology accounts for 50% of the wind energy market. The scheme of the variable DFIG WECS is shown in Figure 2.4. The gearbox is still required because a multi-pole low speed DFIG is not technically feasible [2.12]. The DFIG stator is directly connected to the grid, while the three-phase winding rotor is connected to the grid by a power electronic converter through slip rings. The power electronic converter is a back-to-back converter, which allows bidirectional power flow. One end is connected to the rotor and the other to the grid. The wind energy is delivered to the grid through the generator at both super-synchronous and sub-synchronous speeds. The rotor active power is controlled by the rotor side converter current. Generally 25% to 30% of nominal generator power is fed into the grid through the rotor power converter [2.13], which saves on the cost of the power converter. By controlling the rotor active power flow direction, the rotor speed can be varied by approximately ±30% of nominal speed.

For the DFIG, since the grid-side converter is connected to the grid, the stator active power and reactive power can be controlled independently by controlling the rotor current provided by power converter. The grid-side converter can provide flexible reactive power from zero to a value within the converter’s rating, which is independent of generator operation. Thus it can provide voltage support to the grid. Because of the partial-scale power converter and voltage support mentioned, the DFIG with a partial-scale power converter is attractive and popular. However, the DFIG system has some disadvantages [2.14]:

- A multi-stage step-up gearbox is required, which has drawback such as cost, higher-than-expected failure rates, and noise.
- slip rings are also needed for the rotor-side converter, which decreases reliability and increases maintenance.
- It is sensitive and mechanically fragile to grid disturbances and fault conditions, since the generator stator is directly connected to the grid [2.15].

In the case of grid disturbances, a complicated control strategy is required for DFIG ride-through capability. Under grid fault conditions, large rotor currents occur as a result of the large stator currents. Thus high torques are imposed on the wind turbine drive train. The power converter must be protected from these large currents.

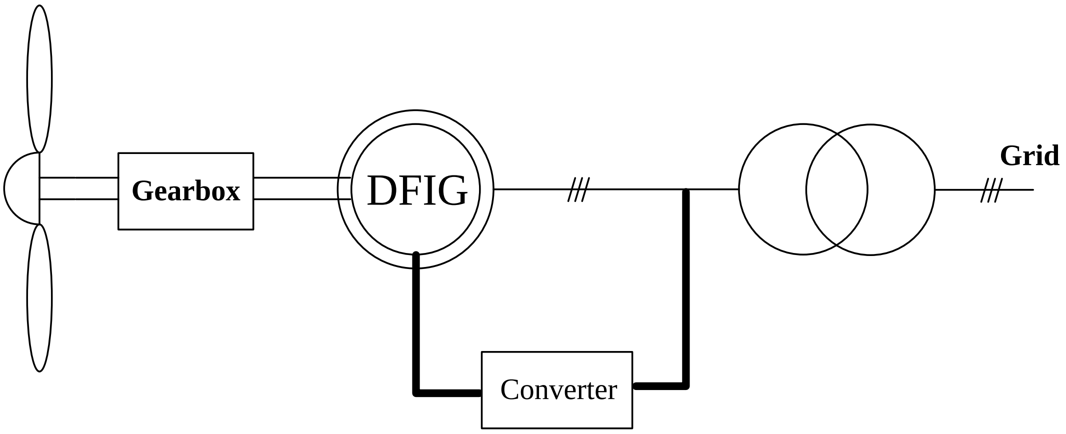

Figure 2.4 Scheme of variable DFIG WECS.

iii. Permanent magnet synchronous generator system

The PMSG is an alternative generator and is integrated to the grid via a full-scale power converter as shown in Figure 2.5.

In terms of the drive train system, a PMSG system can be classified into two types. One type is the gear drive type, which has a gearbox. This system has been used by Spanish company Gamesa and in the GE multi-megawatt series. The other type is direct drive without a gearbox, which Harakosan and Mitsubishi are using in their 2MW wind turbines. The most important difference between the generator types is the rotational speed of the generator. The geared generator can rotate at high speed with a gearbox, while the direct-drive generator rotates at low speed. For a given power, higher torque is produced at low speed in the direct-drive generator. The high torque increases the size and weight of the direct-drive generator, but the direct-drive PMSG WECS has high efficiency, reliability and availability due to the absence of a gearbox. Compared to a DFIG system, a PMSG system uses a full-scale power converter connected to the grid, which decouples generator and grid interaction. Thus the grid-fault ride-through control strategy is less complex. It also can provide flexible reactive power to support a grid voltage dip. Based on considerations of system reliability and stability, the direct-drive PMSG system becomes an attractive and powerful configuration. Therefore it is employed in this research.

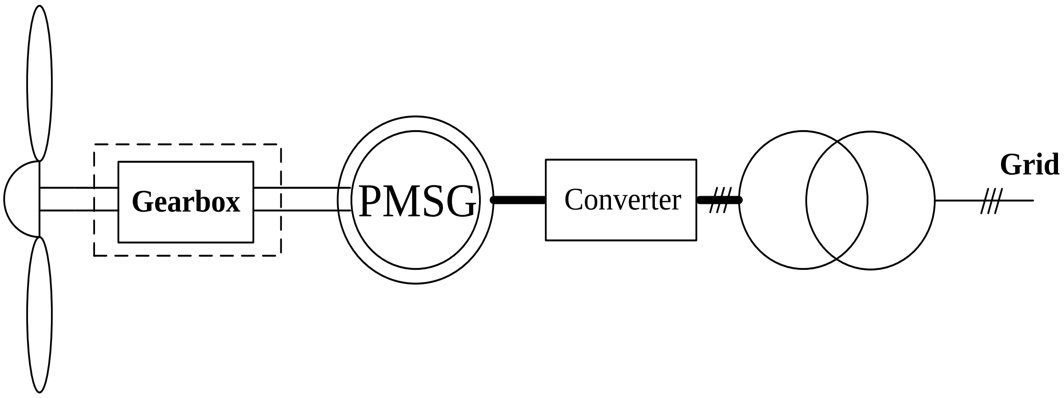

Figure 2.5 Scheme of variable PMSG WECS.

2.2 Permanent magnet synchronous generator

The PMSG has good performance, high efficiency, and is smaller in size when compared to other types of generators, resulting in it receiving much attention in wind energy applications [2.16]. According to the direction of generator flux, PM machines can be classified into three types: radial flux, axial flux and transverse flux. There is no additional power supply for the magnetic field excitation for the PMSG. The permanent magnet on the PMSG rotor produces the magnet field excitation, which avoids magnetizing current through the stator for a constant air-gap flux. The PMSG operates at a higher power factor. Mechanical components such as slip rings are absent, improving reliability.

The electrical model of the PMSG is expressed in the rotor reference frame (q-d frame):

$$\frac{d}{dt}i_d = \frac{1}{L_d}v_d - \frac{R}{L_d}i_d + \frac{L_q}{L_d}p\omega i_q \tag{2.1}$$

$$\frac{d}{dt}i_q = \frac{1}{L_q}v_q - \frac{R}{L_q}i_q + \frac{L_d}{L_q}p\omega i_d - \frac{\lambda p\omega}{L_q} \tag{2.2}$$

Equations (2.1) and (2.2) show the relationship between q and d axis currents and voltages. Electrical torque is described by:

$$T_e = 1.5p\left[\lambda i_q + \left(L_d - L_q\right)i_d i_q\right] \tag{2.3}$$

where (all quantities in the rotor reference frame are referred to the stator)

L_q, L_d	q and d axis inductances
R	resistance of the stator windings
i_q, i_d	q and d axis currents
v_q, v_d	q and d axis voltages
ω	angular velocity of the rotor
λ	amplitude of the flux in the stator phases induced by the permanent magnets in the rotor
p	number of pole pairs
T_e	electromagnetic torque

The mechanical model equations of the PMSG are given by

$$\frac{\mathrm{d}}{\mathrm{dt}}\omega = \frac{1}{\mathrm{J}}(\mathrm{T_e} - \mathrm{T_m} - \mathrm{F}\omega) \tag{2.4}$$

$$\frac{\mathrm{d}\theta}{\mathrm{dt}} = \omega \tag{2.5}$$

where

J	combined inertia of rotor and load
F	combined viscous friction of rotor and load
θ	rotor angular position
T_m	input mechanical torque

The PMSG dynamics are modelled in MATLAB/Simulink based on electrical model equations (2.1)-(2.3) and mechanical model equations (2.4), (2.5). The PMSG input is the mechanical torque signal from the wind turbine. The outputs of PMSG are phase voltages and currents. Figure 2.6 shows the schematic diagram of the MATLAB PMSG block.

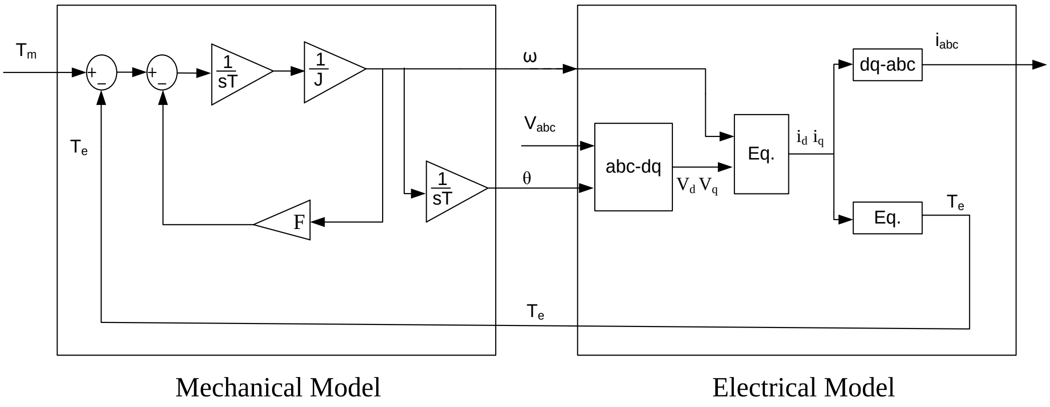

Figure 2.6 The schematic diagram of PMSG block.

2.3 Power converter system

The power electronic converters used in the WECS are receiving more attention due to their flexible controllability and maturing technology. For a wind turbine generator with a full-scale power converter for grid connection, the output voltage (amplitude, frequency, phase angle) is variable as the wind speed changes. It cannot be directly connected to the grid. Thus the ac power should be rectified to dc, then converted to ac power which meets the grid requirement. This process has two conversion stages: ac/dc and dc/ac, as shown in Figure 2.7(a). Due to the low generator voltage, a bulky 50/60Hz transformer is required to step up voltage after the dc/ac stage. In order to avoid the use of a bulky transformer, a configuration which incorporates a dc/dc stage between the ac/dc and dc/ac stages is shown in Figure 2.7(b). The dc/dc stage boosts the dc voltage using dc/dc converters. The possibility of using a matrix converter is not considered because of the low generator voltage being incompatible with transformerless grid level voltages.

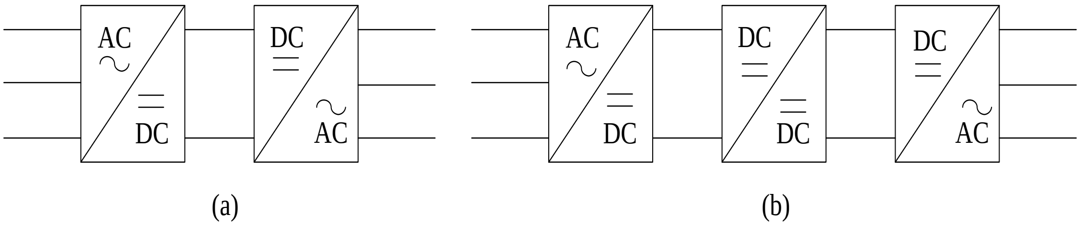

Figure 2.7 the power converter configuration for grid connection (a) ac/dc-dc/ac (b) ac/dc-dc/dc-dc/ac.

For the configuration shown in Figure 2.7(a), the basic topology uses back-to-back converters, which could be either PWM voltage source converters [2.17] or current source converters [2.18]. The rotor speed and reactive power can be controlled independently by the generator-side converter, while the grid-side inverter controls the dc link voltage and reactive power. High power factor is achieved on the generator side and good performance on grid side. But its cost is high and control is complicated. In order to reduce system cost and control complexity of low-power wind turbines, a diode rectifier can replace the ac/dc PWM converter, while the grid side inverter can be VSI or CSI. Maximum power point tracking (MPPT) can still be achieved.

For the configuration shown in Figure 2.7(b), the dc/dc converter can be controlled to maintain the dc link voltage constant or to achieve MPPT depending on the type of ac/dc converter used. A controlled ac/dc rectifier is connected to the generator to track the MPP and regulate constant the dc/dc converter input voltage, while the dc/dc converter is used to regulate its output voltage constant [2.19]. Using a diode rectifier as an ac/dc converter, the dc/dc converter usually tracks the MPP, and the output voltage is regulated by the subsequent dc/ac converter [2.20-21]. There are different dc/dc topologies used in WECS. A boost converter is used for MPPT control and dc link voltage regulation [2.22]. In [2.23], the voltage-output full-bridge dc/dc converter with a VSI inverter is used for WECS grid connection.

Considering system cost, control complexity, and wind farm topology, for low-power turbines a diode rectifier based ac/dc-dc/dc-dc/ac configuration is used in this research. Figure 2.8 shows the wind energy conversion system configuration.

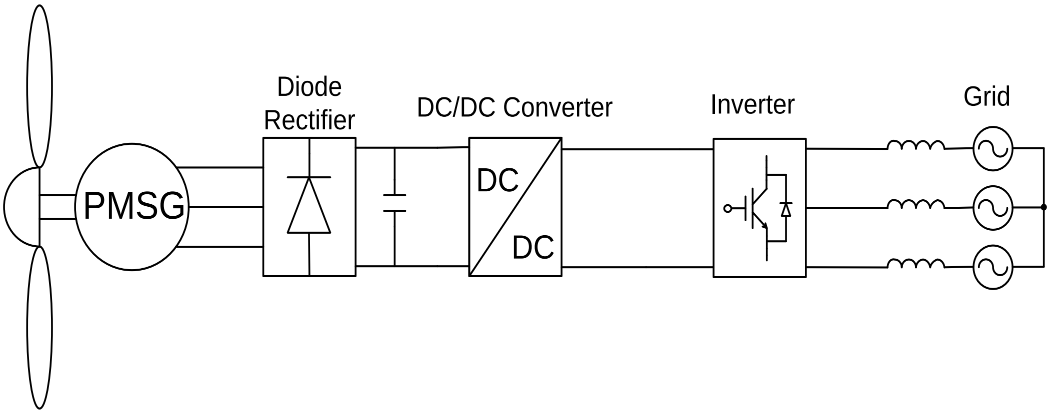

Figure 2.8 The wind energy conversion system configuration used in this research.

2.3.1 Diode bridge rectifier

The diode bridge rectifier consists of six naturally commutated power electronic devices (diodes), which are connected in the full bridge configuration shown in Figure 2.9. It is an ac/dc converter, which converts ac power to dc power.

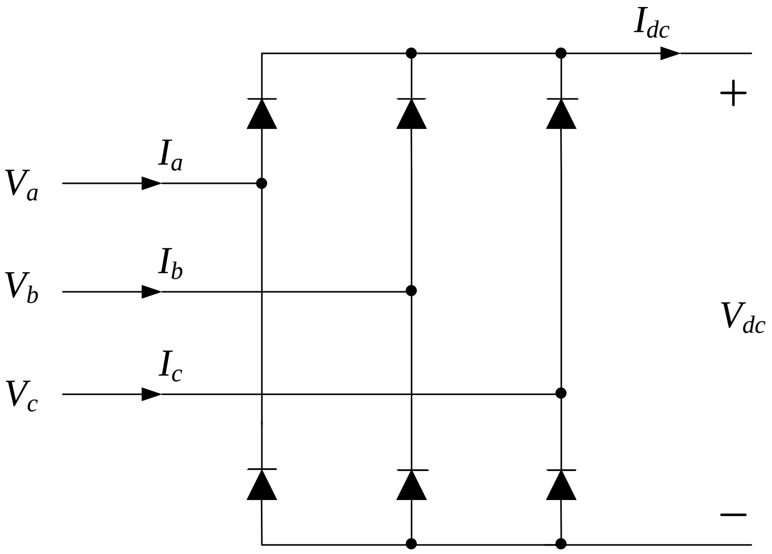

Figure 2.9 Three-phase diode bridge rectifier.

For a three-phase diode bridge rectifier, the mean dc output voltage is calculated by [28]

$$V_{dc} = \frac{3}{\pi}\int_{-\frac{\pi}{6}}^{\frac{\pi}{6}} \sqrt{2}\, V_{LL}\, cos\, \omega t\, d\omega t = \frac{3}{\pi}\sqrt{2} V_{LL} \tag{2.6}$$

where V_{LLmax} is the maximum line-to-line voltage

Assuming that no power is lost within the diode bridge rectifier circuit, the electrical power (P_e) is

$$P_e = 3V_a I_a = V_{dc} I_{dc} \tag{2.7}$$

where V_a, I_a, V_{dc} and I_{dc} are the rms phase voltage and phase current, and dc side voltage and current respectively. From (2.6) and (2.7), the dc side current I_{dc} is

$$I_{dc} = \frac{\pi}{\sqrt{6}} I_a \tag{2.8}$$

Using equations (2.6)-(2.8), the voltage and current between the ac and dc sides of the three-phase diode bridge rectifier can be examined.

2.3.2 Boost converter

The boost converter is a voltage step-up converter, consisting of two semiconductor switches (a diode and a power transistor) and two energy storage elements (an inductor and a dc smoothing capacitor). Figure 2.10 shows the boost converter topology. As the name implies, the output voltage is always greater than the input voltage. When the power transistor is on, the diode is reversed biased, thus isolating the output stage. The input supplies energy to the inductor. When the switch is off, the output stage receives energy from the inductor as well as from the dc input.

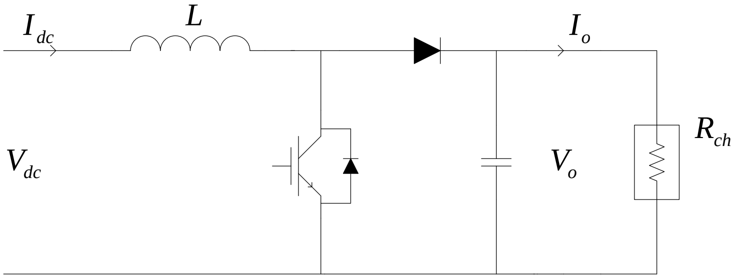

Figure 2.10 The boost converter topology.

In a continuous inductor conduction mode, the relationship between the output V_o and input V_{in} voltages can be derived as

$$\frac{V_o}{V_{in}} = \frac{1}{1-\delta} \tag{2.9}$$

where δ is the switch on-state duty cycle.

2.3.3 Full-bridge converter

The current-output, full-bridge converter used in this research is shown in Figure 2.11. Compared to the conventional boost converter, it can readily step up the low input voltage with a high-frequency intermediate transformer, and also isolate the generator side and dc link. Each wind turbine using a generator and full-bridge converter can be considered as a dc current source due to the converter output inductor L_o. A wind energy conversion system based on the current-source full-bridge converter is investigated and studied in Chapter 4.

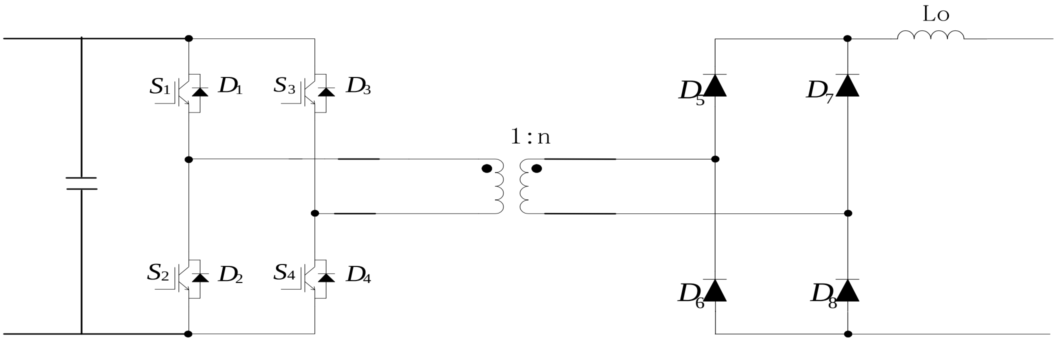

Figure 2.11 The current output full-bridge isolated converter.

2.3.4 Resonant converter

The series-parallel resonant LCC converter is shown in Figure 2.12. It allows high frequency operation with reasonable efficiency, which reduces magnetic component size. Three resonant converters, including series, parallel, and series parallel resonant converters, are explained and investigated in detail and a WECS based on the LCC resonant converter is designed and analyzed in Chapter 5.

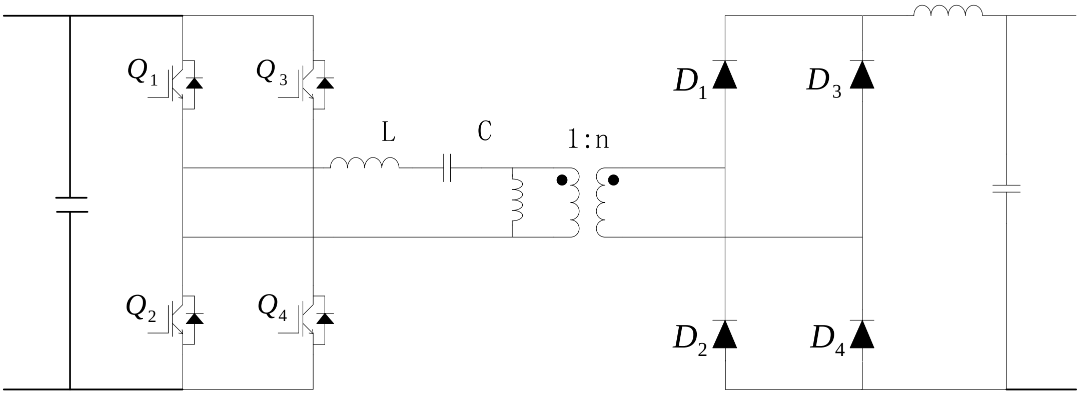

Figure 2.12 Series parallel resonant LCC converter.

2.4 Grid-side inverter

The grid-side inverter interfaces the dc source to the grid. The grid-side inverter has been used widely in renewable energy systems for grid connection. Generally, it can be classified into two types according to the topology: VSI and CSI.

2.4.1 Voltage source inverter

Figure 2.13 shows a simplified schematic of the grid converter, which consists of a three-phase PWM inverter, a dc side capacitor, and series impedances connecting the output of the inverter to the utility grid. Generally, VSI control is based on a synchronously rotating dq reference frame, where the d-axis is orientated to the grid voltage vector.

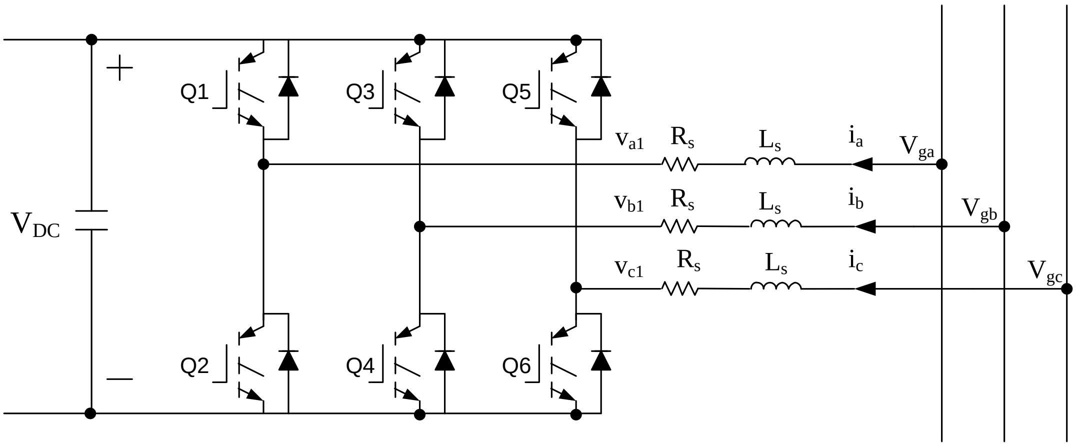

Figure 2.13 A simplified configuration of the grid converter.

The voltage equations from Figure 2.13 according to KVL are:

$$\frac{d}{dt}\begin{bmatrix} i_a \\ i_b \\ i_c \end{bmatrix} = -\frac{R_S}{L_S}\begin{bmatrix} 1 & 0 & 0 \\ 0 & 1 & 0 \\ 0 & 0 & 1 \end{bmatrix}\begin{bmatrix} i_a \\ i_b \\ i_c \end{bmatrix} + \frac{1}{L_S}\begin{bmatrix} V_{ga} - V_{a1} \\ V_{gb} - V_{b1} \\ V_{gc} - V_{c1} \end{bmatrix} \tag{2.10}$$

The voltage equation (2.10) can be transformed to the d-q axis by applying *dq* transformations:

$$\frac{d}{dt}\begin{bmatrix} i_d \\ i_q \end{bmatrix} = \begin{bmatrix} -\frac{R_s}{L_s} & 0 \\ 0 & -\frac{R_s}{L_s} \end{bmatrix}\begin{bmatrix} i_d \\ i_q \end{bmatrix} + \frac{1}{L_s}\begin{bmatrix} V_{gd} - V_{d1} + \omega_g i_q L_s \\ -V_{q1} - \omega_g i_d L_s \end{bmatrix} \tag{2.11}$$

where V_{gd} is the grid voltage magnitude.

From equation (2.11), the plant of the d and q axis current control loop is given by:

$$\mathrm{F(s)} = \frac{\mathrm{i_d(s)}}{\mathrm{v'_d(s)}} = \frac{\mathrm{i_q(s)}}{\mathrm{v'_q(s)}} = \frac{1}{\mathrm{Ls+R}} \tag{2.12}$$

where

$$V^*_{d1} = -v'_d + (\omega_g L_s i_q + V_{gd}) \tag{2.13}$$

$$V^*_{q1} = -v'_q - (\omega_g L_s i_d) \tag{2.14}$$

$V_{d1}{}^*$ and $V_{d1}{}^*$ are the reference values for the output of the converter, and the terms in brackets are for voltage compensation.

Figure 2.14 shows the inner loop design for the VSI system.

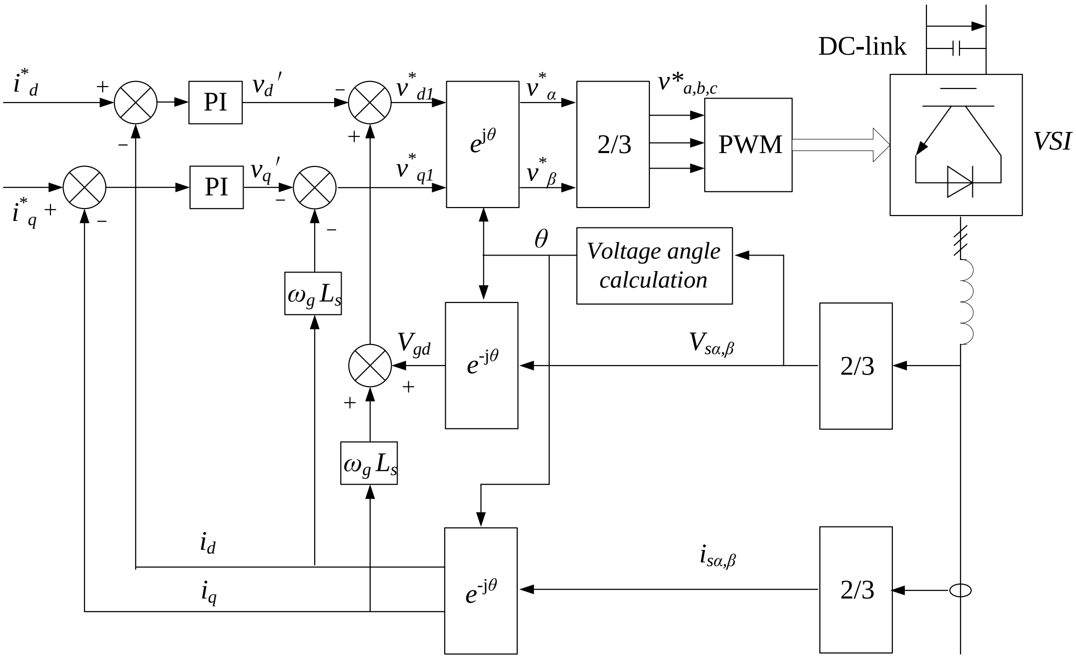

Figure 2.14 Inner loop design for the VSI system.

Compared to a conventional HVDC LCC, the VSI can provide flexible reactive power independent of active power. The outer loop design of the VSI is shown in Figure 2.15.

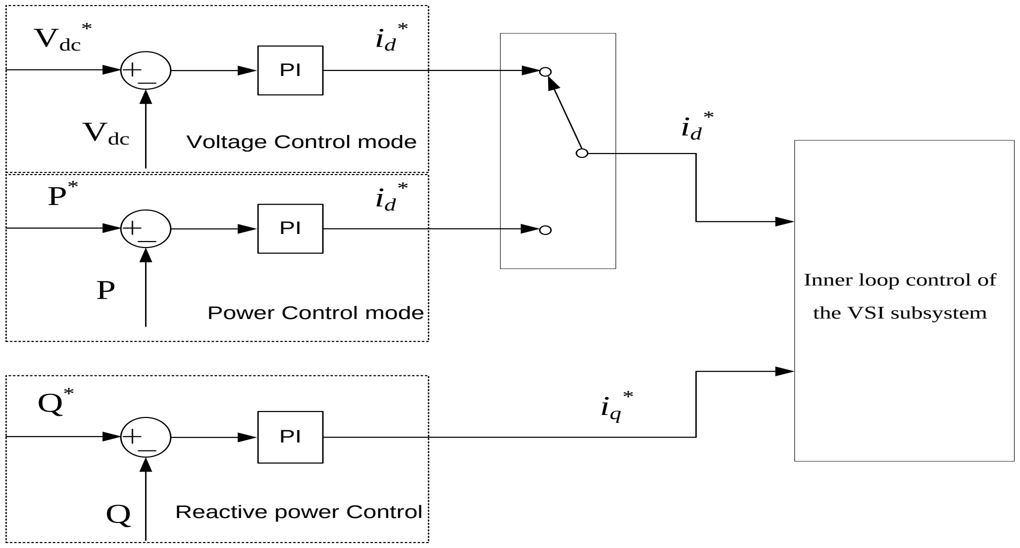

Figure 2.15 Outer loop design for VSI system.

The active power reference is determined by the grid power demand. Normally, the reactive power reference is set to zero to maintain high power factor, but is adjusted to support the grid ac voltage during a grid fault condition.

2.4.2 Current source inverter

Traditionally, the current source inverter is based on naturally-commutated thyristors due to their high power capability, low cost and low loss. It has been widely used in the HVDC technology. The drawback of the thyristor-based CSI is that the active and reactive power controls are coupled, thus it cannot achieve independent reactive power control. As power electronic devices and control technologies have developed, the CSI, using forced-commutated devices such as gate turn-off thyristors (GTOs), integrated gate-commutated thyristors (IGCTs) or insulated-gate bipolar transistors (IGBTs), has received much attention. Compared to the thyristor based CSI, the forced-commutated CSI can provide flexible reactive power to the grid due to one more control degree of freedom, and hence can meet grid code requirements. Figure 2.16 shows the two CSI topologies based on different switching devices. As shown in Figure 2.16 (a), a diode is in series connection with the IGBT to block reverse voltage, while for the GTO and IGCT based CSI, the diode can be omitted since these devices are capable of blocking reverse voltage. Both configurations incorporate a dc link inductor and an ac side second-order output filter, and have similar control.

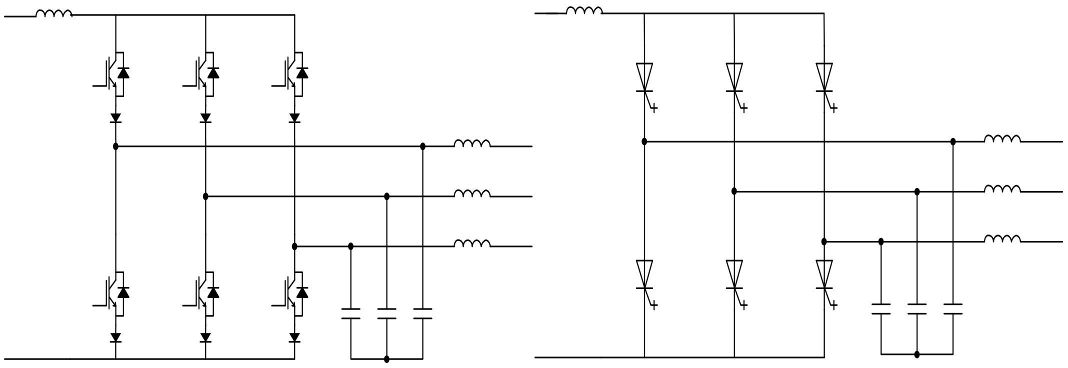

(a) (b)

Figure 2.16 CSI topologies based on IGBTs and GTO (IGCT): (a) IGBT based (b) GTO (IGCT) based.

Figure 2.17 shows the equivalent circuit of the CSI system.

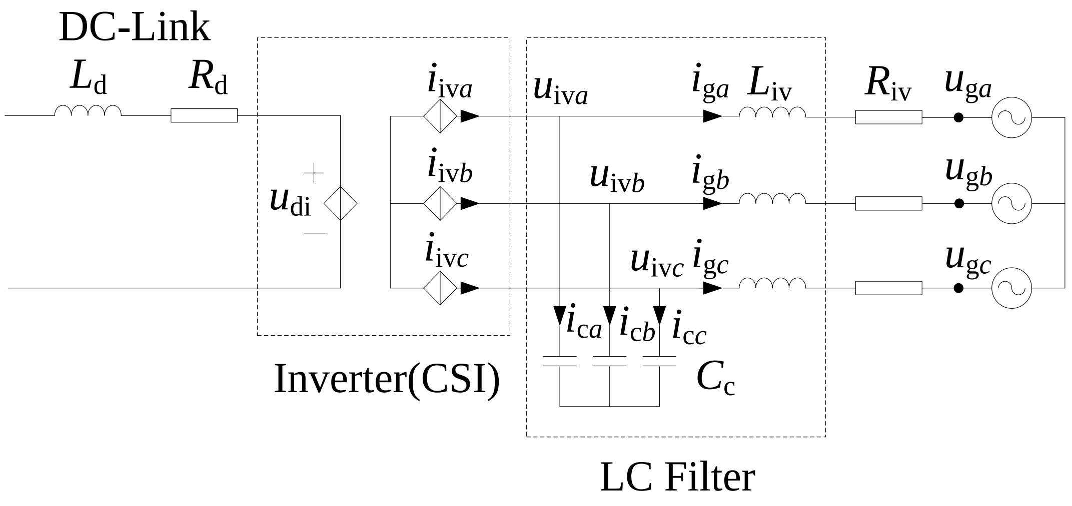

Figure 2.17 Equivalent circuit of the CSI system.

Like the VSI system, the CSI system uses the dq reference frame, which is synchronised to the grid voltage. After a dq axis transform, the averaged model is given by:

$$\frac{C_c du_{ivd}}{dt} = i_{ivd} - i_{gd} + \omega_g C_c u_{ivq} \tag{2.15}$$

$$\frac{C_c du_{ivq}}{dt} = i_{ivd} - i_{gq} - \omega_g C_c u_{ivd} \tag{2.16}$$

$$\frac{L_{iv} di_{gd}}{dt} = -R_{iv} i_{gd} + u_{ivd} - u_{gd} + \omega_g L_{iv} i_{gq} \tag{2.17}$$

$$\frac{L_{iv}di_{gq}}{dt} = -R_{iv}i_{gq} + u_{ivq} - u_{gq} - \omega_g L_{iv}i_{gq} \tag{2.18}$$

$$u_{di} = 3/2(m_{ivd}u_{ivd} + m_{ivq}u_{ivq}) \tag{2.19}$$

$$i_{ivd} = m_{ivd}i_d \tag{2.20}$$

$$i_{ivq} = m_{ivq}i_d \tag{2.21}$$

where ω_g is the angular frequency of the grid voltage, m_{ivd} and m_{ivq} are the modulating indices, u_{iv} is 3-phase voltages of the inverter output filter, i_{iv} is the 3-phase inverter output currents. i_g is the 3-phase grid input currents. C_c is inverter output filters capacitance. R_{iv} and L_{iv} are the equivalent parameters of the inverter transformer and cables. u_{di} is the inverter side dc link voltage.

The CSI system control includes active and reactive power control. The active and reactive powers are proportional to the active current i_{gd} and reactive current i_{gd} respectively. The active power control can regulate the dc link voltage u_{di} or current i_d depending on the operational mode (current control mode and voltage control mode). Figure 2.18 shows the outer loop design for the CSI.

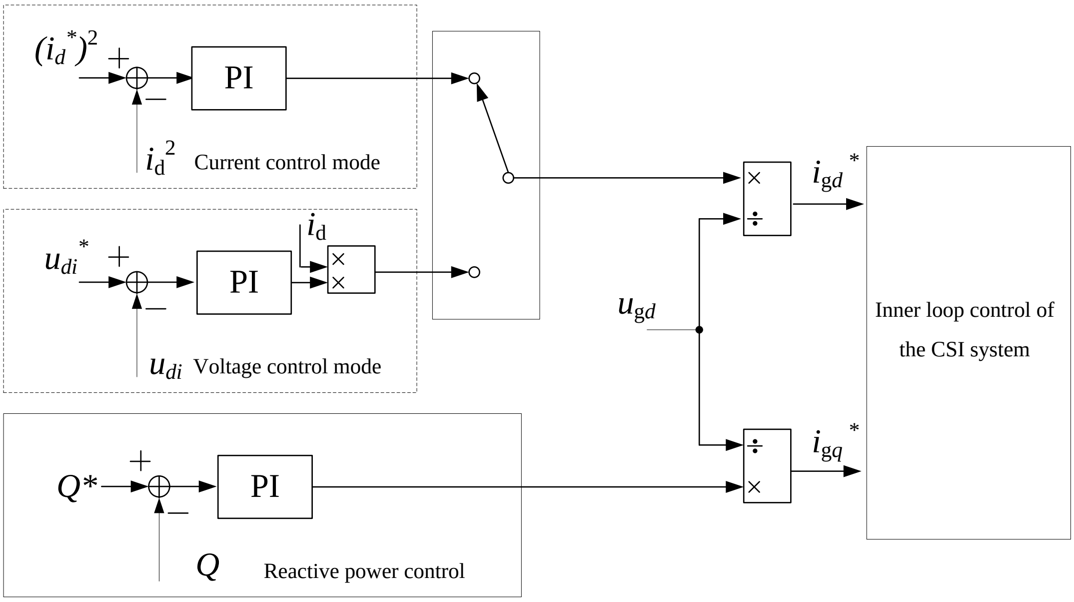

Figure 2.18 Outer loop design for CSI system.

According to the equations (2.15)-(2.21), the feedback compensator is designed as:

$$m_{iv} = {i_d}^{-1}(v_{iv} + Kx_{iv} + Lu_g) \tag{2.22}$$

where $v_{iv}=[v_{ivd}, v_{ivq}]$ is the compensated plant input, $x_{iv}=[u_{ivd}, u_{ivq}, i_{gd}, i_{gq}]^T$.

The decoupling matrix is

$$K = \begin{bmatrix} 0 & 2\omega_g C_c & 1 + {\omega_g}^2 L_{iv} C_c & {\omega_g}^2 L_{iv} C_c \\ 2\omega_g C_c & 0 & -{\omega_g}^2 L_{iv} C_c & 1 + {\omega_g}^2 L_{iv} C_c \end{bmatrix}$$

The compensation matrix is

$$L = \begin{bmatrix} 0 & \omega_g C_c \\ -\omega_g C_c & 0 \end{bmatrix}$$

Thus the inner loop for the CSI system is design as shown in Figure 2.19. The reference values for the active current i_{gd}^* and reactive current i_{gq}^* are derived from the output of the outer loop as shown in Figure 2.18. The modulation indices m_{ivd} and m_{ivq} used to control the CSI are obtained from equation (2.22).

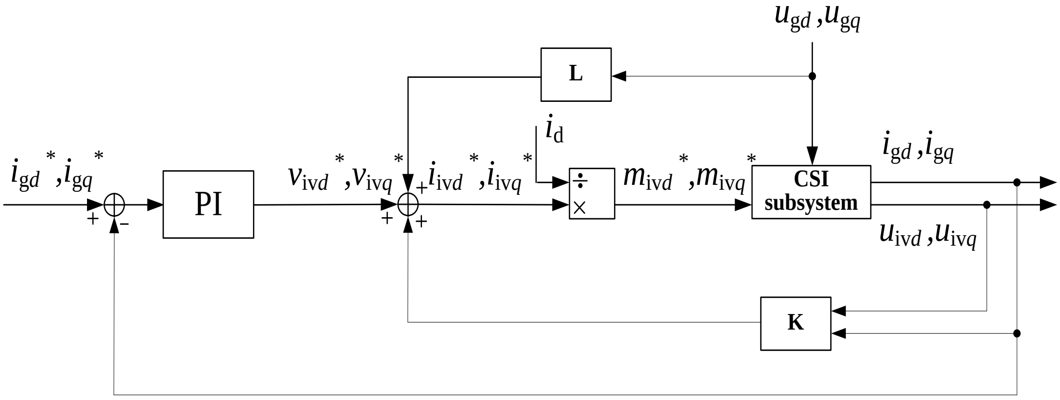

Figure 2.19 Inner loop design for the CSI system.

2.5 Summary

Three types of wind turbine generator have been briefly compared, highlighting their advantages and disadvantages. The different power electronic converter systems used in WECS were presented. A diode rectifier based WECS configuration was chosen for this research, since it was assessed as applicable at low power levels. Several types of dc/dc converters were briefly introduced. Finally different VSI and CSI control strategies for grid connection were outlined.

References

[2.1] A. D. Hansen, F. Lov, and F. Blaabjerg, "Review of contemporary wind turbine concepts and their market penetration," *WIND ENGINEERING*, Vol. 28, No. 3, pp. 247-263, 2004.

[2.2] C. Zhe, J. M. Guerrero, and F. Blaabjerg, "A Review of the State of the Art of Power Electronics for Wind Turbines," *Power Electronics, IEEE Transactions on,*Vol. 24, No. 8, pp. 1859-1875, 2009.

[2.3] F. Blaabjerg, C. Zhe, and S. B. Kjaer, "Power electronics as efficient interface in dispersed power generation systems," *Power Electronics, IEEE Transactions on,* Vol. 19, No. 5, pp. 1184-1194, 2004.

[2.4] H. Li and Z. Chen, "Overview of different wind generator systems and their comparisons," *Renewable Power Generation, IET,* Vol. 2, No. 2, pp. 123-138, 2008.

[2.5] A. Ragheb and M. Ragheb, "Wind turbine gearbox technologies," in *Nuclear & Renewable Energy Conference (INREC), 2010 1st International*, 2010, pp. 1-8.

[2.6] S. Muller, M. Deicke, and R. W. De Doncker, "Doubly fed induction generator systems for wind turbines," *Industry Applications Magazine, IEEE,* Vol. 8, No. 3, pp. 26-33, 2002.

[2.7] L. H. Hansen;, L. Helle;, and F. B. ;, "Conceptual survey of Generators and Power Electronics for Wind Turbines," Denmark, Riso National Laboratory Technical Report Riso-R-1205(EN) Roskilde, December, 2001.

[2.8] Z. Chen and F. Blaabjerg, "The World's Fastest Growing Energy Source.," *IEEE Power Electronics Society Newsletter,* Vol. 18, No. 3, pp. 15-19, 2006.

[2.9] M. E. Haque, M. Negnevitsky, and K. M. Muttaqi, "A Novel Control Strategy for a Variable-Speed Wind Turbine With a Permanent-Magnet Synchronous Generator," *Industry Applications, IEEE Transactions on,* Vol. 46, No. 1, pp. 331-339, 2010.

[2.10] K. Rothenhagen and F. W. Fuchs, "Doubly Fed Induction Generator Model-Based Sensor Fault Detection and Control Loop Reconfiguration," *Industrial Electronics, IEEE Transactions on,* Vol. 56, No. 10, pp. 4229-4238, 2009.

[2.11] G. Abad, M. A. Rodriguez, G. Iwanski, and J. Poza, "Direct Power Control of Doubly-Fed-Induction-Generator-Based Wind Turbines Under Unbalanced Grid Voltage," *Power Electronics, IEEE Transactions on,* Vol. 25, No. 2, pp. 442-452, 2010.

[2.12] M. Liserre, Ca, x, R. rdenas, M. Molinas, and J. Rodriguez, "Overview of Multi-MW Wind Turbines and Wind Parks," *Industrial Electronics, IEEE Transactions on,* Vol. 58, No. 4, pp. 1081-1095, 2011.

[2.13] R. Pena, J. C. Clare, and G. M. Asher, "Doubly fed induction generator using back-to-back PWM converters and its application to variable-speed wind-energy generation," *Electric Power Applications, IEE Proceedings-,* Vol. 143, No. 3, pp. 231-241, 1996.

[2.14] Z. Xiangjun, C. Zhe, and F. Blaabjerg, "Design and comparison of full-size converters for large variable-speed wind turbines," *Power Electronics and Applications, 2007 European Conference on*, 2007, pp. 1-10.

[2.15] J. Lopez, P. Sanchis, X. Roboam, and L. Marroyo, "Dynamic Behavior of the Doubly Fed Induction Generator During Three-Phase Voltage Dips," *Energy Conversion, IEEE Transactions on*, Vol. 22, No. 3, pp. 709-717, 2007.

[2.16] C. Tze-Fun and L. L. Lai, "Permanent-Magnet Machines for Distributed Power Generation: A Review," *Power Engineering Society General Meeting, 2007. IEEE*, 2007, pp. 1-6.

[2.17] M. Chinchilla, S. Arnaltes, and J. C. Burgos, "Control of permanent-magnet generators applied to variable-speed wind-energy systems connected to the grid," *Energy Conversion, IEEE Transactions on,* Vol. 21, No. 1, pp. 130-135, 2006.

[2.18] D. Jingya, D. D. Xu, and W. Bin, "A Novel Control Scheme for Current-Source-Converter-Based PMSG Wind Energy Conversion Systems," *Power Electronics, IEEE Transactions on,* Vol. 24, No. 4, pp. 963-972, 2009.

[2.19] L. Max, "Design and Control of a dc Collection Grid for a wind farm," Dep. of Energy and Environment, Chalmers University of Technology, 2009.

[2.20] R. Morales, R. Ordoez, M. A. Morales, and V. Flores, "Control System Design and Simulation of an ac/dc - dc/dc - dc/ac Power Converter for a Permanent Magnet Wind Power Generator in Rural Power Generation," E*lectrical, Communications, and Computers, 2009. CONIELECOMP 2009. International Conference on*, 2009, pp. 79-83.

[2.21] Y. Chuanwei, L. Hui, and J. Jiuchun, "Modeling and Simulation of ac-dc-ac Converter System for MW-Level Direct-Drive Wind Turbine grid Interface," *Power Electronics Specialists Conference, 2006. PESC '06. 37th IEEE*, 2006, pp. 1-4.

[2.22] F. Shixiong, J. E. Fletcher, Z. Huibin, S. J. Finney, and B. W. Williams, "Optimization of One-Power-Point operation for variable speed wind turbine with synchronous generators," *IECON 2010 - 36th Annual Conference on IEEE Industrial Electronics Society*, 2010, pp. 2874-2879.

[2.23] J. Darbyshire and C. V. Nayar, "Modelling, simulation and testing of grid connected small scale wind systems," *Power Engineering Conference, 2007. AUPEC 2007. Australasian Universities*, 2007, pp. 1-6.

Chapter 3

MPPT Scheme for a Variable Speed Wind Turbine

This chapter presents an optimized One-Power-Point method for maximum power tracking in a variable speed wind energy conversion system that uses a boost converter. Different MPPT schemes are illustrated. One-Power-Point maximum power tracking is preferable due to its ease of implementation and fast tracking ability. Its drawback is that power coefficient C_p deteriorates during wind speed drops. An optimization method based on One-Power-Point is developed to improve the system performance and energy conversion efficiency. There is no additional equipment, mechanical sensors or measurements. Simulation results confirm the functionality and feasibility of the method.

3.1 Background

Clean renewable energy sources, such as wind and solar are developing rapidly, especially wind energy. The installed wind power capacity in the world has been growing by more than 30% per year over the past decade [3.1]. Maximum power point tracking (MPPT) is an active research topic, and is essential for extracting the maximum power from a wind turbine. For a variable-speed wind energy conversion system (WECS), better efficiency at a lower cost is a key objective. Many MPPT schemes have been developed for variable speed wind energy conversion. MPPT schemes can be classified into two types, depending on whether the turbine characteristics are known or not. For the first type, predictive control, the wind generator (WG) characteristics and accurate mechanical sensors (e.g. anemometer and speed sensor) are required, which increase control system complexity and cost [3.2-6]. The second type, Perturbation & Observation (P&Q) is mostly used, due to its ease of implementation and the lack of any requirement for mechanical sensors [3.7-9]. Reference [3.10] proposes an on-line training MPPT method using a hill climbing technique. After the training mode, the reference variables are stored and directly applied in the control mode. The problem with this on-line training method is the PI parameters cannot be adjusted in the control mode online.

3.2 Wind turbine aerodynamic characteristics

In a wind generation system, a wind turbine is used to extract power from the wind. The output mechanical power of the turbine captured from the wind is expressed as [3.11]:

$$P_m = \frac{1}{2}\rho S C_p V^3 \tag{3.1}$$

where ρ is air density (kg/m^3), S is swept area (m^2), C_p is the wind turbine power coefficient, and V is the wind speed (m/s).

The C_p power coefficient is related to the pitch angle β and tip speed ratio (TSR) λ. TSR is defined as:

$$\lambda = \frac{\omega R}{V} \tag{3.2}$$

where ω is the wind generator rotor speed of rotation (rad/s) and R is the blade radius (m).

Figure 3.1 gives the power coefficient C_p (λ) curve, which can be obtained from field-test data [3.10][3.12]; here β=0°. From Figure 3.1, the point (6, 0.398) is the maximum value corresponding to the maximum power point at different wind speeds.

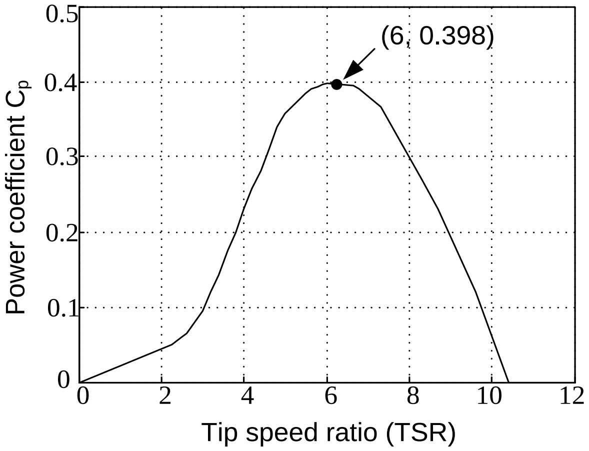

Figure 3.1 Power coefficient versus tip speed ratio.

3.3 Existing MPPT schemes

Several MPPT schemes are introduced in this chapter. They are tip speed ratio (TSR) control, power signal feedback (PSF) control, perturbation & observation, and One-Power-Point MPPT respectively. Each has its own advantages and disadvantages.

3.3.1 TSR and PSF control

TSR [3.13] and PSF [3.14-15] control both need the WG characteristics and accurate mechanical sensors (e.g. anemometer or speed sensor). TSR control regulates the generator speed to maintain an optimal tip speed ratio, but the instantaneous TSR values need to be calculated on-line according to the measured wind and generator speeds. The curve of the power coefficient versus TSR is required to be constructed before setting an optimal TSR value in practice. The problem of TSR control is the wind speed measurement, which increases system cost due to the use of an anemometer and presents difficulties in practical implementation. The block diagram for TSR control is shown in Figure 3.2.

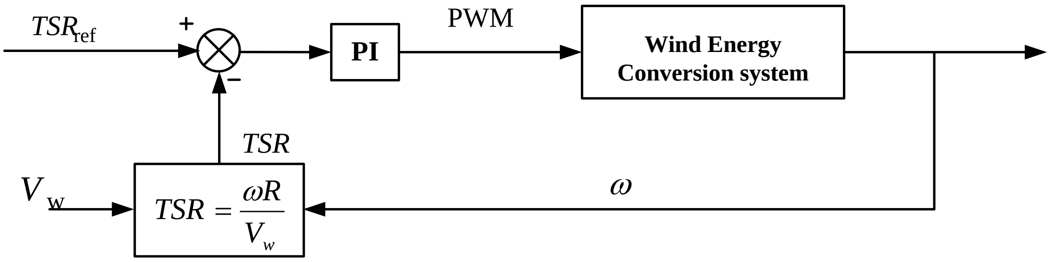

Figure 3.2 Block diagram of TSR control.

PSF control requires knowledge of the wind turbine's maximum power curve versus WG rotating speed, as illustrated in Figure 3.3. The WG rotating speed is measured, then the optimal output power is calculated from the power curve and compared to the actual WG output power. The resulting error is used to control a power converter.

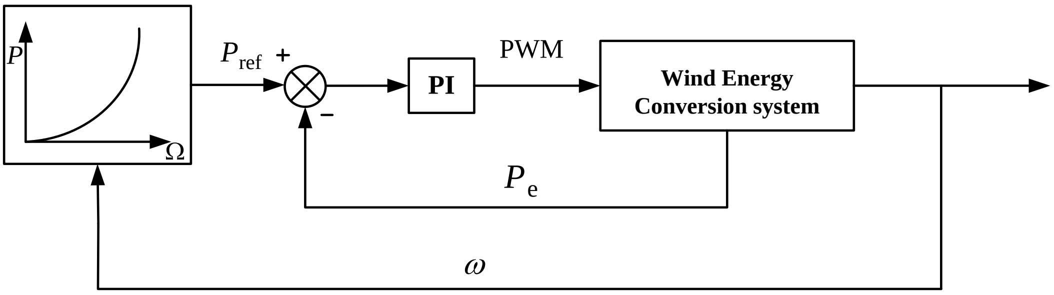

Figure 3.3 Block diagram of PSF control.

3.3.2 Perturbation & observation (P&O)

P&O control effort climbs the power curve in the direction of increasing output power. It is independent of the turbine and generator. The sign of the next perturbation is decided by the increase or decrease in measured output power due to the previous perturbation. The control law is shown as follow:

$$D_k = D_{k-1} + D_{step} \times sign(\Delta P_{k-1}/\Delta D_{k-1}) \tag{3.3}$$

where D_k and D_{k-1} are the duty cycle values at iterations k and k-1, respectively; $\Delta P_{k-1}/\Delta D_{k-1}$ is the wind turbine output power gradient at iteration k-1; D_{step} is the constant duty cycle step change.

The function sign(x) is defined as:

$$sign(x) = \begin{cases} 1 & if\ x \geq 0 \\ -1 & if\ x < 0 \end{cases} \tag{3.4}$$

The flow chart is as shown in Figure 3.4:

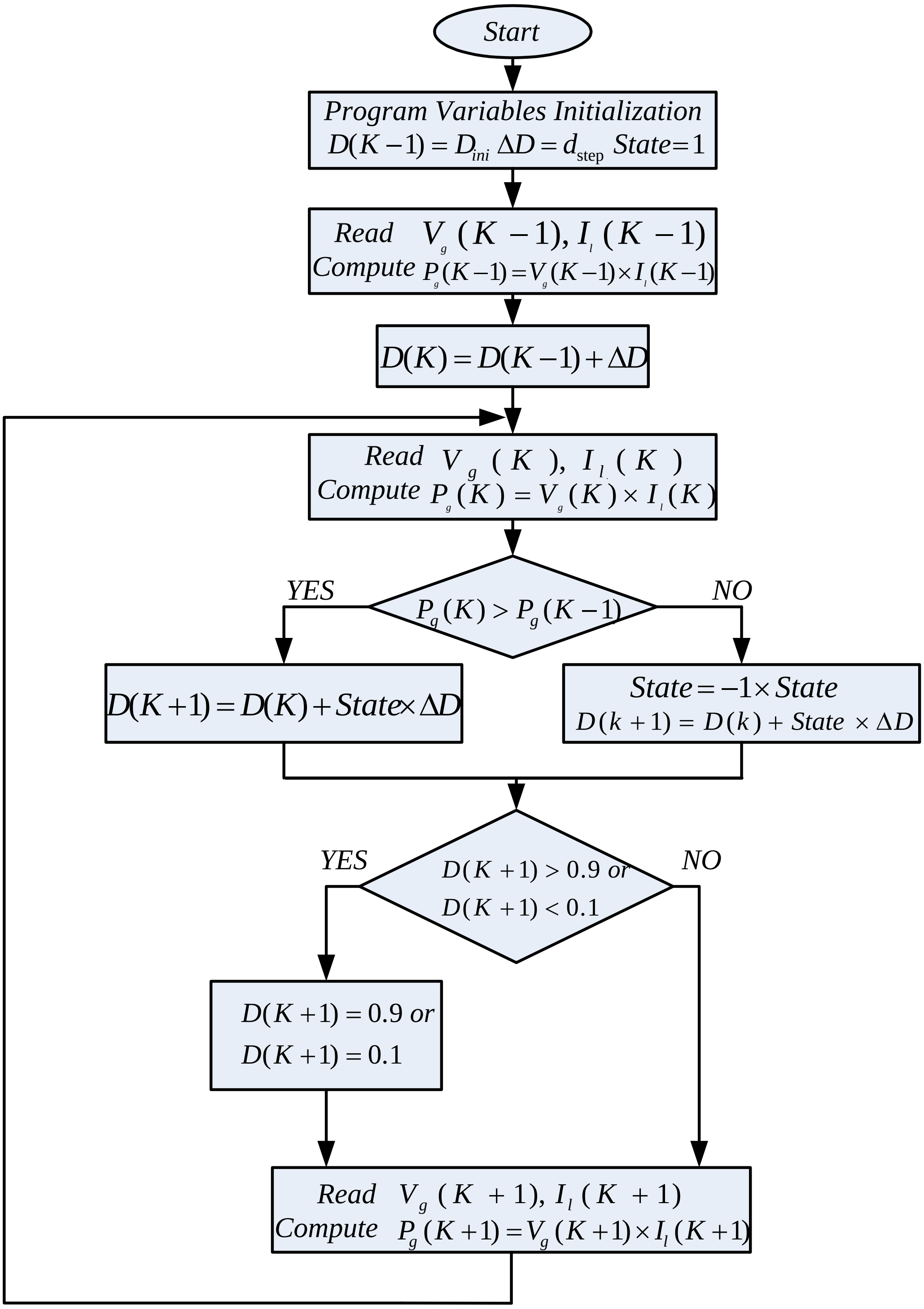

Figure 3.4 P&O control MPPT process flow chart.

The value of step change affects the maximum power tracking speed. A large D will increase the tracking speed but causes bigger oscillation at the maximum power point. A smaller D will improve the system stability but loses its tracking speed.

Besides the step change value, the interval time of P&O is determined by the system inertia which also affects the tracking speed. P&O is mostly used in small scale wind turbine systems. The drawback of P&O is that it loses tracking when the wind speed changes rapidly. Several P&O improvements prevent the wind turbine from stalling at a sudden wind speed drop [3.16], but methods slow down the tracking speed and lower the efficiency during changing wind speeds.

3.3.3 One-Power-Point MPPT tracking

The one-power-point control scheme is a new maximum power tracking method for variable speed wind energy systems [3.17], which is different from other control schemes. It is quicker than an online training method for maximum power tracking [3.18]. It avoids wind turbine stalling during wind speed drops and also yields fast tracking maximum power ability by changing the boost converter duty ratio, which is calculated via the boost converter input voltage and current. As the name suggests, only one maximum power status point of the WECS for any specific wind speed in the working range needs to be acquired. Once obtained, the WECS can extract maximum power from the wind according to the maximum power point P_{base} (v_{base}, i_{base}). In OPP control, the variable duty ratio (D) is changed every sampling time, which allows OPP control to track the maximum power fast. The duty cycle ratio can be calculated by the input voltage and current and maximum power point P_{base} (v_{base}, i_{base}):

$$D = 1 - [V_i - ((V_i/V_{base})^2 \times i_{base} - i_i) \times L/T]/V_o \tag{3.5}$$

where L is the inductor inductance, V_o is dc link voltage, and T is the sampling time, V_i and i_i are the input voltage and current of boost converter.

A drawback of the OPP MPPT technique is that C_p tracking deteriorates during wind speed decreases, which the wind turbine cannot quickly track following the wind speed change. The rate of rotational speed is determined not only by the WECS inertia but also by the difference between the mechanical power and the electromagnetic power. OPP directly controls the duty cycle ratio due to changes in the input voltage. When the wind speed drops, the generator speed should decrease as the wind speed changes. From an energy balance view, the energy stored in the shaft mechanical system will be released to the WECS as the generator speed decreases. While the input voltage decreases rapidly as wind speed drops, the input current calculated by OPP control is reduced. This results in less energy available for released into the grid. The energy stored in the shaft system cannot be transferred quickly, and this determines the maximum power tracking speed. Thus the worse C_p occurs during wind speed drops.

3.4 Proposed optimized MPPT algorithm

To improve the Cp value and energy efficiency during wind speed drops, an optimization scheme based on OPP control with maximum-power differential voltage (MPDV) control is proposed. The proposed algorithm combines maximum-power differential voltage (MPDV) control and OPP control. This combined control allows the wind turbine to extract more energy during rapid wind speed changes. The flowchart for the optimized OPP algorithm is depicted in Figure 3.5.

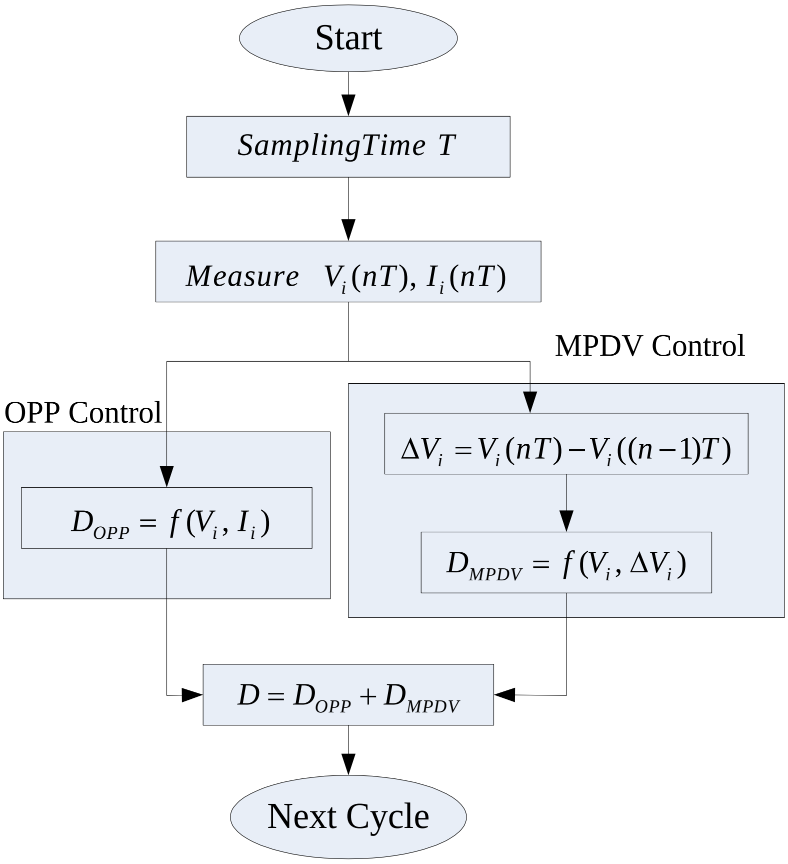

Figure 3.5 The flowchart for the optimized OPP algorithm.

With the proposed MPDV control, this problem is resolved by providing an auxiliary duty cycle term to increase the input current. The energy stored in the shaft system can then be released quickly to the grid. The control variable (D_{MPDV}) is related to the product of input voltage and differential input voltage and is expressed as:

$$D_{MPDV} = f(V_i, \Delta V_i) = \begin{cases} 0 & \Delta V \geq 0 \\ -K_1 V \Delta V & \Delta V < 0 \end{cases} \tag{3.6}$$

where K_1 is a positive constant, and the value of D_{MPDS} depends on the product of the input voltage and the differential input voltage $V_i(nT)(\Delta V/\Delta t)(nT)$.

For WECS applications, assuming rotor friction can be ignored, the mechanical model equations of the permanent magnet synchronous generator (PMSG) are:

$$T_m - T_e = j\frac{d\omega}{dt} \tag{3.7}$$

$$P_m - P_e = \omega j\frac{d\omega}{dt} \tag{3.8}$$

where J is the moment of inertia, T_m is wind turbine mechanical torque, T_e is electromagnetic torque, P_m is wind turbine mechanical power and P_e is electrical power. From equations (3.7) and (3.8), rate of speed changes are determined by the moment of inertia and the difference between the mechanical and electromagnetic torque.

The input voltage V_i is linearly proportional to the rotor speed, assuming negligible voltage drop across the stator impedance [3.17].

$$V_i \quad \propto \quad \omega \tag{3.9}$$

$$\Delta V_i/\Delta t \quad \propto \quad \Delta\omega/\Delta t \tag{3.10}$$

From equations (3.8), (3.9), and (3.10)

$$P_m(nT) - P_e(nT) = \omega(nT)J\frac{d\omega}{dt} \quad \propto \quad V_i(nT)(\Delta V/\Delta t)(nT) \tag{3.11}$$

$$(\Delta V/\Delta t)(nT) = (V(nT) - V((n-1)T))/T \tag{3.12}$$

From equation (3.11), the variable $V_i(\Delta V/\Delta t)$ is proportional to the difference between the mechanical and electromagnetic powers. Thus for a given sampling period, $V_i\Delta V$ denotes the distance between the wind turbine and generator operating points, and also indicates the distance between the wind turbine actual operating point and the optimal point for the corresponding wind speed.

When the wind speed drops, the rotor speed decreases due to the lagging electrical control. The differential rotor speed $\Delta\omega$ and input voltage ΔV are negative. Hence the *MPDV* control variable D_{MPDV} is positive, from equation (3.6). The input current is larger than without MPDV control. Consequently the electromagnetic torque increases. The rotor speed decreases faster, effectively reducing the time to reach the maximum power point. C_p is improved during the wind speed decrease. When the wind speed rises, the differential rotor speed $\Delta\omega$ and input voltage ΔV are positive, but D_{MPDV} is clamped to zero. When the wind speed is constant, the system reaches steady state, where ΔV and D_{MPDV} both equal zero. The two cases mean *MPDV* control idles during constant wind speed and increasing wind speed.

For *MPDV* control, the differential of the input voltage ΔV is an important variable. In this study, the sampling frequency is 10 kHz. The input voltage to the rectifier bridge varies, with ripple at six times the frequency of the voltage at the generator stator terminal (with respect to different rotor speeds). This ripple will lead to control system error because of the high sampling frequency (10 kHz). This problem can be solved with a digital low pass filter. The OPP algorithm with *MPDV* control can optimize C_p performance during wind speed drop, meaning wind turbines can extract more energy with the proposed algorithm, without additional measurements. The effectiveness of the proposed algorithm is demonstrated by simulation.

3.5 Simulation results

The WECS simulation is performed in Matlab/simulink, where the grid converter is replaced by a chopped resistor circuit that maintains the DC link voltage constant. The block diagram of the proposed system is depicted in Figure 3.6. It consists of a wind turbine, a permanent magnet synchronous generator (PMSG), diode rectifier, boost converter, and an inverter for the grid connection. The time delay is Z^{-1}.

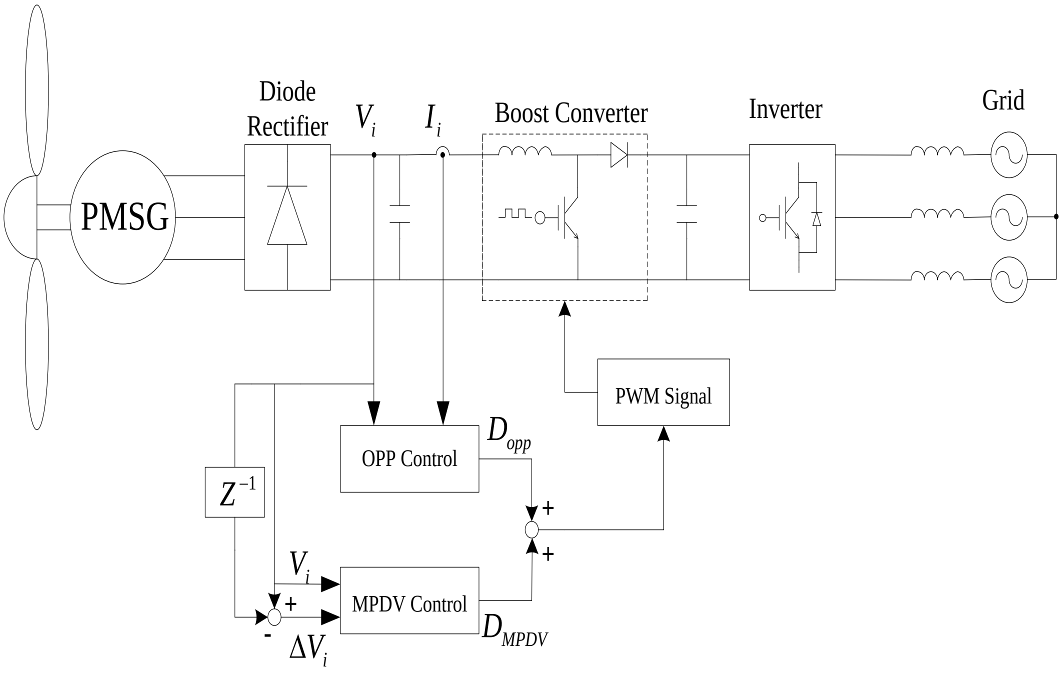

Figure 3.6 Block diagram of the proposed system.

Table 3.1 and Table 3.2 show the wind turbine and control system simulation specifications.

Table 3.1 Wind turbine specifications.

Items	Specification
Air density	1.220 kg/m^3
Turbine blade radius	2.75m
Swept area	23.8m^2
Turbine inertia J	6kg.m^2
Maximum power at 11m/s	7.68kW
Generator	Direct drive 3 phase PMSG
Stator resistance R_a	1.4Ω
Stator inductance (L_d, L_q)	5.8mH, 5.8mH
Flux induced by magnets	2.6Wb
Pole pairs	6

Table 3.2 Control parameters.

Items	Specifications
Switching frequency	10kHz
Capacitance (C_1, C_2)	2000 µF
Inductance (L)	12mH
dc link voltage (v_o)	690V

To validate the proposed algorithm, the same system is also implemented with a traditional control algorithm. Two-wind speed profiles are used in the comparative analysis. One is a linear change of wind speed; the other is a realistic wind profile.

The latter is constructed with gust and noise wind components according to reference [3.19].

In order to assess the merit of the proposed algorithm, the values of C_p, energy captured by the wind turbine, and energy conversion efficiency during wind speed change, are the important parameters in the comparative analysis.

The energy conversion efficiency η is the ratio of the energy captured by the wind turbine using MPPT to the ideal energy extracted from the wind. It is defined as follows:

$$\eta\%(t) = \frac{\Delta E}{\Delta E^{max}} = \frac{\int_{t_1}^{t} 0.5\rho A C_p V^3}{\int_{t_1}^{t_2} 0.5\rho A C_{pmax} V^3} \times 100\% \quad (t_1 \leq t \leq t_2) \tag{3.13}$$

where ΔE and ΔE_{max} represent the energy captured by the wind turbine and ideal energy extracted during the time intervals t_1 to t and t_1 to t_2, respectively.

Scenario 3.5.1 compares optimized OPP and OPP, with a linear wind speed. Scenario 3.5.2 shows the results with a realistic wind profile. In each case, power coefficient and energy conversion efficiency are the important parameters in the comparative analysis.

In the simulation results, the maximum power point P_{base} (v_{base}, i_{base}) is used with v_{base} =484V and i_{base} =5.6A, which can be obtained by a conventional method (e.g. hill climbing searching control) or manual adjustment in Matlab/simulink. Choosing a different maximum power point P_{base} (v_{base}, i_{base}) as a reference point will result in a different energy conversion efficiency. The closer the reference and actual maximum power points, the higher the energy conversion efficiency.

3.5.1 Simulation results with linear wind speed changes

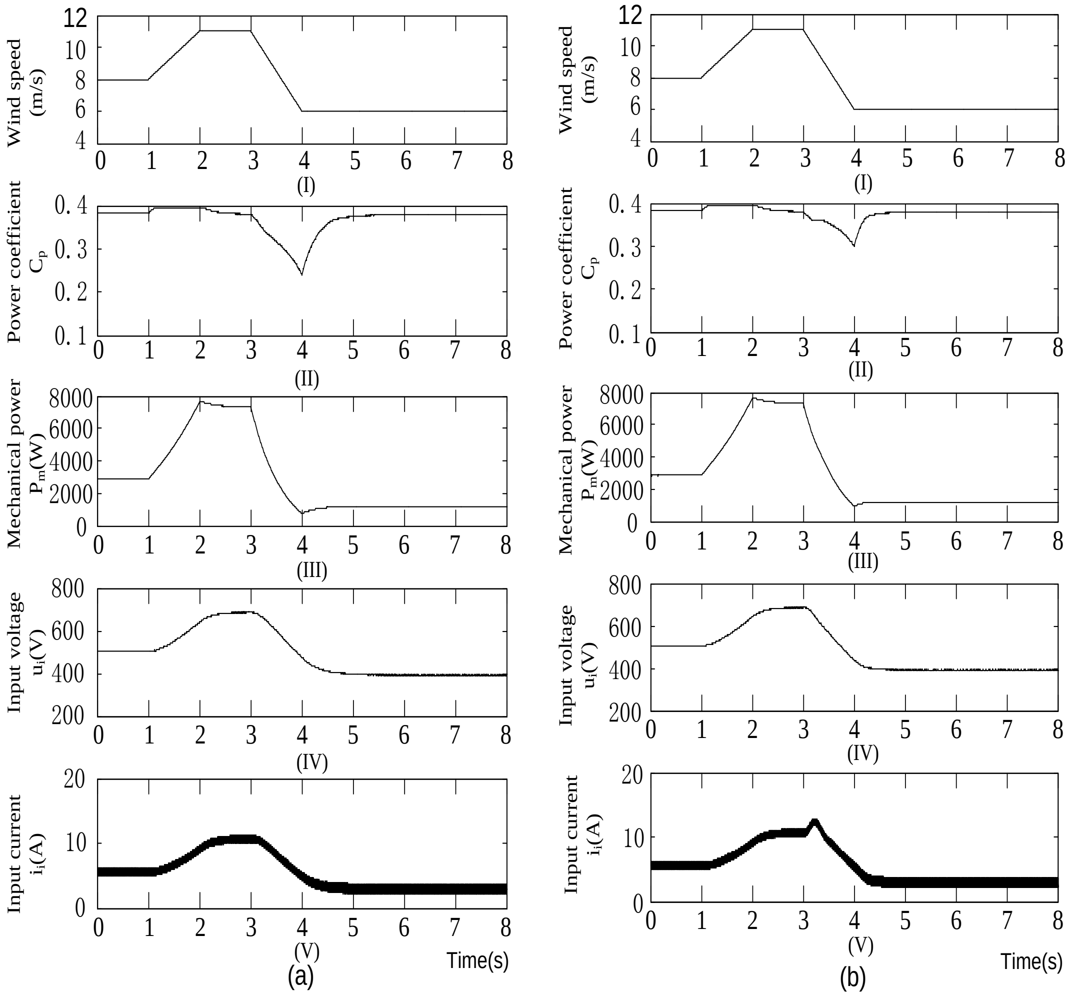

(a) (b)

Figure 3.7 Comparison of OPP and Optimized OPP operation during linear changes of wind speed. (a) OPP operation. (b) Optimized OPP operation.

Figure 3.7 (a) and (b) show power coefficient C_p, mechanical power P_m, input voltage V_i, and input current I_i respectively with different control algorithms during the same wind speed. The wind speed is 8 m/s during the initial 2s, then rises to 11 m/s at time t=3s. It begins to decrease at t=4s, and finally is maintained constant at 6 m/s during t=5 to 8s. The system is in a stable state at t=0s. From Figure 3.7 b.(II), during wind speed increases, the WECS maintains a higher power coefficient (C_p) at t=0~4s, while a poorer C_p performance is observed during the wind speed decrease from t=4 to 6s. This means the WECS extracts less energy from the wind as the wind speed decreases. The reason why C_p deteriorates is related to system inertia and the location of the tip speed ratio (TSR) corresponding to the chosen maximum power point P_{base} (v_{base}, i_{base}) at the bend of TSR versus C_p curve. For the presented WECS, generally the TSR corresponding to the chosen maximum power point P_{base} (v_{base}, i_{base}) using the conventional method, is located to the right of the optimized (TSR_{op}, C_{pmax}), because this is the region where the WECS operates in a stable state. The generator speed corresponding to the chosen maximum power point is slightly greater than the actual optimal speed. Although the generator speed lags the rising velocity of the wind speed, C_p can be around the maximum value. Thus a poor C_p often results during wind speed decreases. The case can be improved by using an optimized OPP with MPDV control. Figure 3.8 compares power coefficient C_p for optimized OPP and OPP control and the improvement in C_p with optimized OPP control. The improvement is defined as:

$$\eta_{C_p} = \frac{C_{P\_OPP_{opt}} - C_{P\_OPP}}{C_{Pmax}} \times 100\% \tag{3.14}$$

where C_{P_OPPopt} and C_{P_OPP} are the power coefficients for optimized OPP and OPP, respectively. C_{pmax} is 0.398. In both cases, C_p decreases to a certain extent during wind speed decreases. The C_p decreases to approximately 0.24 with OPP control, while it only reduces to approximately 0.3 with optimized OPP control. The worse case C_p occurs at t=5s, at same time, the improvement in C_p can reach approximately 15% with MPDV control, hence more wind energy can be converted.

The comparison of instantaneous extracted energy and improvement in energy conversion efficiency for optimized OPP and OPP MPPT, is presented in Figure 3.9, where the integrated time is from t=3 to 5 s. The improvement in energy conversion efficiency represents the difference between ΔE_{O_OPP} and ΔE_{OPP} compared to ΔE_{max}, where ΔE_{max} represents the ideal energy extractable during the linear changes of wind speed at t=3 to 5s and ΔE_{O_OPP} and ΔE_{OPP} denote the energy captured with optimized OPP and OPP MPPT at the same wind speed respectively. It can be expressed as:

$$\eta_{im} = \frac{\Delta E_{O\_OPP} - \Delta E_{OPP}}{\Delta E^{max}} \times 100\% = \eta_{O\_OPP} - \eta_{OPP} \tag{3.15}$$

where ΔE_{max} is 5095J during t=3 to 5s. At t=5s, ΔE_{O_OPP} is 4587J and ΔE_{OPP} is 4290J. Using equation (3.13), the energy conversion efficiencies with optimized OPP and OPP control are: $\eta\%_{O\_OPP}$=90%, $\eta\%_{OPP}$ =84.2%. According to (3.15), the energy conversion efficiency can be increased by 5.8 % at t=5s with MPDV control.

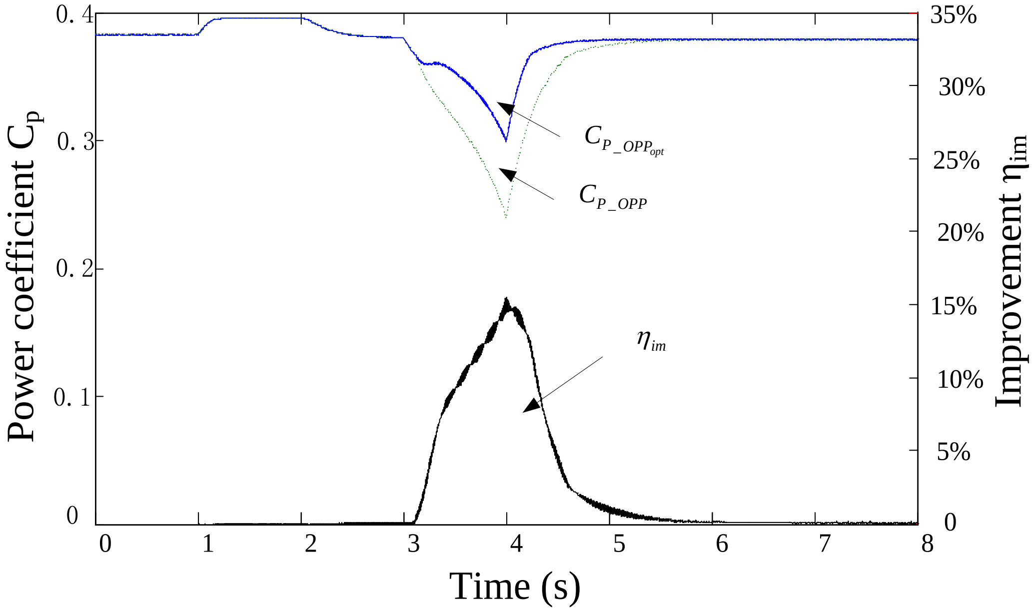

Figure 3.8 Compared power coefficient for OPP and optimized OPP control with linear wind profiles.

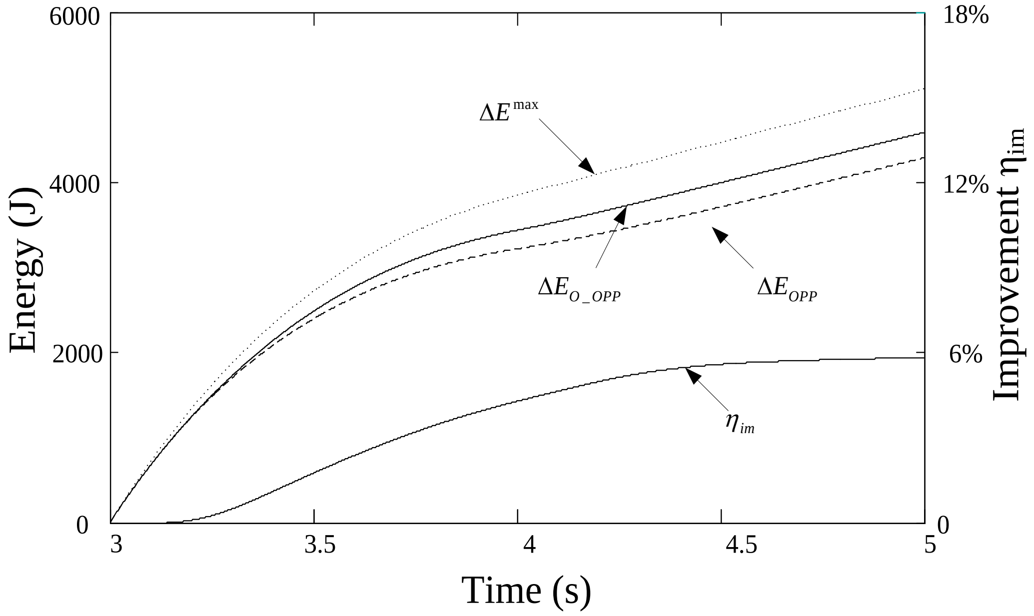

Figure 3.9 Compared extracted energy for OPP and optimized OPP control with linear wind profiles.

3.5.2 Simulation results with a Realistic Wind Profile

In this scenario, a realistic wind profile is generated, which contains gust and noise wind components. This makes the system close to an actual situation, which is better for validating optimized OPP operation.

Like Figure 3.7 (a) and (b), corresponding Figure 3.10 (a) and Figure 3.10 (b) show WECS performance with OPP and optimized OPP control, during realistic wind profiles. The wind speed starts at 6m/s, with a noise component. Two 2-second wind gusts exist in the wind profiles, with the peak gust speed of approximately 11m/s. At time t=0s, the WECS operates in the maximum power point tracking state. C_p is maintained at a high value, close to 0.4, as shown in Figure 3.10a.(II) and Figure 3.10B.(g). C_p decreases when the gust occurs, especially when the gust speed drops, which is same situation with C_p during linear wind speed changes. In Figure 3.10a.(II), the worst C_p occurs at t=3s, while C_p is better with MPDV control in Figure 3.10b.(II).

Comparison of the C_p curve with optimized OPP and OPP control and improvement in C_p are shown in Figure 3.11. Unavoidable dips occur when the gust speed drops, because of shaft inertia in the WECS. There is a need to respond to and track the wind speed changes, thus C_p cannot be maintained at the optimized value. C_p can however be improved, so as to approach the optimized value. The worst C_p is approximately 0.26 with optimized OPP control at t=2.8s and t=5.8s, while the worst C_p is approximately 0.2 with OPP control. C_p can be improved by approximately 20% with MPDV control.

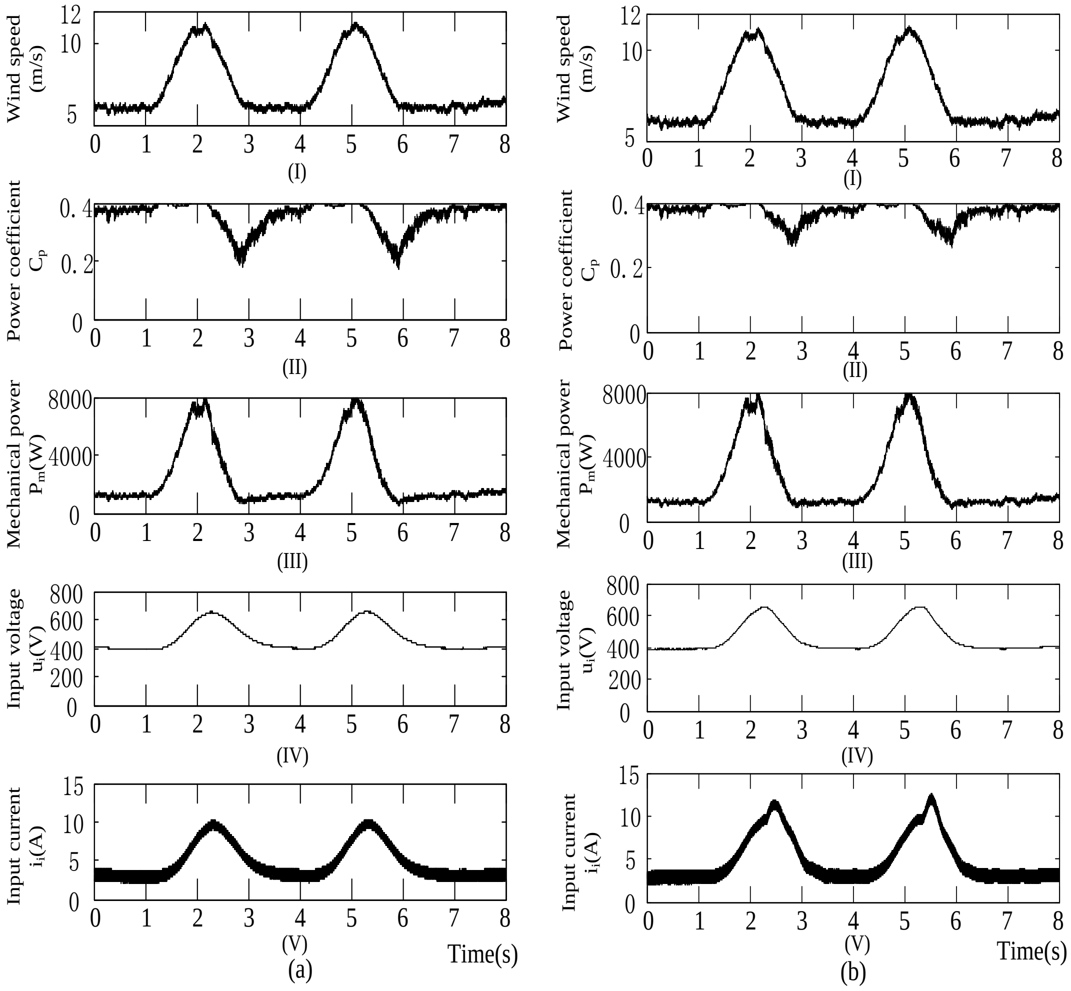

Figure 3.10 Comparison of OPP and Optimized OPP operation with realistic wind profiles (a) OPP operation. (b) Optimized OPP operation.

The comparison of extracted energy with realistic wind profiles for optimization of OPP and OPP MPPT and improvement in energy conversion efficiency, are presented in Figure 3.12. The energy is integrated from t=2 to 8s. ΔE_{max} is 16238J. At t=8s, ΔE_{O_OPP} is 15272J and ΔE_{OPP} is 14788J. The energy conversion efficiency with optimized OPP and OPP control can be calculated from (3.13), respectively: $\eta\%_{O\_OPP}$ =94.05%, $\eta\%_{OPP}$ =91.07%. With MPDV control, the improvement in energy conversion efficiency reaches 3% at t=8s.

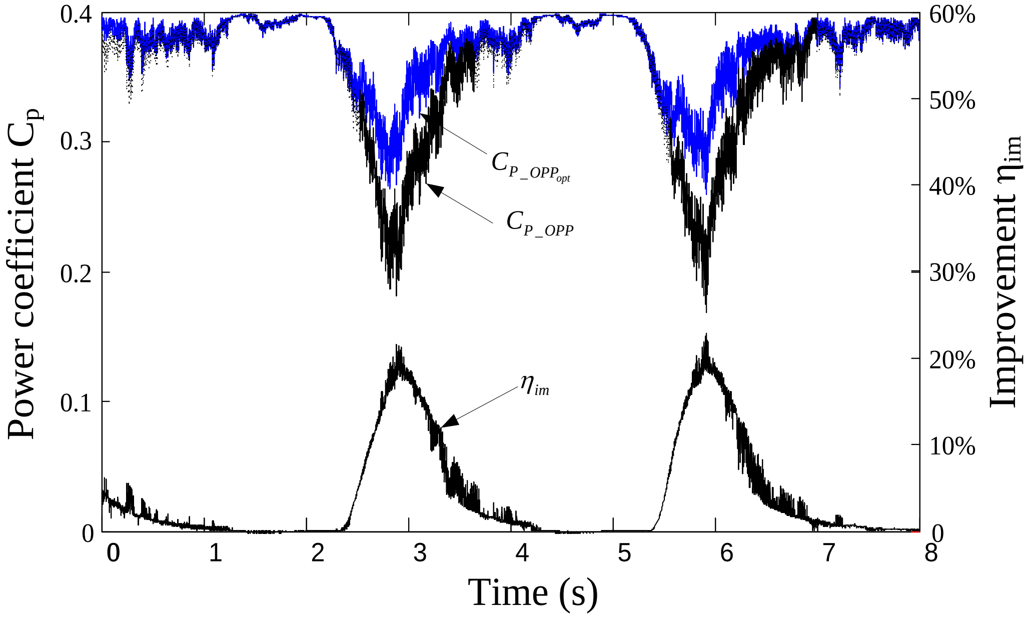

Figure 3.11 Compared power coefficient for OPP and optimized OPP control with realistic wind profiles.

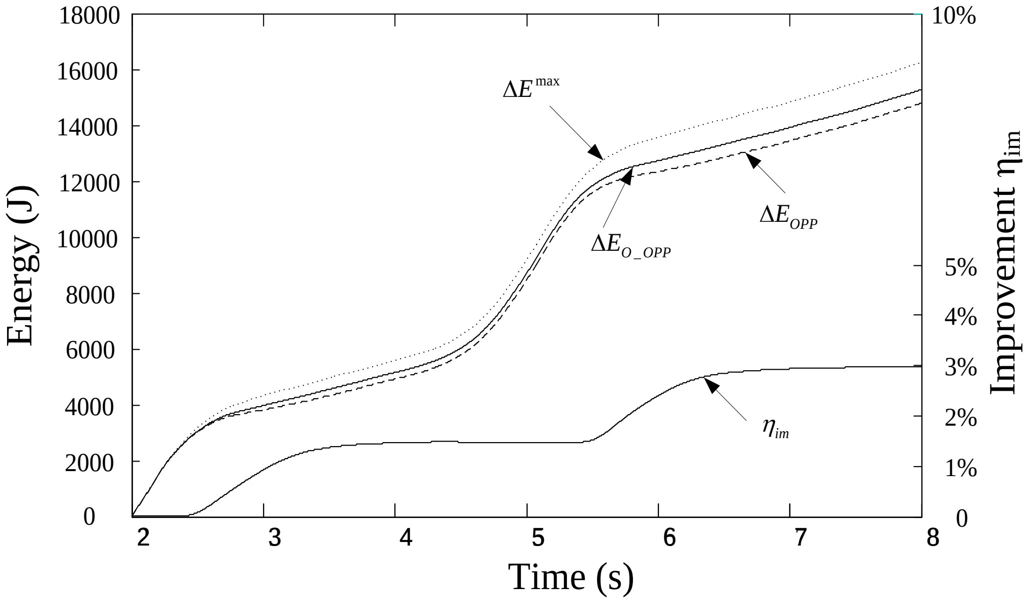

Figure 3.12 Compared extracted energy for OPP and optimized OPP control with realistic wind profiles.

3.6 Summary

In this chapter, optimized OPP is presented, which incorporates OPP control and MPDV control. These are implemented without extra mechanical sensors. This not only reduces the cost of building the wind energy conversion system but also improves the energy conversion efficiency. A higher energy conversion efficiency means more energy can be extracted from the wind, which is the objective of all maximum power point tracking methods. The simulation results of the proposed control scheme indicate that the WECS energy extractable from the wind during wind speed drops is increased by more than 2%, compared to non-optimized OPP approaches.

References

[3.1] M. Jujawa, "Large wind rising," *Renewable Energy World,* Vol. 6, No. 2, pp. 39-51, Mar./Apr. 2003.

[3.2] V. Valtchev, A. Van den Bossche, J. Ghijselen, and J. Melkebeek, "Autonomous renewable energy conversion system," *Renewable Energy,* Vol. 19, No. 1–2, pp. 259-275, 2000.

[3.3] E. Muljadi and C. P. Butterfield, "Pitch-controlled variable-speed wind turbine generation," *Industry Applications, IEEE Transactions on,* Vol. 37, No. 1, pp. 240-246, 2001.

[3.4] R. Chedid, F. Mrad, and M. Basma, "Intelligent control of a class of wind energy conversion systems," *Energy Conversion, IEEE Transactions on,* Vol. 14, No. 4, pp. 1597-1604, 1999.

[3.5] M. Chinchilla, S. Arnaltes, and J. C. Burgos, "Control of permanent-magnet generators applied to variable-speed wind-energy systems connected to the grid," *Energy Conversion, IEEE Transactions on,* Vol. 21, No. 1, pp. 130-135, 2006.

[3.6] D. Jingya, D. D. Xu, and W. Bin, "A Novel Control Scheme for Current-Source-Converter-Based PMSG Wind Energy Conversion Systems," *Power Electronics, IEEE Transactions on,* Vol. 24, No. 4, pp. 963-972, 2009.

[3.7] M. G. Molina and P. E. Mercado, "A new control strategy of variable speed wind turbine generator for three-phase grid-connected applications," *Transmission and Distribution Conference and Exposition: Latin America, 2008 IEEE/PES*, 2008, pp. 1-8.

[3.8] E. Koutroulis and K. Kalaitzakis, "Design of a maximum power tracking system for wind-energy-conversion applications," *Industrial Electronics, IEEE Transactions on,* Vol. 53, No. 2, pp. 486-494, 2006.

[3.9] R. Esmaili, L. Xu, and D. K. Nichols, "A new control method of permanent magnet generator for maximum power tracking in wind turbine application," *Power Engineering Society General Meeting, 2005. IEEE,* 2005, pp. 2090-2095 Vol. 2093.

[3.10] Q. Wang, "Maximum wind energy extraction strategies using power electronic converter," Phd, Univ. New Brunswick, Fredericton, NB Canada, June 2003.

[3.11] E. Muljadi, S. Drouilhet, R. Holz, and V. Gevorgian, "Analysis of permanent magnet generator for wind power battery charging," *Industry Applications Conference, 1996. Thirty-First IAS Annual Meeting, IAS '96., Conference Record of the 1996 IEEE,* 1996, pp. 541-548.

[3.12] T. Burton, D. Sharpe, N. Jenkins, and E. Bossanyi, "Wind Energy Handbook," ed: John Wiley & Sons, 2001.

[3.13] T. Thiringer and J. Linders, "Control by variable rotor speed of a fixed-pitch wind turbine operating in a wide speed range," *Energy Conversion, IEEE Transactions on,* Vol. 8, No. 3, pp. 520-526, 1993.

[3.14] R. M. Hilloowala and A. M. Sharaf, "A rule-based fuzzy logic controller for a PWM inverter in a stand alone wind energy conversion scheme," *Industry Applications, IEEE Transactions on,* Vol. 32, No. 1, pp. 57-65, 1996.

[3.15] M. Ermis, H. B. Ertan, E. Akpinar, and F. Ulgut, "Autonomous wind energy conversion system with a simple controller for maximum-power transfer," *Electric Power Applications, IEE Proceedings B,* Vol. 139, No. 5, pp. 421-428, 1992.

[3.16] R. J. Wai, C. Y. Lin, and Y. R. Chang, "Novel maximum-power-extraction algorithm for PMSG wind generation system," *Electric Power Applications, IET,* Vol. 1, No. 2, pp. 275-283, 2007.

[3.17] H. B. Zhang, J. Fletcher, N. Greeves, S. J. Finney, and B. W. Williams, "One-power-point operation for variable speed wind/tidal stream turbines with synchronous generators," *Renewable Power Generation, IET,* Vol. 5, No. 1, pp. 99-108, 2011.

[3.18] W. Quincy and C. Liuchen, "An intelligent maximum power extraction algorithm for inverter-based variable speed wind turbine systems," *Power Electronics, IEEE Transactions on,* Vol. 19, No. 5, pp. 1242-1249, 2004.

[3.19] P. M. Anderson and A. Bose, "Stability Simulation Of Wind Turbine Systems," *Power Apparatus and Systems, IEEE Transactions on,* Vol. PAS-102, No. 12, pp. 3791-3795, 1983.

Chapter 4

Design and Control of a WECS based on a hard-switched H-Bridge DC/DC Converter

This chapter presents a current output hard-switched full-bridge with an intermediate high frequency transformer for a wind energy conversion system. The wind turbine simulator, based on an induction machine driving a three-phase permanent magnet synchronous generator, is built to simulate the real wind turbine characteristics. The mathematical model of a hard-switched full-bridge (HSFB) is analysed, and the design and control of the HSFB is described. The dynamic response of the combined mechanical and electrical system of the WECS is investigated with wind speed step changes. Simulation and experimental results demonstrate the feasibility and stability of an HSFB based WECS.

4.1 Background

The dc/dc converter is widely used in industry, and in renewable energy source systems (wind energy and photovoltaic) and with fuel cells, batteries, etc. It is the preferred first stage in the integration of renewable energy sources, in order to achieve multi-terminal dc transmission needed for interfacing multiple wind turbines. However, most dc/dc topologies have disadvantages. The conventional single-switch boost converter is one type of dc/dc converter which cannot achieve high voltage gain or handle higher power due to the output diode high current and its recovery [4.1-2]. Additionally there is no electrical isolation between the generator side and the common dc link side. Comparative analysis of switch stress in the boost converter and the current output HSFB is studied in Section 4.3. For the voltage source converter (VSC) HVDC link based ac collection grid wind farm [4.3-6], to get a high transmission level dc voltage, the VSC input ac voltage should be stepped up to a high level due to the relationship between low ac input voltage and high dc voltage [4.7]. Thus a 50Hz/60Hz bulky and high cost ac transformer is needed to step the low generator voltage to a high level voltage. The full-bridge (FB) dc-dc converter with an intermediate high-frequency transformer handles the issue of higher voltage gain and power. The transformer used in the dc-dc converter operates at a high switching frequency, which leads to dramatic reductions in volume and weight in contrast to a bulky 50Hz/60Hz transformer. In [4.8], FB dc-dc converter loss is considered with phase shift control, but there is no mention of the wind turbine associated characteristics or inverter information. A FB dc-dc converter is adopted for an offshore dc-based wind farm for hvdc interconnection in [4.2]. The generator–side converter, which is located in the front of the dc-dc converter, controls the active power to make the wind turbine track the maximum power point and reactive power, while the FB dc-dc converter is used to maintain the offshore hvdc station voltage at the desired level. The VSI is used for grid connection. Reference [4.9] presents the control method and snubber selection of a single active bridge (SAB) dc-dc converter for a 5MW wind turbine. Compared to the hard-switched FB topology shown in Figure 4.1, the SAB converter shown in Figure 4.2 does not have an output inductor, thus has a voltage stiff output. Large capacitance is required to stabilise the high dc link voltage level, which increases WECS volume and cost. In this chapter, a current output HSFB converter is presented for the parallel connection of converters in WECS. Figure 4.3 shows the topology of the current output HSFB. Each wind turbine has a current output HSFB configured as a current source, which is beneficial in stabilising the WECS.

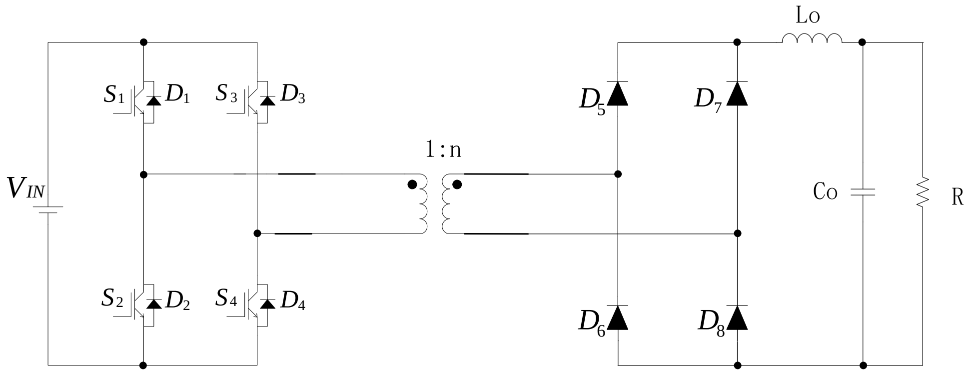

Figure 4.1 Hard-switched FB topology.

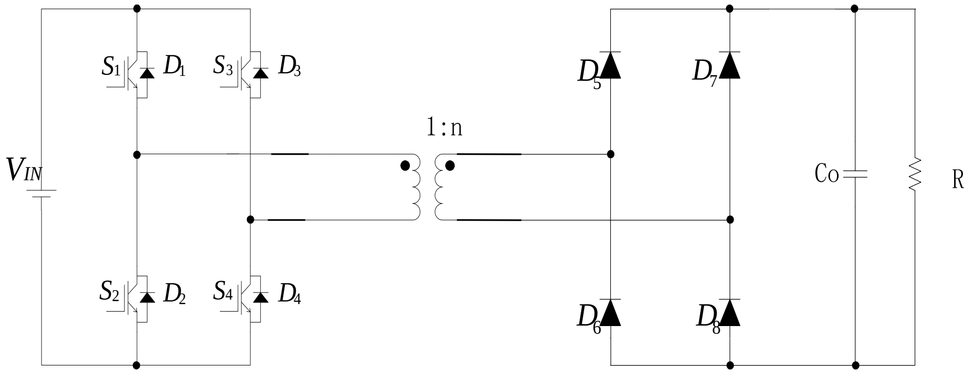

Figure 4.2 Single active bridge converter.

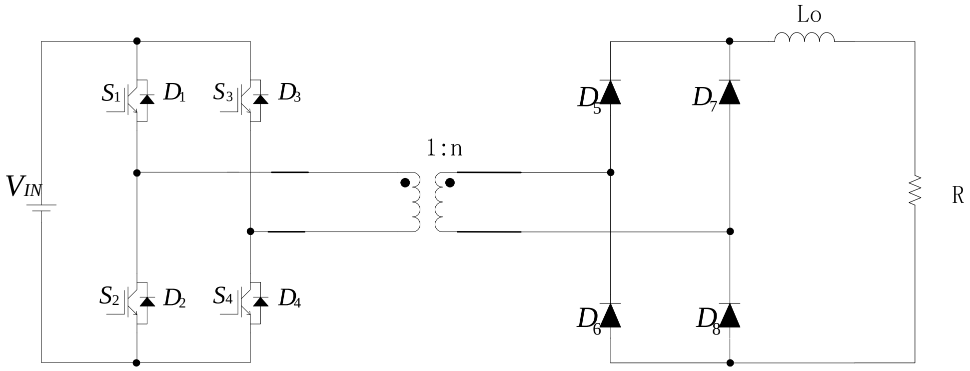

Figure 4.3 Current output HSFB.

4.2 Three-phase PMSG based wind turbine emulator system

The wind turbine generator is the WECS component that converts kinetic energy to electrical power. In order to demonstrate the current output HSFB based WECS, a wind turbine emulator system is built to simulate a real wind turbine according to its mathematic equation. The scheme consists of a DSP (TRICORE TC1796), variable speed drive, induction machine and gearbox, and a three-phase PMSG. Figure 4.4 shows the emulator system configuration. A vector controlled induction motor drive, driving a three phase PMSG though a step-down gearbox, is controlled by an Infineon DSP. The wind profile is programmed by mathematical functions. The DSP generates a torque command for the variable speed motor drive. The variable speed motor drive is configured in a torque mode/vector control mode. It converts the DSP torque command into a torque signal which is supplied to the induction machine. The induction machine converts the electrical torque into mechanical rotation torque on the motor shaft. A step-down gearbox converts the induction machine high speed to a lower PMSG-compatible speed. The mechanical power from the induction machine, via the gearbox, is converted to electrical power by the PMSG.

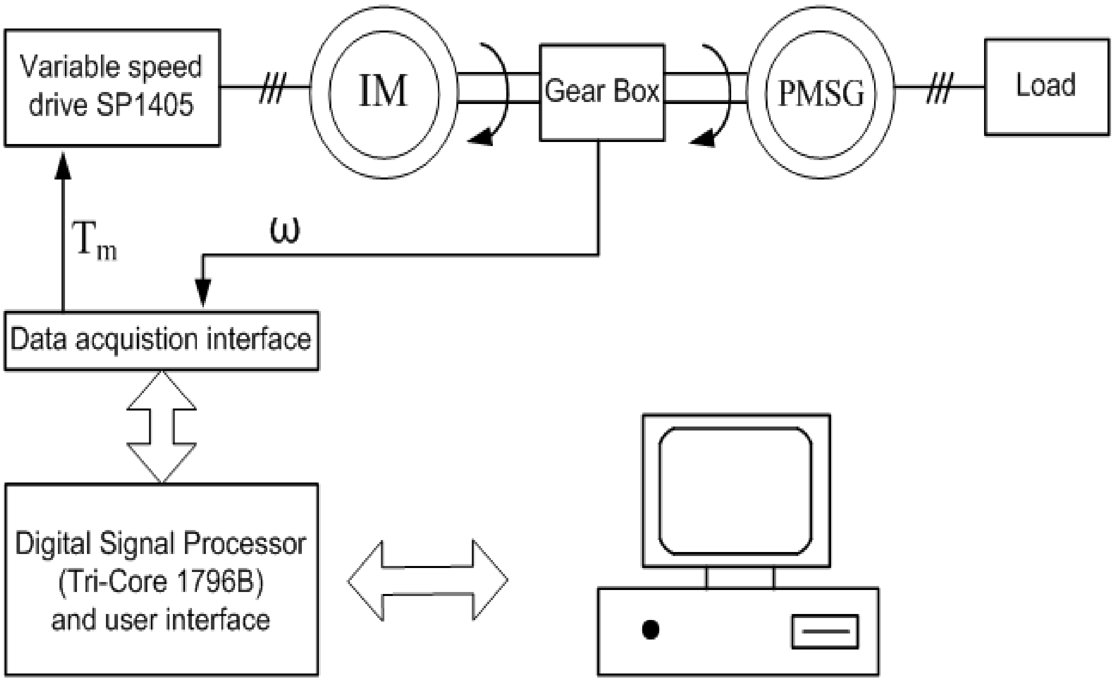

Figure 4.4 Hardware structure of the wind turbine emulator system.

Wind turbine aerodynamic characteristics are illustrated in Section 3.2. In the wind turbine emulator system, a generic equation is used to model power coefficient $C_p(\lambda,$

β), which is based on the modelled turbine characteristics of [4.10-12]. It is expressed as a function of the tip speed ratio (λ) and pitch angle (β) as follow:

$$C_p = 0.22(116/\lambda_i - 0.4\beta - 5)e^{-12.5/\lambda_i} \tag{4.1}$$

where λ_i is defined as:

$$\lambda_i = \frac{1}{\frac{1}{\lambda+0.08\beta} - \frac{0.035}{\beta^3+1}} \tag{4.2}$$

Assuming a pitch angle β=0°, the power coefficient C_p (λ) curve versus tip speed ratio is shown in Figure 4.5.

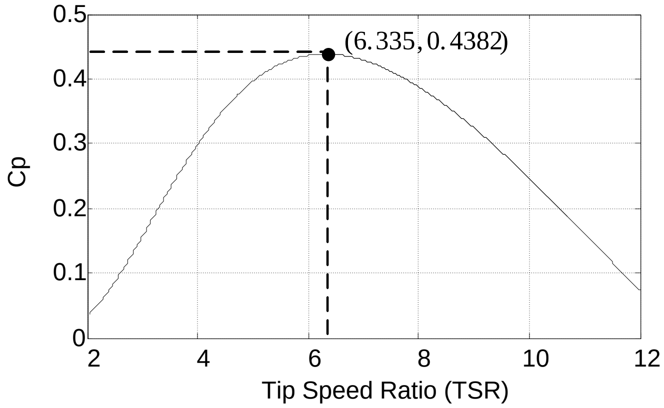

Figure 4.5 Power coefficient C_p versus tip speed ratio relation in turbine simulator.

The wind turbine output power given in equation (3.1) can be rewritten by substituting equation (3.2):

$$P_m = \frac{1}{2}\rho S C_p \left(\frac{R}{\lambda}\right)^3 \omega^3 \tag{4.3}$$

From Figure 4.5, (TSR, C_p) = (6.335, 0.4382) corresponds to the maximum power point at different wind speeds. For the variable speed WECS, the wind turbine is always controlled to operate at maximum power during wind speed changes via a subsequent dc/dc converter. The maximum wind power can be obtained if C_p can be maintained at its maximum value C_{pmax} corresponding to the optimal tip speed ratio for different wind speeds. The maximum power at different wind speeds can be written as:

$$P_{max} = k\omega^3 \tag{4.4}$$

where k is a constant, $k=1/2\rho SC_{pmax}(R/\lambda_{opt})^3$.

According to equations (3.1) and (4.4), Figure 4.6 gives the wind turbine output power and optimum power versus turbine speed curves at different wind speeds in per-unit values. As seen, the optimum power for different wind speeds is a cubic function of turbine speed.

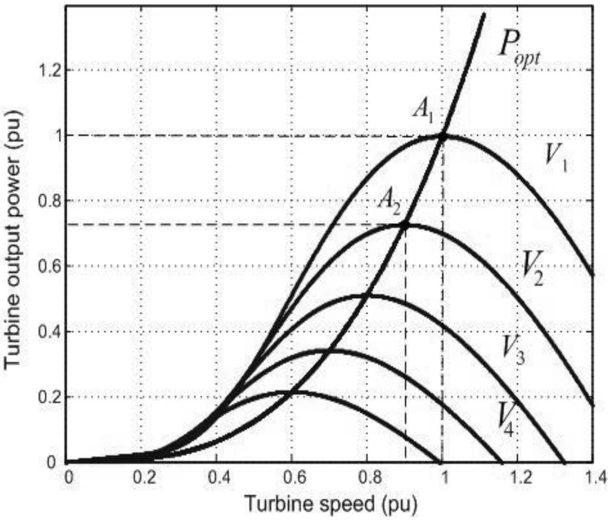

Figure 4.6 Wind turbine power characteristic with different wind speed for pitch angle β=0°.

The control flow chart (for torque command generation) is shown in Figure 4.7. Initially, C_p is calculated according to the wind speed, blade radius and rotor speed. The wind speed profile and blade radius are pre-installed in DSP RAM, while the rotor speed signal is obtained from the motor drive. Pitch control is not considered in this chapter, thus pitch angle β is set to a minimum value, 0°. The mechanical power P_m is determined from the wind turbine output power formula equation (4.4). The target torque reference is calculated and applied to the PMSG. The whole wind emulator system produces real wind turbine characteristics via the control flow process in Figure 4.7.

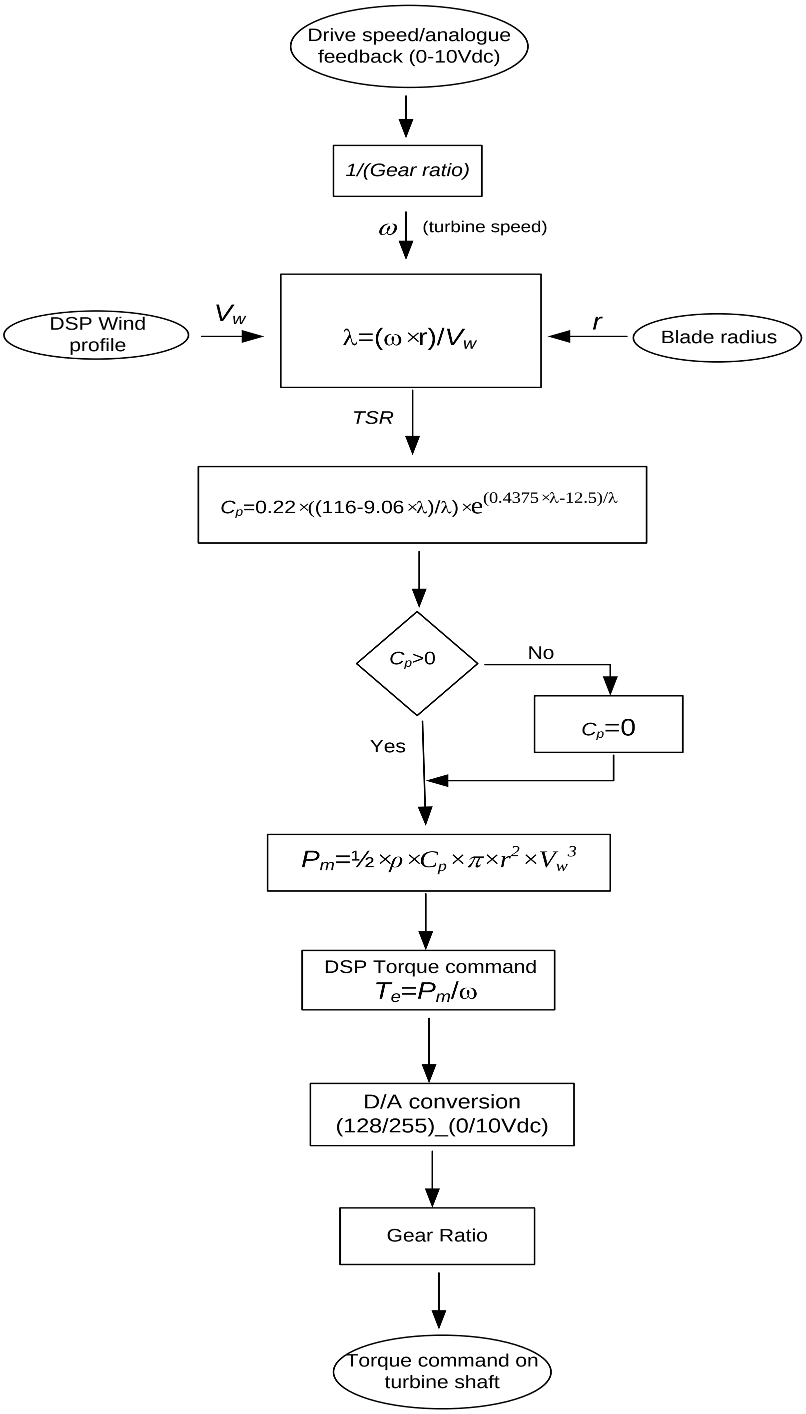

Figure 4.7 Control flow for the wind turbine emulator system.

The wind turbine emulator, is based on a 2.5kW axial-flux three-phase PMSG developed during a collaborative project with the UK company Proven Energy, and has the specifications shown in Table 4.1. The emulator does not account for the mechanical system.

Table 4.1 Proven 2.5 kW PMSG specifications.

Parameter	Proven Energy Wind Turbine Generators (Axial- Gap PM Machines)
Power, kW	2.5
Phase Resistance, Ω	3.989
Inductance, mH	16.72
Back emf constant (v/rpm)	543.5/400
Rated Power, kW	2.5
Rated Speed, RPM	300
RMS Current Rating, A	7.4
Cut In Speed, RPM	200
Cut Out Speed, RPM	NA
Voltage Power Profile	260Vdc = 0 kW,260 - 300Vdc = 0.4 kW, 300 - 320Vdc = 1.25 kW,<320Vdc = 2.5 kW
Tip Speed, m/s	60
Number of Magnets per Plate	8
Magnet dimensions,	$100\times100\times25$
Magnet Plate OD, mm	470
Back Plate, mm	10
Shaft OD, mm	45
Voltages, V	48
Turns	57
Windings	1.6mm wire, 24 segments in 3 layers
Number of parallel paths	1

The turbine emulator is tested with specification shown in Table 4.2.

Table 4.2 Wind turbine parameter.

Parameter	Wind Turbine Parameters
Air density	ρ=1.220kg/m^3
Blade radius	r=1.893m
C_{pmax}	0.4382
TSR_{op}	6.335
Gear ratio	3.08

4.3 Analysis of the H-Bridge converter

4.3.1 H-bridge converter modelling

As shown in Figure 4.3, the hard-switched full-bridge dc/dc converter contains four switches, a high-frequency (HF) transformer, a diode rectifier and an output inductor. The hard-switched H-bridge converts dc input voltage to an ac square wave voltage which is impressed across a HF transformer winding. Thus ac voltage is stepped up through the HF transformer. The dc output voltage can be obtained via a diode rectifier. The dc output voltage is stepped up through the dc/ac/dc conversion process. For a continuous conduction mode, the relationship between the input and output voltage is expressed as:

$$V_{out} = V_{IN} \times D \times N \tag{4.5}$$

where V_{in} is the input voltage of dc/dc converter, V_{out} is the output voltage, N is transformer turn ratio, and D is switch duty cycle.

The switch duty cycle can be defined as:

$$D = \frac{t_{on}}{T_s} \tag{4.6}$$

where t_{on} is the on-duration of the switches and $1/T_s$ is switching frequency.

Figure 4.8 shows the waveforms of the input current and input voltage to the HF transformer.

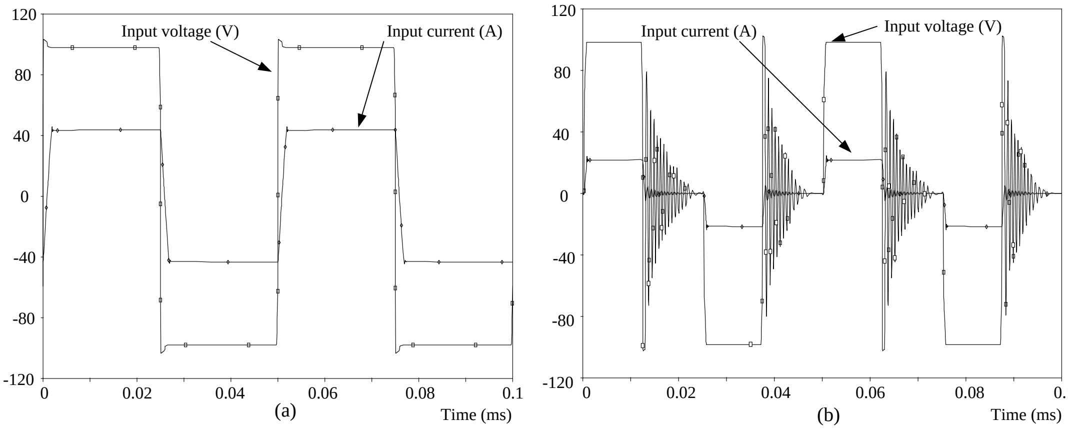

Figure 4.8 Input current and input voltage to the HF transformer (a) Full duty cycle (b) Partial duty cycle.

For a variable-speed wind energy conversion system, the dc/dc converter is controlled to keep the dc link voltage constant or to track the maximum power during wind changes, and the control depends on the dc/ac rectifier type connected to the generator. A controlled dc/ac rectifier gives a constant output voltage and maximum power tracking, but increases the system cost and control complexity, with higher loss [4.13]. The uncontrolled dc/ac rectifier (diode rectifier) has an output voltage proportional to the generator speed, assuming negligible stator impedance and diode forward voltage drop. Considering the simplicity and low cost of a diode rectifier, a full-wave diode rectifier is used in the proposed low power WECS.

4.3.2 Comparative study of the boost converter and the H bridge converter

The boost converters and H-bridge converters used in WECS are controlled to maintain the wind turbine at the maximum power point in the steady state at different wind speeds. The average and peak switch currents are compared at the maximum power point corresponding to the different wind speeds:

If the power conversion efficiency of the turbine/generator is η, then the maximum output electrical power P_e at each wind speed can be expressed as:

$$P_e = \eta \mathrm{P}_{\max} = \eta k \omega^3 = k_1 \omega^3 \tag{4.7}$$

where $k_1 = \eta k$.

The electrical power is transferred to the grid by the intermediate converters. The input electrical power at the boost converter side is:

$$P_e = v_i \times i_i \tag{4.8}$$

In order to simplify the expression, all the quantities are expressed using the per unit system. It is assumed that the variables at rated wind speed are 1pu and the common dc link voltage is k_2 pu ($k_2 \geq 1$). Thus equations (4.7) and (4.8) can be normalized, in the pu system, and expressed as:

$$P_e = v_{i\_pu} \times i_{i\_pu} = {\omega_{pu}}^3 \tag{4.9}$$

where V_{i_pu} is rated pu input voltage, i_{i_pu} is rated pu input current, and P_{e_pu} is rated pu electrical power, each at rated wind speed.

The maximum pu mechanical power P_{m_pu} is:

$$P_{m\_pu} = \frac{1}{\eta}\omega_{pu}{}^{3} \tag{4.10}$$

The output voltage transfer function of the boost converter is [4.14]:

$$\frac{v_{0\_pu}}{v_{i\_pu}} = \frac{k_2}{v_{i\_pu}} = \frac{1}{1-\delta} \tag{4.11}$$

where δ is the duty cycle.

The output voltage is maintained constant by the subsequent inverter, thus equation (4.11) can be rewritten as:

$$v_{i\_pu\_BT} = k_2(1-\delta) \tag{4.12}$$

For the HSFB converter, the input voltage is derived according to equation (4.5).

$$v_{i\_pu\_HB} = \frac{k_2}{DN} \tag{4.13}$$

Substituting (4.12) and (4.13) into (4.9) respectively, and eliminating $v_{i,}$ gives:

$$i_{i\_pu\_BT} = \frac{\omega_{pu}{}^{3}}{k_2(1-\delta)} \tag{4.14}$$

$$i_{i\_pu\_HB} = \frac{\omega_{pu}{}^{3}DN}{k_2} \tag{4.15}$$

Equations 4.14 and 4.15 show the average input current of the boost converter and H-bridge in terms of rotor speed, duty cycle, and transformer ratio.

For a synchronous generator with a diode rectifier bridge, the rectifier output voltage can be expressed as:

$$v_i = \varphi(\psi, i_g) \times \omega \tag{4.16}$$

The flux ψ is constant for permanent magnet generators. Thus φ is only related to the generator current i_g and ω. Assuming the generator stator impedance voltage drop caused by i_g can be ignored, the term $\varphi(\psi, i_g)$ can be considered as a constant value. Hence v_i is proportional to ω which can be expressed in pu as:

$$v_{i\_pu} = \omega_{pu} \tag{4.17}$$

Equations (4.12) and (4.17) give:

$$\omega_{pu\_BT} = k_2(1 - \delta) \tag{4.18}$$

Equations (4.13) and (4.17) give:

$$\omega_{pu\_HB} = \frac{k_2}{DN} \tag{4.19}$$

Substituting (4.18) and (4.19) into (4.14) and (4.15) respectively, and eliminating δ, gives:

$$i_{i\_pu} = i_{i\_pu\_BT} = i_{i\_pu\_HB} = {\omega_{pu}}^2 \tag{4.20}$$

Equation 4.20 shows the average input current of the boost converter and H-bridge converter in terms of rotor speed ω. From this equation, the boost converter and H-bridge average currents are independent of duty cycle and transformer ratio. They are proportional to the square of rotor speed.

Figure 4.9 shows the average input current versus rotor speed with variable wind speed. The thick black curve represents the relationship between average input current and rotor speed at the maximum power point at different wind speeds.

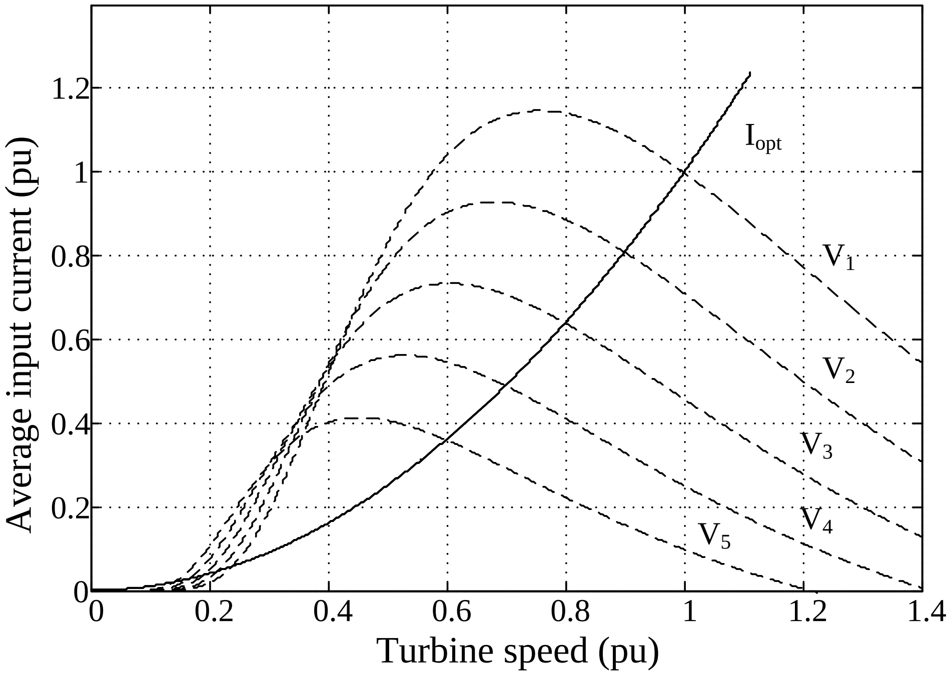

Figure 4.9 Average input current of boost converter and H-bridge versus rotor speed (pu) at different wind speeds.

The boost converter average switch current can be derived as:

$$i_{av\_pu\_BT} = \delta i_{i\_pu} = \delta {\omega_{pu}}^2 \tag{4.21}$$

The H-bridge converter average switch current is half of the average input current due to the symmetric circuit, that is:

$$i_{av\_pu\_HB} = i_{i\_pu}/2 = {\omega_{pu}}^2/2 \tag{4.22}$$

The switch peak current is determined by the average switch current and the duty cycle. The peak switch currents of the two converters can be expressed as:

$$i_{pk\_pu\_BT} = i_{i\_pu} = {\omega_{pu}}^2 \tag{4.23}$$

$$i_{pk\_pu\_HB} = i_{i_{pu}}/D = {\omega_{pu}}^2/D \tag{4.24}$$

For a variable-speed wind energy conversion system, due to the use of an uncontrolled diode rectifier, the dc/dc converter is controlled to track the maximum power point. In order to achieve MPPT, the dc/dc converter needs to provide sufficient dc gain when the wind speed changes, otherwise the wind turbine may only operate on the right hand side of the power characteristics curve. The input voltage of the HSFB converter varies as wind speed changes, which is proportional to the generator speed. The dc output voltage of the dc/dc converter is regulated by the subsequent inverter. In order to achieve a high voltage level, the transformer turns ratio should be considered. Thus the typical transformer turns ratio for the HSFB converter is based on the minimum input voltage at low wind speed. When the wind speeds up, the duty cycle of the FB converter is reduced in order to reduce the transformer gain for voltage regulation. Consequently, a higher peak current occurs due to a small duty cycle at high wind power.

For the variable speed WECS, it is assumed that the cut-in wind speed (V_{cut_in}) is k_3 pu. Thus the maximum power P_{m_pu} corresponding to the wind speed from k_3 pu to 1pu is from k_3^3/η pu to 1pu. The converter input voltage (V_{in_pu}) ranges from k_3 pu to 1pu, when neglecting stator impedance and rectifier diodes voltage drops. For the HSFB converter, the transformer turns ratio is designed for the minimum input voltage and maximum output voltage, to ensure the converter output voltage reaches the dc link voltage. Thus the transformer turns ratio is $1{:}k_2/k_3$. The transformer secondary voltage V_{sec_pu} at rated input voltage is k_2/k_3 pu. For the HSFB, the bridge diode rectifier on the high-voltage side experiences severe voltage overshoot and oscillation due to transformer leakage inductance and the output filter inductor [4.15], causing rectifier peak voltages larger than the transformer secondary voltage V_{sec}. In order to reduce the rectifier side voltage spike, a conventional resistor-capacitor-diode (RCD) snubber circuit is used [4.16]. The use of several energy recovery clamp circuits (ERCC) [4.17-19] has also been proposed.

Assuming a lossless converter, and that the output voltage and average output current I_o of the boost converter and H-Bridge converter are the same,

$$i_{o\_pu\_BT} = i_{o_{pu_{HB}}} = i_o = \frac{\omega^3}{k_2} \tag{4.25}$$

The average output diode currents of the two converters are:

$$i_{D\_pu\_BT} = i_o \tag{4.26}$$

$$i_{D\_pu\_HB} = \frac{i_o}{2} \tag{4.27}$$

The peak output diode currents of the two converters can be expressed as:

$$I_{D\_pk\_pu\_BT} = \frac{i_o}{1-\delta} \tag{4.28}$$

$$I_{D\_pk\_pu\_HB} = i_o \tag{4.29}$$

From equations (4.20) and (4.25), the average input and output currents of the two converters are related to the rotor speed and output voltage, and are independent of duty cycle and transformer turns ratio. Equations (4.21) and (4.23) show that the boost converter switch average current is related to the duty cycle and rotor speed while switch peak current is only related to the rotor speed. According to equations (4.22) and (4.24), the H-Bridge average and peak diode currents are the opposite of the boost converter currents. From equations (4.25)-(4.29), the average diode current in the two converters and the H-Bridge converter diode peak current are only related to the rotor speed and dc voltage. The H-Bridge average diode current is half that of the boost converter diode current, while the peak diode current in the boost converter is inversely related to 1-δ, which means higher voltage gain and larger diode current.

Assuming a cut-in wind speed V_{cut_in}=1/3 pu, the transformer turns ratio for the H-Bridge converter should be 1:3k_2. Figure 4.10 and Figure 4.11 compare average and peak switch currents for the boost converter and H-Bridge converter. The dashed lines represent the boost converter switch currents, while the solid lines represent the H-Bridge converter switch currents. Figure 4.10 (a) and Figure 4.11 (a) show the switch currents of the two converters corresponding to different rotor speeds, at wind speeds v_1 and v_2 respectively. The switch currents of the two converters at maximum power point with different wind speeds are shown in Figure 4.10 (b) and Figure 4.11 (b). Note that the maximum average current does not occur at the maximum power point at a certain wind speed, while the maximum peak current occurs at the maximum power point, as shown in Figure 4.10 (a) and Figure 4.11 (a). From Figure 4.10 (b) and Figure 4.11 (b), the H-Bridge average switch current at the MPP is smaller than for the boost converter with k_2=2 and k_2=6. The boost converter average switch current is close to 1pu at ω_s=1 as the dc link voltage k_2 increases, while the H-Bridge peak switch current at the MPP is larger than the boost converter current at the MPP.

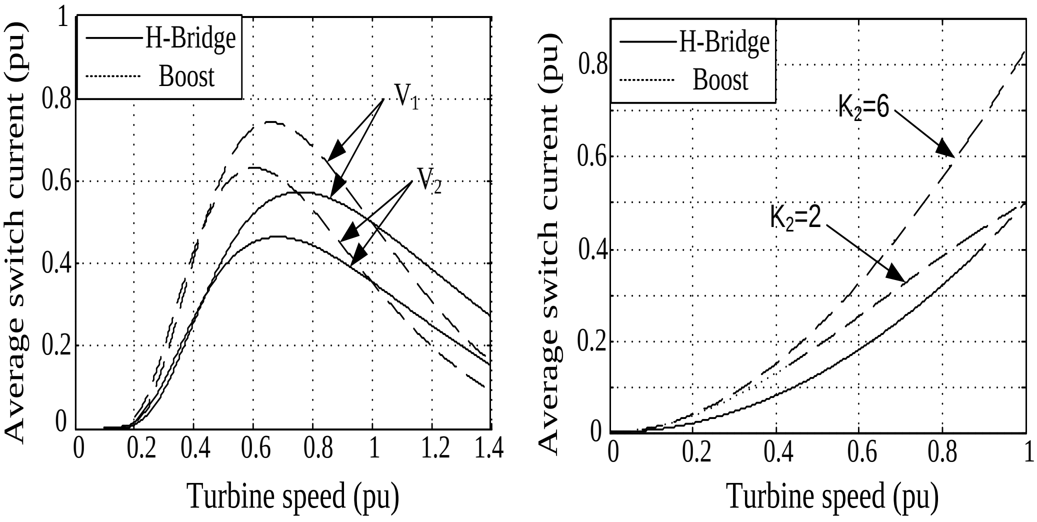

(a)

(b)

Figure 4.10 Compared average switch currents for boost converter and H-Bridge converter (a) at different wind speed (b) at maximum power point.

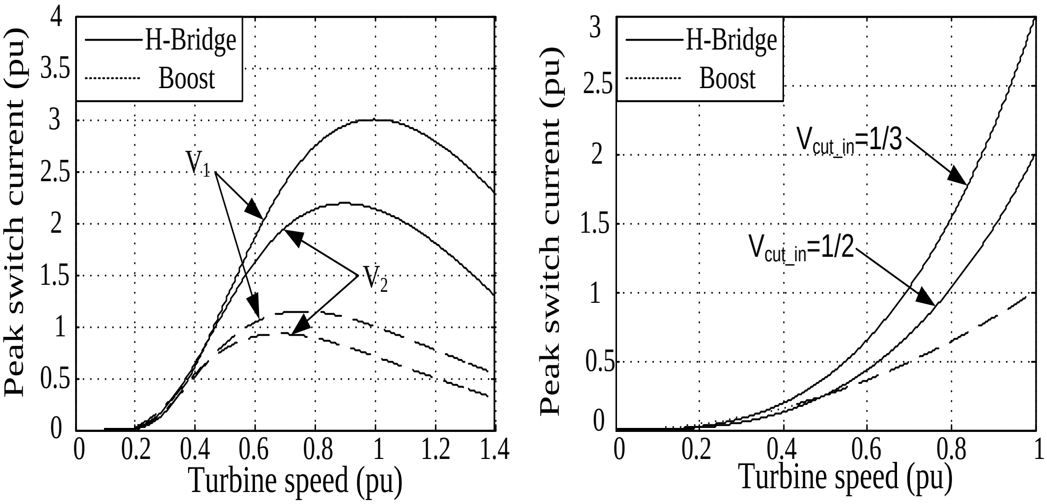

(a)

(b)

Figure 4.11 Compared peak switch currents for boost converter and H-Bridge converter (a) at different wind speed (b) at maximum power point.

The switch and diode currents in the boost converter and H-Bridge converter have been compared. A high voltage gain cannot be achieved with the boost converter due to practical components characteristics and high output diode current. The compared results form a basis for designing the H-Bridge converter.

4.4 Control of the HSFB

For the HSFB converter, both push-pull duty cycle and phase shift control have been studied [4.1]. The HSFB input voltage is varied as wind speed varies due to the uncontrolled diode rectifier characteristics. The losses using duty cycle control and phase shift control are compared in [4.20]. Duty cycle control results in lower conduction losses but higher switching losses, while the converse applies to phase shift control. The power losses with duty cycle control are lower than phase shift control, thus the duty cycle control is used for the HSFB.

Several types of MPPT schemes are illustrated in Chapter 3. TSR and PSF control both need the WG characteristics and accurate mechanical sensors (e.g. anemometer or speed sensor), which increases control system complexity and system cost. P&O control results in slow tracking speed and oscillation at the maximum power point, although there is no need for WG characteristics and accurate mechanical sensors. Since the HSFB converter topology is different from that of the boost converter, the OPP control method used with the boost converter is not applicable to the HSFB converter. A new modified OPP control method is presented in this chapter. From equations (4.17) and (4.20), the average input current at the MPP can be expressed as:

$$\overline{I_{sw\_pu}} = {v_{i\_pu}}^2 \tag{4.30}$$

The average input current is proportional to the input voltage. Once one maximum power status point of the WECS for any specific wind speed in the working range is obtained, the curve of input current at MPP versus input voltage can be derived. The wind turbine utilises the curve to track the maximum power point. Like OPP control, there is also no need for sensors. It has fast tracking speed with a PI controller, compared to P&Q control. Figure 4.12 shows the control diagram of modified OPP control. The input voltage is measured, and then the corresponding input current is calculated using equation (4.30). The PI controller is used to produce the PWM signals.

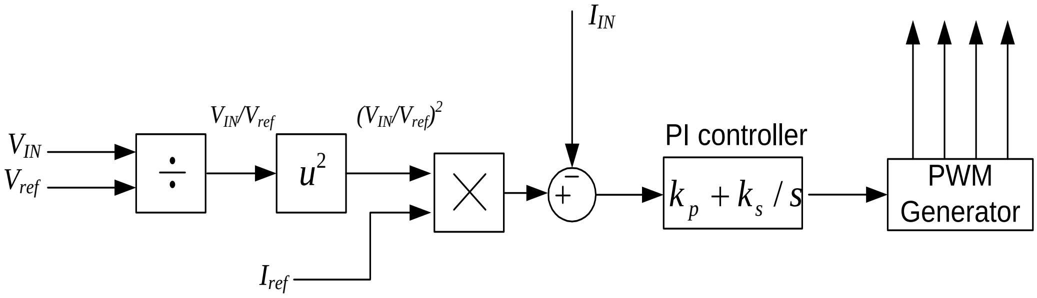

Figure 4.12 Control diagram of modified OPP control.

4.5 Simulation and experimental results

To verify the functionality and feasibility of the proposed system, the WECS is simulated in MATLAB/Simulink with specific wind changes. The current source grid inverter is modelled by a dc-chopper circuit in parallel with a shorting switch that maintains the average dc link voltage constant by controlling the duty cycle of the two switches. The two switches are controlled with complementary gate signals with overlap. Figure 4.13 shows the WECS schematic. The details of the calculation block shown in Figure 4.13 are depicted in Figure 4.12. The wind turbine parameters used in the simulation and experimentation are the same as shown in Table 4.2. The electrical system parameters are summarized in Table 4.3.

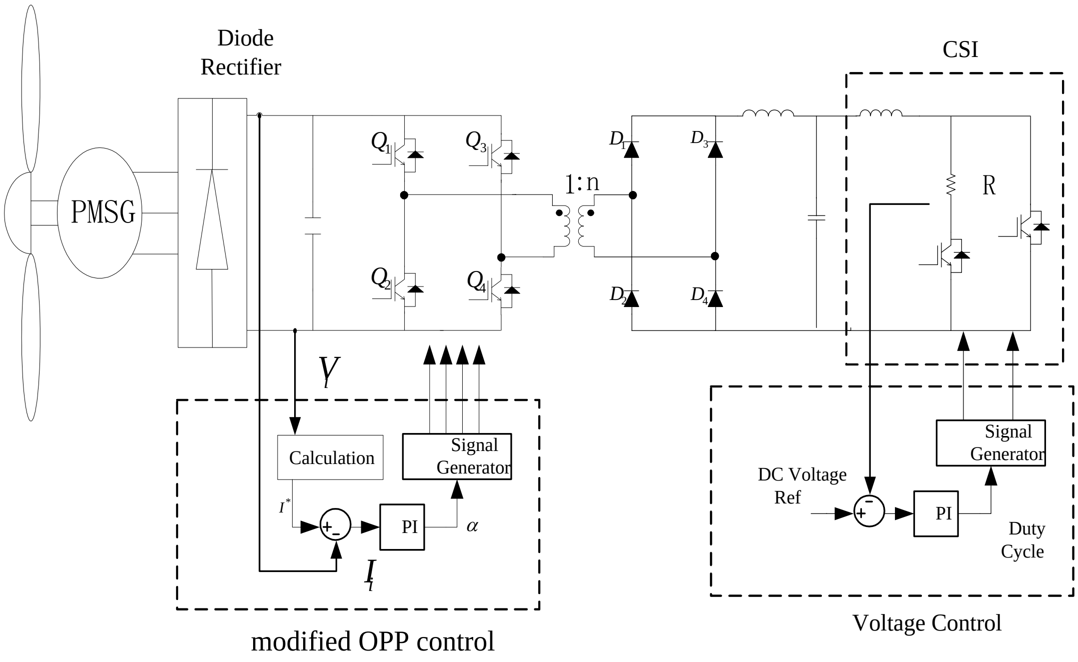

Figure 4.13 Schematic of the WECS.

Table 4.3 Electrical system parameters.

Parameters	Specification	
Input capacitance	3000	µF
Transformer turns ratio	10:14	
Output inductor	5	mH
Output capacitance	1	µF
Resistor	50	Ω
Switching frequency	38.8	kHz

Figure 4.14 shows simulation results of the mechanical system dynamic response, which includes wind speed profile, power coefficient C_p, rotor speed, and mechanical power. A step wind speed change is used in the simulation and experiment in order to determine the system dynamic characteristic limits. As shown in Figure 4.14, the wind speed is 5.8 m/s during the initial 1s, and steps up to 6.2 m/s at 4s, after which

the wind speed is stepped down to 5.8 m/s. The power coefficient C_p is maintained around the maximum value 0.4382, which means the wind turbine tracks maximum power from the wind during wind speed step changes. The rotor speed is also regulated to a value corresponding to the maximum power point. The practical results of the mechanical system dynamic response based wind turbine simulator are shown in Figure 4.15. The same wind speed change as in the simulation is applied. The rotor speed is changed to track the maximum power, which assures the power coefficient is around the maximum value.

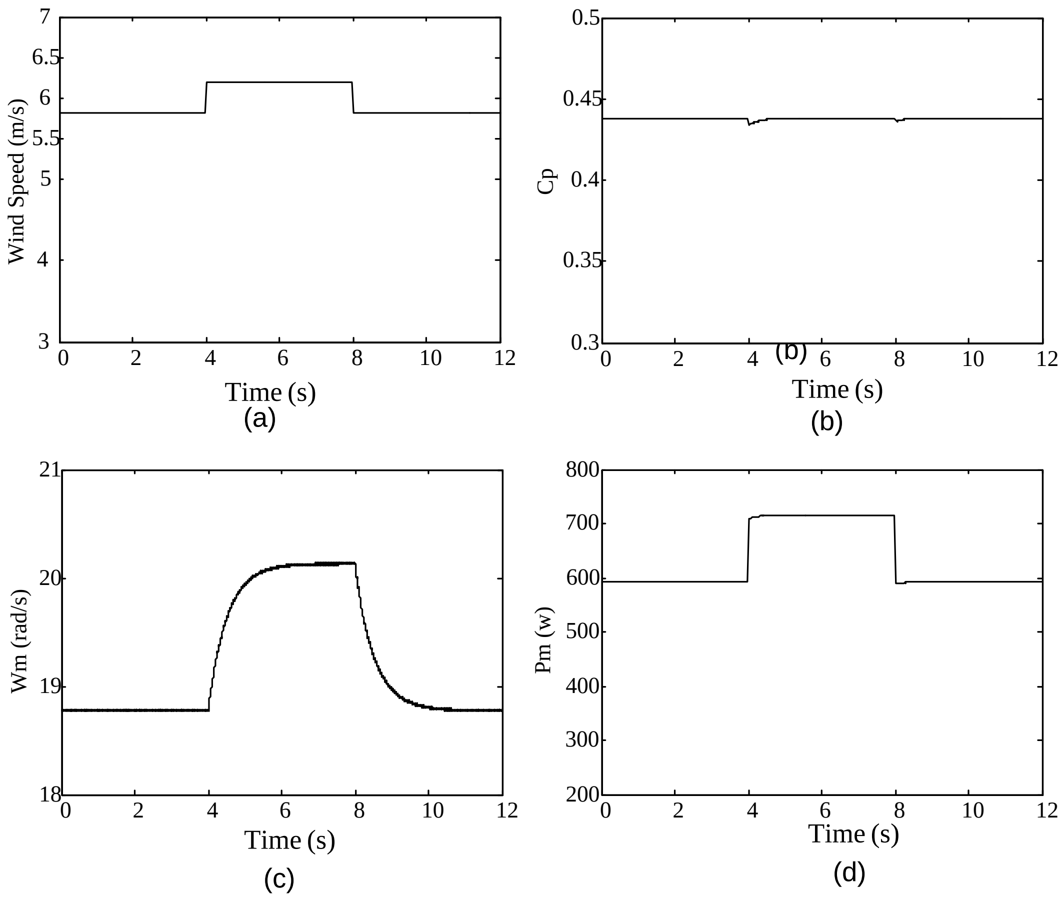

Figure 4.14 Simulation results of mechanical system dynamical response.

The dynamic response of the electrical system is shown in Figure 4.16, including dc link voltage and output current. The dc power produced by the PMSG is to be transmitted to the ac grid side. Thus inverter dc side voltage should be kept constant to stabilize the whole WECS. As shown in Figure 4.16, the dc link voltage is maintained constant during a wind speed step change, thus the output current is changed as power extracted by the wind turbine changes.

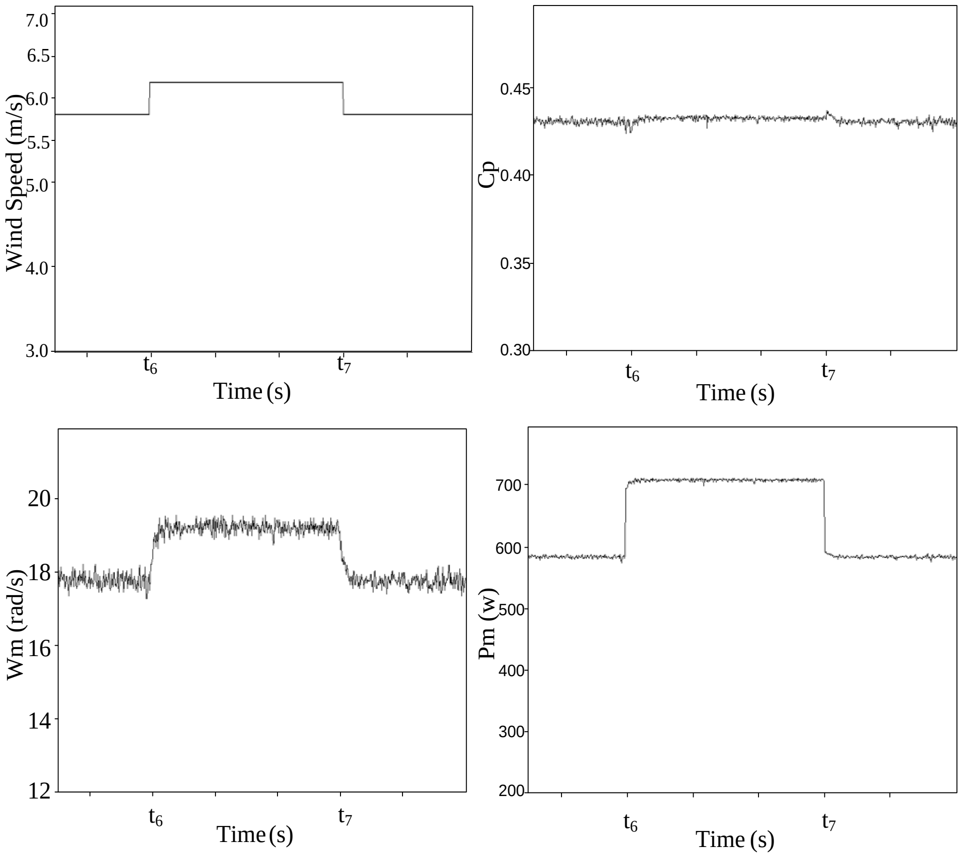

Figure 4.15 Practical results of mechanical system dynamical response.

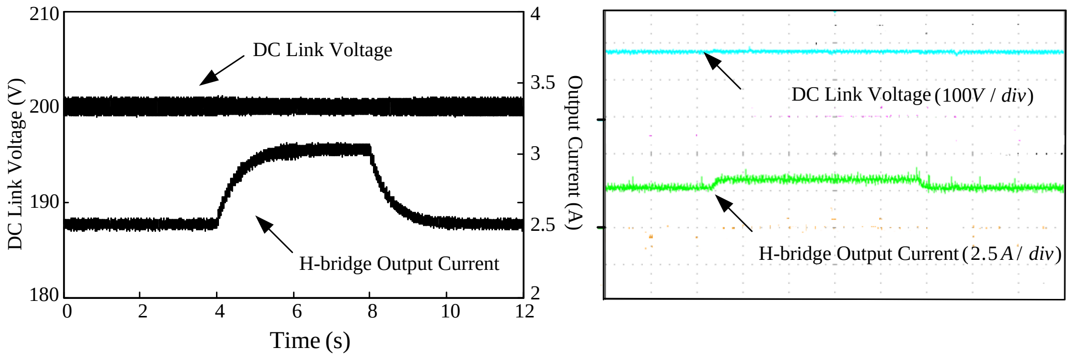

Figure 4.16 Dynamic response of electrical system.

4.6 Summary

In this chapter, a current source based Hard-Switched H-Bridge converter with an intermediate high frequency transformer is proposed for interfacing the wind turbine and inverter. It tracks the maximum power of the wind energy and steps up the low generator voltage to a high voltage level. The wind turbine simulator based on 3-phase PMSG is built to simulate the real wind turbine characteristics. The switch and diode average and peak currents in the boost and H-Bridge converters are compared. The H-Bridge dc/dc converter is better than the boost converter in terms of high voltage gain and low peak diode current. The penalty is more semiconductors and associated control circuitry. Modified OPP control is also proposed for WECS without sensors, which tracks the maximum power point quickly. The proposed WECS dynamic performance was verified by the simulation and experimental results.

References

[4.1] N. Mohan, T. M. Undeland, and W. P. Robbins, "Power Electronics - Converters, Applications, and Design (3rd Edition)," ed: John Wiley & Sons, 2003.

[4.2] S. M. Muyeen, R. Takahashi, T. Murata, and J. Tamura, "Control strategy for HVDC interconnected DC-based offshore wind farm," in *Electrical Machines and Systems, 2009. ICEMS 2009. International Conference on*, 2009, pp. 1-6.

[4.3] N. Flourentzou, V. G. Agelidis, and G. D. Demetriades, "VSC-Based HVDC Power Transmission Systems: An Overview," *Power Electronics, IEEE Transactions on,* vol. 24, No. 3, pp. 592-602, 2009.

[4.4] P. Bresesti, W. L. Kling, R. L. Hendriks, and R. Vailati, "HVDC Connection of Offshore Wind Farms to the Transmission System," *Energy Conversion, IEEE Transactions on,* vol. 22, No. 1, pp. 37-43, 2007.

[4.5] X. Lie, Y. Liangzhong, and C. Sasse, "Grid Integration of Large DFIG-Based Wind Farms Using VSC Transmission," *Power Systems, IEEE Transactions on,* vol. 22, No. 3, pp. 976-984, 2007.

[4.6] O. Gomis-Bellmunt, A. Junyent-Ferre, A. Sumper, and J. Bergas-Jane, "Control of a Wind Farm Based on Synchronous Generators With a Central HVDC-VSC Converter," *Power Systems, IEEE Transactions on,* vol. 26, No. 3, pp. 1632-1640, 2011.

[4.7] D. Jovcic, L. A. Lamont, and L. Xu, "VSC transmission model for analytical studies," in *Power Engineering Society General Meeting, 2003, IEEE,* 2003, p. 1742 Vol. 1743.

[4.8] T. Nyikos and T. Tomaschett, "Experimental verification of a DC-DC converter for a DC wind farm," Master's thesis, Dep. of Energy and Environment, Chalmers University of Technology, 2006.

[4.9] L. Max and T. Thiringer, "Control method and snubber selection for a 5 MW wind turbine single active bridge DC/DC converter," in *Power Electronics and Applications, 2007 European Conference on*, 2007, pp. 1-10.

[4.10] J. Hu, Y. He, L. Xu, and B. W. Williams, "Improved Control of DFIG Systems During Network Unbalance Using PI-R Current Regulators," *Industrial Electronics, IEEE Transactions on,* vol. 56, No. 2, pp. 439-451, 2009.

[4.11] A. O. Ibrahim, N. Thanh Hai, L. Dong-Choon, and K. Su-Chang, "A Fault Ride-Through Technique of DFIG Wind Turbine Systems Using Dynamic Voltage Restorers," *Energy Conversion, IEEE Transactions on,* vol. 26, No. 3, pp. 871-882, 2011.

[4.12] Y. Jun, L. Hui, L. Yong, and C. Zhe, "An Improved Control Strategy of Limiting the DC-Link Voltage Fluctuation for a Doubly Fed Induction Wind Generator," *Power Electronics, IEEE Transactions on,* vol. 23, No. 3, pp. 1205-1213, 2008.

[4.13] J. Robinson, D. Jovcic, Joo, x, and G. s, "Analysis and Design of an Offshore Wind Farm Using a MV DC Grid," *Power Delivery, IEEE Transactions on,* vol. 25, No. 4, pp. 2164-2173, 2010.

[4.14] B. W. Williams. *Power electronics: devices, drivers, applications, and passive components:* Available: http://homepages.eee.strath.ac.uk/~bwwilliams/book.htm

[4.15] C. Honnyong, C. Lihua, D. Rongjun, T. Qingsong, and P. Fang Zheng, "An Alternative Energy Recovery Clamp Circuit for Full-Bridge PWM Converters With Wide Ranges of Input Voltage," *Power Electronics, IEEE Transactions on,* vol. 23, No. 6, pp. 2828-2837, 2008.

[4.16] L. H. Mweene, C. A. Wright, and M. F. Schlecht, "A 1 kW 500 kHz front-end converter for a distributed power supply system," *Power Electronics, IEEE Transactions on,* vol. 6, No. 3, pp. 398-407, 1991.

[4.17] K. Eun-Soo, J. Kee-Yeon, K. Moon-Ho, K. Yoon-Ho, and Y. Byung-Do, "An improved soft-switching PWM FB DC/DC converter for reducing conduction losses," *Power Electronics, IEEE Transactions on,* vol. 14, No. 2, pp. 258-264, 1999.

[4.18] C. Jung-Goo, B. Ju-Won, J. Chang-Yong, Y. Dong-Wook, and J. Kee-Yeon, "Novel zero-voltage and zero-current-switching full bridge PWM converter using transformer auxiliary winding," *Power Electronics, IEEE Transactions on,* vol. 15, No. 2, pp. 250-257, 2000.

[4.19] A. Bendre, S. Norris, D. Divan, I. Wallace, and R. W. Gascoigne, "New high power DC-DC converter with loss limited switching and lossless secondary clamp," *Power Electronics, IEEE Transactions on,* vol. 18, No. 4, pp. 1020-1027, 2003.

[4.20] L. Max and T. Thiringer, "Design and control of a 5MW medium frequency DC/DC converter for a wind turbine," in *Proc. the 2nd EPE Wind Energy Chapter*, 2009.

Chapter 5

Design and Control of a WECS based on the Resonant Converter

Recent wind energy harvesting technology development has focused on using a dc collection grid due to its high energy efficiency and possible smaller passive components in the converter system. This chapter evaluates and compares the hard-switched H-bridge dc-dc converter and the series-parallel LCC resonant dc-dc converter in terms of efficiency, switch stresses, etc.: both are suitable for wind energy conversion systems. Experimental results substantiate their merits and drawbacks in variable wind speed conditions. The unique, previously unexploited feature of the LCC resonant converter is high gain at low output power, low speed, and low input voltage. A hardware wind turbine simulator based on a five-phase PMSG emulating an actual wind turbine is used. Its design and control are briefly highlighted. This chapter demonstrates the feasibility of utilizing an LCC resonant converter for wind energy conversion systems through simulation and experimental results, both at the same power level.

5.1 Background

Wind power generation is developing fast globally, however most wind farms are located far from their grid connection point, making HVDC the preferred method for grid connection. For conventional HVAC systems, large, heavy, and bulky 50/60Hz transformers in the wind generator towers and converter station are still required to step up voltage [5.1]. An alternative solution is a dc grid, which uses dc/dc converters with a high frequency transformer. The hard-switched full-bridge (FB) dc-dc converter with an intermediate high-frequency transformer can be used in high-voltage, high-power applications. Compared to a 50/60Hz transformer, a high-frequency transformer has the advantages of smaller volume and lighter weight. High switching frequency causes significant switching loss in semiconductor devices. Thus there is a trade-off between switching frequency and device losses. In [5.2-3], simulation based loss evaluation of three dc/dc converter topologies (full bridge converter, single active bridge converter, and series parallel LCC resonant converter) has been performed. However, stresses and component selection were not studied. Moreover, dynamic WECS performance with a dc/dc converter was not demonstrated experimentally. For the hard-switched FB converter, there is voltage overshoot and oscillation across the diode rectifier on the high-voltage side, due to transformer leakage inductance and the output filter inductor [5.4]. This increases the number of series diodes for higher voltage sharing and also introduces EMI problems. Higher power loss and voltage overshoot occur due to the poor reverse recovery characteristics of high-voltage diodes. Reference [5.5] presents a new step-up dc-dc converter with variable frequency control, without transformer isolation, for the integration of renewable sources. Variable frequency control complicates resonant component and output filter design.

Resonant converters have been demonstrated as a feasible option for high-voltage power converters [5.6]. They allow high-frequency operation which results in magnetic component size reduction without decreasing converter efficiency.

5.2 A five phase PMSG based wind turbine emulator system

The wind turbine emulator system consists of a DSP (TRICORE TC1796), a variable speed drive, an induction machine and gearbox, and a five-phase PMSG.

Traditionally electrical energy has been generated by three-phase generators. The performance of three and five-phase PMSGs feeding a diode rectifier system are compared for small-scale wind generator systems [5.7]. It has been established that a five-phase PMSG can offer improved performance in the renewable energy applications such as wind turbine generators. The benefit includes improved torque density, efficiency and fault tolerance, and reduced torque ripple and dc-link energy storage.

For a wind turbine emulator system based on a five-phase PMSG, the power coefficient C_p curve is stored in the DSP and the control flow diagram is the same as that for the three-phase wind turbine emulator system presented in Chapter 4. Table 5.1 shows the parameters for the five-phase PMSG based wind turbine emulator system.

Table 5.1 The parameters for the five-phase PMSG.

Parameter	Five-Phase PMSG
Power	2.5 kW
Phase resistance	2 Ω
Phase inductance	35.42 mH
Number of pole pairs	8
Gear ratio	4.88
Blade radius	2.86 m

5.3 Resonant converter

The three resonant converters to be discussed, when selecting the dc/dc converter for the wind energy conversion system, are series-resonant, parallel-resonant, and a combination of series-parallel resonant converters.

The basic converter operating concept for the three resonant converters involves an H-bridge producing a square wave of voltage which is applied to the resonant tank. A sine wave current will flow through the resonant circuit due to the filtering effect of the resonant circuit. The current lags the voltage when it operates above the resonant frequency, which allows power devices to achieve zero voltage switching, ZVS. Thus there are no turn-on switching losses in the IGBTs. Also the inverse conducting diode with ZVS turn off ceases conduction before the inverse voltage is applied to the diode. Thus there is no reverse recovery current to causes diode losses. Also the diode can be a medium speed type. However, converters operating above the resonant frequency cannot turn off the device with zero current switching, ZCS. If switching frequency is slightly higher than the resonant frequency, turn-off loss will be small due to switching off at a small current. If necessary, a lossless capacitor snubber can be placed across the IGBT. The capacitors only discharged when the opposite IGBT in the same leg turns off. Thus energy stored in the capacitors will be returned to the dc side. For the converter operating below the resonant frequency, power devices turn on with switching losses and diode switching losses (high-speed diodes are needed). Although ZCS turn off occurs in the IGBT when operating below resonance, its paralleled diode has reverse recovery loss because the inverse voltage is applied across the conducting diodes. Thus operation above resonance is a better choice for a resonant converter operating at high frequency.

In the following section, classical ac analysis techniques are used, and the characteristics of each of the three resonant converters above and below resonance are described and compared, which will highlight the unique feature of the LCC resonant converter topology suitable for WECS.

5.3.1 Series resonant converter

Figure 5.1 shows the series resonant converter circuit diagram, where the rectifier-load network is placed in series with the L-C resonant tank, thus the output is a current source. In order to simplify the circuit, the rectifier circuit in the secondary side can be replaced with an equivalent load resistance which is different from the actual load resistance.

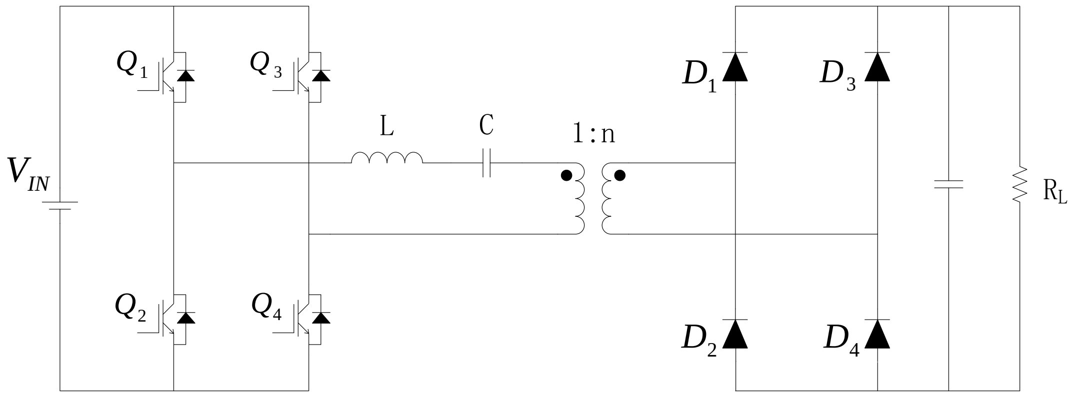

Figure 5.1 Circuit diagram of a series resonant converter.

Figure 5.2 shows the derivation of the equivalent ac resistance. For the series LC resonant converter, a capacitive output filter is used and therefore a square wave voltage and a sinusoidal current appear at the input to the rectifier. Fundamental mode approximation (FMA) analysis is used for brevity.

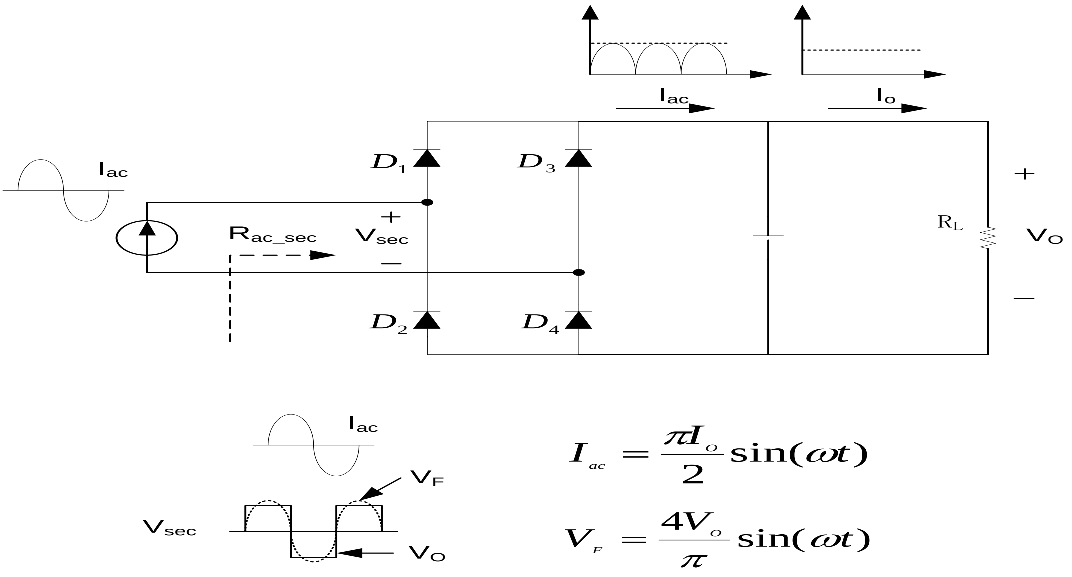

Figure 5.2 Derivation of the equivalent ac resistance.

The fundamental component of *V* is given as:

$$V^F = \frac{4V_O}{\pi} sin\,\omega_s t \tag{5.1}$$

The equivalent ac load resistance can be calculated as:

$$R_{ac\_sec} = \frac{V^F}{I_{ac}} = \frac{8}{\pi^2} R_L \tag{5.2}$$

Considering the transformer turns ratio N, the equivalent load resistance on the primary side is expressed as:

$$R_{ac} = \frac{8}{\pi^2 N^2} R_L \tag{5.3}$$

By using the equivalent load resistance, the ac equivalent circuit resonant tank is obtained, as shown in Figure 5.3.

$$E_{in} = \frac{4V_{in}}{\pi} sin\, \omega_s t \tag{5.4}$$

$$E_o = \frac{4V_0}{\pi N} sin\, \omega_s t \tag{5.5}$$

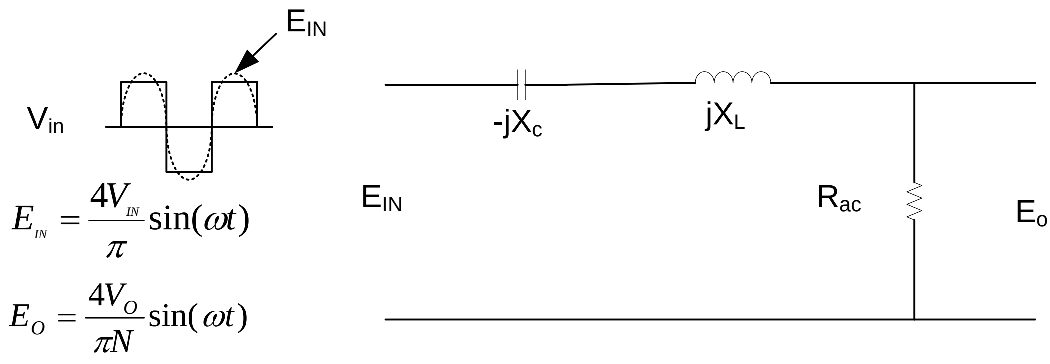

Figure 5.3 Ac equivalent circuit for series resonant converter.

From Figure 5.3, by using the voltage divider equation, the ac gain of the series resonant circuit can be obtained as:

$$\frac{E_o}{E_{in}} = \frac{1}{1+j(\frac{X_L}{R_{ac}} - \frac{X_C}{R_{ac}})} \tag{5.6}$$

where E_{in} and E_o are the fundamental components of the driving voltage V_{in} and the reflected output voltage.

Substituting equations (5.3-5.5) into (5.6), the dc gain of the series resonant converter is:

$$\left|\frac{V_O}{V_{in}}\right| = \frac{N}{\sqrt{1+((\frac{\omega_S}{\omega_O}-\frac{\omega_O}{\omega_S})Q_L)^2}} \tag{5.7}$$

where:

$$\omega_O = \frac{1}{\sqrt{LC_S}} \tag{5.8}$$

$$Q_{\mathrm{L}} = \frac{\omega_O L}{R_{ac}} \tag{5.9}$$

The gain magnitude of equation (5.7) is plotted in Figure 5.4 for different Q_L with a transformer turns ratio N=1.

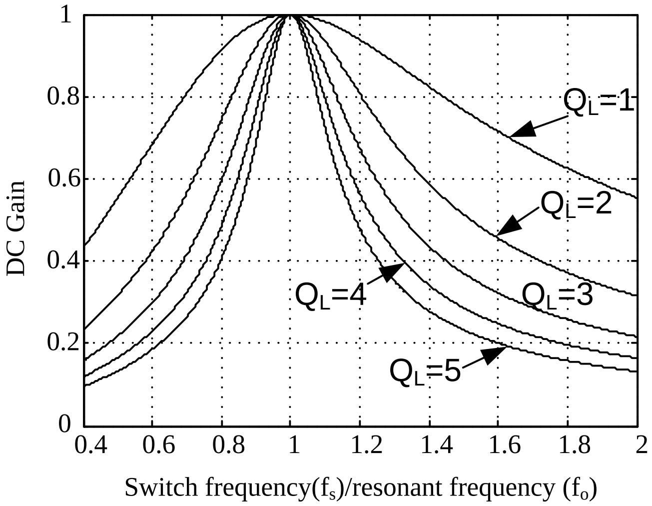

Figure 5.4 DC gain characteristic of series resonant converter.

It is known that the series-resonant converter has the main disadvantage that the output voltage cannot be regulated for the no-load case, as seen in the dc characteristics curve of the resonant converter in Figure 5.4. The peak dc voltage gain is equal to 1 at the resonant frequency. For smaller Q, the dc gain is less sensitive to switching frequency. Another disadvantage of this converter is that the output filter capacitor has to carry high ripple current to maintain the output voltage constant. Larger capacitance is needed for a voltage stiff output.

5.3.2 Parallel resonant converter

The schematic of the parallel resonant converter is shown in Figure 5.5. The series L-C resonant tank is the same as for the series resonant converter, but the voltage rectifier-load network is parallel to an L-C resonant tank component. The output is therefore a voltage source. Unlike the series resonant converter’s capacitive output filter, the parallel resonant converter uses a series inductor output filter. A square wave voltage and a sinusoidal current appear at the input to the rectifier.

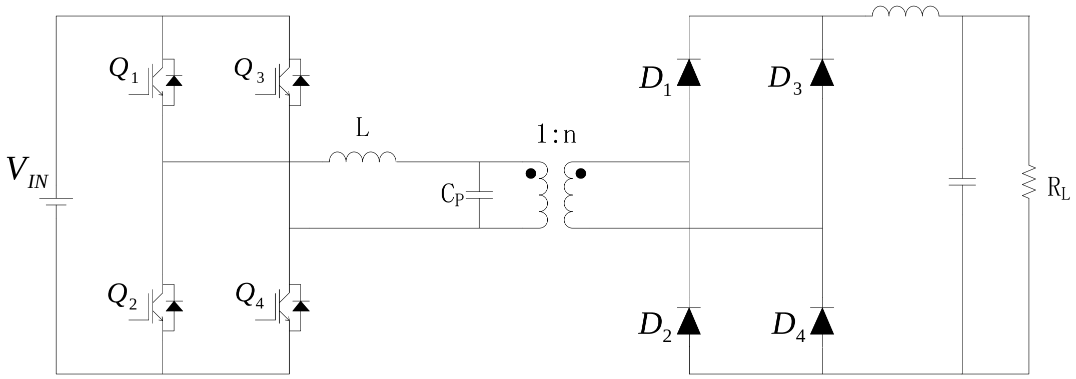

Figure 5.5 The circuit diagram of a parallel resonant converter.

The derivation of the equivalent ac resistance is shown in Figure 5.6.

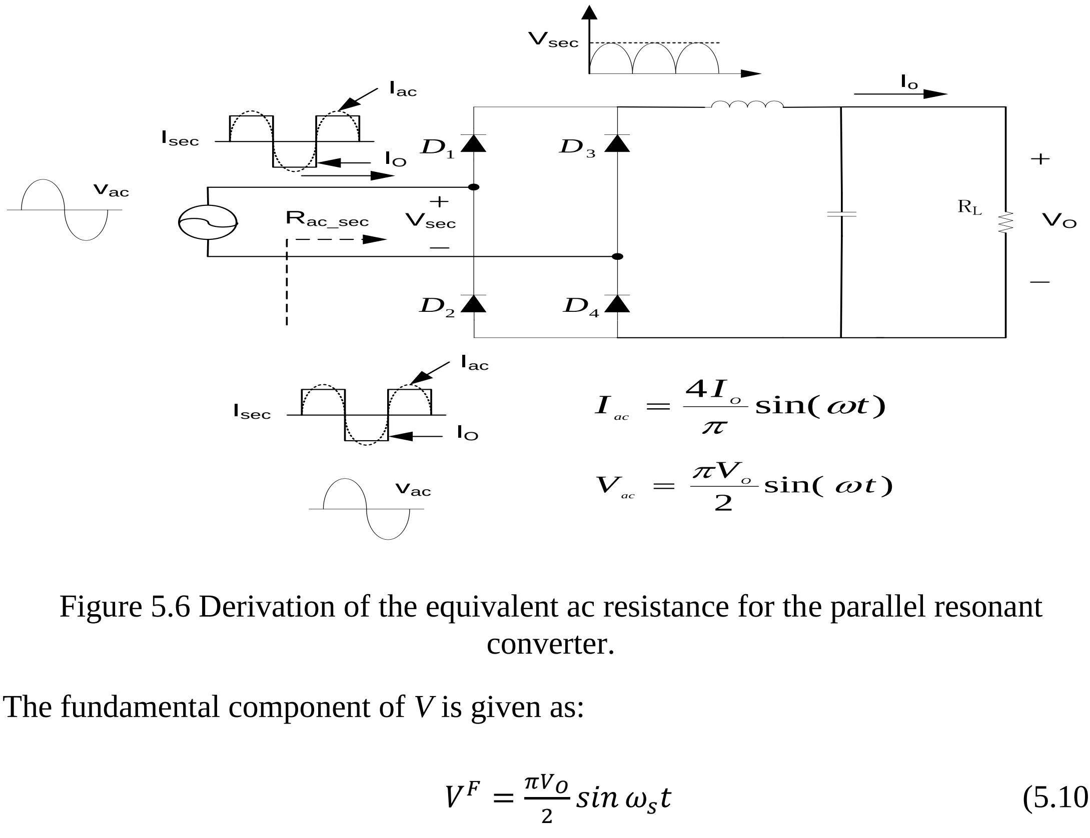

Figure 5.6 Derivation of the equivalent ac resistance for the parallel resonant converter.

The fundamental component of V is given as:

$$V^F = \frac{\pi V_O}{2} sin\, \omega_s t \tag{5.10}$$

From Figure 5.6, considering the transformer turns ratio N, the equivalent load resistance on the primary side is expressed as:

$$R_{ac} = \frac{\pi^2}{8N^2} R_L \tag{5.11}$$

With the equivalent load resistance obtained in Equation (5.11), the ac equivalent circuit of the parallel resonant converter is obtained, as illustrated in Figure 5.7, where

$$E_{in} = \frac{4V_{in}}{\pi} sin\, \omega_s t \tag{5.12}$$

$$E_o = \frac{\pi V_0}{2N} sin\, \omega_s t \tag{5.13}$$

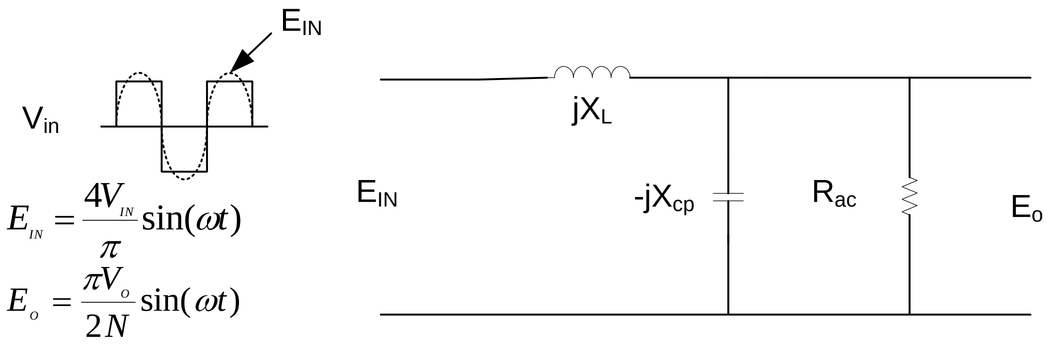

Figure 5.7 The ac equivalent circuit of parallel resonant converter.

Using the ac equivalent circuit of Figure 5.7, the ac gain of the series resonant circuit can be obtained as:

$$\frac{E_O}{E_{in}} = \frac{1}{1 - \frac{X_L}{X_C} + j\frac{X_L}{R_{ac}}} \tag{5.14}$$

Substituting the equations (5.12) and (5.13) into (5.14), the dc gain of the parallel resonant converter is:

$$\left|\frac{V_O}{V_{in}}\right| = \frac{8N}{\pi^2 \sqrt{(1-(\frac{\omega s}{\omega_o})^2)^2 + (\frac{\omega s}{\omega_o Q})^2}} \tag{5.15}$$

where:

$$\omega_O = \frac{1}{\sqrt{LC_P}} \tag{5.16}$$

$$\mathrm{Q_L} = \frac{R_{ac}}{\omega_O L} \tag{5.17}$$

Figure 5.8 shows the dc gain characteristic of the parallel resonant converter.

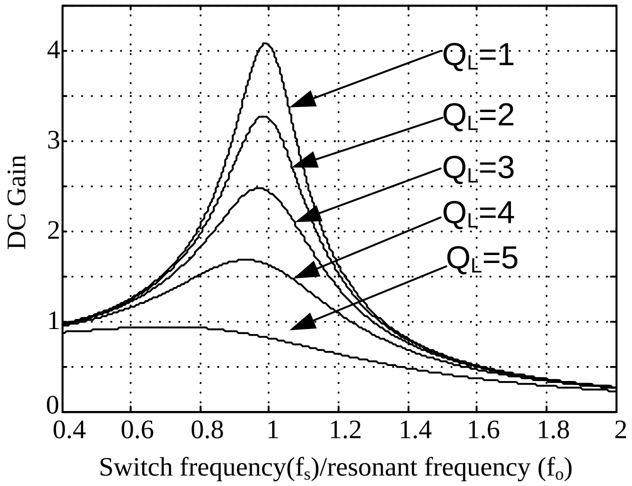

Figure 5.8 DC gain characteristic of the parallel resonant converter.

From Figure 5.8, the peak voltage gain can exceed unity. The dc gain at resonance increases as load reduces. The main disadvantage of the parallel resonant converter is that circulating energy is high even at light load, which leads to high conduction losses. The parallel resonant converter is resilient to short circuit. This property makes the parallel resonant converter desirable for applications with short circuit requirements.

5.3.3 Series-parallel resonant converter

The Figure 5.9 shows the circuit diagram of a series-parallel resonant converter. Its resonant tank consists of three resonant components: L, C_s and C_p. Series and parallel resonant converters have disadvantages and advantages, with the series-parallel resonant converter having the desirable characteristics of both these resonant converters. It can operate with a large input voltage variation and a wide load range (no-load to full-load) at reasonable efficiency [5.8].

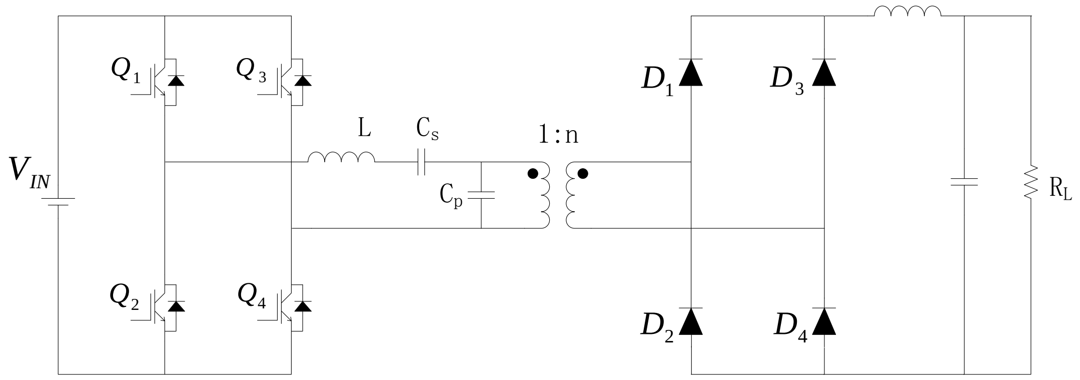

Figure 5.9 The circuit diagram of a series-parallel resonant converter.

Like the parallel resonant converter, the series-parallel resonant converter also uses an inductor output filter, and the equivalent ac resistance is the same as equation (5.11). Also the input and output ac voltages E_{in} and E_o are the same as equations (5.12) and (5.13). Figure 5.10 shows the ac equivalent circuit of the series parallel resonant converter.

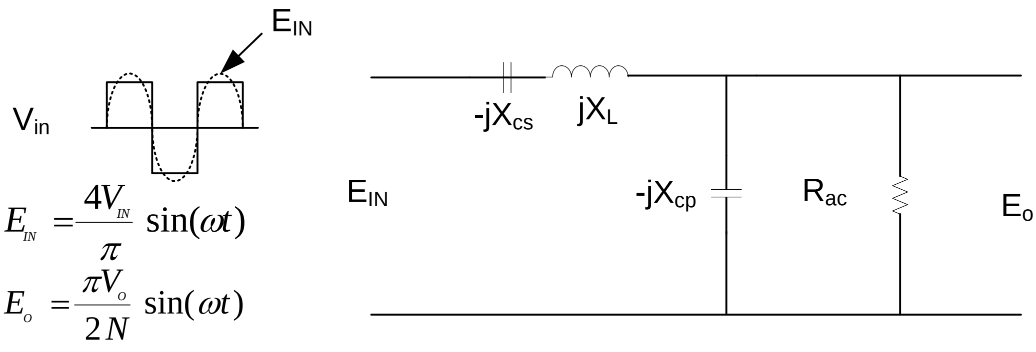

Figure 5.10 AC equivalent circuit of series-parallel resonant converter.

Using the ac equivalent circuit of Figure 5.10, the ac gain of the series resonant circuit is:

$$\frac{E_o}{E_{in}} = \frac{1}{1-\frac{X_L}{X_C}+j\frac{X_L}{R_{ac}}} \tag{5.18}$$

Substituting the equations (5.12) and (5.13) into (5.18), the dc gain of the parallel resonant converter is:

$$\frac{V_0}{V_{in}} = \frac{8N}{\pi^2 \sqrt{(1+A^2)(1-\left(\frac{\omega_S}{\omega_0}\right)^2)^2 + \frac{1}{{Q_L}^2} \times (\frac{\omega_S}{\omega_0} - \frac{\omega_0 A}{\omega_S(1+A)})^2}} \tag{5.19}$$

where, *N* is the transformer turns ratio, ω_0 is the undamped natural frequency of the tank, *A* is the ratio of parallel and series capacitances, and Q_L is loaded quality factor at the corner frequency.

The natural frequency is:

$$\omega_0 = 2\pi f_0 = \frac{1}{\sqrt{L_S C}} \tag{5.20}$$

where

$$C = \frac{C_P \times C_S}{C_P + C_S} \tag{5.21}$$

The ratio of the parallel and series capacitances is:

$$A = \frac{C_P}{C_S} \tag{5.22}$$

The loaded quality factor is:

$$Q_L = \frac{R_{ac}}{\omega_S L_S} = \frac{R_{ac}}{\sqrt{L_S/C}} = \frac{\left(\frac{\pi^2}{8}\right)R_L}{N^2\sqrt{L_S/C}} \tag{5.23}$$

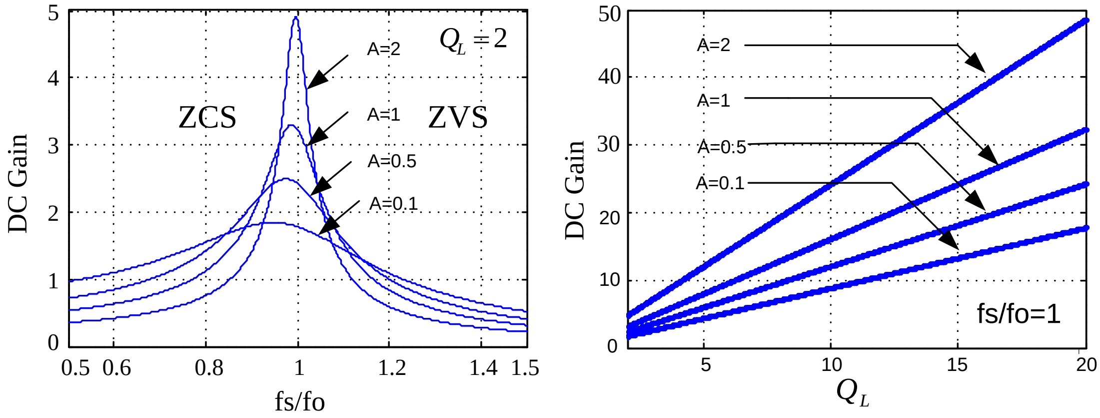

(a) (b)

Figure 5.11 DC gain versus f_s/f_0 and Q_L with different $A=C_p/C_s$. (a) f_s/f_0 and (b) Q_L.

Figure 5.11 (a) shows LCC dc gain with different parallel and series capacitance ratios, A, at a load quality factor Q_L=2. The dc gain increases as A increases. Figure 5.11 (b) shows dc gain versus load quality factor Q_L for different A at f_s/f_0=1. The figure indicates that the LCC resonant converter can provide a high gain as Q_L increases (load decreases).

The feature of the LCC resonant converter, previously not exploited in this specific WECS application, is that it has a dc gain determined by the output load.

For a wind energy conversion system, the output power reduces as the wind speed decreases. In terms of dc link output, the load decreases as the dc link voltage is regulated constant by the grid connected inverter. The system needs higher gain due to the input voltage decrease, which is caused by a wind speed reduction. The LCC resonant converter characteristic inherently fulfils this wind energy conversion system requirement. It can provide high gain when the wind energy conversion system (WECS) operates at low output power, low speed, and low input voltage. In contrast, the hard-switched dc-dc converter and pure series or parallel (and LLC) resonant converters, lower the dc gain when reducing the duty cycle at high power. This undesirable characteristic imposes a large electrical stress on the semiconductors.

5.4 Comparative study between the HSFB converter and the LCC resonant converter

DC/DC converters used in the WECS, connect the wind turbine to the dc link. They track the maximum power by controlling the converter duty cycle during wind speed changes. The dc/dc converter input varies as the wind speed changes. Two dc/dc converter types, based on H bridge topologies, employed in the wind energy conversion system, are compared in terms of semiconductor stress and loss, and transformer loss and size. The first converter is the current-output hard-switched full-bridge converter; the second is the LCC resonant converter.

The rotor speed of the variable speed wind turbine is controlled by the converter according to the wind profile. It is assumed that the variables at rated wind speed are 1pu and the common dc link voltage is k pu. The cut-in wind speed is 0.3pu. Thus the converter input voltage V_{in} ranges from 0.3pu to 1pu, when neglecting stator impedance and rectifier diodes voltage drops. For both the hard-switched converter and LCC resonant converter, the peak currents I_{peak} occur at rated wind speed. The bridge IGBT voltages in both cases are the rated input voltage. For the HSFB converter, the transformer turns ratio is designed for the minimum input voltage and maximum output voltage, to ensure the converter output voltage reaches the dc link voltage. Thus the transformer turns ratio is 1: $3k$, while for the LCC resonant converter, the transformer turns ratio is determined at rated input voltage. Assuming the LCC resonant converter tank gain G_t is 1, the transformer turns ratio is 1:k. For the HSFB the bridge diode rectifier on the high-voltage side experiences severe voltage overshoot and oscillation, causing rectifier peak voltages larger than the transformer secondary voltage V_{sec}. In order to reduce the rectifier side voltage spikes, a conventional resistor-capacitor-diode (RCD) snubber circuit is used [5.9] or the use of several energy recovery clamp circuits (ERCC) [5.10-12] has been proposed. Reference [5.4] shows the rectifier peak voltage is 2.9 times V_{sec} without the snubber circuits, but the rectifier peak voltage is still 1.3 times V_{sec} with the proposed ERCC. Although the rectifier peak voltage and diode reverse losses can be reduced by the mentioned methods, they introduce extra components on the high-voltage side. The extra circuitry itself experiences high voltage levels which increases component costs. For the hard-switched full-bridge converter, the transformer secondary voltage V_{sec} at rated input voltage is $3k$ pu. The rectifier diode reverse voltage rating should exceed $3.9k$ pu with ERCC. For the LCC resonant converter, due to the sinusoidal voltage waveform at the transformer secondary side, the rectifier peak voltage occurs at the peak of the sinusoidal waveform, viz., $1.57k$ pu. There is no need for the snubber circuit to reduce the overshoot, hence snubber losses are not incurred. This also means, for a given transformer core area and flux level, more primary turns, 11%, are needed for the LCC case ($V=4.44N\varphi f$:$V=4N\varphi f$), but due to the voltage gain, the number of output winding turns is in fact reduced.

The transformer dimensions for both topologies can be derived by calculating the required area product. The area product is defined by [5.13]:

$$A_P = A_W \times A_E = \frac{P_t \times 10^4}{K_u \times K_f \times \Delta B \times f_T \times J} \ (\text{cm}^4) \tag{5.24}$$

where A_W = transformer core window area (cm^2)

A_E = transformer cross-sectional area (cm^2)

P_t = total apparent power (W),

K_u = window utilization factor,

K_f = 4 for square wave, 4.44 for sine wave,

ΔB = flux density swing (T),

f_T = transformer operating frequency (Hz), and

J = current density (A/cm^2).

Equation (5.24) shows that the area product for a hard-switched full-bridge and LCC resonant converter transformer is determined by the K_f factor when all other parameters are constant. The LCC gives a smaller A_W than the HSFB: specifically a 10% reduction in the winding area for a given transformer cross-sectional area is achieved with the LCC topology. This allows a smaller transformer core for the LCC resonant converter.

The voltages across the full-bridge rectifier and resonant converter output inductor range from $-k$ to k and $-k$ to $0.57k$, respectively. The current through the inductor and the output voltage are the same for both. The LCC resonant converter has short circuit protection capability due to the tank inductance. The series capacitor, acting as a dc blocking capacitor, in the resonant tank helps prevent transformer saturation. Table 5.2 shown the comparative results based on a wind speed range of 0.3 pu to 1 pu.

Table 5.2 HSFB and LCC resonant converter comparative results.

	Standard full bridge	**LCC resonant converter**
IGBT Voltage	1 pu	1 pu
IGBT peak current	3 pu	1.57 pu
Transformer ratio	1:3k	1:k
Transformer winding area	1 pu	0.9 pu (10% reduction)
Transformer saturation protection	No	Yes
Diode bridge voltage	high	low
Diode bridge current	same	same
Short circuit protection capability	No	Yes

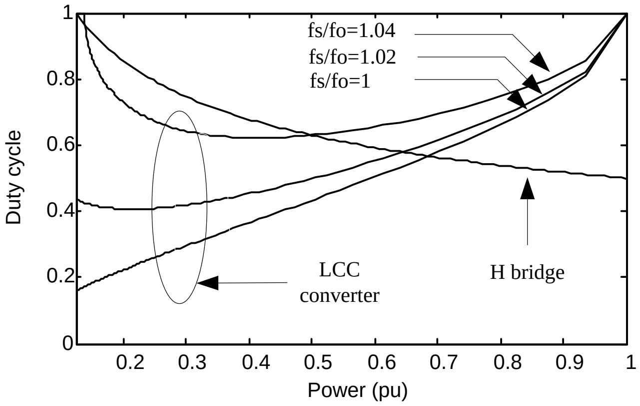

Figure 5.12 Duty cycle of LCC resonant converter (at full load Q_F=4) and H-bridge at the MPPT.

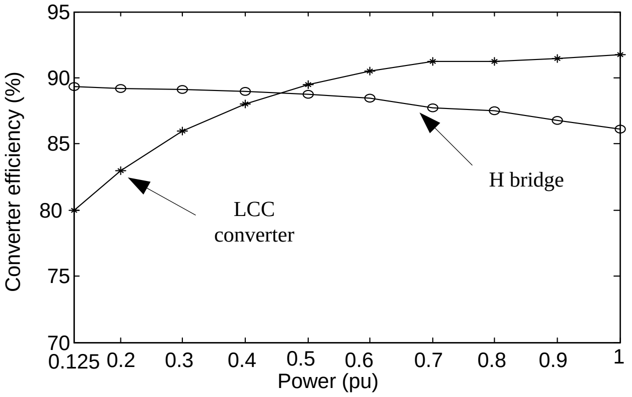

Figure 5.13 Converter measured efficiency at the MPP with different wind speeds.

Figure 5.12 shows the duty cycle of the LCC resonant converter and the hard-switched H-Bridge based on the MPP at different wind speeds. The H-bridge duty cycle is inversely proportional to power, while the LCC resonant converter duty cycle depends on Q_F and f_s/f_0. When the switching frequency f_s is close to f_0, the duty cycle changes over a wide range, from power 0.125 pu to 1 pu.

Figure 5.13 shows the measured efficiency of the two converters at the MPP with different wind speeds. The LCC resonant converter attains highest efficiency at full-load. Since the switching frequency is near resonance, the peak resonant current decrease is not drastic for larger Q_F, which means decreased efficiency at light load. For the HSFB converter, the inverter peak current decreases as the load current decreases: it therefore has better light load efficiency. But due to the lower duty cycle at full-load power, larger peak current and lower efficiency occur. Figure 5.13 shows the LCC resonant converter has the better efficiency above 0.45pu power, with the

HSFB converter having better efficiency at light load. Although currently, the wind farms in operation have a capacity factor of less than 50% on average, the future development trend aims to greatly increase this, which is achievable by either improving the primary energy available - more accurate wind speed prediction and site location, or proposing optimal conversion technologies - better turbine characteristics and MPPT algorithms and control. The LCC resonant converter should be a promising option in such future applications.

5.5 Control and design method

Conventional phase-shifted PWM at a constant frequency [5.14] is utilised to control the LCC resonant converter, which then allows simple output filter and transformer design.

5.5.1 MPPT tracking

For a variable-speed WECS, it is essential to extract and convert maximum power from the wind turbine. In order to achieve MPPT, the LCC resonant converter must provide high dc gain when the wind speed changes, otherwise the wind turbine may only operate on the right side of the power characteristics curve shown in Figure 4.6. In Figure 5.11, the LCC dc gain becomes insensitive when the switching frequency is not near the resonant frequency, where the LCC resonant converter cannot operate at the MPP. Thus the switching frequency should be near the resonant frequency.

The overall gain of the LCC dc/dc resonant converter G_r can be derived as a combination of the resonant tank gain G_t and transformer gain, viz., the turns ratio N:

$$G_r = G_t \times N \tag{5.25}$$

Figure 4.6 shows two maximum power points, A_1 and A_2, at different wind speeds. G_{t1}, Q_1, V_1, P_1 and G_{t2}, Q_2, V_2 P_2 represent the resonant tank gain, loaded quality factor, LCC input voltage and wind power corresponding to A_1 and A_2. The LCC resonant converter voltage equations are:

$$V_1 \times G_{t1} \times N = V_{dc} \tag{5.26}$$

$$V_2 \times G_{t2} \times N = V_{dc} \tag{5.27}$$

So

$$G_{t2} = V_1/V_2 \times G_{t1} \tag{5.28}$$

From (3.1) and (4.17)

$$\frac{V_1}{V_2}=\frac{\omega_1}{\omega_2}=(\sqrt{\frac{P_1}{P_2}})^3=(\frac{P_1}{P_2})^{\frac{3}{2}} \tag{5.29}$$

If the LCC resonant converter efficiency is η:

$$P_1=\frac{{V_{dc}}^2}{R_{L1}}\times\eta \tag{5.30}$$

$$P_2=\frac{{V_{dc}}^2}{R_{L2}}\times\eta \tag{5.31}$$

Substituting equations (5.30) and (5.31) into (5.29) gives:

$$\frac{V_1}{V_2}=(\sqrt{\frac{R_{L2}}{R_{L1}}})^3=(\frac{R_{L2}}{R_{L1}})^{\frac{3}{2}} \tag{5.32}$$

Substituting (5.23) into (5.32) gives:

$$\frac{V_1}{V_2}=(\sqrt{\frac{Q_2}{Q_1}})^3=(\frac{Q_2}{Q_1})^{\frac{3}{2}} \tag{5.33}$$

The resonant tank gain at the maximum power point, with different wind speed, can be obtained from:

$$G_{t2}=G_{t1}\times(\sqrt{\frac{Q_2}{Q_1}})^3=G_{t1}\times(\frac{Q_2}{Q_1})^{\frac{3}{2}} \tag{5.34}$$

Figure 5.14 shows a 3D plot of the dc gain at different switching frequencies and Q_L with A=1. Figure 5.14 (a) and Figure 5.14 (b) compare the resonant tank gains at the MPP with different wind speeds, and LCC resonant converter dc gain at different Q_L values (full-load), respectively. The lower surface (red) represents the resonant tank gain at the MPP, while the upper surface (blue) represents the LCC resonant converter dc gain that can be produced. When the resonant tank gain at the MPP is larger than the maximum dc gain at the corresponding load, then the wind turbine cannot operate at the MPP. Thus the LCC resonant converter must develop gain to enable the wind turbine to operate at the specified MPP. Both figures indicated that a wide switching frequency range is allowable when a full-load small Q_L is used. Figure 5.14 (a) shows the Q_L is between 2 and 20, while Figure 5.14 (b) shows the Q_L is between 8 and 80, both from 10% full-load to 100% full-load. The switching frequency can be between 1pu and 1.03pu with small Q_L. For larger Q_L, the switching frequency which can achieve MPP wind turbine operation should be close to the resonant frequency.

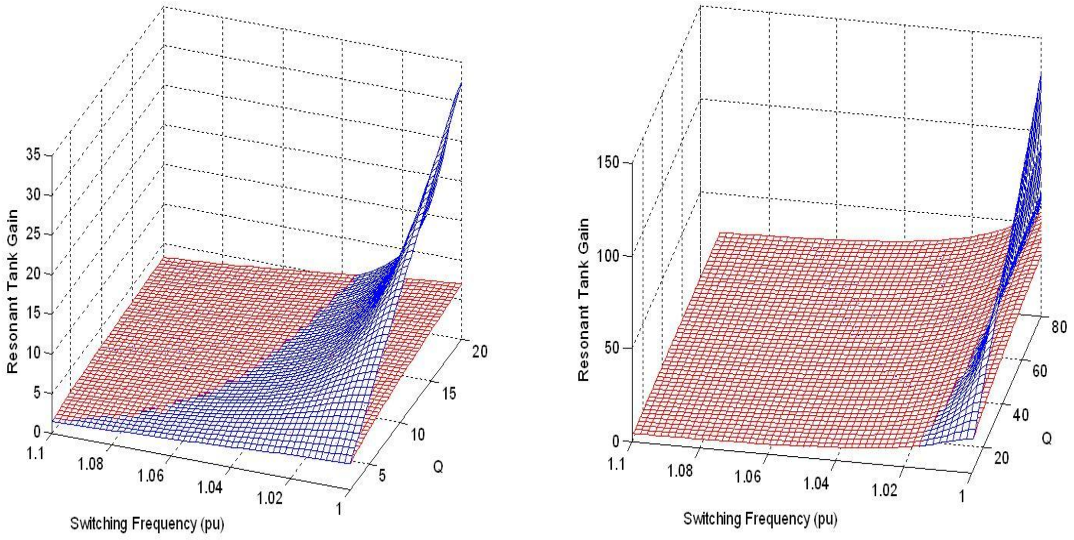

(a) Full load (at Q_L=2) (b) Full load (at Q_L=8)

Figure 5.14 The 3D plot of dc gain at different switching frequencies and Q_L.

5.5.2 LCC resonant converter design

Fundamental Mode Approximately (FMA) analysis is used for converter design, where the author in [5.15] verified that FMA analysis gives a reasonably accurate LCC resonant converter design procedure. When designing the resonant tank parameters, transformer leakage inductance is ignored due to its low value.

As shown in Figure 5.11, working in the positive slope region of the dc versus frequency characteristic results in zero current switching (ZCS), while zero voltage switching (ZVS) occurs in the negative slope region.

In [5.16], it is established that operation at the resonant frequency is preferable, minimizing the resonant current and thus reducing electrical stresses. In this study, the LCC switching frequency is slightly above the resonant frequency, which maintains a high dc gain with zero voltage switching.

The FMA analysis equations for the LCC current-output are derived in [5.15][5.17]. Reference [5.18] establishes the necessity for Q_L > 2.5 in order to provide near sinusoidal waveforms for accurate FMA analysis. It also shows the relationship between the minimum A value and a given G_t (resonant tank gain), which gives the basis for choosing the resonant tank parameters. For convenience, the ratio of parallel to series capacitance A is often chosen as 1 as a good compromise between bandwidth, component sizing, electrical stresses, and impedance matching [5.19].

Typically, the transformer turns ratio in hard-switched inverters is based on the minimum input voltage, whereas the LCC resonant converter topology uses the maximum input voltage to determine the transformer turns ratio, which minimizes transformer copper loss. In a hard-switched inverter or boost converter topology, the duty cycle variation is inversely proportional to the wind speed. A higher wind speed change results in a duty cycle reduction in order to reduce the converter gain for output voltage regulation. As a result, switching devices sustain a higher peak current during conduction. The LCC resonant converter increases its duty cycle during higher wind speed conditions. The LCC resonant converter characteristics reduce the converter gain at a large output load. With an automatic gain reduction during increased loading, the duty cycle will need to be increased for output voltage regulation. A smaller peak current will be conducted by the switches, compared to the hard-switched inverter.

The design procedure is summarised as follows:

1) Calculate the overall gain and minimum load resistance of the LCC resonant converter at rated power

$$G_r = \frac{V_{dc}}{V_{rated}} \tag{5.35}$$

$$R_{L\_min} = \frac{{V_{dc}}^2}{P_{rated}} \tag{5.36}$$

where V_{dc} is the dc link voltage, V_{rated} is the rated diode rectifier voltage, and P_{rated} is the rated electrical power.

2) Determine the resonant tank parameters

Selecting A=1, the LCC dc characteristic with A=1 is shown in Figure 5.11, where the dc gain increases as Q_L increases. For a given Q_L, which corresponds to the minimum load resistance, using equation (5.19), the resonant tank gain G_t and switching frequency f_s (pu) can be obtained. Figure 5.11 (a) and (b) is a design guide for the switching frequency f_s and LCC tank gain G_t. Then from equations (5.25) and (5.35), the transformer turns ratio is obtained.

Substituting equation (5.36) into equation (5.23) gives:

$$\sqrt{\frac{L_S}{C}} = \frac{\left(\frac{\pi^2}{8}\right)R_L}{N^2 Q_L} \tag{5.37}$$

After choosing a switching frequency f_s, the natural frequency can be obtained by substituting f_0 into equation (5.20):

$$\sqrt{L_S C} = \frac{1}{2\pi f_0} \tag{5.38}$$

L_s and C can be obtained by solving (5.37) and (5.38):

$$L_S = \frac{\pi R_L}{16 N^2 Q_L f_0} \tag{5.39}$$

$$C = \frac{4 N^2 Q_L}{\pi^3 f_0 R_L} \tag{5.40}$$

By substituting A into equation (5.22), C_p and C_s are obtained. Reference [5.17] gives a method which doubles the output voltage without minimum load change. Besides doubling the transformer turns ratio, the parallel capacitance quadruples and resonant inductance is quartered, doubling the output voltage while the switching frequency is unchanged. For the WECS, the LCC resonant converter output minimum load is varied according to the dc voltage and power. Equations (5.35), (5.36), (5.39), and (5.40) indicate that the dc link voltage can be changed to a different level, via the transformer turns ratio without changing the resonant tank parameters or switching frequency. This is a simple way to boost the output voltage.

3) Power rating of the switches

The switch power rating is based on the input voltage and resonant current. The voltage rating can be determined from the generator characteristic reference. The peak current through the switching devices is the resonant current. The resonant current can be calculated from (using FMA analysis):

$$I_p = \frac{4 \times V_{rated}}{\pi |Z_{eq}|} \tag{5.41}$$

where $|Z_{eq}|$ is the equivalent impedance looking into the H-Bridge output terminals.

4) Output filter inductor, L

The output filter inductor limits the current variation per cycle (ripple) to less than a specified margin ΔI (1 to 5%). The inductance is determined by ΔI and the inductor voltage, according to:

$$L = \frac{1}{\Delta I}\int_{t_1}^{t_2} \frac{\pi}{2}\left(V_{dc}\, sin(\omega_{s1} t) - V_{dc}\right)dt \qquad (5.42)$$

where V_{dc} is dc link voltage, t_1, t_2 are the time boundaries of the dc link voltage per cycle, and ω_{s1} is angular frequency of the inductor current. Then the output capacitance is derived from the filter cut-off frequency which is based on the desired attenuation level of the switching frequency harmonics in the output.

5.6 System Simulink results and practical experiments

A) Test system description

To verify the functionality and feasibility of the proposed system, a critical wind speed step change is applied to the proposed system, both in MATLAB simulations and using the experimental test rig. The current source grid inverter is modelled by a dc-chopper circuit in parallel with a shorting switch that maintains the average dc link voltage constant by controlling the duty cycle of the two switches. The two switches are controlled by complementary gate signals with overlap. Figure 5.15 shows the WECS schematic, while the experimental WECS is shown in Figure 5.16.

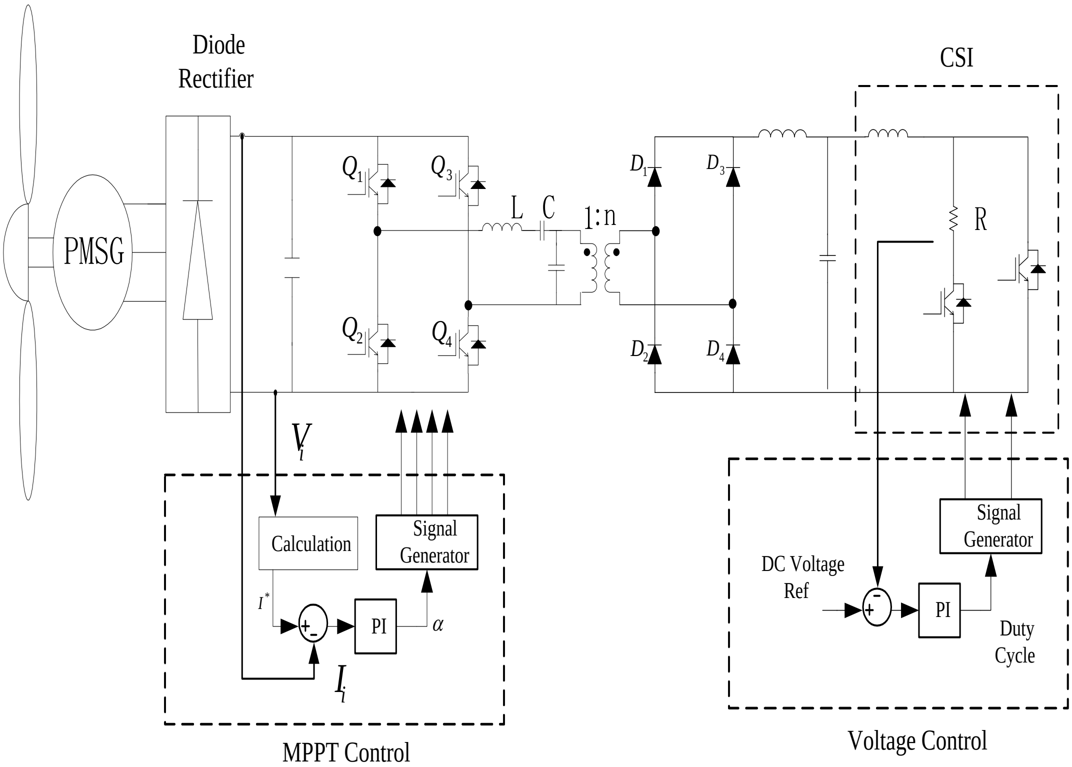

Figure 5.15 Schematic of the wind energy conversion system.

Figure 5.16 Test rig.

The dc/dc resonant converter is designed according to the method described, with parameters shown in Table 5.3. A ferrite core is used in the 493µH resonant inductor. The resonant capacitor dielectric material is polypropylene. The isolating high frequency transformer is designed with a nanocrystalline core due to its high permeability (μ_r > 20,000) and high saturation flux density (1.2T), compared to others materials (ferrite and powder) at >10kHz [5.20].

Table 5.3 LCC resonant converter parameters.

Parameter	Value
Parallel capacitor (C_p)	73.3 nF (3×220nF series)
C_s	73.3 nF (3×220nF series)
L	493 µH
Transformer ratio	1:1
Resonant frequency (f_0)	37.4 kHz
Switching frequency (f_s)	38.8 kHz
f_s/f_0	1.03

B) Simulation Results

Figure 5.17 and Figure 5.18 show the simulated performance of the WECS with a wind speed step change (a step change is used in order to determine the system dynamic characteristic limits). Figure 5.17 shows the dynamic response of the mechanical system while Figure 5.18 displays the dynamic response of the electrical system.

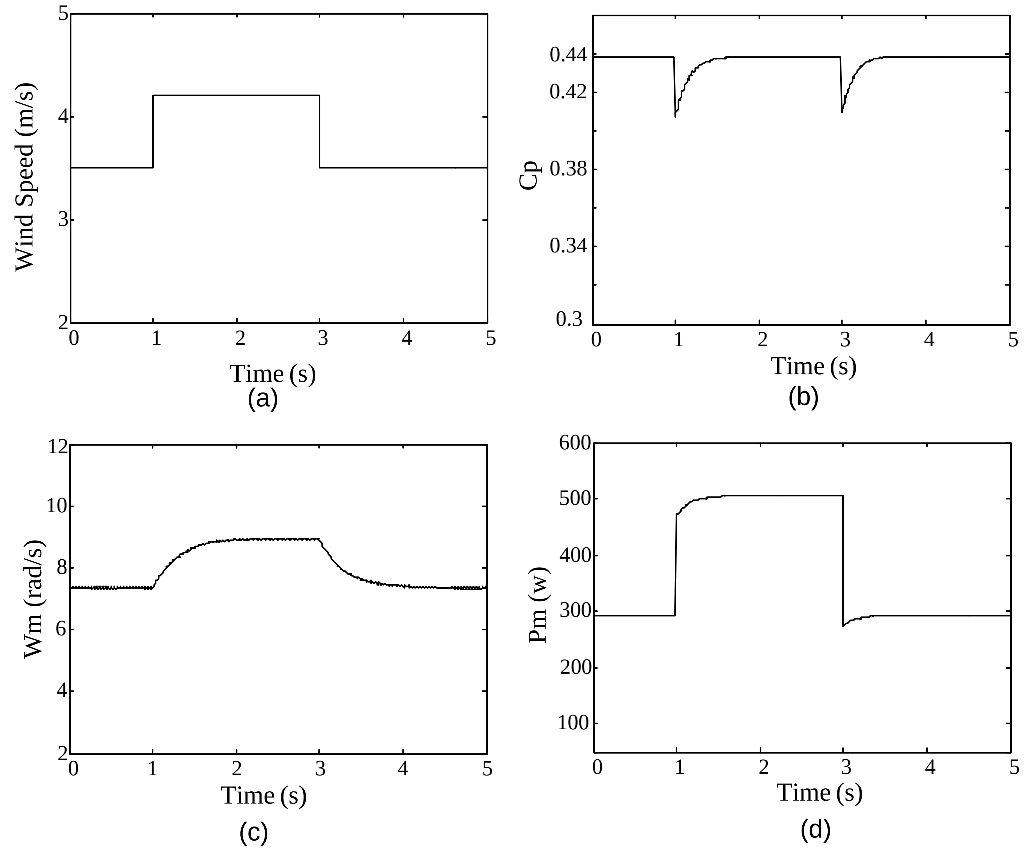

Figure 5.17 Dynamic response of the mechanical system for wind speed changes: (a) wind speed, (b) power coefficient, (c) rotor speed, and (d) mechanical power.

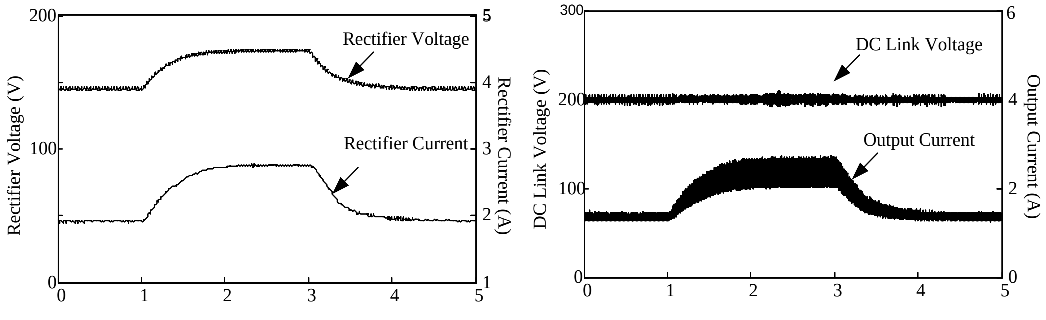

(a) Rectifier voltage and current

(b) DC link voltage and output current

Figure 5.18 Dynamic response of the electrical system for wind speed changes: (a) Rectifier voltage and current (b) dc link voltage and output current.

The wind speed is 3.5m/s and stable during the initial 1s, and steps up to 4.2m/s at *t*=1s. After a 2s interval, the wind speed is stepped down to and maintained constant at 3.5m/s. The power coefficient C_p is maintained around the maximum value of 0.4382. The rotor speed and rectifier output voltage and current are changed to extract and track the maximum power from wind. The dc link voltage is maintained constant by controlling the duty cycle of the load side dc chopper. The output current depends on the power that is extracted by the wind turbine.

C) Experimental results

Figure 5.19 (a) shows the wind profiles, where a step change of the wind speed is shown. The initial wind speed is maintained at 3.5m/s, then steps instantaneously to 4.2m/s after a 30s interval. It steps down to 3.5m/s at 60s. Figure 5.19 (b) shows the power coefficient, where C_p is maintained at the maximum value, which means the wind turbine operates at the maximum power point during step wind speed changes. Figure 5.19 (c) and Figure 5.19 (d) show rotor speed and mechanical power.

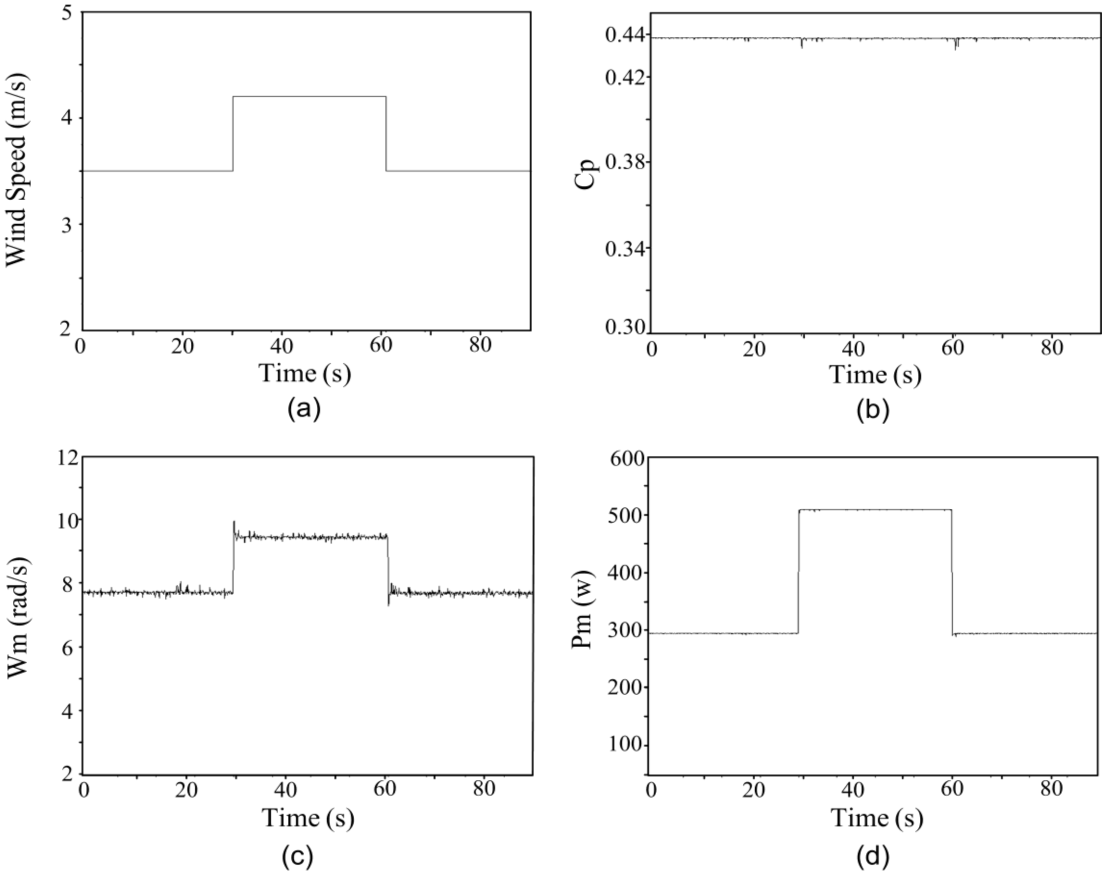

Figure 5.19 Dynamic response of the mechanical system for wind speed changes: (a) wind speed, (b) power coefficient, (c) rotor speed, and (d) mechanical power.

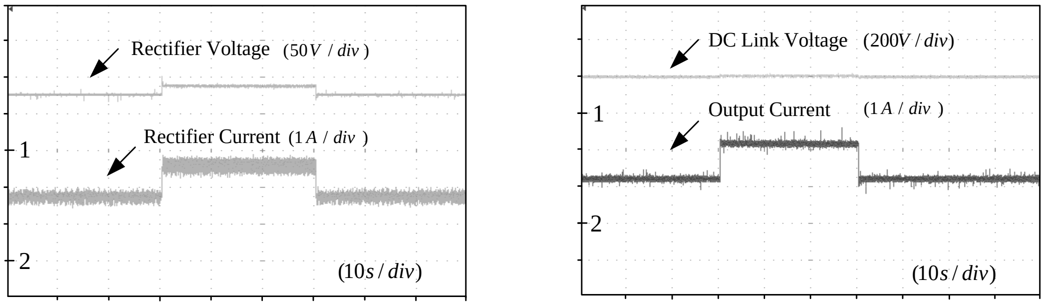

(a) Rectifier voltage and current

(b) DC link voltage and output current

Figure 5.20 Dynamic response of the electrical system for wind speed changes: (a) rectifier voltage and current (b) dc link voltage and output current

The power and rotor speed change as the wind speed changes, indicates input power variation.

Figure 5.20 (a) shows the voltage and current waveforms of the diode bridge rectifier. Figure 5.20 (b) shows the dc link voltage and output current. The dc link voltage is maintained constant with wind speed changes. The output current changes as the power extracted from wind changes. Figure 5.21 expands the input three-phase rectifier current waveform shown in Figure 5.20 (a), where the current ripple frequency is related to the generator stator frequency and rotor speed.

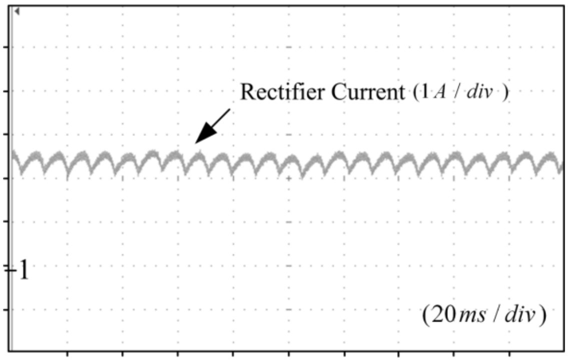

Figure 5.21 Zoom-in waveform of input three-phase rectifier current.

Figure 5.22 shows the voltage across the current source inverter with different wind speeds. The current source is replaced by a dc-chopper circuit in parallel with a switch, thus the voltage is a square wave with varying duty cycle. The average voltage is controlled by changing the duty cycle of the two switches. As is shown, the duty cycle decreases as the output power increases to maintain the dc link voltage constant. The peak voltage becomes larger when wind speed increases.

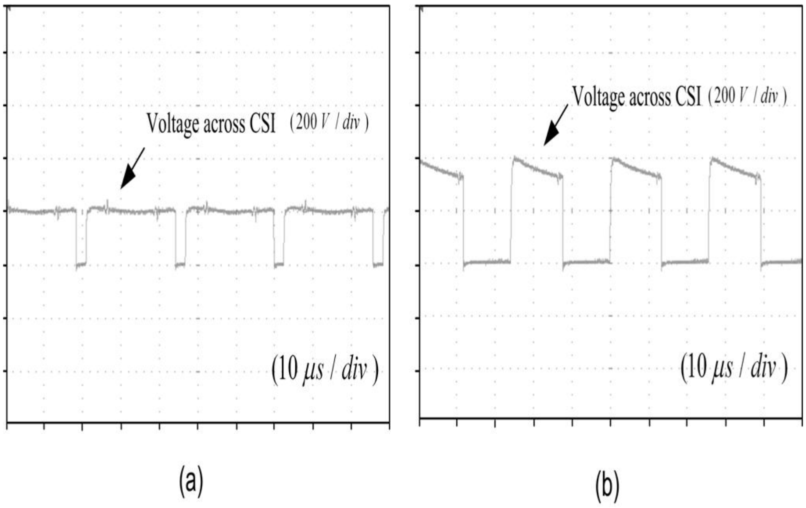

Figure 5.22 Voltage across the CSI at wind speed: (a) 3.5m/s and (b) 4.2m/s.

5.7 Passive component hardware specification

In this section summarises in the table following tables, the specification of the passive components, such as the AC inductor, the output DC filtering inductor, and the power transformer used in the DC/DC converter.

Table 5.4 shows the specification of the AC inductor used in the resonant tank.

Table 5.4 Specification of AC inductor.

Core type	Ferrite 9920UC (p type)
Inductance	493.7μH
Number of turns	78 turns
Air gap	8.7 mm

The specification of the output DC filtering inductor is shown in Table 5.5.

Table 5.5 Specification of DC filtering inductor.

Core Type	Power Core (Kool Mu)
Inductance	4 mH
Number of turns	240 turns

Table 5.6 shows the specification of the power transformer in the resonant converter.

Table 5.6 Specification of power transformer

Core Type	NANOPERM M-049-02 U7 (oval)
Transformer ratio	1:1
Primary turns	20 turns
Secondary turns	20 turns

The detailed design process is illustrated in Appendix A.

5.8 LCC resonant converter efficiency analysis

The LCC resonant converter losses mainly occur in the IGBTs, anti-parallel diodes, resonant inductor, and diode rectifier. The LCC resonant converter is designed for a full-load condition, operating above the resonant frequency and at full duty cycle. At full duty cycle, the four converter switches (IGBT) turn on with near zero-current and zero-voltage switching, while turn off is hard switched. The anti-parallel diode conducts during the turn-on transition. As the switching frequency is slightly greater than the resonant frequency, the switches turn off with a small current, thus low turn-off losses occur. The converter maintains high efficiency around full-load. As the load decreases, the duty cycle of the voltage across the H-bridge terminals reduces, resulting in switches S_1 and S_2 turning on with zero-current and zero-voltage but turn-off is hard switched. The switches S_3 and S_4 in other leg turn off with zero-current and zero-voltage but turn-on is hard switched. Due to phase-shift PWM control, the inverter leg comprising S_1 and S_2 sustains only turn-off switching loss while S_3 and S_4 in the other inverter leg sustain only turn-on switching loss. Suitable snubber circuits can limit the losses in the switches. With reference to Figure 5.9, switches S_3 and S_4 turn on with reverse recovery current in the diodes D_4 and D_3 of the same leg, causing an unavoidable short-circuit during the reverse recovery time. Thus D_3 and D_4 have to be fast recovery type diodes, whereas, switches S_1 and S_2 turn on at ZVS, taking up the current from their anti-parallel diodes. A fast recovery requirement for D_1 and D_2 is not critical.

For the hard switched full-bridge, there is a high overshoot voltage and losses in the high-voltage side rectifier diodes [5.4], due to the step change in voltage across the transformer which has transformer leakage and rectifier diode junction capacitance. V_{rec_pk} (rectifier peak voltage) is almost 2.9 times that of V_{sec} (rectifier voltage) without snubbers. Thus conventional RCD snubbers or energy recovery clamp circuits are needed on the rectifier circuit due to the high voltage overshoot and reverse recovery loss. For the LCC resonant converter, the voltage across the transformer is sinusoidal which results in reduced voltage overshoot.

The resonant inductor loss has two components: core loss and winding loss. Design of the ac resonant inductor is different from the gapped dc filter inductor. Core loss is an important factor due to the large flux swing. The maximum core operating flux is limited to give acceptable core losses. Ferrite material is suitable for the high frequency resonant inductor.

5.9 Summary

The hard-switched FB converter and the series-parallel resonant converter have been compared in terms of switch stress, efficiency, etc. The series-parallel resonant converter has a better efficiency than the HSFB converter above half load. The series parallel resonant converter is proposed as an interface to a wind energy electrical source. Design procedures and analysis of the series-parallel resonant converter for WECS have been presented based on FMA. The design process of the passive hardware components, which include the ac inductor, dc filtering inductor and power transformer used in the dc/dc converter, are illustrated. The dc/dc resonant converter is designed at the rated power, but provides increasing dc gain as the wind speed decreases without having to increases the transformer turns ratio, as is necessary for other converters topologies. WECS performance was investigated and analyzed, while the simulation and experimental results demonstrate that the dc/dc resonant converter allows the wind turbine to operate at the maximum power point. The dc/dc resonant converter efficiency has been measured at different wind speeds, with an efficiency of 92% at rated power.

References

[5.1] P. Bresesti, W. L. Kling, R. L. Hendriks, and R. Vailati, "hvdc Connection of Offshore Wind Farms to the Transmission System," *Energy Conversion, IEEE Transactions on,* Vol. 22, No. 1, pp. 37-43, 2007.

[5.2] L. Max and S. Lundberg, "System efficiency of a dc/dc converter-based wind farm," *Wind Energy,* Vol. 11, No. 1, pp. 109-120, 2008.

[5.3] L. Max, "Design and Control of a dc Collection Grid for a wind farm," Dept. of Energy and Environment, Chalmers University of Technology, 2009.

[5.4] C. Honnyong, C. Lihua, D. Rongjun, T. Qingsong, and P. Fang Zheng, "An Alternative Energy Recovery Clamp Circuit for Full-Bridge PWM Converters With Wide Ranges of Input Voltage," *Power Electronics, IEEE Transactions on,* Vol. 23, No. 6, pp. 2828-2837, 2008.

[5.5] D. Jovcic and B. T. Ooi, "High-power, resonant dc/dc converter for integration of renewable sources," *PowerTech, 2009 IEEE Bucharest,* 2009, pp. 1-6.

[5.6] S. D. Johnson, A. F. Witulski, and R. W. Erickson, "Comparison of resonant topologies in high-voltage dc applications," *Aerospace and Electronic Systems, IEEE Transactions on,* Vol. 24, No. 3, pp. 263-274, 1988.

[5.7] N. A. M. Hassanain and J. E. Fletcher, "Analysis three- and five-phase permanent magnet machines supplying diode bridge rectifiers for small-scale wind generators," *Power Engineering, Energy and Electrical Drives, 2007. POWERENG 2007. International Conference on*, 2007, pp. 648-653.

[5.8] R. L. Steigerwald, "A comparison of half-bridge resonant converter topologies," *Power Electronics, IEEE Transactions on,* Vol. 3, No. 2, pp. 174-182, 1988.

[5.9] L. H. Mweene, C. A. Wright, and M. F. Schlecht, "A 1 kW 500 kHz front-end converter for a distributed power supply system," *Power Electronics, IEEE Transactions on,* Vol. 6, No. 3, pp. 398-407, 1991.

[5.10] K. Eun-Soo, J. Kee-Yeon, K. Moon-Ho, K. Yoon-Ho, and Y. Byung-Do, "An improved soft-switching PWM FB dc/dc converter for reducing conduction losses," *Power Electronics, IEEE Transactions on,* Vol. 14, No. 2, pp. 258-264, 1999.

[5.11] C. Jung-Goo, B. Ju-Won, J. Chang-Yong, Y. Dong-Wook, and J. Kee-Yeon, "Novel zero-voltage and zero-current-switching full bridge PWM converter using transformer auxiliary winding," *Power Electronics, IEEE Transactions on,* Vol. 15, No. 2, pp. 250-257, 2000.

[5.12] A. Bendre, S. Norris, D. Divan, I. Wallace, and R. W. Gascoigne, "New high power dc-dc converter with loss limited switching and lossless secondary clamp," *Power Electronics, IEEE Transactions on,* Vol. 18, No. 4, pp. 1020-1027, 2003.

[5.13] Y. A. Wang and D. M. Xiao, "Prototype design for a high-voltage high-frequency rectifier transformer for high power use," *Power Electronics, IET,* Vol. 4, No. 6, pp. 615-623, 2011.

[5.14] C. Bo-Yuan and L. Yen-Shin, "Switching Control Technique of Phase-Shift-Controlled Full-Bridge Converter to Improve Efficiency Under Light-Load and Standby Conditions Without Additional Auxiliary Components," *Power Electronics, IEEE Transactions on,* Vol. 25, No. 4, pp. 1001-1012, 2010.

[5.15] M. C. Tsai, "Analysis and implementation of a full-bridge constant-frequency LCC-type parallel resonant converter," *Electric Power Applications, IEE Proceedings -,* Vol. 141, No. 3, pp. 121-128, 1994.

[5.16] K. K. Sum, *Recent developments in resonant power conversion*: Intertec Communications, 1988.

[5.17] A. J. Gilbert, D. A. Stone, and C. M. Bingham, "Rapid design of LCC current-output resonant converters with reduced electrical stresses," *Electronics Letters,* Vol. 41, No. 6, pp. 365-366, 2005.

[5.18] M. K. Kazimierczuk and D. Czarkowski, *Resonant Power Converters*: John Wiley & Sons, 2011.

[5.19] A. J. Gilbert, C. M. Bingham, D. A. Stone, and M. P. Foster, "Normalized Analysis and Design of LCC Resonant Converters," *Power Electronics, IEEE Transactions on,* Vol. 22, No. 6, pp. 2386-2402, 2007.

[5.20] *Magnet-Technologie Company Europe. [online]*. Available: http:www.magnetec.de/magnetic.html.

Chapter 6

Current Source Converter based Multi-terminal DC WECS

This chapter presents a current source dc/dc converter based multi-terminal dc WECS. The current source dc/dc converter is adopted to connect the wind turbine to the inverter with maximum power point control. Each turbine is associated with a dc current source that is capable of parallel connection to a common dc link. After dc power collection, a current source inverter (CSI) that uses gate turn off components (GTOs or IGCTs and IGBTs) is used for grid connection due to its flexible reactive power control and short-circuit protection capabilities. For such a parallel connection configuration, the CSI should operate in an input voltage control mode, which keeps the common dc link voltage constant. The dynamic response of the combined mechanical and electrical system is investigated with three different operation cases. The simulation and experimental results demonstrate the feasibility and stability of a current source dc/dc converter based multi-terminal dc WECS.

6.1 Background

Most onshore and offshore wind farms are located long distances from an ac grid. The wind farms produce electrical energy that must be collected locally and bulk transmitted to the grid. Generally, existing electrical collection systems for wind farms can be divided into two types: ac grid and dc grid as mentioned in Chapter 1. For an ac collection grid, the variable speed wind generator is connected to the ac bus using a partial (DFIG) or full rating converter (PMSG), and then a 50Hz transformer located in the base of the tower steps up the voltage to the collection grid voltage level. The transformer has a large volume and weight. For a dc collection grid, the ac voltage from the wind generator is rectified an by ac-dc converter and a dc/dc converter then steps up the voltage to a high voltage level. The interest in dc grid based WECS has increased significantly due to the amount of space available (lower weight of the magnetic components and cables) and the prospect of unlimited transmission length.

6.2 DC wind farm topology

DC wind farm topologies can be divided into series connected and parallel connected. Reference [6.1] proposed a new wind farm topology, which uses series connection as the method of interconnection between the wind turbine units. The series connection wind farm topology is show in Figure 6.1.

As shown in Figure 6.1, all the wind turbine units with their own thyristor converters are connected in series, and a common dc link delivers the power to the grid through a current source inverter (CSI). The wind turbine units are controlled to track maximum power through their corresponding thyristor converter control angle, while the dc link current which is calculated according to the wind speed is governed by controlling the thyristor inverter commutation leading angle. The dc link voltage of the proposed series connection wind farm is changed as wind speed changes, thus the insulation design and losses of dc transmission system should be carefully considered. The increasing thyristor converter control angle results in an increase in system reactive power, which affects the power factor of the PMSG during wind speed changes. For such a configuration, a bypass path is required when one of the wind turbine units fails, which increases the system control complexity and cost. It is difficult to incorporate or remove a single turbine unit for system integration or maintenance. There is no discussion on the wind farm start up or shut down processes, which still require investigation.

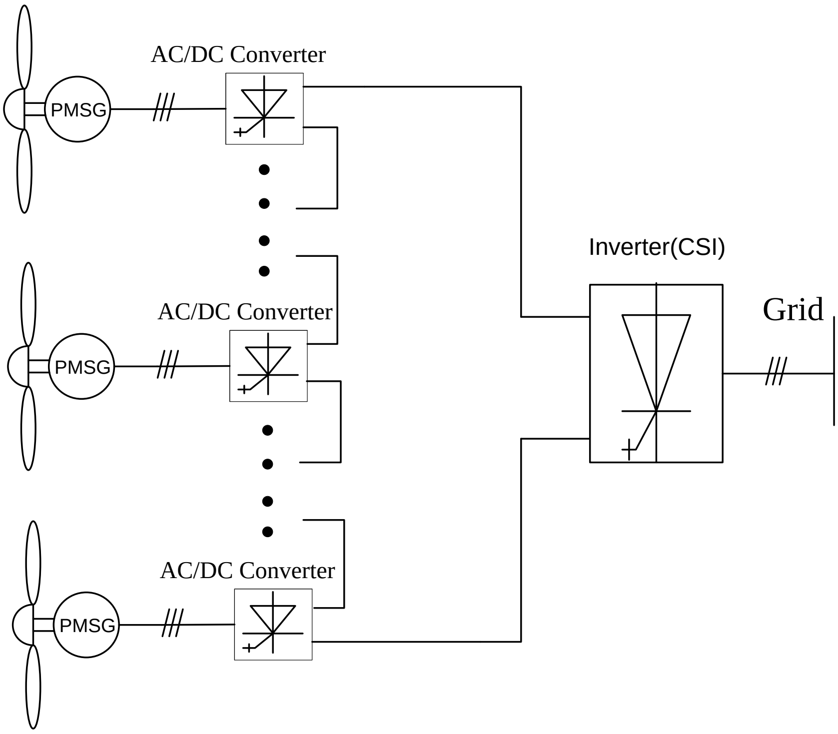

Figure 6.1 Series connection wind farm topology.

The parallel connection wind farm topology is favoured. Each of wind turbine units is connected in parallel to a common dc link. The collected power is transferred to the grid through either a voltage source inverter (VSI) or a current source inverter (CSI). Depending on the connection point to the dc link, there are two different connections, star and string connection respectively [6.2], as shown in Figure 6.2. The dotted area in Figure 6.2 (a) and (b) denotes single wind turbine units (WT) which incorporate a wind turbine, generator, and an ac/dc converter.

For the star connection, each turbine unit has its own collection cable and switchgear connected to a dc bus. It is easier to incorporate or remove a wind turbine unit from a star connection system, which enhances system reliability during system failure and maintenance. The wind turbine units are connected together with similar cable lengths with the string connection. From Figure 6.2, it can be seen that if a fault occurs, the wind turbine units which are located downstream of the fault location have to be tripped.

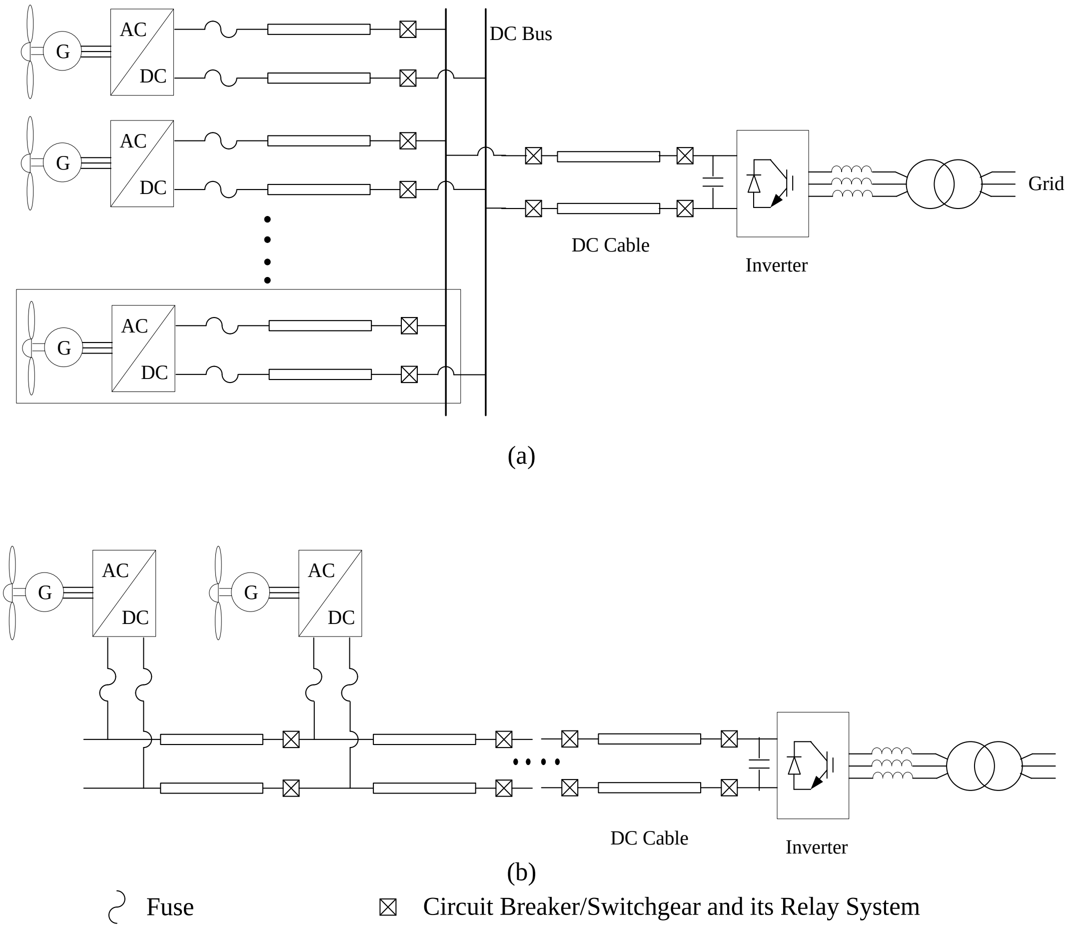

Figure 6.2 DC wind farm parallel connection with switchgear configuration (a) Star collection (b) String collection.

In this research, a star connection based dc wind farm is adopted for grid connection.

6.3 Proposed WECS and control

A novel current source converter based WECS is proposed. The configuration and control of this WECS are illustrated in this section.

6.3.1 System configuration description

The types of converters suitable for a star connection based dc wind farm are considered. Reference [6.3] compares the efficiency of two rectifier topologies used to implement three control regimes: (a) a rectifier VSC with fixed output voltage, (b) a rectifier VSC with variable output voltage, and (c) a diode rectifier. The diode rectifier method has the lowest loss among the three. In addition, the diode rectifier has a simple topology and control, and most importantly, low cost. It will, however, cause harmonic currents and torque pulsation on the generator due to the uncontrolled circuit. Several methods are given to reduce the torque harmonics in [6.4]. The rectifier VSC has lower torque harmonics due to a current control loop, but is more expensive and complex. The two rectifier converters both have advantages and disadvantages. They are both options for a wind turbine system depending on the requirements of whole system. As a low-power system (2 to 3kW turbines) is being investigated, a diode rectifier is used in the proposed system.

In a multi-terminal dc wind farm, dc-dc converters with large output capacitors are connected in parallel to the common dc link [6.5-6]. The voltage source inverter (VSI) is widely used for grid interfacing in WECS due to its flexible control of active power and reactive power [6.7-8]. VSI controllability can cater for grid-side ac disturbances using appropriate control and protection methods [6.9-10]. The dc side short circuit fault is the most severe fault for a voltage source topology due to uncontrolled currents flowing through the bridge freewheel diodes into the fault, with a large recovery current to recharge the large dc link capacitor [6.2]. Conventional ac breakers are not applicable due to the absence of a zero current crossing point and due to slow switching time. A dc breaker is more expensive than an ac breaker [6.11]. For a high dc link voltage, the lifetime, volume and cost are major capacitor problems. For the multi-terminal parallel system, the individual wind turbines, via dc/dc converters, are to be configured as current sources for grid connection, which is beneficial in stabilizing the WECS.

In order to solve the above problems, the novel current source converter based multi-terminal dc wind farm configuration is proposed as shown in Figure 6.3.

In the proposed configuration, a current source full-bridge dc/dc converter is used, with the topology shown in Figure 4.3. Each turbine units is configured as a current source. The basic difference between the VSI and CSI is on the dc-link side where the VSI incorporates a dc-link capacitor, while the CSI incorporates a dc-link inductor. This inductor gives the CSI short circuit properties. For the conventional line-commutated converter (LCC) hvdc using thyristors, the active and reactive power controls are tightly coupled, hence independent reactive power support to the grid cannot be achieved. Flexible reactive power control capability is required by the utility grid codes with increasing wind penetration levels. Reference [6.12] proposes a new CSI scheme using self-commutated devices such as gate turn-off thyristors (GTCs) or integrated gate-commutated thyristors (IGCTs), which gives the same control flexibility as the VSI. Two operation modes are illustrated in Chapter 2, which are voltage mode control and current mode control respectively. Both control modes can provide flexible reactive power support. Thus the CSI has recently received attention for use in wind power systems [6.13-15] due to its compact size, high-power capabilities, excellent short-circuit protection, and flexible power flow control capabilities.

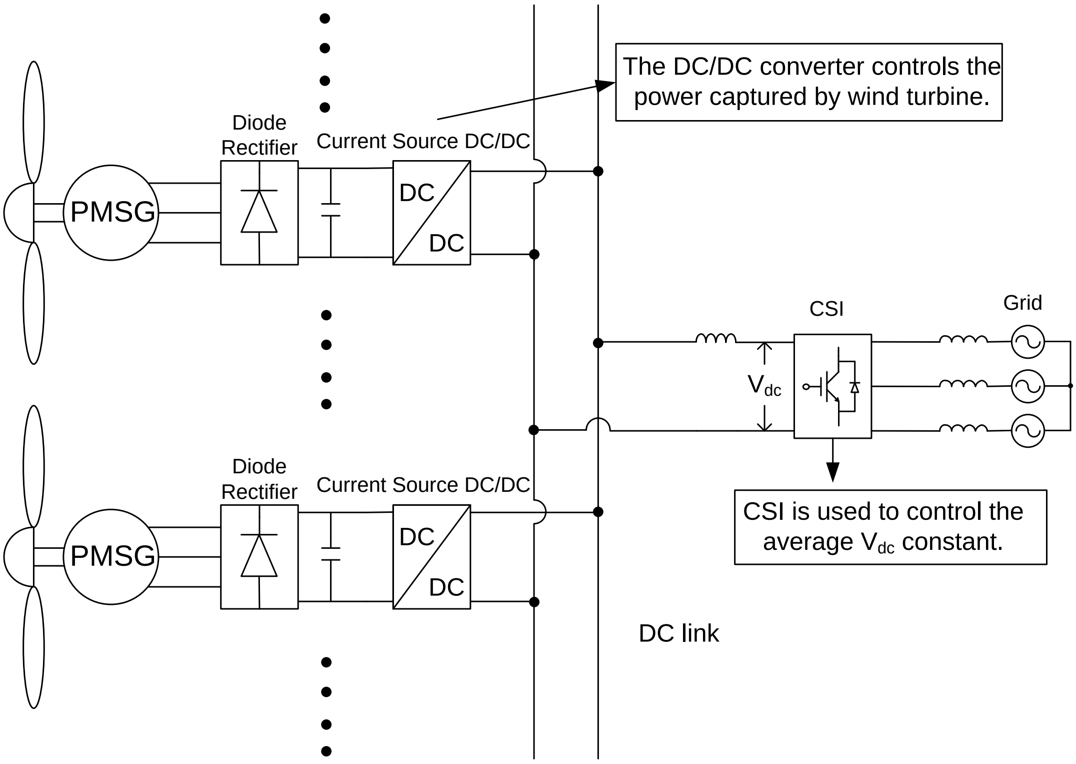

Figure 6.3 Proposed current source converter based multi-terminal dc wind farm configuration

6.3.2 Control of the proposed WECS

In the proposed WECS, the diode rectifier is uncontrollable, thus the current source dc/dc converter either controls the wind turbine to track its MPP or regulates its output voltage to be constant, depending on the WECS configuration. For the proposed WECS, which has one common grid connection inverter, if the dc link voltage is controlled by the dc/dc converters, the CSI is required to control active power flow from the turbine units. Control of each turbine at its MPP using the CSI is both complex and non-trivial. Generally a dc/dc converter is preferred to control the power captured by the wind turbine, with the control scheme shown in Figure 4.12. Voltage mode control is applied to the CSI, which maintains the average dc link voltage constant and reactive power at zero (normal operation).

6.4 System simulink results and practical experimentation

To verify the functionality and feasibility of the proposed dc system based on a current source dc/dc converter, the performance of the proposed dc WECS with two wind turbines was simulated in Matlab/simulink. Performance was also demonstrated experimentally. The test rig schematic is shown in Figure 6.4.

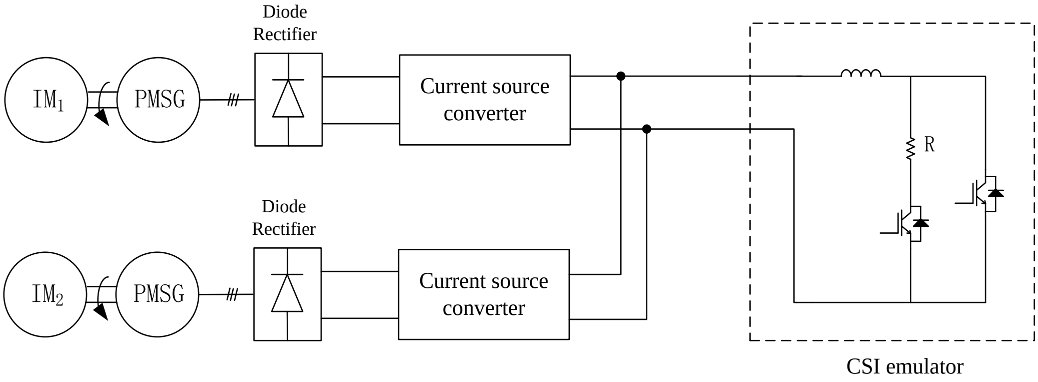

Figure 6.4 Test rig schematic.

The two induction machines IM_1 and IM_2, which drive the PMSGs, are each controlled by variable speed drives to simulate wind turbine characteristics. The turbine units operating as current sources are parallel connected to the common dc link. Each dc/dc converter is controlled to make the turbine operate at its maximum power point with variable wind speed. The wind power is collected and consumed by the CSI emulator. The CSI emulator maintains the dc link voltage constant, which is the same as the CSI voltage mode control illustrated in Chapter 2. The CSI side practical results presented below are from another work package of the collaborative project supporting the research. The current source inverter test rig shown in Figure 6.5 verifies the voltage mode control for the grid connected CSI.

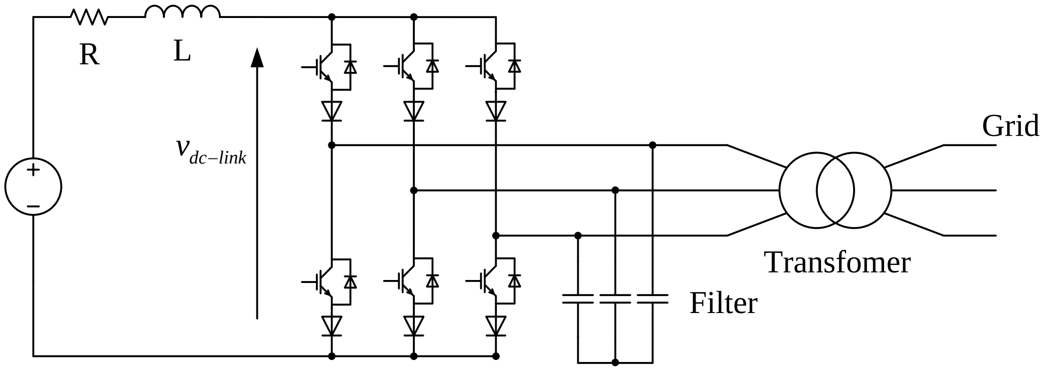

Figure 6.5 CSI test rig.

The CSI test rig consists of DC voltage source, resistor, inductor, current source inverter, filter and transformer. The DC voltage source in series with resistor/inductor is used as a variable input power source, which feeds the CSI. The CSI output is connected to the grid through an AC transformer and a variac. The test rig system parameters are summarized in Table 6.1.

Table 6.1 CSI test rig parameters.

Items	Specification	
Power rating	1.8	kW
DC link inductor	10	mH
Filter capacitor	40	μF
Grid voltage (rms)	110	V
Grid voltage frequency	50	Hz
Switching frequency	4	kHz
DC link resistance	8	Ω
Average DC link voltage, $v_{dc\text{-}link}$	200	V

In order to establish CSI voltage control, an input real power change is applied to the CSI to simulate the variable wind power. Figure 6.6 shows the CSI practical results.

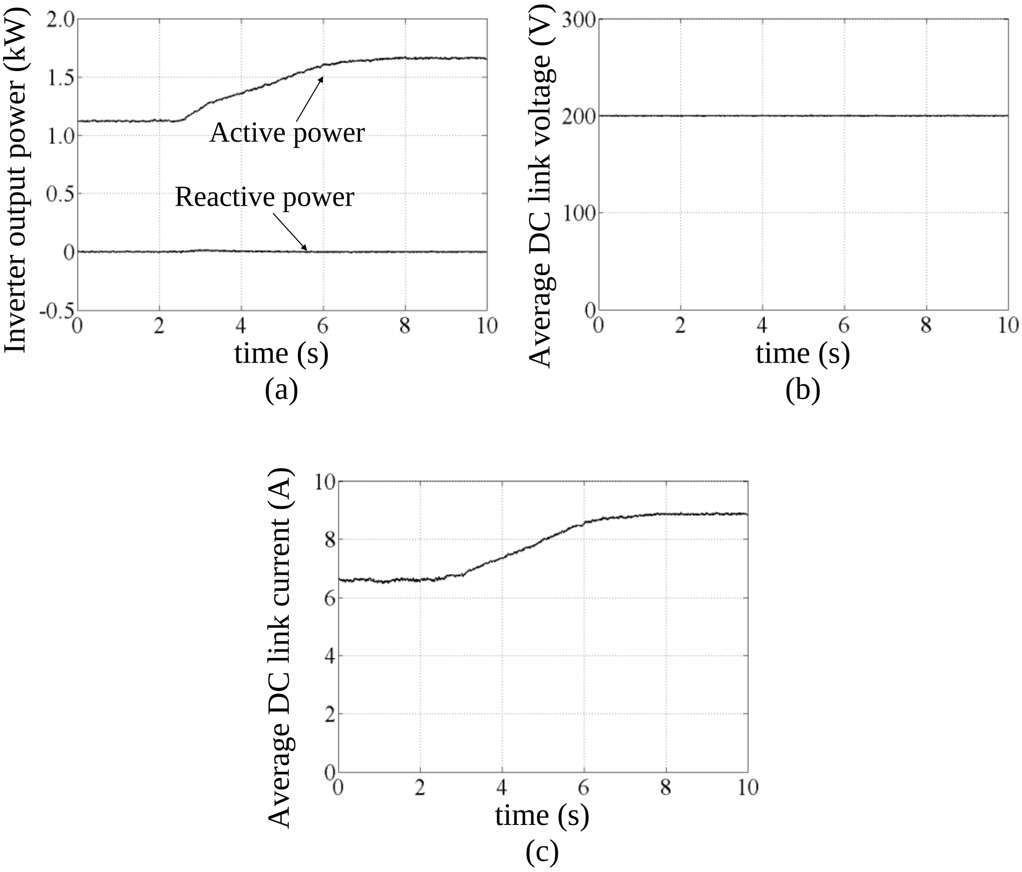

Figure 6.6 Practical results with active power change: (a) inverter output power, (b) average DC link voltage, and (c) average DC link current.

As shown in Figure 6.6 (a), the active power increases from 1.1kW to 1.7kW within 2 seconds, which is a reasonable interval considering the large time constant of a wind turbine. From Figure 6.6 (a) and (b), the average DC link voltage is maintained at 200 V with zero reactive power in the CSI voltage control mode. Figure 6.6 (c) shows the average DC link current increases as the input power increase due to the constant dc link voltage.

From the generator side, the CSI system with average dc link voltage control is same as CSI emulator with average dc link voltage control. Using a CSI emulator is justified by the fact that the large dc link inductance decouples the two parts of the system.

In this section, the stability of the system is investigated. In order to establish its stability, three scenarios are studied, specifically a wind speed change of one and two wind turbines and shutdown of one wind turbine. The performance of the wind turbines and dc link side are observed.

6.4.1 Simulation results

i. Case 1: Wind speed change of one wind turbine

The wind speed change is applied to WT1, with constant wind speed applied to WT2. The wind turbine output power changes as the wind speed changes due to maximum power point control by its associated dc/dc converter. Figure 6.7 shows the dynamic response of WT1, including wind speed, power coefficient C_p, rotor speed and mechanical power Pm. The dynamic response of WT2 is depicted in Figure 6.8. From Figure 6.7, the wind speed is initially 3.5 m/s, then stepped up to 4 m/s at t_1 s, and stepped down to 3.5 m/s at t_2 s. As is shown, WT1 power coefficient C_p is maintained around the maximum value 0.4382 during wind speed changes. The rotor speed and mechanical power also change, tracking the maximum power. For WT2, the power coefficient C_p, rotor speed, and mechanical power are constant with unchanged wind speed during power changes in WT1, which means there is no impact on WT2 through the common dc link during wind speed and power change in WT1. They can operate independently.

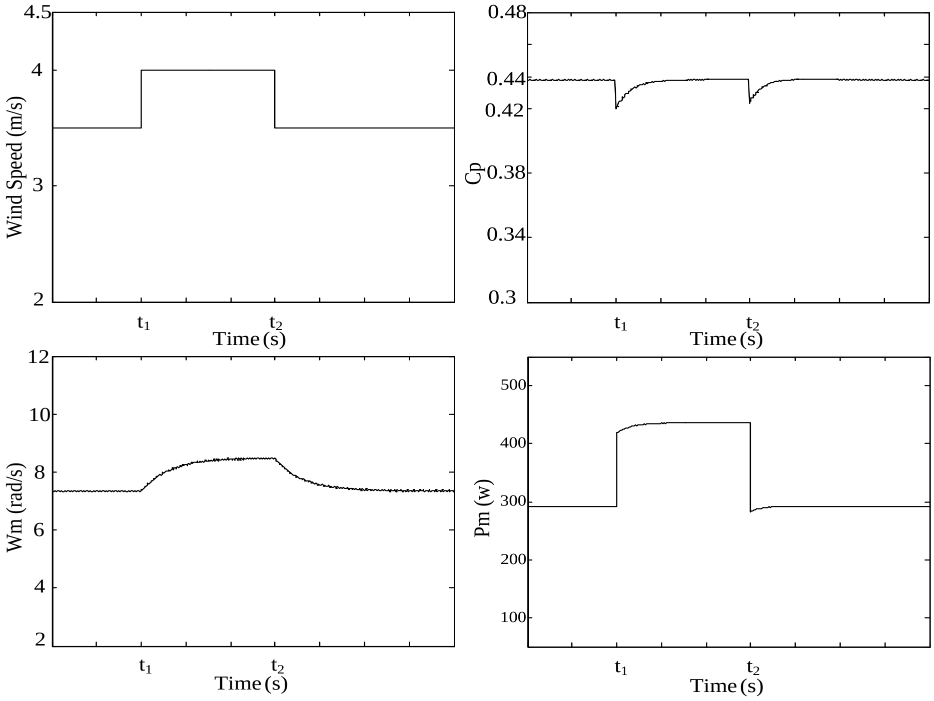

Figure 6.7 Dynamic response of mechanical system of WT1.

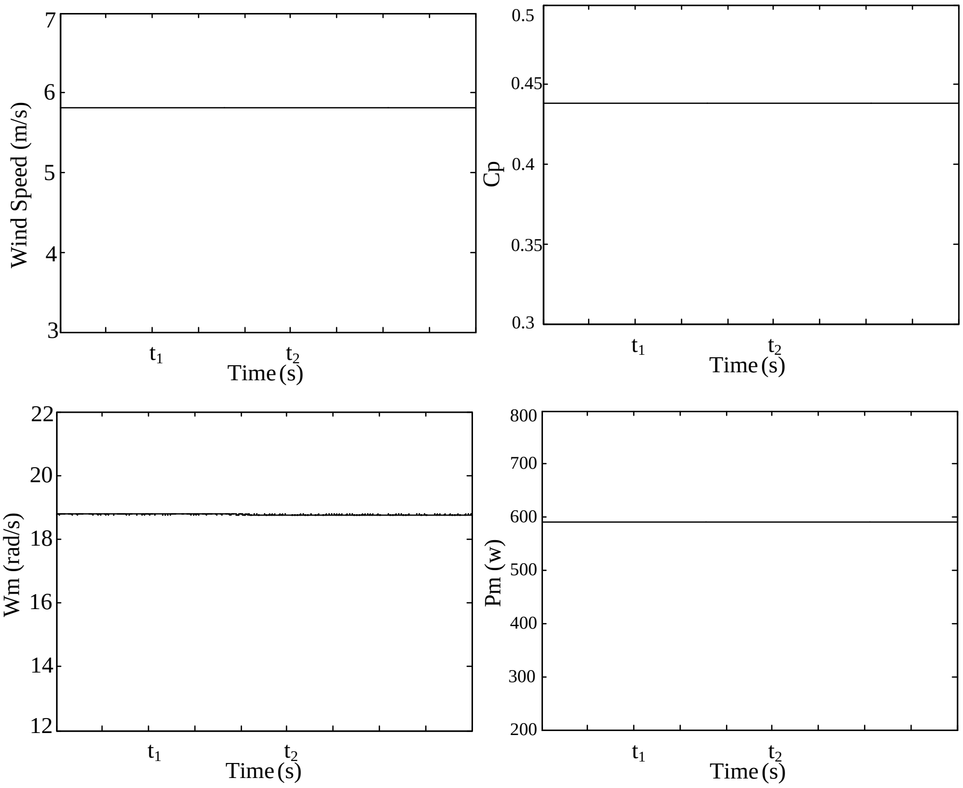

Figure 6.8 Dynamic response of mechanical system of WT2.

Figure 6.9 shows dc link voltage and the output currents of the dc/dc converters and total dc link current. During the wind speed changes in WT1, the common dc link voltage is kept constant by the CSI. WT1 output current changes as the wind speed changes, while WT2 output current is unchanged. Thus the system shows good dynamics and responds to one WT change.

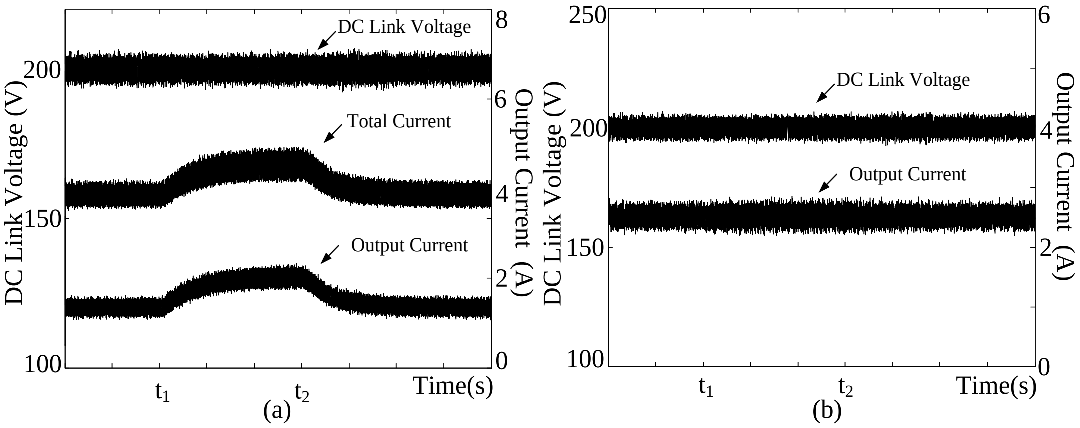

Figure 6.9 Dynamic response of the electrical system (a) WT1 (b) WT2.

ii. Case 2: Shutdown of a single wind turbine

Shutdown of one WT can occur due to a failure. The other WTs should continue to operate normally during the shutdown period. If not, the whole system may be unstable, which is not desirable. Figure 6.10 shows the dynamic response of WT2 when WT1 is shut down: wind speed, power coefficient C_p, rotor speed, and mechanical power P_m. WT1 is shut down at t_3 s, which can be achieved with a mechanical brake or using pitch control. From Figure 6.10, the power coefficient C_p, rotor speed, and mechanical power of WT2 are maintained independent of the WT1 failure. The dc link voltage, the dc/dc converter output currents and the total dc link current are shown in Figure 6.11. The WT1 dc/dc converter output current reduces to zero after shutdown, while WT2 the dc/dc converter output current is unchanged. The dc link voltage is also maintained constant during WT1 shutdown.

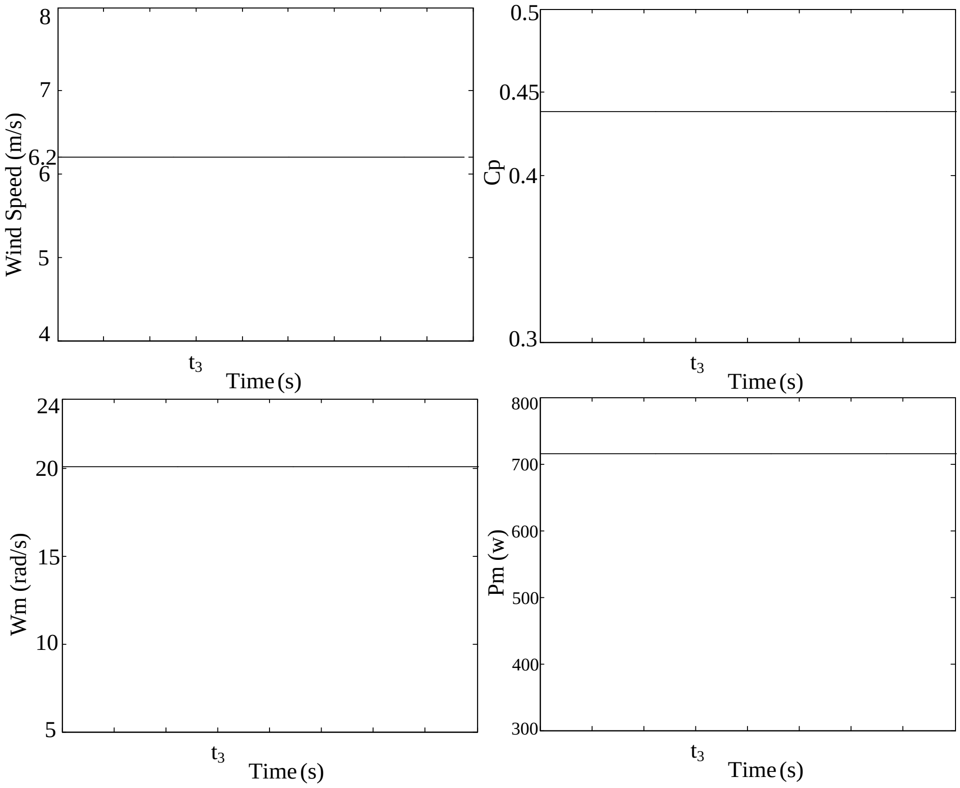

Figure 6.10 Dynamic response of mechanical system of WT2.

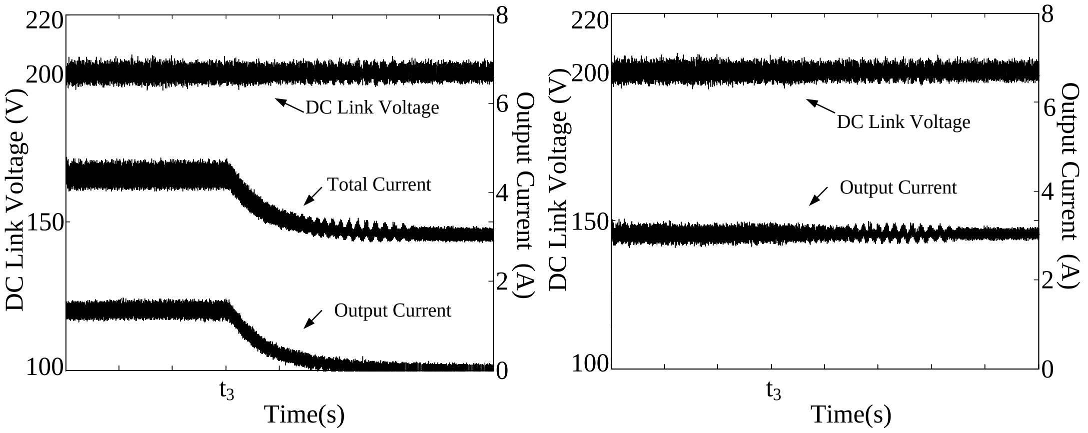

Figure 6.11 Dynamic response of the electrical system (a) WT1 (b) WT2.

iii. Case 3: Wind speed changes for both of wind turbines.

Under similar conditions as Case 1, step wind speed changes are applied to both turbines. Figure 6.12 and Figure 6.13 show mechanical dynamic responses of WT1 and WT2 respectively, where the wind speed changes from 3.5 m/s to 4 m/s at t_5 and 4 m/s to 3.5 m/s at t_7 for WT1, and 5.82 m/s to 6.2 m/s at t_4 and 6.2 m/s to 5.82 m/s at t_6 for WT2. The two wind turbines still operate at the maximum power point with the wind speed changes. Figure 6.14 shows the dynamic response of the electrical system, with the common dc link voltage constant and stable. The WT output currents are changed due to the different powers captured from the wind by the wind turbines.

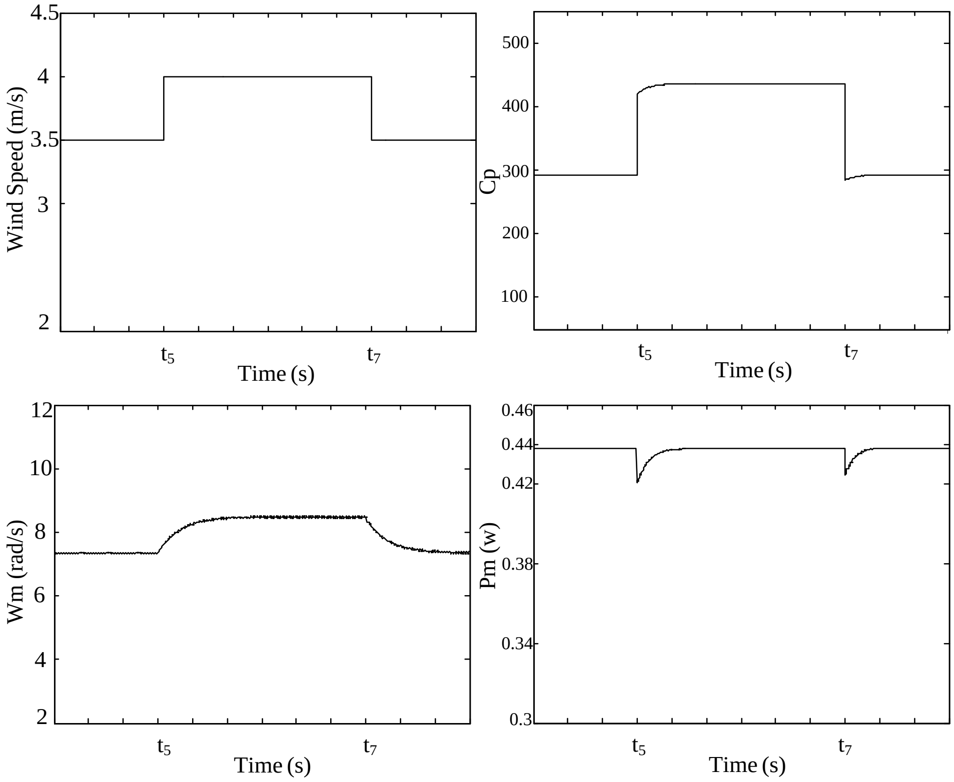

Figure 6.12 Dynamic response of mechanical system of WT1.

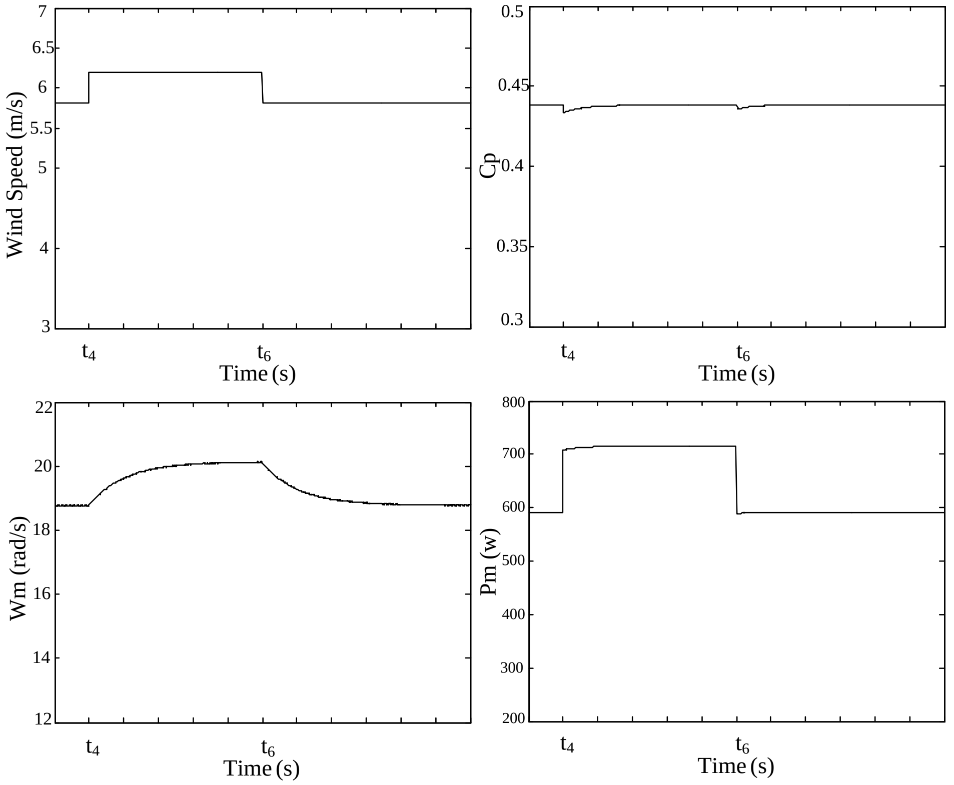

Figure 6.13 Dynamic response of mechanical system of WT2.

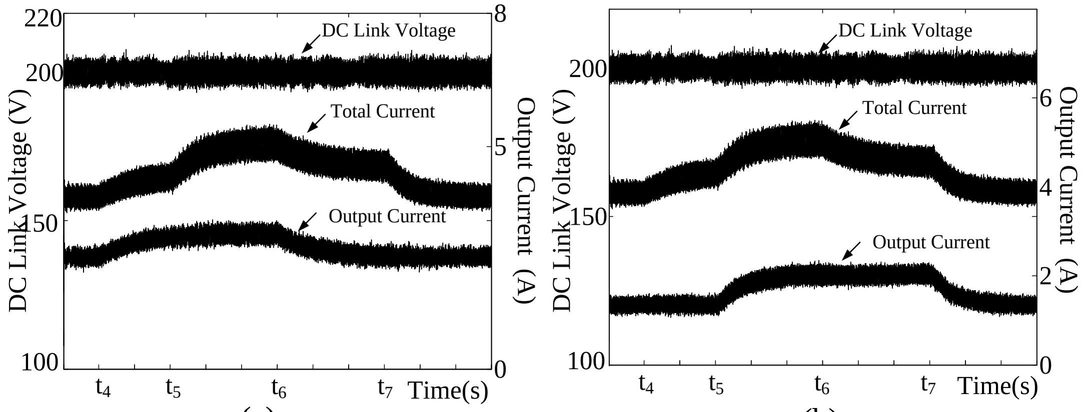

(a) (b)

Figure 6.14 Dynamic response of the electrical system (a) WT1 (b) WT2.

6.4.2 Practical implementation of the proposed WECS

The performance of the proposed WECS was investigated with Matlab simulations in section 6.4.1. A test rig is used to confirm the functionality and stability of the proposed WECS. The previously defined three simulation cases and conditions are applied to the test rig.

i. Case 1: Wind speed change of one wind turbine

A step wind speed change is applied to WT_1, with the practical dynamic response results of WT1 and WT2 shown in Figure 6.15 and Figure 6.16. The rotor speed and power of WT1 change to track the MPP according to the step wind speed change. Thus C_p is maintained around the maximum value as shown in Figure 6.15. During the process of the step wind speed change in WT1, the C_p, rotor speed, and power of WT2 are unchanged, as shown in Figure 6.16.

Figure 6.17 shows the practical electrical results of WT1 and WT2. The output voltage is kept constant by the CSI emulator. For WT1, the output current changes due to the step wind speed change, while WT2 output current is unchanged.

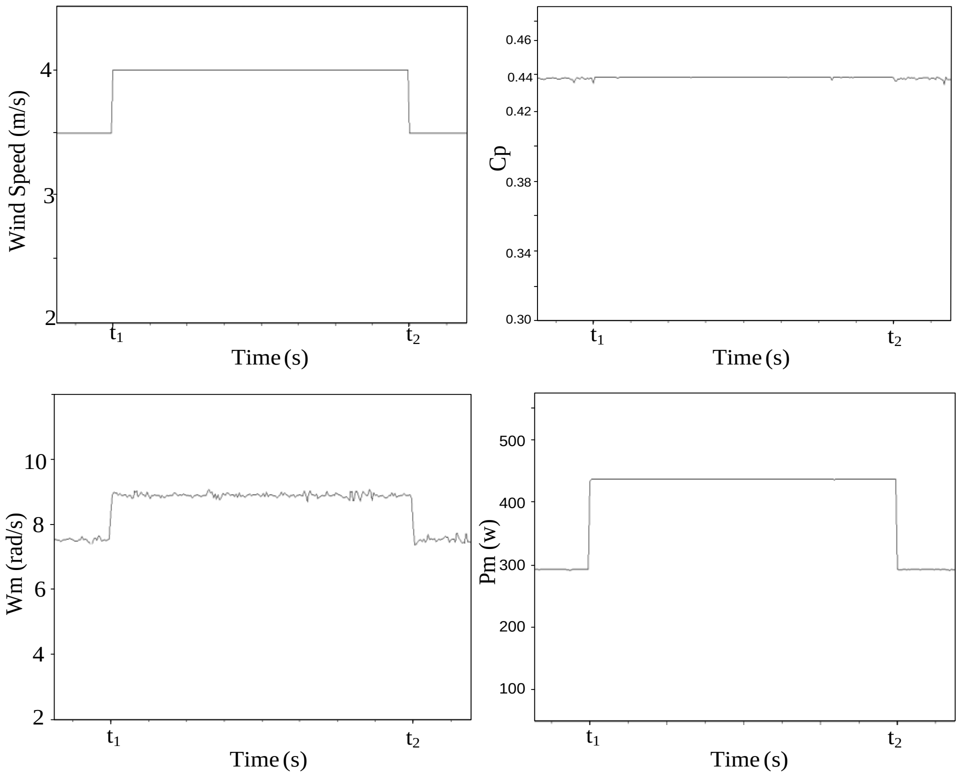

Figure 6.15 Practical dynamic response of the mechanical system of WT1.

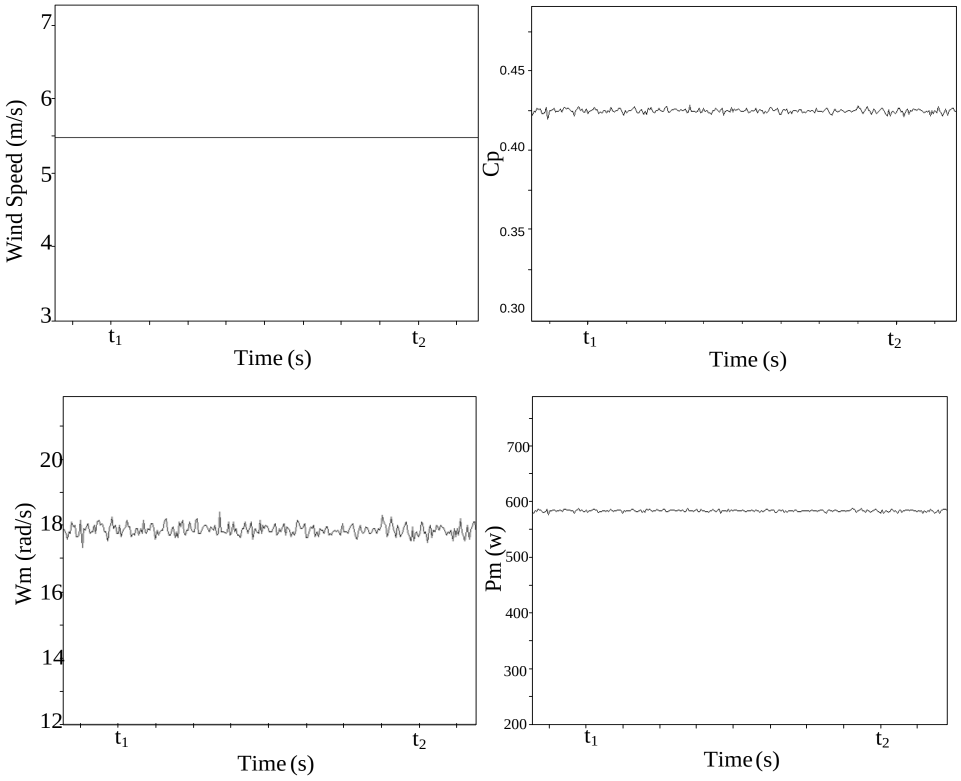

Figure 6.16 Practical dynamic response of the mechanical system of WT2.

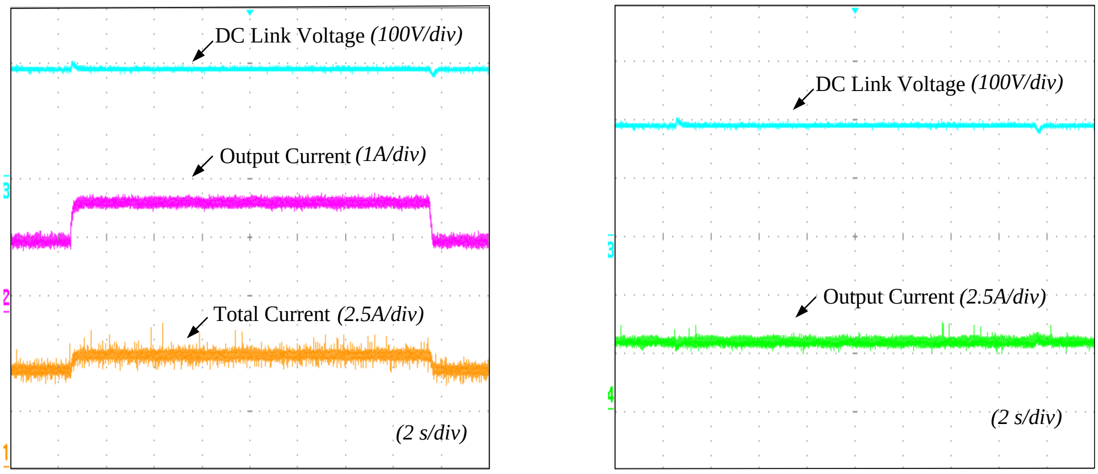

(a) (b)

Figure 6.17 Practical dynamic response of the electrical system (a) WT1 (b) WT2.

ii. Case 2: Shutdown of one WT

WT1 is shutdown during the system operation. Figure 6.18 and Figure 6.19 show the practical dynamic response results for WT1 and WT2. When WT1 is shutdown, the rotor speed and power decrease to zero as shown in Figure 6.18. WT2 operation is unaffected by WT1. Figure 6.20 and Figure 6.21 show the electrical response of the output voltage and current. The output current of WT1 becomes zero since it is shutdown, while the output voltage and current of WT2 are maintained constant. Figure 6.20 (b) and Figure 6.21 (b) show the zoomed-in waveforms of the output voltage and current during the shutdown process of WT1.

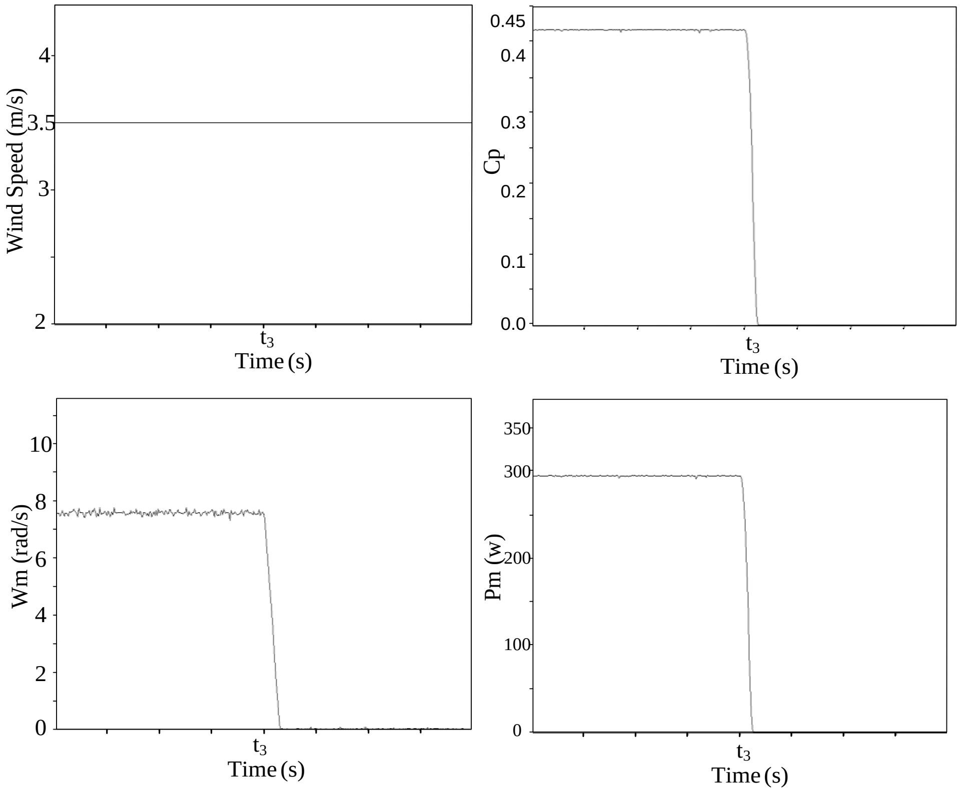

Figure 6.18 Practical dynamic response of the mechanical system of WT1.

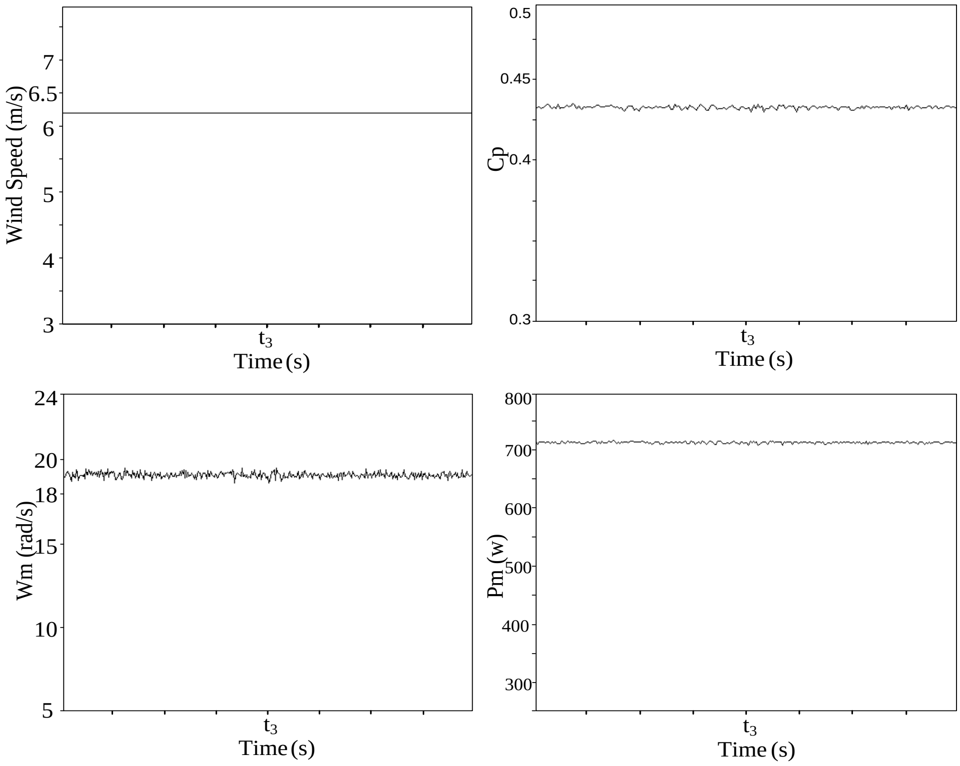

Figure 6.19 Practical dynamic response of the mechanical system of WT2.

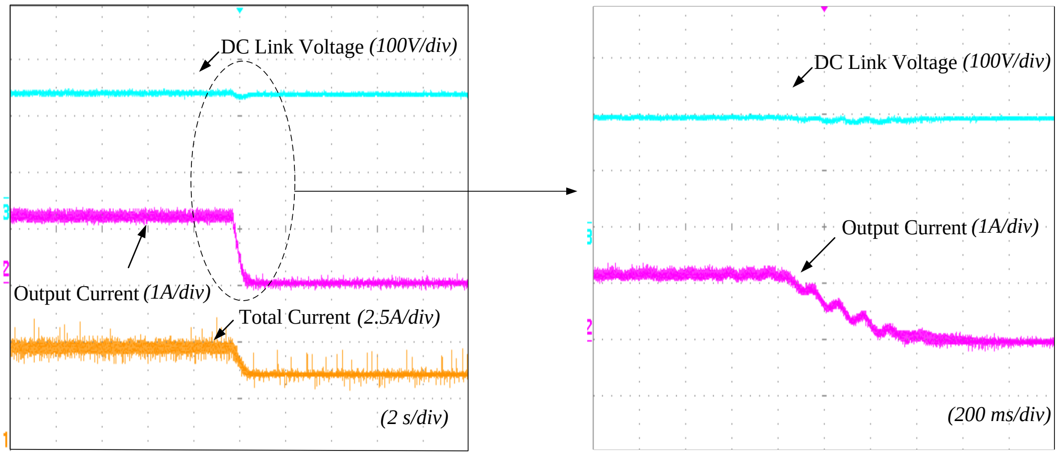

(a) (b)

Figure 6.20 Practical dynamic response of electrical system of WT1.

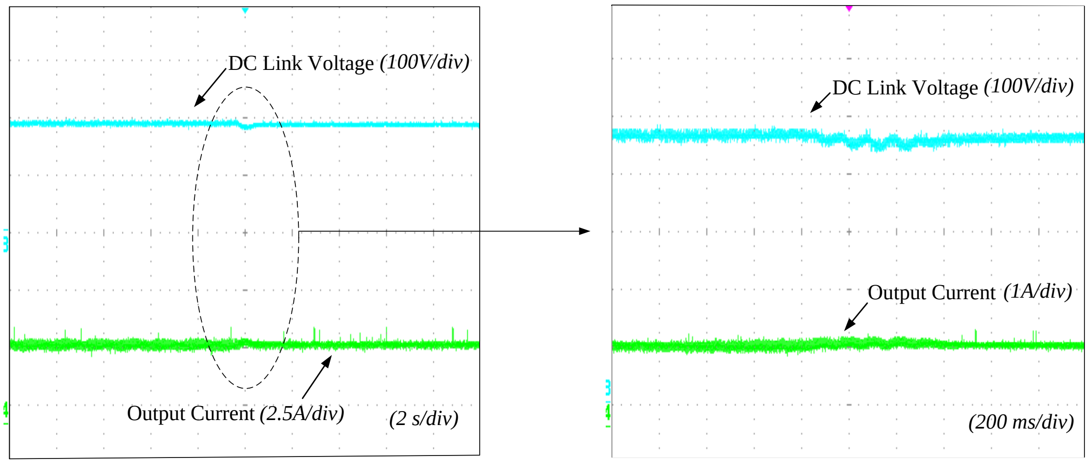

(a) (b)

Figure 6.21 Practical dynamic response of electrical system of WT2.

iii. Case 3: Wind speed changes for both wind turbines

Step wind speed changes are imposed on WT1 and WT2. Figure 6.22 and Figure 6.23 show the practical dynamic response results for WT1 and WT2. The rotor speed and power of each WT is changed according to its wind speed change. There is no interaction between WT1 and WT2. The practical electrical response results are shown in Figure 6.24, with detailed waveforms shown in Figure 6.24 (b). The output voltage is controlled and stable when step wind speed changes occur on WT1 and WT2.

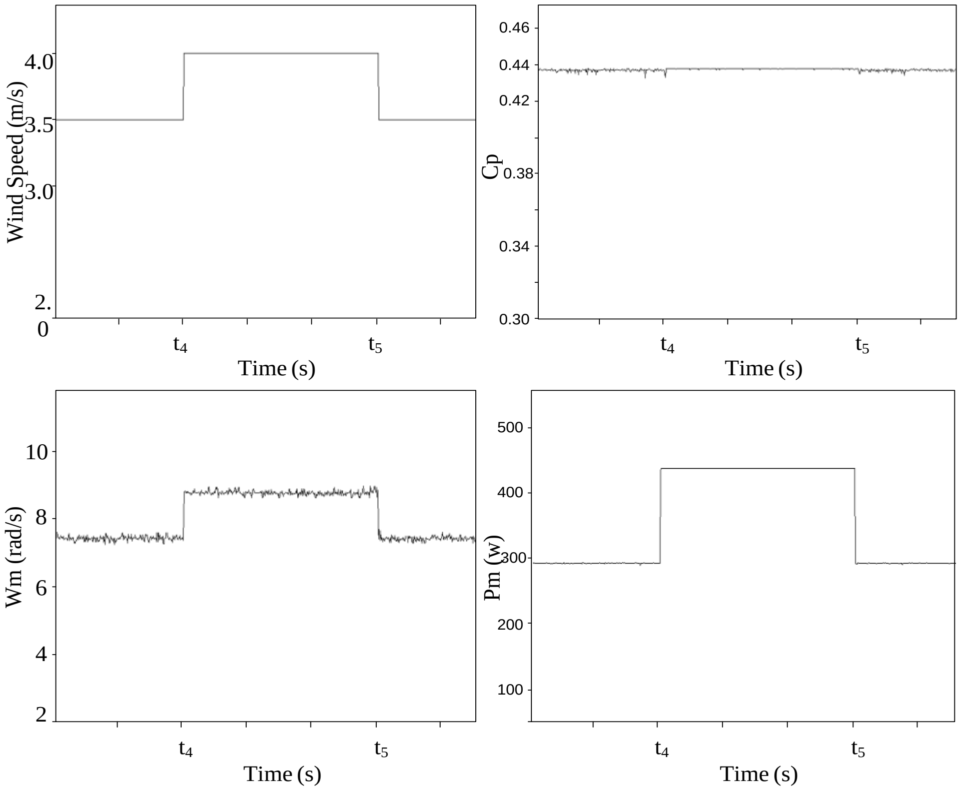

Figure 6.22 Practical dynamic response of the mechanical system of WT1.

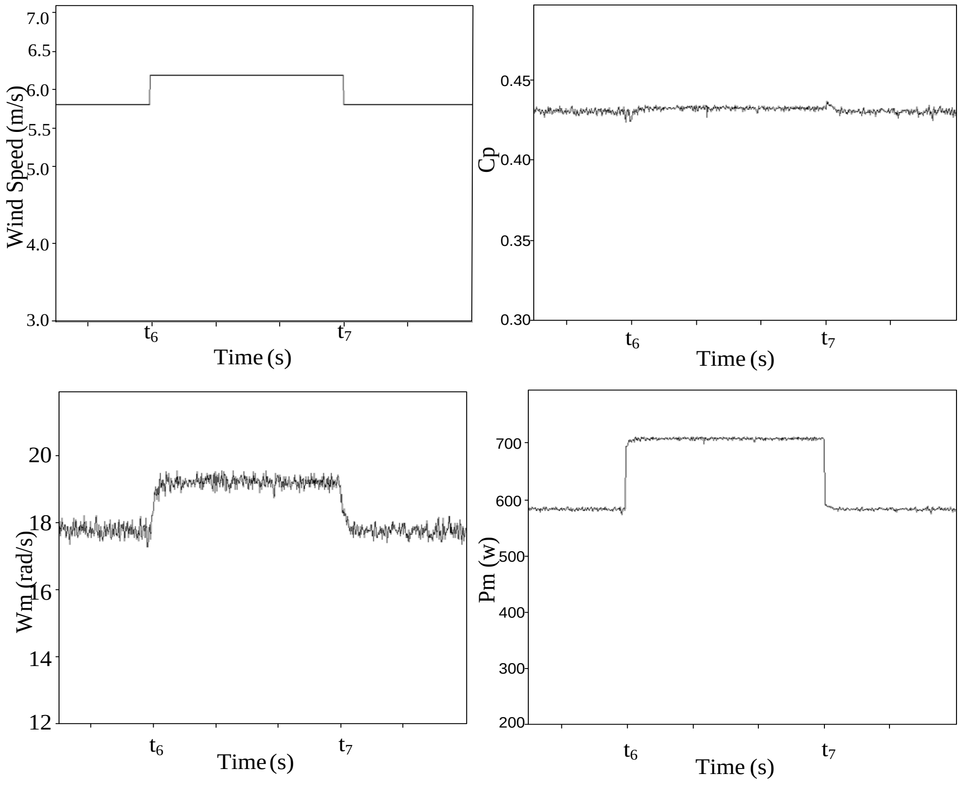

Figure 6.23 Practical dynamic response of the mechanical system of WT2.

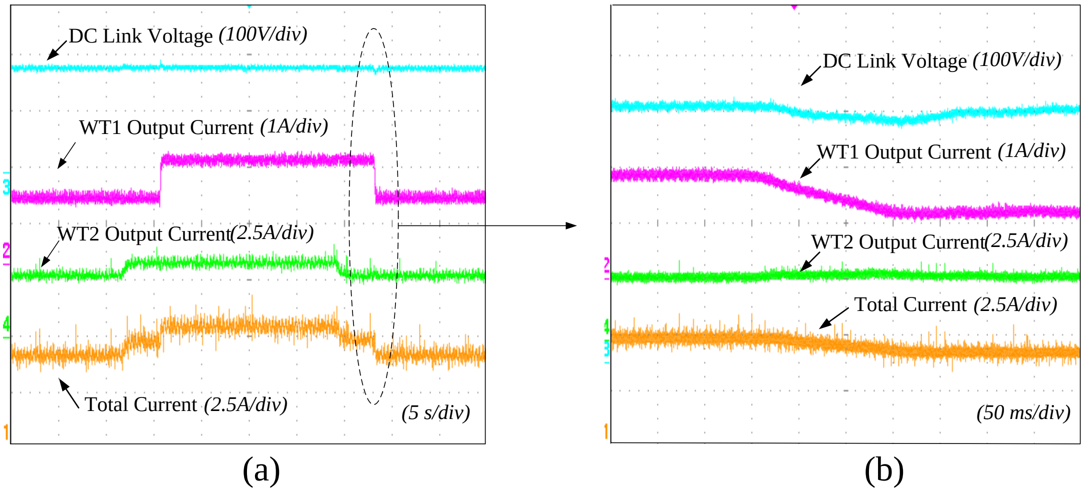

Figure 6.24 Practical dynamic response of the electrical systems of WT1 and WT2.

The practical results also demonstrate the stability of proposed dc WECS in all three cases.

6.5 Summary

In this chapter, the current source dc/dc converter-based multi-terminal dc WECS is proposed. In this system, dc/dc converters are controlled to track the maximum power. A forced-commutated devices based CSI can be used for grid connection, which also allows reactive power support as with a VSI. With current-feeding and parallel connection to the common dc link, dc/dc converter output capacitors are eliminated, saving on system costs and volume. WECS performance was investigated and analyzed for three different system cases, with the simulations and experimental results establishing system control functionality and feasibility. Finally, it is concluded that the proposed system is a solution viable for a multi-terminal dc grid wind farm.

References

[6.1] S. Nishikata and F. Tatsuta, "A New Interconnecting Method for Wind Turbine/Generators in a Wind Farm and Basic Performances of the Integrated System," *Industrial Electronics, IEEE Transactions on,* Vol. 57, No. 2, pp. 468-475, 2010.

[6.2] Y. Jin, J. E. Fletcher, and J. O'Reilly, "Multiterminal dc Wind Farm Collection Grid Internal Fault Analysis and Protection Design," *Power Delivery, IEEE Transactions on,* Vol. 25, No. 4, pp. 2308-2318, 2010.

[6.3] J. Robinson, D. Jovcic, Joo, and G. "Analysis and Design of an Offshore Wind Farm Using a MV dc Grid," *Power Delivery, IEEE Transactions on,* Vol. 25, No. 4, pp. 2164-2173, 2010.

[6.4] X. Yuanye, K. H. Ahmed, and B. W. Williams, "Different torque ripple reduction methods for wind energy conversion systems using diode rectifier and boost converter," *Electric Machines & Drives Conference (IEMdc), 2011 IEEE International*, 2011, pp. 729-734.

[6.5] Y. Jin, J. E. Fletcher, and J. O'Reilly, "Multi-terminal dc wind farm collection and transmission system internal fault analysis," *Industrial Electronics (ISIE), 2010 IEEE International Symposium on*, 2010, pp. 2437-2442.

[6.6] L. Fei, M. Zhiwen, Y. Xiaojie, and Z. Trillion, "The grid connected converter control of multi-terminal dc system for wind farms," *Electrical Machines and Systems, 2005. ICEMS 2005. Proceedings of the Eighth International Conference on*, 2005, pp. 1021-1023 Vol. 1022.

[6.7] M. Chinchilla, S. Arnaltes, and J. C. Burgos, "Control of permanent-magnet generators applied to variable-speed wind-energy systems connected to the grid," *Energy Conversion, IEEE Transactions on, V*ol. 21, No. 1, pp. 130-135, 2006.

[6.8] D. Jovcic and N. Strachan, "Offshore wind farm with centralised power conversion and dc interconnection," *Generation, Transmission & Distribution, IET,* Vol. 3, No. 6, pp. 586-595, 2009.

[6.9] A. Yazdani and R. Iravani, "A unified dynamic model and control for the voltage-sourced converter under unbalanced grid conditions," *Power Delivery, IEEE Transactions on*, Vol. 21, No. 3, pp. 1620-1629, 2006.

[6.10] X. Lie, B. R. Andersen, and P. Cartwright, "VSC transmission operating under unbalanced ac conditions - analysis and control design," *Power Delivery, IEEE Transactions on*, Vol. 20, No. 1, pp. 427-434, 2005.

[6.11] T. Lianxiang and O. Boon-Teck, "Locating and Isolating dc Faults in Multi-Terminal dc Systems," *Power Delivery, IEEE Transactions on*, Vol. 22, No. 3, pp. 1877-1884, 2007.

[6.12] H. Zhou, G. Yang, J. Wang, and H. Geng, "Control of a hybrid high-voltage dc connection for large doubly fed induction generator-based wind farms," *Renewable Power Generation, IET*, Vol. 5, No. 1, pp. 36-47, 2011.

[6.13] D. Jingya, X. Dewei, W. Bin, N. R. Zargari, and L. Yongqiang, "Dynamic performance analysis and improvements of a current source converter based PMSM wind energy system," *Power Electronics Specialists Conference, 2008. PESC 2008. IEEE*, 2008, pp. 99-105.

[6.14] D. Jovcic, "Off Shore Wind Farm with a Series Multiterminal CSI hvdc," *Electric Power Systems Research, Elsevier*, Vol. 78, No. 4, pp. 747-755, April 2008.

[6.15] S. A. Azmi, K. H. Ahmed, S. J. Finney, and B. W. Williams, "Comparative analysis between voltage and current source inverters in grid-connected application," *Renewable Power Generation (RPG 2011), IET Conference on*, 2011, pp. 1-6.

Chapter 7

A Coordinated Control Scheme for Power Demand Changes in a PMSG based Multi-terminal DC Wind Farm

Although maximum power point tracking (MPPT) is crucial in the design of a wind power generation system, the necessary control strategies should also be considered for conditions that require a power reduction: called de-loading. A coordinated control scheme for the proposed current source converter (CSC) based dc wind energy conversion system is presented. This scheme combines coordinated control of the pitch, a dc load dumping chopper and the dc/dc converter, to quickly achieve wind farm de-loading control. Matlab/Simulink simulations and experiments are used to validate the purpose and effectiveness of the de-loading.

7.1 Background

Generally, wind turbines are controlled to operate along a MPPT curve to extract maximum energy from the wind resources. It is an emerging requirement that wind farms should possess flexible generation characteristics as close as possible to conventional power plants. The kinetic energy stored in the rotating mass of turbine blades can be utilised to support primary generation control for a short period, which gives the flexibility for turbines to operate on either side of their power characteristic curves [7.1-2]. A turbine cannot provide more than maximum power for a long period, since the maximum power is limited by the wind speed and power coefficient. Therefore wind turbines cannot provide long term frequency control when the connection point frequency drops below that required. In this case, a fast-responding gas-fired or pre-heated coal-fired station is needed to provide extra power to support the grid frequency [7.3]. Conversely, when the power demand reduces, the power generated from the power source must be reduced to maintain power balance for frequency control. Once a conventional power station goes offline, it may stay off-line for a long period of time [7.4]. Given the start-up time and cost, coal-fired power station shut down is not favoured. With power electronic converters and turbine pitch control systems, output power from each individual wind turbine can be rapidly controlled, although the adjustment range is limited. Nevertheless, a large-scale gigawatt wind farm will have a collective capability sufficient for frequency control. The main challenge is to design a smooth power de-loading scheme for the wind farm, during which each turbine operating point will move away from the MPPT curve. Figure 7.1 shows wind turbine operation when it move away from the MPPT curve. From the turbine power curve, the rotor speed decreases (under speeding) on the left side, while rotor speed increases (over speeding) on the right side. The over speeding case is preferable since this gives improved small signal stability [7.5-6].

The wind farm output power can be reduced through pitch control [7.7] or converter control [7.8]. Since wind farm start-up time is shorter than other power stations, such as coal-fired stations or a nuclear power station, de-loading the wind farm is an option for maintaining power balance.

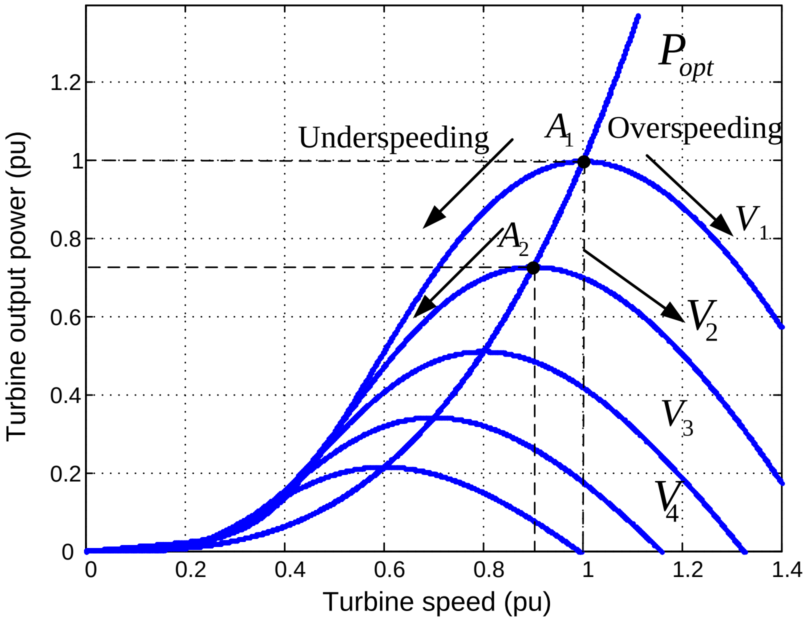

Figure 7.1 Wind turbine operation possibility during de-loading process.

De-loading of wind turbines means not all of the available wind energy is converted into grid electricity. In order to avoid power loss and to maintain a safely operating system, external energy storage must be used in conjunction with the wind farm, which can be a flywheel, compressed-air, pumped hydro [7.9] or a battery [7.10]. Reference [7.11] presents a scheme for supervisory control of wind farms, which may utilize either an external energy storage device or power reserve achieved through part-loading of one or more turbines in a wind farm. Battery storage is considered for external energy storage, connected to a power system. Both methods have been validated by simulations that focus on the grid side. Performance within the wind farm is not detailed. The energy storage control approach is that the energy storage provides energy when the power demand is greater than the wind farm output power, and absorbs surplus energy when the grid power demand is less than the wind farm output power. Energy storage increases system complexity, as well as capital and maintenance costs. Also there is power loss during the process of energy exchange. Additionally, any energy storage device has its own capacity limit, thus the amount of energy that can be stored is a limiting factor. Energy storage for a long period may be problematic. The economics of wind energy are important, but the cost-benefit analysis of a wind farm with energy storage is beyond the scope of this research.

Pitch control can be used for both variable speed and fixed speed wind turbines. Pitch control response is slower than power electronic control due to its servo time constant (seconds) [7.12]. Thus power dumping de-loading control with pitch control cannot respond fast enough to the load change.

In this study, a new coordinated control scheme with de-loading control with fast dynamic response is proposed. The scheme integrates dc/dc converter control, dc chopper control, and turbine pitch control, enabling the wind turbine to operate safely.

The proposed scheme is validated by Matlab/Simulink simulations and experimentation. Both confirm the effectiveness of the scheme for controlling wind farm output power.

7.2 The system configuration (current source converter)

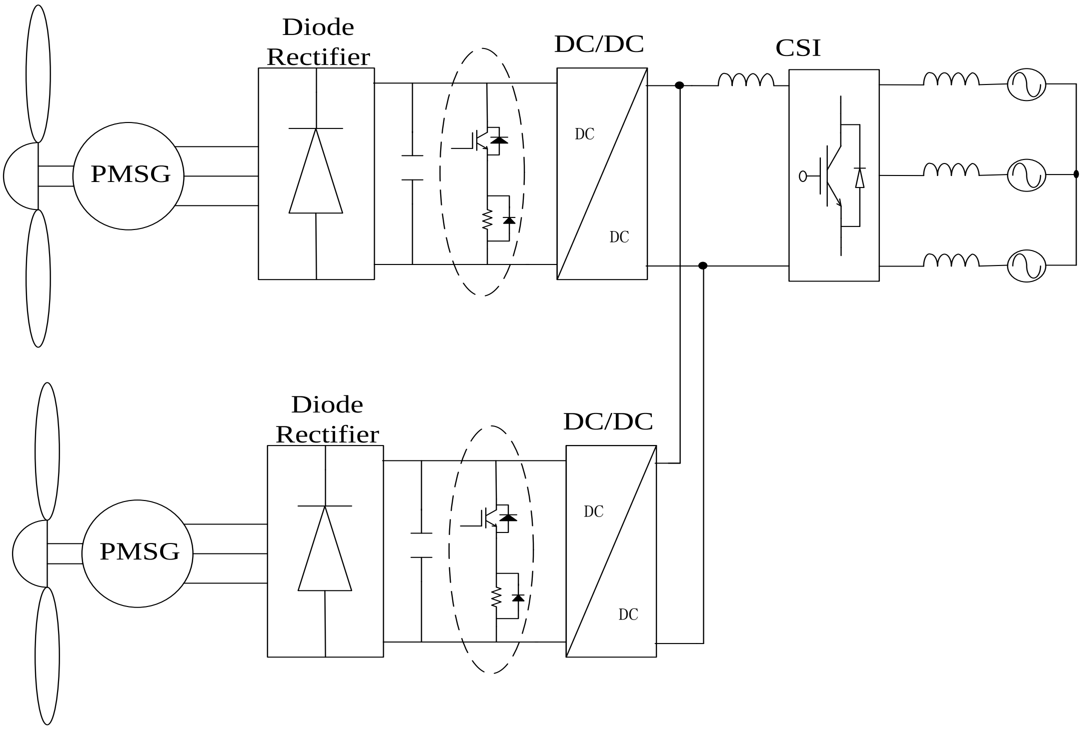

Figure 7.2 Multi-terminal dc transmission WECS configuration.

Figure 7.2 shows a multi-terminal dc transmission WECS configuration that consists of wind turbines, PMSGs, diode rectifiers, current source dc/dc converters, and a centralised current source inverter for the grid connection. Each wind turbine is connected to the dc link through its own diode output bridge rectifier and dc/dc converter. This dc configuration uses one inverter to deliver power to the grid, which saves on system cost. A controlled dumping resistor, using a dc chopper, is added to absorb the wind power during a short term fault condition, and is parallel connected to the filter capacitor as shown Figure 7.2.

7.3 Proposed De-loading Control Scheme

De-loading control can be implemented with a combination of pitch control and/or power electronic converter control. Figure 7.3 shows the proposed de-loading control scheme flow chart, where scheme operation depends on the dc link voltage. When the power demand changes, there is imbalance between the input wind power and the output power to the grid, which causes a dc link voltage change. The wind turbines continue to operate at MPP since the dc/dc converters decouple the wind turbines and the dc link network. When the input wind power is greater than the output power, the dc link voltage increases, and may exceed component insulation levels and destroy the power electronics devices. In order to decrease the dc link voltage, the surplus energy should be consumed or reserved. In this protection scheme, dc voltage control is applied to the dc/dc converter when dc link voltage exceeds the pre-limited V_{dclim}. The surplus energy is stored in turbine inertia, thus the rotor speed increases. In a WECS, rotor speeds are also required to be controlled to below a limit value. Once rotor speed reaches this limit, dc chopper control or pitch control is activated to ensure the rotor speed does not exceed its limit value. Compared to dc chopper energy dumping control, pitch control has a slower response due to its servo time constant [7.13]. But the dc chopper control dumps the energy to a resistor tank, which needs extra equipment such as fans for resistor cooling: resistor cooling wastes energy. Thus dc chopper control is applied in the short term, allowing time for pitch control to be effective in reducing the converter energy. For the selection of ω_{lim} and $V_{inlim,}$ the voltage limit V_{inlim} should be slightly greater than the voltage corresponding to the rotor speed limit ω_{lim}. Thus, after rotor speed control has been replaced by pitch control (10 or so seconds), the dc chopper ceases to operate. Thus the dc dumping chopper is only short term rated.

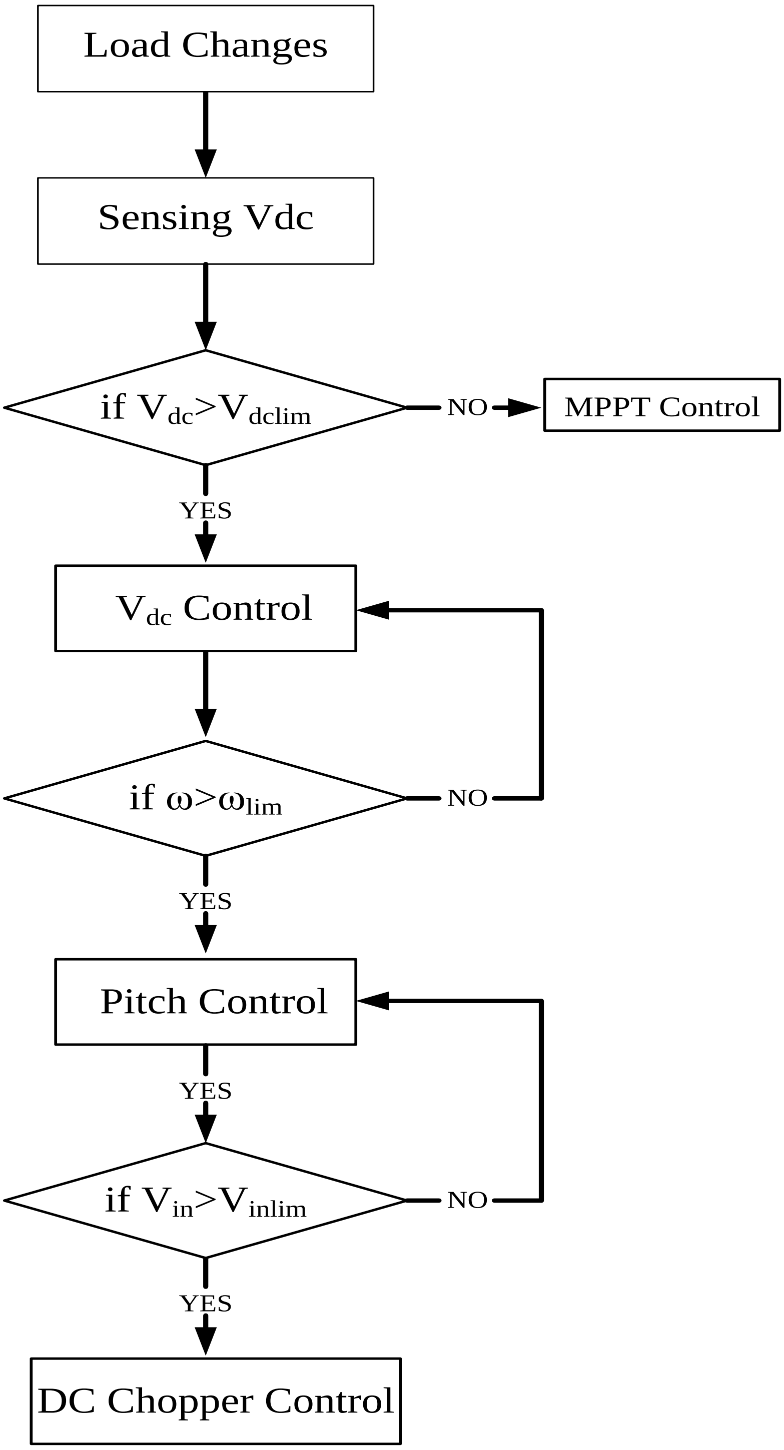

Figure 7.3 The proposed de-loading control scheme flow chart.

7.3.1 Pitch Control

Pitch control is used in variable speed and fixed speed WECS, and limits the wind turbine rotor speed and power to prevent the turbine from being destroyed during high wind speeds and abnormal operating conditions. Figure 7.4 shows the power coefficient C_p versus tip speed ratio curves for different pitch angles based on the C_p, equation (4.1), under constant wind speed. From Figure 7.4, the power coefficient and output power are reduced as the pitch angle of turbine blades increases, which means the rotor speed and output power can be controlled with pitch control.

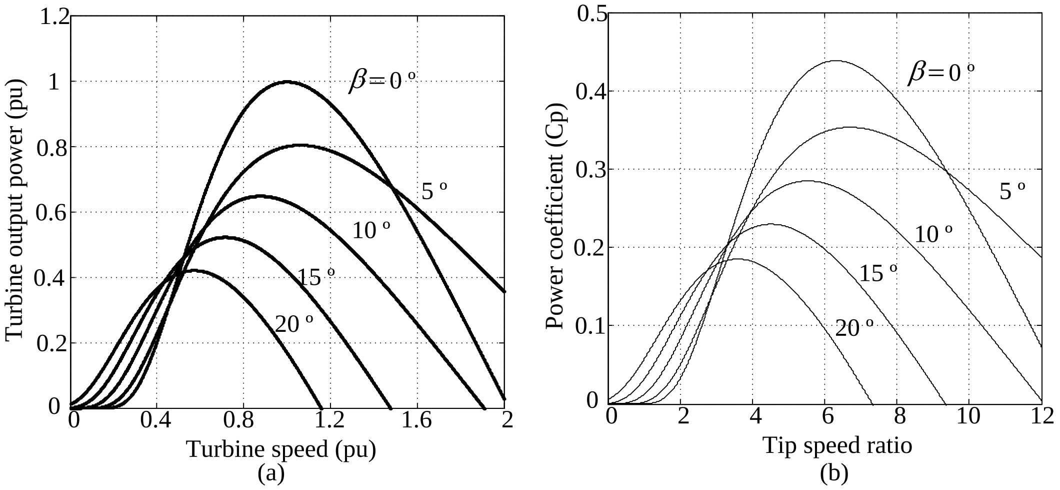

Figure 7.4 The wind turbine characteristics in pu with different pitch angle β (a) turbine output power versus turbine speed (b) C_p versus tip speed ratio.

Pitch control in a variable speed wind turbine is activated when the rotational speed exceeds the maximum allowed value due to a high wind speed condition [7.14]. The pitch controller is shown in Figure 7.5.

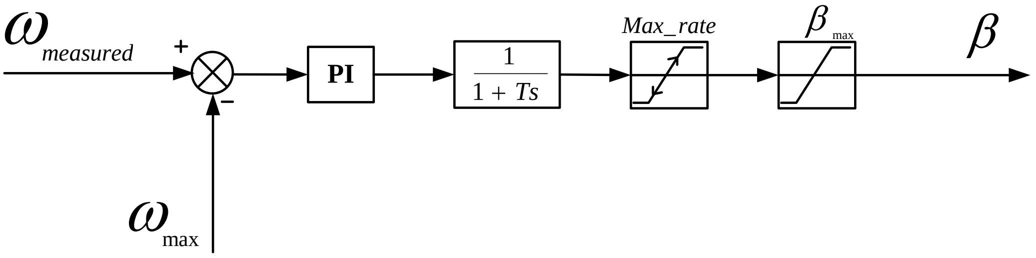

Figure 7.5 Pitch controller in a variable speed wind turbine.

In a fixed speed wind turbine, the necessary pitch controller is shown in Figure 7.6[7.15]. The reference and measured powers are compared, and the resulting error controls the pitch angle of the blades. Therefore the generator output power will be limited to within rated power during high wind speeds.

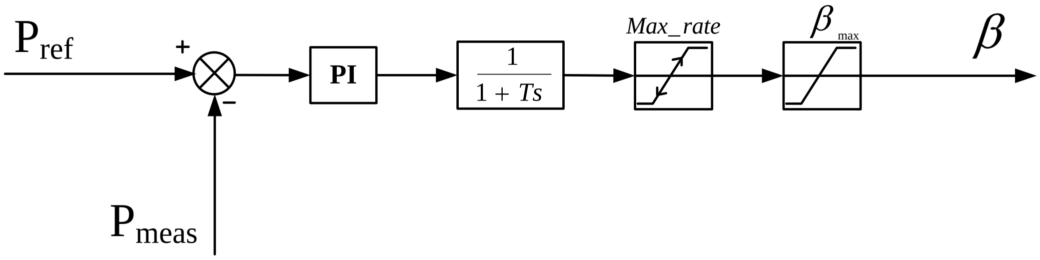

Figure 7.6 Pitch controller in fixed speed wind turbine.

In this chapter, wind turbine output power is controlled by the dc/dc converter, thus the pitch control shown in Figure 7.5 is adopted.

7.3.2 DC/DC converter control

The dc/dc converter control has two modes during operation: MPPT mode and voltage mode. When the dc link voltage is below the limit value V_{dclim}, MPPT mode control is applied to the dc/dc converter. The controller senses the input voltage and calculates the reference current. When the dc link voltage exceeds the limited value, voltage mode control operates, keeping the dc link voltage at a pre-limited level. During this process, the reference current decreases due to the dc link voltage error, which causes the electrical power to be less than the mechanical input power. Thus the rotor speed increases, which means the WECS operating point moves from the MPP to the right side of wind turbine curve, as shown in Figure 7.1. Figure 7.7 shows the dc/dc converter voltage control block diagram.

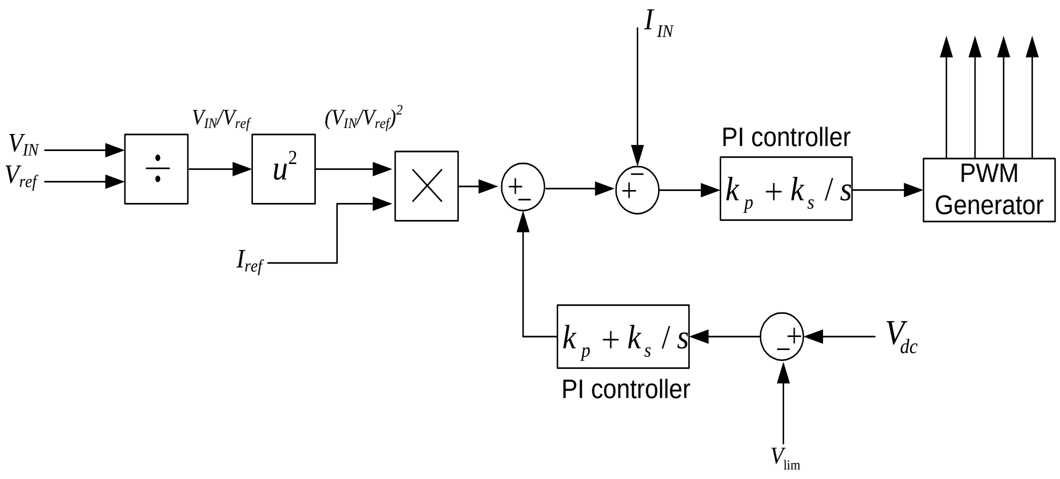

Figure 7.7 DC/DC converter control block diagram.

7.3.3 DC chopper control

The controlled dc chopper has been widely used in WECS [7.16]. A dc dumping chopper is used in VSC based hvdc systems for wind farms [7.17]. During a fault, the controlled dc chopper is used to dissipate the wind farm output power and thus limit the dc voltage to within safe levels. The dc dumping chopper consists of an IGBT and a resistor tank, as shown in Figure 7.8. It has simple on/off control as shown Figure 7.9, and is activated based on the input voltage of the dc/dc converter. No switching losses are incurred. The resistor tank rating is related to the rating of the generator machine.

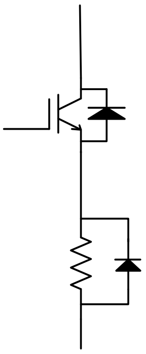

Figure 7.8 DC dumping chopper topology.

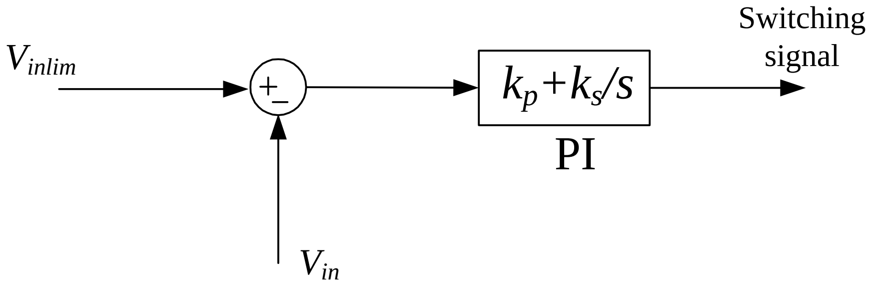

Figure 7.9 Control schematics for dc dumping chopper.

7.4 Simulation and experiment results

The performance of the proposed coordinated control scheme for the multi-terminal wind farm is investigated with MATLAB/Simulink simulations and experimentally. The multi-terminal dc WECS is based on two PMSG wind turbine units. The system parameters are the same as in Chapter 6. A step change of duty cycle is applied to the CSI emulator to simulate the grid power change. WECS performance is studied for three cases: with and without the proposed coordinated control scheme, and with only dc/dc converter voltage control.

7.4.1 Simulation results

In the simulation, the duty cycle of the CSI emulator is stepped up from 0.5 to 0.9 at 0.5 s. the wind speed of each wind turbine is unchanged.

i. Case 1: Without the proposed coordinated control scheme

Figure 7.10 and Figure 7.11 show the dynamic response of turbines WT1 and WT2 respectively without the proposed coordinated control scheme, and include wind speed, power coefficient C_p, rotor speed, and mechanical power P_m. As shown, when the power demand from the grid is a step change, the power coefficient C_p is maintained around the maximum value. The rotor speed and mechanical power are unchanged. The wind turbines are not affected and continue to operate at the MPP.

Figure 7.12 shows the dc link voltage and wind turbine output dc voltage. The dc link voltage is changed due to the power imbalance. When the power demand reduces, the surplus wind power increases the dc link voltage, which can exceed the insulation level of components and destroy the system. Assuming the rotor speed and the dc link voltage before the power demand changes are 1 pu, then from Figure 7.12, the dc link voltage increases to 1.4 pu. However, the general safety threshold of the dc-link overvoltage is required not to exceed 1.2 pu.

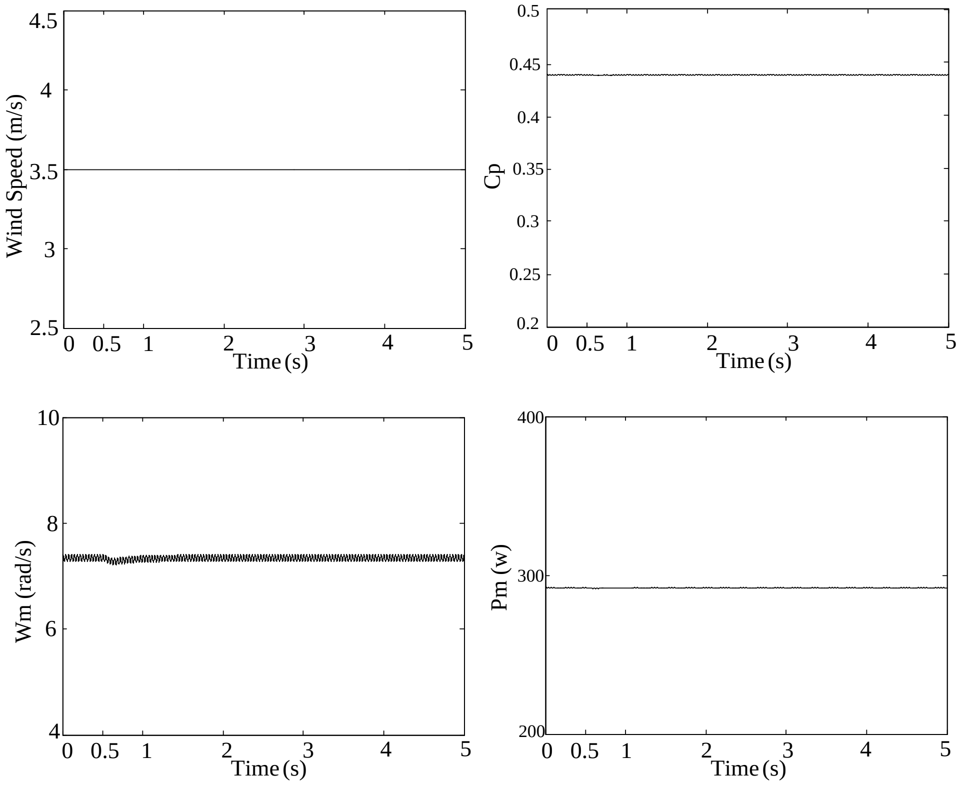

Figure 7.10 Dynamic response of WT1 without the proposed control.

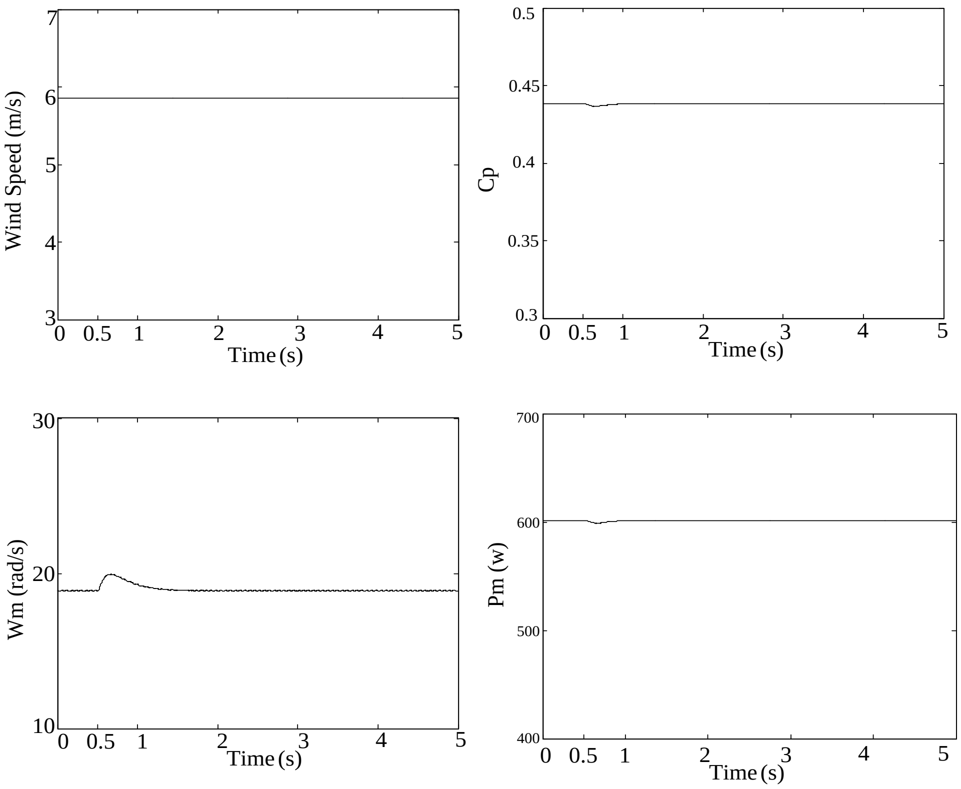

Figure 7.11 Dynamic response of WT2 without the proposed control.

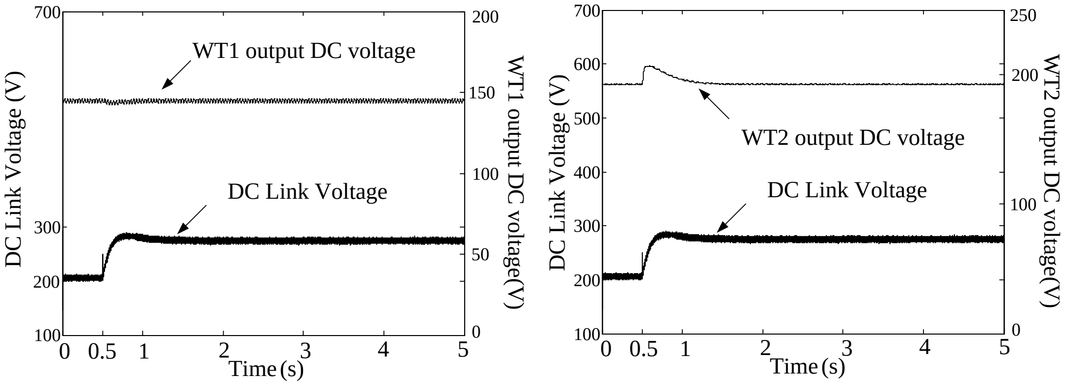

(a)

(b)

Figure 7.12 DC link voltage and wind turbine output dc voltage without the proposed control (a) WT1 (b) WT2.

ii. Case 2: With dc/dc dumping converter voltage control

In order to control the dc link voltage to within a safe level, the input power from the wind turbine should be reduced, which means the wind turbine operating point should move away from the MPP. DC/DC converter voltage control is applied to the WECS when the power demand changes. Figure 7.13 and Figure 7.14 show the dynamic responses of WT1 and WT2 respectively. In Figure 7.13, WT1 wind speed is 3.5m/s and C_p has decreased from 0.43 to approximately 0.28. This shift from the MPP results in shaft over-speed, from approximately 7 rad/s to over 11 rad/s (an increase of 57%). The performance of WT2 under this condition is shown in Figure 7.14. Under different wind speed (6 m/s), the same tendency of reducing C_p and power output, and shaft over-speed are observed. The over-speed is not as significant as WT1 with WT2 showing a 37% increase from 19 to 26 rad/s.

The dc link voltage and wind turbine output voltage are shown in Figure 7.15. From Figure 7.15, it can be seen that the dc link voltage can be regulated to 1.2 pu with dc/dc converter voltage control. While the rotor speed increases and the power coefficient C_p decreases, the wind turbines operate away from the MPP, to the right hand side of power characteristic curve.

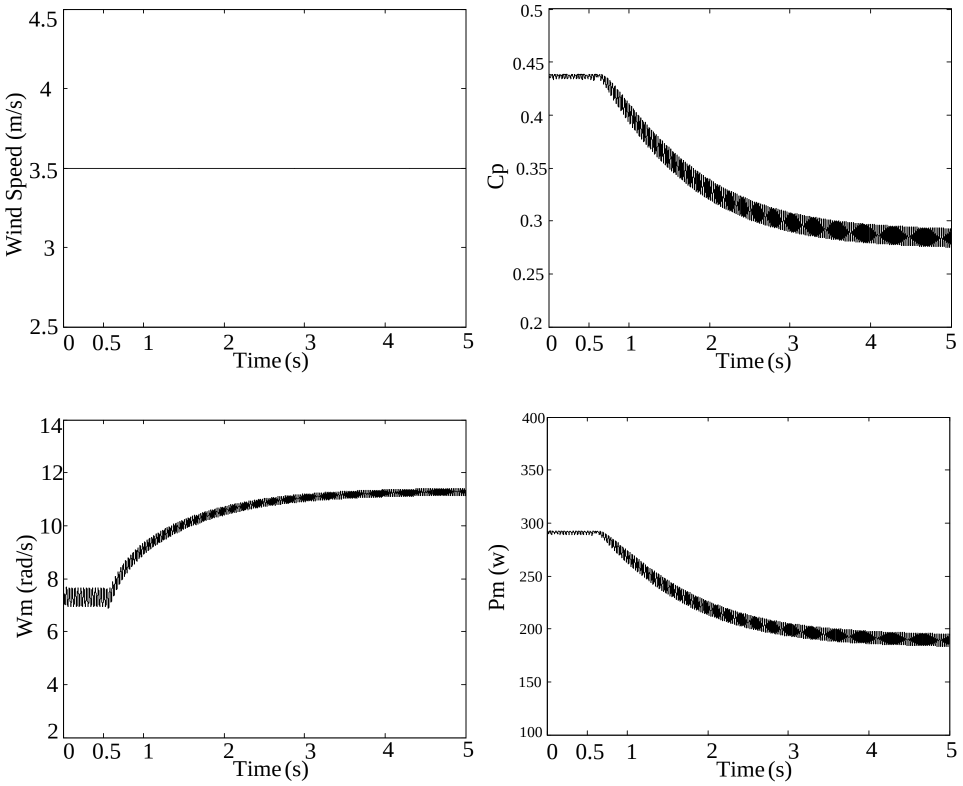

Figure 7.13 Dynamic response of WT1 with dc/dc converter voltage control.

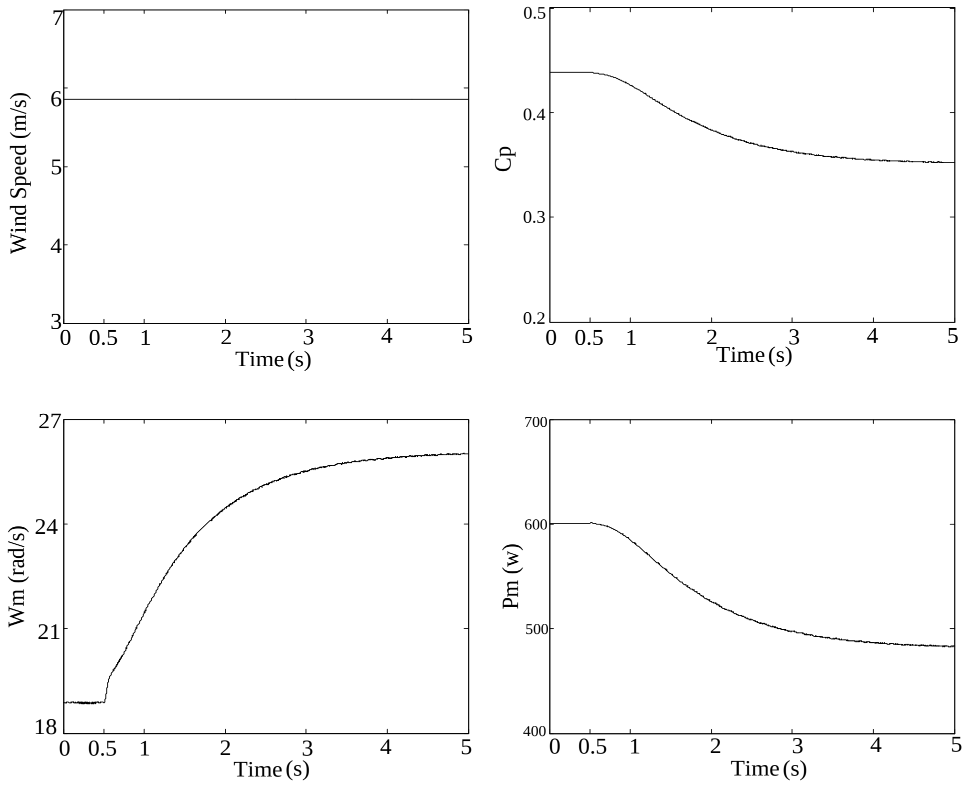

Figure 7.14 Dynamic response of WT2 with dc/dc converter voltage control.

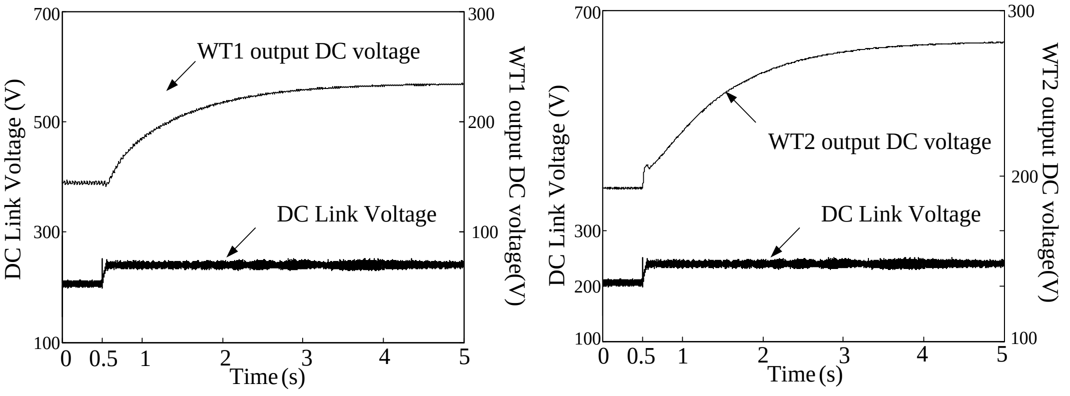

(a) (b)

Figure 7.15 DC link voltage and wind turbine output dc voltage with dc/dc converter voltage control (a) WT1 and (b) WT2.

iii. Case 3: With coordinated control

Although the dc link voltage can be maintain to a safe level with dc/dc converter voltage control, the rotor speed may exceed its limit. Thus both dc chopper dumping control and pitch control should be applied to avoid high rotor speed. Figure 7.16 and Figure 7.17 show the dynamic response of WT1 and WT2 with coordinated control, including power coefficient C_p, rotor speed, mechanical power P_m, and pitch angle. From Figure 7.16 and Figure 7.18, the pitch control is activated at 0.8 s, with the rotor speed limited to 8.2 rad/s, which is comparable with the initial value of 7.2 rad/s

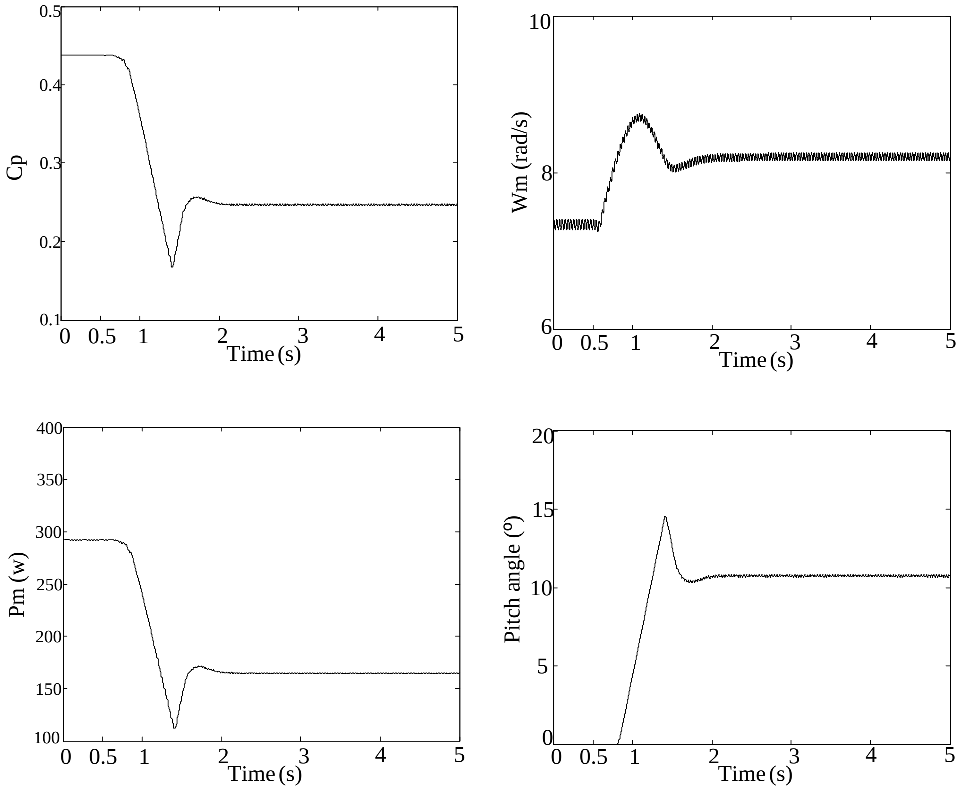

Figure 7.16 Dynamic response of WT1 with the proposed coordinated control.

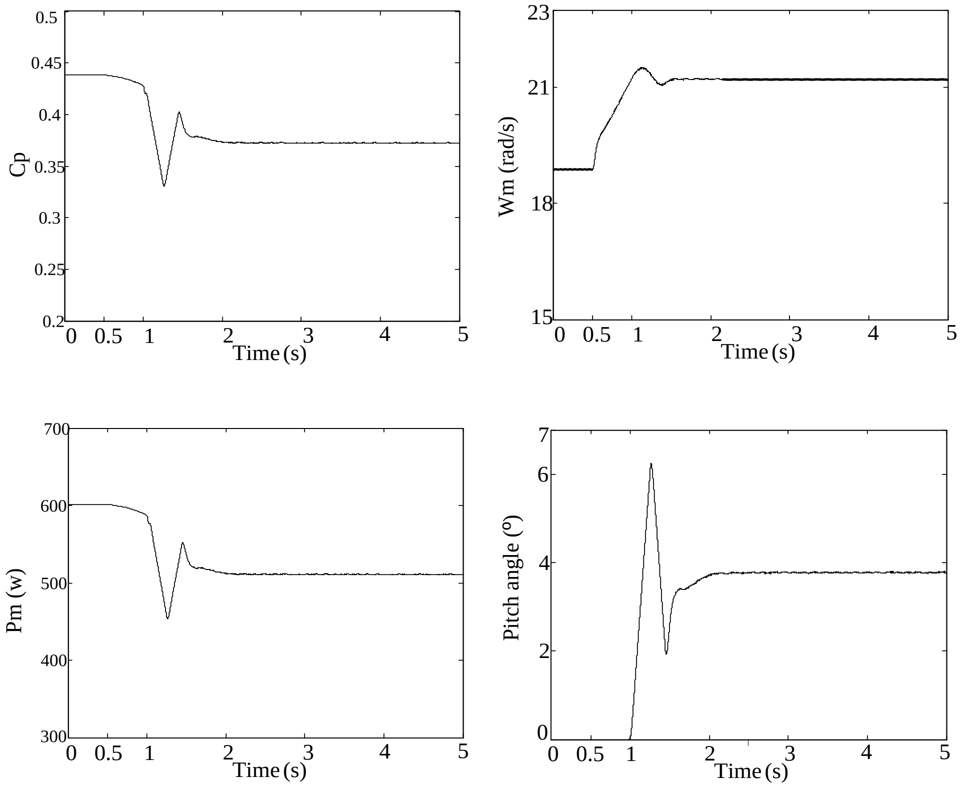

Figure 7.17 Dynamic response of WT2 without the proposed control.

For WT2, from Figure 7.17 and Figure 7.18, the dc link is kept at 1.2 pu, within the safe level. The rotor speed is effectively restrained by dc dumping chopper control and pitch control. The rotor speed after pitch control is 21.2 rad/s, which is comparable with the initial value of 19 rad/s.

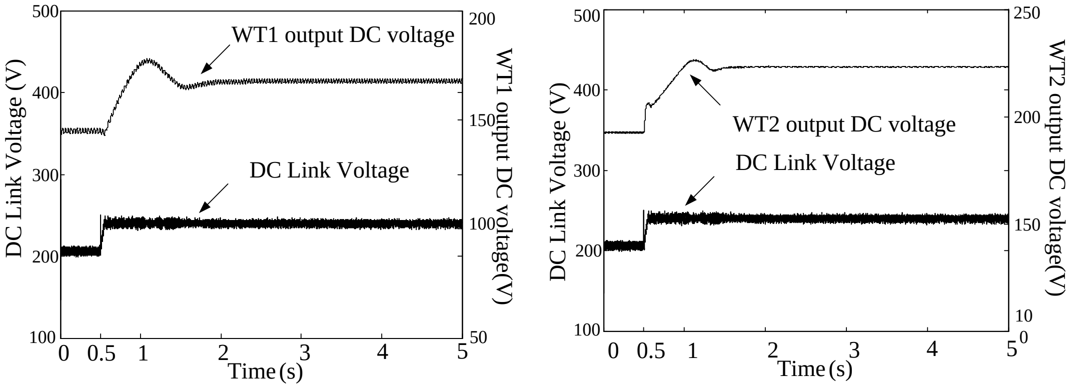

(a) (b)

Figure 7.18 DC link voltage and wind turbine output dc voltage with the proposed coordinated control (a) WT1 (b) WT2.

7.4.2 Experimental results

The experimental system, shown in Appendix B, is used to verify the presented analysis and simulation. The three cases outlined in section 7.4.1 are experimentally investigated. The CSI emulator duty cycle is stepped from 0.5 to 0.9 at 20 s.

i. Case 1: Without the proposed the coordinated control scheme

Figure 7.19 and Figure 7.20 show practical dynamic results for WT1 and WT2 respectively. Wind turbine status is unchanged when the step change of duty cycle occurs. Figure 7.21 shows dc link voltage overshoot at 20s, where it increases from 200V to 275V, exceeding the 1.2pu threshold.

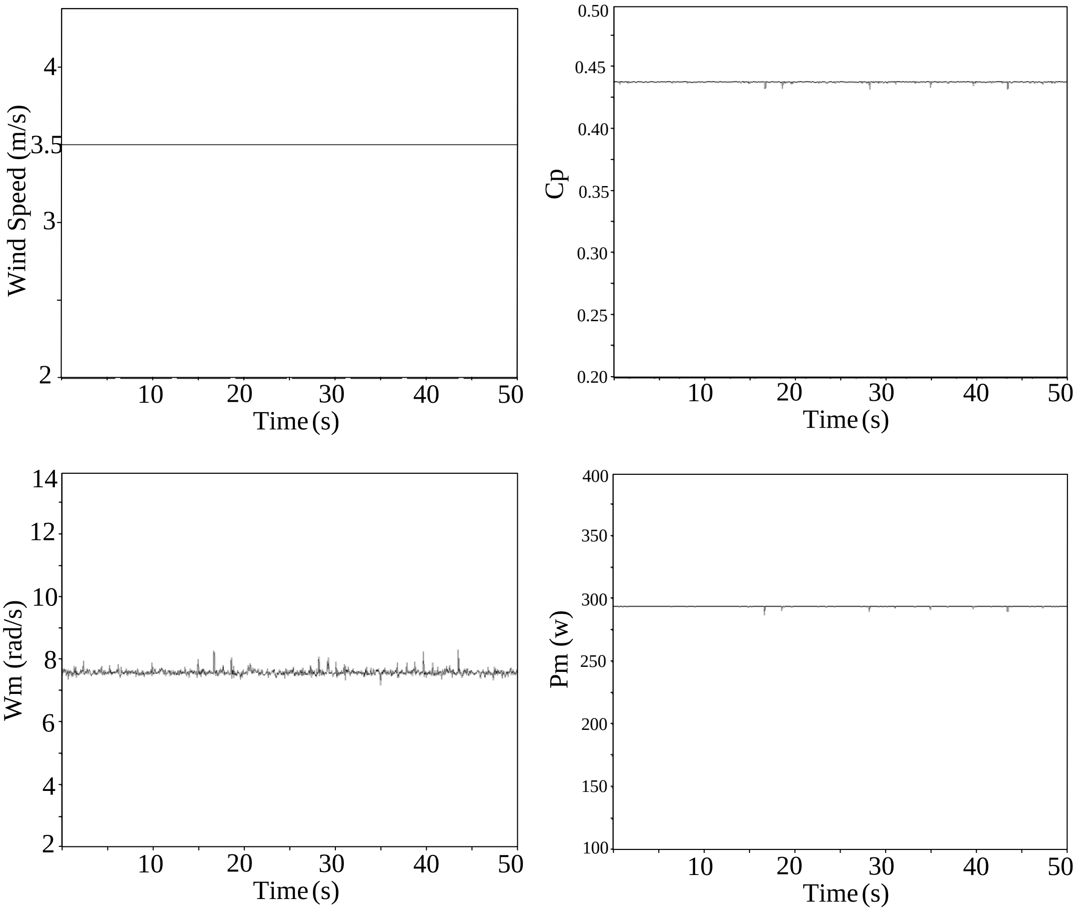

Figure 7.19 Practical dynamic response of WT1 without the proposed control.

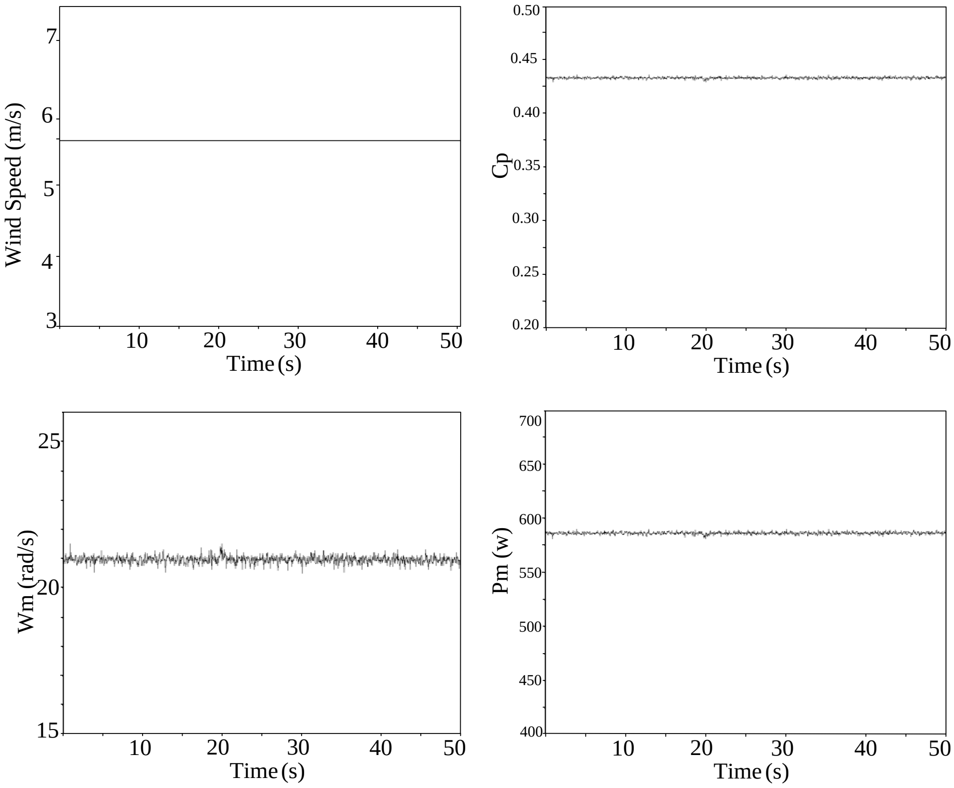

Figure 7.20 Practical dynamic response of WT2 without the proposed control.

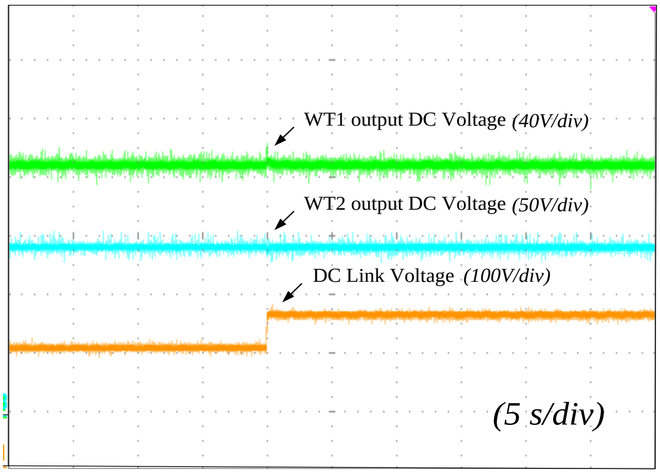

Figure 7.21 Practical dc link voltage and wind turbine output dc voltage without the proposed control.

ii. Case 2: With dc/dc dumping converter voltage control

Figure 7.22 and Figure 7.23 show the practical dynamic response of WT1 and WT2 with dc/dc converter voltage control. The power coefficient and mechanic power are decreased to keep the dc link voltage within a safe level, while the rotor speed increases. In Figure 7.22, WT1 wind speed is 3.5 m/s and C_p decreases from 0.438 to approximately 0.39. This shift from the MPP results in shaft over-speed from approximately 8 rad/s to about 10 rad/s (a 25% increase), thus reducing the power output from WT1 by approximately 40 W. The performance of WT2 under this condition is shown in Figure 7.23. At a different wind speed, 5.82 m/s, the tendency to reduce both C_p and power output with shaft over-speed is seen, although the over-speed is not as significant as for WT1, being from 21 to 25 rad/s.

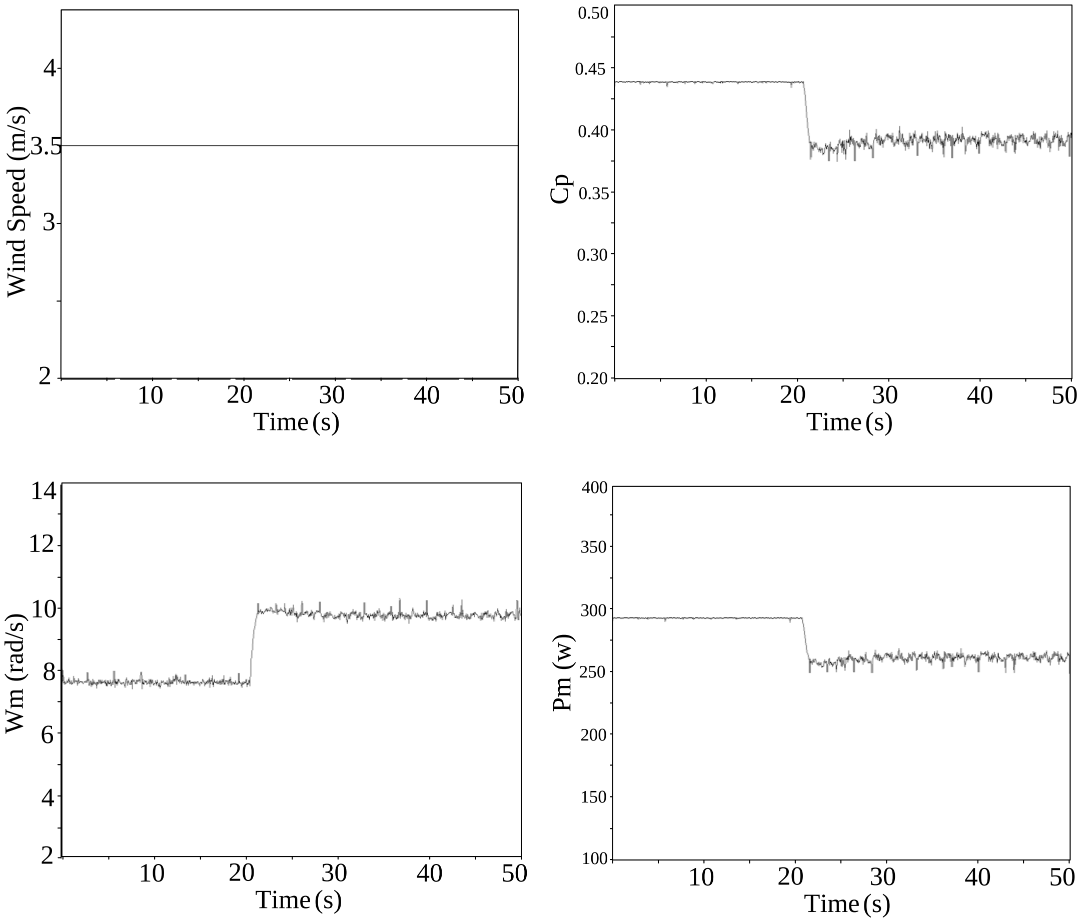

Figure 7.22 Practical dynamic response of WT1 with dc/dc converter voltage control.

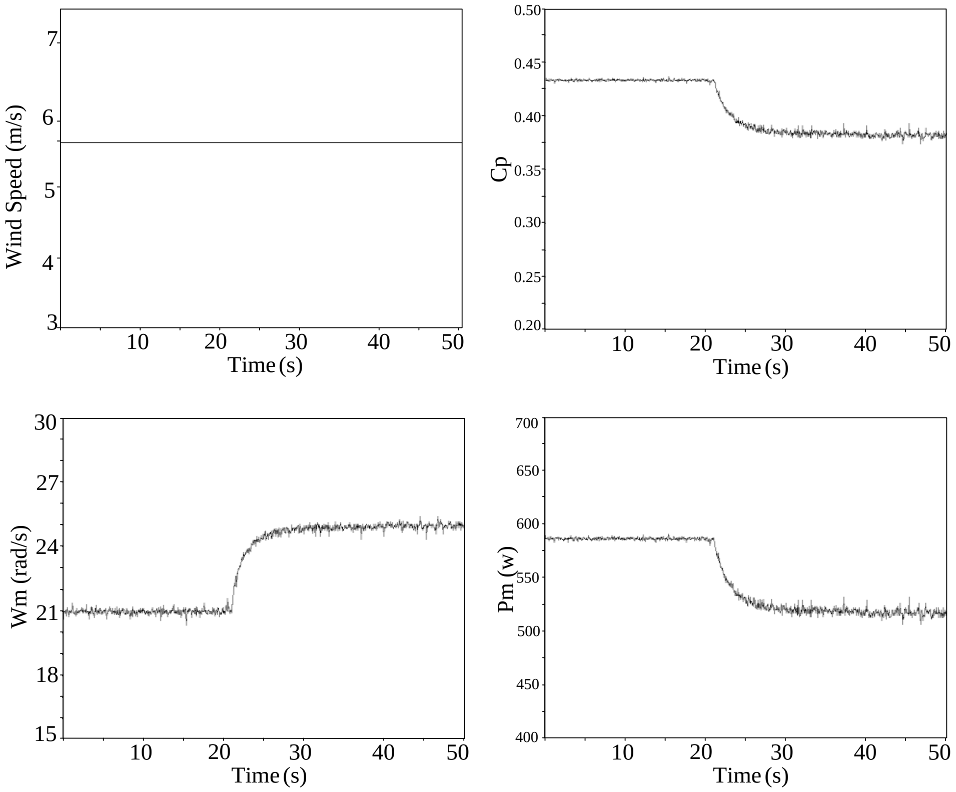

Figure 7.23 Practical dynamic response of WT2 with dc/dc converter voltage control.

Figure 7.24 compares the dc link voltage and wind turbine output dc voltage with and without dc/dc converter voltage control. From Figure 7.24, the dc link voltage can be regulated at 1.2 pu (240 V) with dc/dc converter voltage control. This is less than the 275 V achieved in case 1. The increase in individual output dc voltages is related to turbine over-speed: for WT1, the voltage increase is from 140 V to 181 V and for WT2, the voltage increase is from 170 V to 220 V.

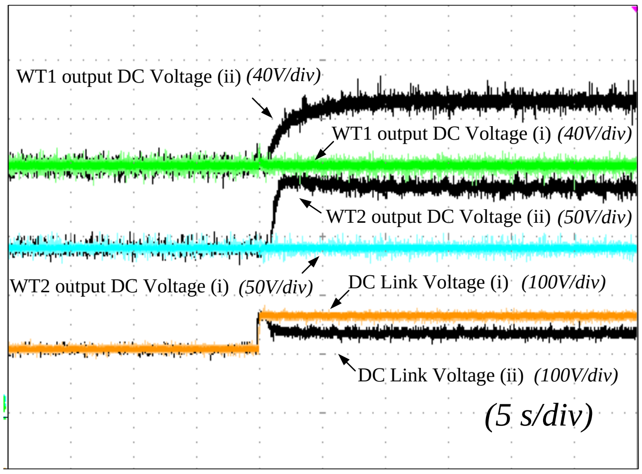

Figure 7.24 Comparison of dc link voltage and wind turbine output dc voltage with and without dc/dc converter voltage control.

iii. Case 3: With coordinated control

The coordinated control scheme is implemented in the WECS with experimental results in Figure 7.25 and Figure 7.26 showing the practical dynamic response of WT1 and WT2. The dc link voltage and wind turbine output voltage with dc/dc converter voltage control and with the proposed coordinated control is shown in Figure 7.27.

In Figure 7.25, the pitch angle is increased from 0 to approximately 8 degrees. The C_p is further reduced to approximately 0.3 compared with approximately 0.39 previously. After approximately 10 s of fluctuation, the shaft speed settles approximately 8.5 rad/s, which is within the 1.2 pu limit.

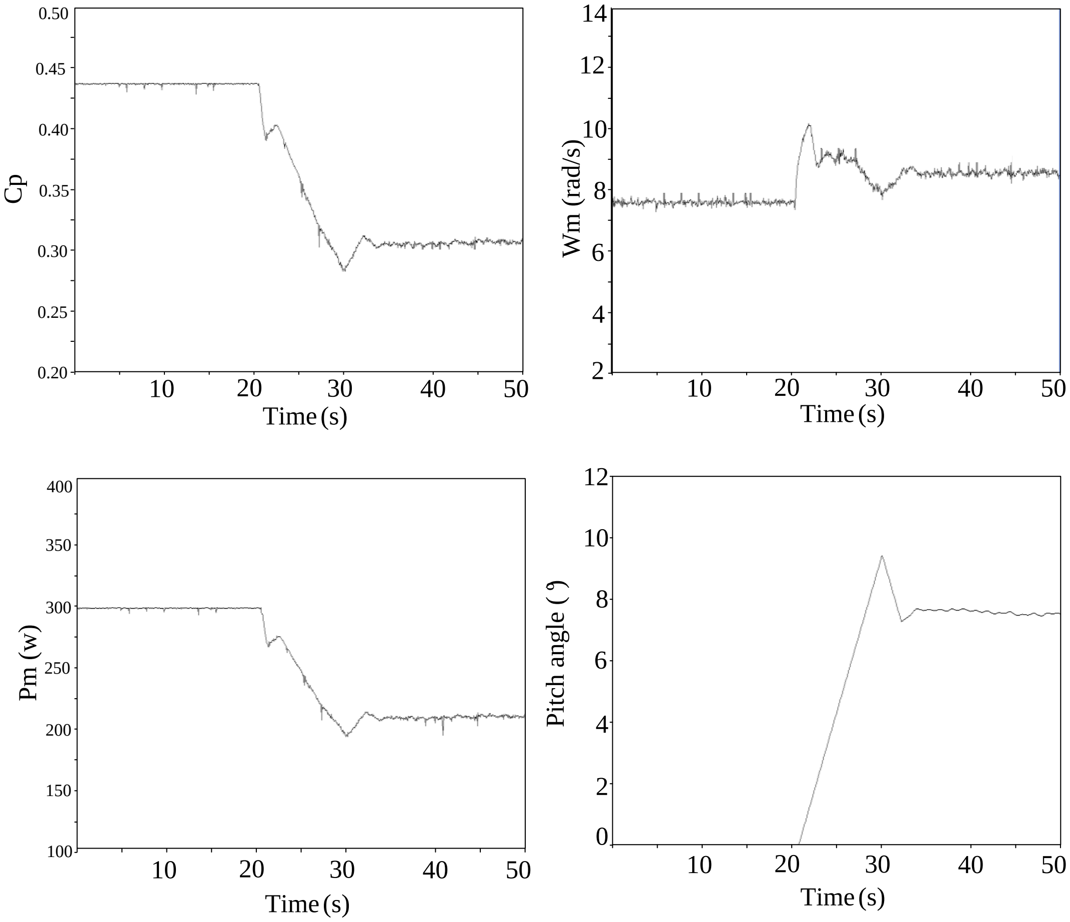

Figure 7.25 Practical dynamic response of WT1 with the proposed control.

Again the same tendency is seen in Figure 7.26 for WT2, but is not as serious as for WT1. This is why the pitch angle had been adjusted back to zero by the pitch control. The WT2 shaft speed finally steadies at 23 rad/s, well within the threshold compared with its original value of 21 rad/s.

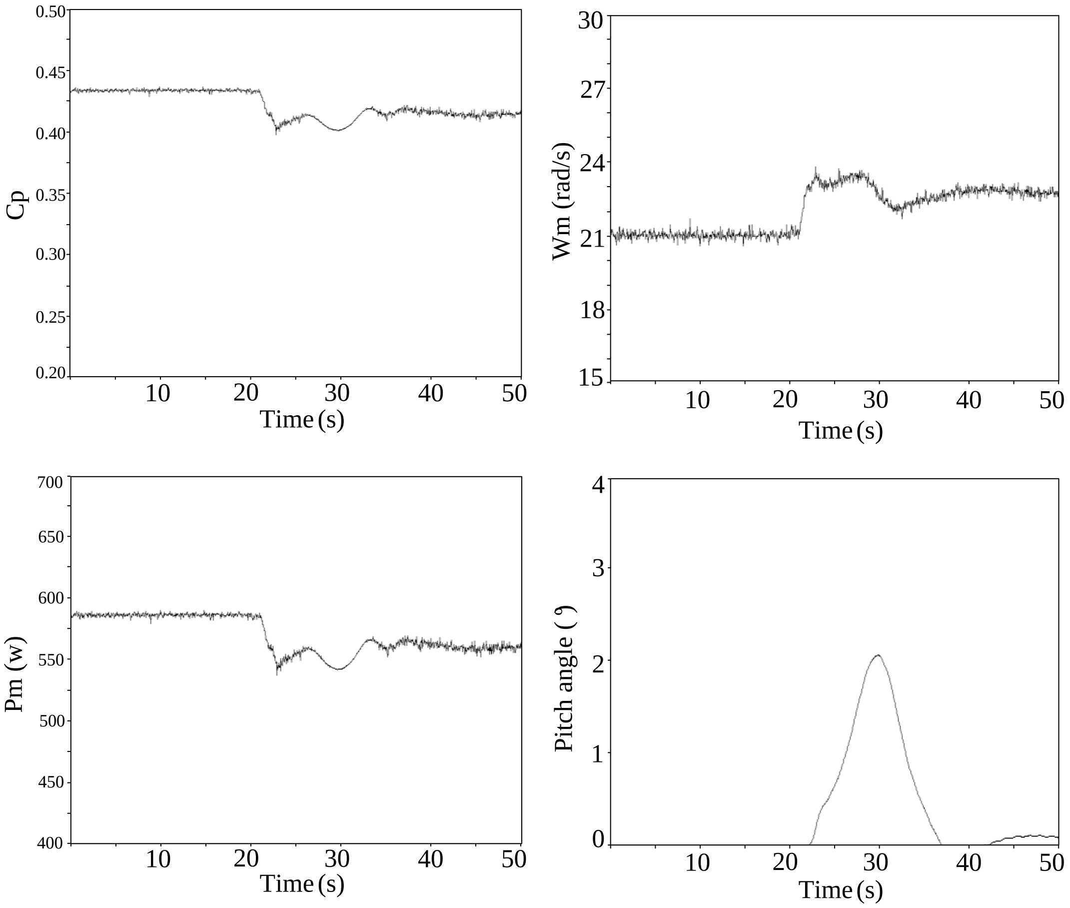

Figure 7.26 Practical dynamic response of WT2 with the proposed coordinated control.

The dc output voltages of WT1 and WT2 are shown in Figure 7.27. The dc link voltages for cases 2 and 3 are also shown, and as expected they show effectively limiting to around 240V.

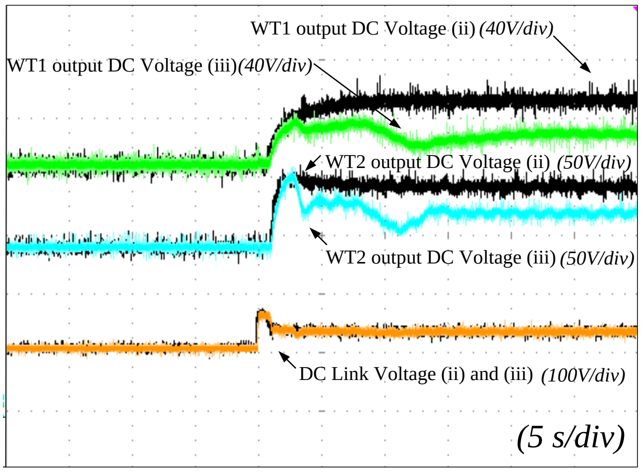

Figure 7.27 Compared dc link voltage and wind turbine output dc voltage with dc/dc converter voltage control and with the proposed control.

7.5 Summary

This chapter considers protection aspects of proposed WECS system under grid power demand changes. During demand changes (simulated by CSI duty cycle adjustment), the dc-link voltage and individual wind turbine shaft over speeds are identified as the critical aspects of the system. With dc/dc converter voltage control, the dc link voltage is effectively limited to a pre-set threshold value which is important for the continuity of wind power supply to the grid. This quick response to electrical stress limiting is effective before any slower mechanical stresses can be seen at the turbine side. To solve the problem, a combined de-loading control scheme is proposed for this multi-terminal dc WECS. It basically combines dc/dc converter control, dc dumping chopper control, and turbine pitch control. To be more specific, the dc energy dumping chopper is used for transition control response to electrical stress, in order to allow time for shaft speed control to be realised by adjusting pitch angles. Simulation and experimental results have been analysed, and confirm the validity of the proposed de-loading control scheme.

References

[7.1] J. Morren, S. W. H. de Haan, W. L. Kling, and J. A. Ferreira, "Wind turbines emulating inertia and supporting primary frequency control," *Power Systems, IEEE Transactions on*, Vol. 21, No. 1, pp. 433-434, 2006.

[7.2] X. Zhu, Y. Wang, L. Xu, X. Zhang, and H. Li, "Virtual inertia control of DFIG-based wind turbines for dynamic grid frequency support," *Renewable Power Generation (RPG 2011), IET Conference on*, 2011, pp. 1-6.

[7.3] S. Schafstall, "Frequency control capability of ABB combined-cycle gas turbine power plants," *Frequency Control Capability of Generating Plant, IEE Colloquium on*, 1995, pp. 7/1-7/8.

[7.4] M. Diesendorf, *Greenhouse solutions with sustainable energy*: University of New South Wales Press, 2007.

[7.5] S. Yuan-zhang, Z. Zhao-sui, L. Guo-jie, and L. Jin, "Review on frequency control of power systems with wind power penetration," *Power System Technology (POWERCON), 2010 International Conference on*, 2010, pp. 1-8.

[7.6] N. A. Janssens, G. Lambin, and N. Bragard, "Active Power Control Strategies of DFIG Wind Turbines," *Power Tech, 2007 IEEE Lausanne*, 2007, pp. 516-521.

[7.7] E. Muljadi and C. P. Butterfield, "Pitch-controlled variable-speed wind turbine generation," *Industry Applications, IEEE Transactions on*, Vol. 37, No. 1, pp. 240-246, 2001.

[7.8] T. Senjyu, R. Sakamoto, N. Urasaki, T. Funabashi, and H. Sekine, "Output power leveling of wind farm using pitch angle control with fuzzy neural network," *Power Engineering Society General Meeting, 2006. IEEE*, 2006, p. 8 pp.

[7.9] F. A. Bhuiyan and A. Yazdani, "Multimode Control of a DFIG-Based Wind-Power Unit for Remote Applications," *Power Delivery, IEEE Transactions on*, Vol. 24, No. 4, pp. 2079-2089, 2009.

[7.10] A. Joseph and M. Shahidehpour, "Battery storage systems in electric power systems," *Power Engineering Society General Meeting, 2006. IEEE,* 2006, p. 8 pp.

[7.11] Z. Lubosny and J. W. Bialek, "Supervisory Control of a Wind Farm," *Power Systems, IEEE Transactions on,* Vol. 22, No. 3, pp. 985-994, 2007.

[7.12] G. Ramtharan, J. B. Ekanayake, and N. Jenkins, "Frequency support from doubly fed induction generator wind turbines," *Renewable Power Generation, IET,* Vol. 1, No. 1, pp. 3-9, 2007.

[7.13] M. Zhixin, F. Lingling, D. Osborn, and S. Yuvarajan, "Wind Farms With HVDC Delivery in Inertial Response and Primary Frequency Control," *Energy Conversion, IEEE Transactions on,* Vol. 25, No. 4, pp. 1171-1178, 2010.

[7.14] M. H. Ali and W. Bin, "Comparison of Stabilization Methods for Fixed-Speed Wind Generator Systems," *Power Delivery, IEEE Transactions on,* Vol. 25, No. 1, pp. 323-331, 2010.

[7.15] E. Valsera-Naranjo, A. Sumper, O. Gomis-Bellmunt, A. Junyent-Ferré, and M. Martínez-Rojas, "Pitch control system design to improve frequency response capability of fixed-speed wind turbine systems," *European Transactions on Electrical Power,* Vol. 21, No. 7, pp. 1984-2006, 2011.

[7.16] S. K. Chaudhary, R. Teodorescu, P. Rodriguez, and P. C. Kjar, "Chopper controlled resistors in VSC-HVDC transmission for WPP with full-scale converters," in *Sustainable Alternative Energy (SAE), 2009 IEEE PES/IAS Conference,* 2009, pp. 1-8.

[7.17] C. Feltes, H. Wrede, F. W. Koch, and I. Erlich, "Enhanced Fault Ride-Through Method for Wind Farms Connected to the Grid Through VSC-Based HVDC Transmission," *Power Systems, IEEE Transactions on,* Vol. 24, No. 3, pp. 1537-1546, 2009.

Chapter 8

Conclusions

8.1 General conclusion

Wind energy is receiving continually increasing attention as an alternative renewable energy source. The characteristics of wind energy and the collection and transmission technologies for wind farms are discussed in chapters one and two.

Chapter three investigates a variable speed wind energy conversion system based on the boost converter. The boost converter is used to step up the voltage and track the turbine maximum power point, while a diode rectifier is used as an ac/dc stage between the generator and boost converter. An ac/dc rectifier is used due to its low cost and high reliability in low power applications. A voltage source inverter is used for grid connection. Several MPPT methods are illustrated and compared, highlighting their advantages and disadvantages. One-power-point maximum power tracking is preferable due to its ease of implementation and fast tracking ability, while the power coefficient C_p deteriorates during wind speed drops. An optimized one-power-point method for maximum power tracking is proposed for the variable speed WECS, which incorporates OPP control and MPDC control. Also there is no need for extra sensors, which reduces system costs. A higher energy conversion efficiency is achieved by the optimized OPP method.

Chapter four investigates another wind energy conversion system based on the current source full-bridge dc/dc converter. The current source inverter is applied in the WECS. A wind turbine simulator is constructed with a vector controlled induction machine and a gearbox coupled PMSG, thereby emulating real wind turbine characteristics using DSP control. A full-bridge converter is used to step the low generator voltage to a high level via an intermediate high frequency transformer. A comparative study between the boost converter and the full-bridge converter was undertaken with regard to average and peak currents in the switching devices during wind speed changes. Compared to the full-bridge converter, the transfomerless boost converter cannot achieve high gain due to practical component characteristics and high output diode current. New modified OPP control is presented for WECS. The reference current is obtained according to the input voltage. Finally, the performance of the complete WECS is investigated with a step wind speed, both in simulation and experimentally.

In Chapter five, resonant converters are investigated in the WECS, including the series-resonant converter, parallel-resonant converter, and a combination series-parallel resonant converter. The dc gain characteristics and topologies of the three are compared. The series-parallel LCC resonant converter is chosen for WECS due to its high DC gain at low load, and it has a current source output. It is compared with the hard-switched FB converter in terms of switch stress, efficiency, etc. at the MPP with different wind speeds. The LCC converter design includes resonant tank design, switch power rating and passive component output inductor design. The LCC resonant converter efficiency is analysed. The test rig of the WECS based resonant converter is used to verify its MPPT ability and stability during step wind speed changes.

Chapter six proposes a current source dc/dc converter based multi-terminal dc WECS. Each wind turbine and its dc/dc converter act as an independent dc current source. A current source converter is used for grid connection due to dc current source feeding properties. Series and parallel connected dc wind farms are illustrated and their features are highlighted. Although the series connection configuration can step up the voltage without transformers, it is problematic to incorporate or remove wind turbine units during system operation. Also there is no electrical isolation between the generator side and the dc network. Compared to the series connected dc wind farm, the parallel dc current source connection is preferable due to wind turbine units' independence of operation. The proposed WECS is based on a star connection. The common current source inverter is applied with a voltage control loop, and the current source dc/dc converter is used to track the MPP. Three cases with proposed WECS are studied, which involve a wind speed change applied to one and then both wind turbines, and shutdown of one wind turbine.

A coordinated control scheme is proposed for the current source converter based dc wind energy conversion system. The scheme decreases the wind turbine output power in order to limit the dc link voltage to a safe level. It combines dc/dc converter control, dc dumping chopper control, and pitch control. The dc chopper is used to absorb (dissipate) the surplus energy quickly to allow time for slow pitch control to become effective. As the pitch control becomes effective, the dc dumping chopper is de-energised. The performance of the coordinated control for the WECS was investigated and discussed.

8.2 Author's contribution

The thesis contributions can be summarized as follows:

- An optimized One-Power-Point method for maximum power tracking is proposed for a variable speed wind energy conversion system that uses a boost converter. The energy conversion efficiency is compared between the proposed optimized OPP and standard OPP.
- Wind turbine emulator systems based on a three-phase PMSG and a novel five-phase PMSG were constructed and commissioned. The control process is presented.
- A current source based hard-switched H-Bridge converter with an intermediate high frequency transformer is proposed for WECS. The semiconductor electrical

stresses are analysed and compared between hard-switched converter and boost converter which are both used in variable speed WECS.

- A series parallel resonant LCC converter is proposed as an interface to a wind energy electrical source. The LCC converter and the hard-switched FB converter are compared in terms of switch stress, efficiency, etc. The unique feature of increased gain at reducing loads allows for an optimally designed transformer.
- The design procedures and analysis of the series-parallel resonant converter based on MPPT and FMA are presented
- A new modified OPP control method is presented for the hard-switched H-bridge converter and LCC converter. It is based on the relationship between voltage and current at the MPP. Fast tracking speed is achieved by incorporating a PI controller.
- A current source dc/dc converter based multi-terminal dc WECS is proposed. The current source inverter with gate turn off components operates in an input voltage mode due to parallel connection. A practical multi-terminal DC WECS based on two wind turbine units achieved dc parallel operation.
- A coordinated control scheme for multi-terminal dc WECS is proposed to cater for grid power demand changes. A sequence of control schemes are presented, namely dc/dc converter voltage control, dc dumping chopper control, and pitch control. The dc dumping chopper is used for transitional control to respond to electrical stress in order to allow time for shaft speed control to be realised by adjusting blade pitch angles.

8.3 Suggestions for future research

Several types of dc/dc converters have been investigated in this research for the WECS. A current source dc/dc converter based multi-terminal dc prototype WECS now exists. Suggestions for future research are:

- The other control methods during normal and abnormal operating conditions of the dc grid wind farm can be assessed and applied with the multi-terminal dc prototype WECS. This could include using only one dumping chopper, on the dc link side which would serve to load all the turbines, and simultaneously adding protection for the dc link to grid side faults.

- A mathematic model of the proposed current source based multi-terminal WECS is required in order to verify WECS stability and to allow assessment of ac grid side and dc link faults.
- A full detailed comparative analysis between current source based and voltage source based multi-terminal DC WECS can be investigated in terms of components stress, system efficiency, and fault condition.

Appendices

Details of the practical implementation are shown in the appendices. The design processes for passive components such as ac inductors, dc filters and power transformers are presented. The test rig for the current source dc/dc converter based multi-terminal dc wind energy conversion system, including hardware components and software programmes, is presented in detail. Lists of figures and tables, as well as the author’s publications, are also included.

Appendix A Passive component hardware design

A.1 AC resonant inductor design

An inductor is used as the energy storage device in a switched-mode power supply. Design considerations for inductors vary depending on the type of circuit application, operating frequency, and temperature rise. The most important limiting factors in inductor design involve core saturation, temperature rise and efficiency considerations arising from core losses and ac and dc winding losses. The inductor used in the resonant tank of the LCC resonant converter is an ac inductor. Table A.1 shows the ac inductor specification.

Table A.1 ac inductor specification

Required inductance	493.7µH
dc current	0A
ac ripple current	35 A peak-peak
ac rms current	12.4 A
Frequency	40 kHz
Max Temperature Rise	80 ℃
Cooling method	Natural convection

i. Core selection

The selection of core material must take into consideration operating switching frequency, operating flux density, the resulting core loss, and temperature of operation. Temperature rise above ambient is a direct result of core losses and copper losses in the windings. In order to limit the temperature rise due to core losses, the operating flux density at the specified switching frequency should be limited. Applicable types of core materials are powder core and ferrite core. Powder type material has a high permeability but high core loss at high frequency, while ferrite material has lower losses at high frequency. For an ac current inductor, the core is loss limited, thus ferrite core (magnetic type P) is the preferred choice. For ferrite cores, a saturation limited flux density B_{max} of 0.3T will be used. The maximum flux density and maximum flux swing at which the core will operate should be below the B_{max}. The core saturation limit will correspond to the B_{max} limit when the peak current is equal to the short-circuit limit value. The maximum peak-peak flux density swing corresponding to the maximum current ripple will then be:

$$\Delta B_{MAX} = B_{MAX}\frac{\Delta I_{PP}}{I_{SCpk}} \tag{A.1}$$

where I_{SCpk} is the maximum peak short-circuit current (A).

For a unipolar flux swing, the calculated ΔB_{MAX} is divided by 2 to convert from peak-peak flux density to peak flux density: this value is used with the core loss curve of Figure A.2 on the ‘flux density’ (peak flux density) axis. From the ripple frequency curve, the resulting core loss is found. If the core loss is significantly less than 100mW/cm^3, the core is likely to be saturation limited, and the calculated ΔB_{MAX} value is likely to be valid. If, however, the indicated core loss is much greater than 100mW/cm^3, the core is likely to be loss limited. ΔB_{MAX} must then be reduced to achieve an acceptable core loss. If the core is loss limited, peak flux density at I_{SCpk} will be less than B_{MAX}.

For an ac current inductor, the core is loss limited. According to Figure A.2, when B_{MAX} = 0.2T, core loss is approximately 100mW/cm^3 on the 40kHz ripple frequency curve. ΔB_{MAX} is also 0.2T.

ii. Core size and air gap

After the core material is determined, the core size is determined. The following area product formulae (A.2 and A.3) are intended to provide an initial estimate of core size for inductor applications.

When core loss is not severe, the flux swing is limited by core saturation:

$$AP = A_W A_E = \left(\frac{LI_{SCpk}}{B_{MAX}} \cdot \frac{I_{FL}}{K_1}\right)^{4/3} \ cm^2 \tag{A.2}$$

When flux swing is limited by core loss:

$$AP = A_W A_E = \left(\frac{L\Delta I}{\Delta B_{MAX}} \cdot \frac{I_{FL}}{K_2}\right)^{4/3} cm^2 \qquad \text{(A.3)}$$

where:

L= inductance, H

I_{SCpk}= maximum pk short-circuit current, A

B_{MAX}= saturation limited flux density, T

ΔI= current swing, A

ΔB_{MAX}= maximum flux density swing, T

I_{FL}= rms current, full load (primary), A

$K_1, K_2 = J_{MAX} K_{PRI} \times 10^{-4}$

where:

J_{MAX} = max current density, A/cm^2

K_{PRI}= primary copper area/window area

10^{-4}= converts dimensions from metres

The core loss limited formula, equation (A.3), is used. A 9920UC (p type) core size, shown in Figure A.3, is used where AP=5.6cm^2×(6.3×7×2)cm^2 = 494cm^4, and core surface area A_{core} = 483.84cm^2. Core volume V_e=268.8 cm^3.

The number of turns that will provide the desired inductance is calculated as:

$$N = \frac{L\Delta I_{MAX}}{\Delta B_{MAX} A_E} \times 10^{-2} = \frac{493.7 \times 17.5}{0.2 \times 5.6} \times 10^{-2} = 78\ turns \qquad \text{(A.4)}$$

where L is in μH and dimensions are in cm.

Then the gap length to achieve the required inductance is:

For a rectangle:

$$l_g = \mu_0 N^2 \frac{A_g}{L} \times 10^4 \tag{A.5}$$

For a circle:

$$l_g = \mu_0 N^2 \frac{A_e}{L}\left(1 + \frac{l_g}{D_{CP}}\right)^2 \times 10^4 \tag{A.6}$$

Thus, from (A.5)

$$l_g = \mu_0 N^2 \frac{A_g}{L} \times 10^4 = 4\pi \times 10^{-7} \times 78^2 \times \frac{5.6}{493.7} \times 10^4 = 0.87\text{cm} \tag{A.7}$$

iii. Calculate the conductor size, winding resistance, losses and temperature rise

With a current density of 4 A/mm^2, the full-load current requires a conductor area of 3.1 mm^2, giving a conductor diameter d_{wire} of 1.99 mm. Skin effect should be considered: it causes a reduction in the effective cross-section of the conductor at higher frequencies and results in an increase in conductor resistance. Skin depth is defined as the distance from the surface of the conductor to the depth where the current density is 1/e times the surface current density. Equation (A.8) calculates the skin depth, d_{open}, in copper at 40 kHz.

$$d_{open} = \sqrt{\frac{2}{2\times\pi\times40\times10^3\times\mu_0\times\delta_e}} = 0.375mm \tag{A.8}$$

From equation (A.8), at 40kHz in copper, d_{open} = 0.375 mm. The diameter of the copper wire used to wind the inductor should therefore be chosen to be less than $2d_{open}$. Eight strands of SWG 22 copper enamel wire are selected, with diameter d_{SWG22}=0.71mm and cross sectional area S_{SWG22}=0.4mm^2.

The number of layers can be calculated as:

$$N_{Layer} = \frac{8\times d'\times N}{l_e} = \frac{8\times0.71\times78}{480} = 0.92 \tag{A.9}$$

where l_e is core path length.

The layer thickness/d_{open}:

$$Q = \frac{0.83\times d\times\sqrt{d/d'}}{d_{open}} = \frac{0.83\times0.70\times\sqrt{0.70/0.71}}{0.375} = 1.54 \tag{A.10}$$

where d is diameter of conductor and *d'* is external diameter including insulation.

Figure A.1 shows Dowell's curves, which plot the ratio of R_{ac}/R_{dc} versus Q (layer thickness/d_{open}) for different numbers of layers in each winding section. Using Dowell's curves with 1 layer and Q=1.54, R_{ac}/R_{dc} is approximately 1.5.

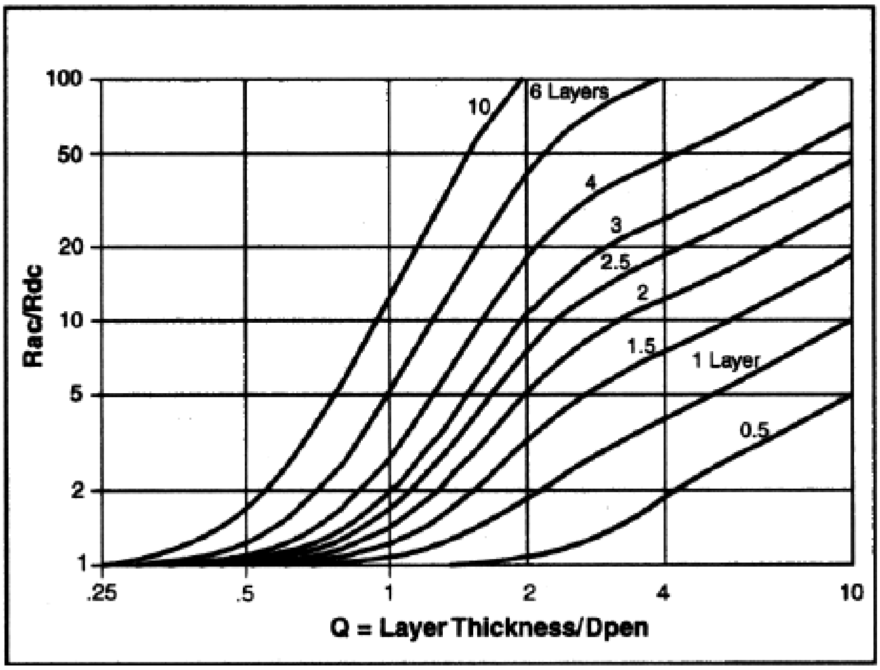

Figure A.1 Dowell's Curves.

DC resistance for SWG 22 is 42Ω/km. The dc winding resistance can therefore be calculated as:

$$R_{dc} = L \times \frac{R}{8} = \frac{42\times10^{-6}\times78\ turns\times(28+20)\times2}{8} = 0.04\,\Omega \qquad \text{(A.11)}$$

Thus the ac winding resistance can be obtained according the value of R_{ac}/R_{dc} from Figure A.1, Dowell's curve.

Using this result, and Figure A.2, the ac and dc winding losses can be expressed as, respectively:

$$P_{dc} = I^2R_{dc}=12.3^2\times0.04=6\text{ W} \qquad \text{(A.12)}$$

$$P_{ac} = I^2R_{ac}=12.3^2\times0.04\times1.5=9\text{ W} \qquad \text{(A.13)}$$

$$P_{core} = P_L \times V_e = 100\,\frac{mW}{cm^3} \times 268.8\,cm^3 = 26.88\,W \qquad \text{(A.14)}$$

The total losses are sum of core loss and ac and dc winding losses.

$$P_T = P_{core} + P_{ac} + P_{dc}\text{=6W+9W+26.88W=42 W} \tag{A.15}$$

The temperature rise is related to the total losses and core surface area, and estimated from:

$$\Delta T = 450 \times \left(\frac{P_T}{A_{CORE}}\right)^{0.826} = 450\left(\frac{42}{483.84}\right)^{0.826} = 59°C \tag{A.16}$$

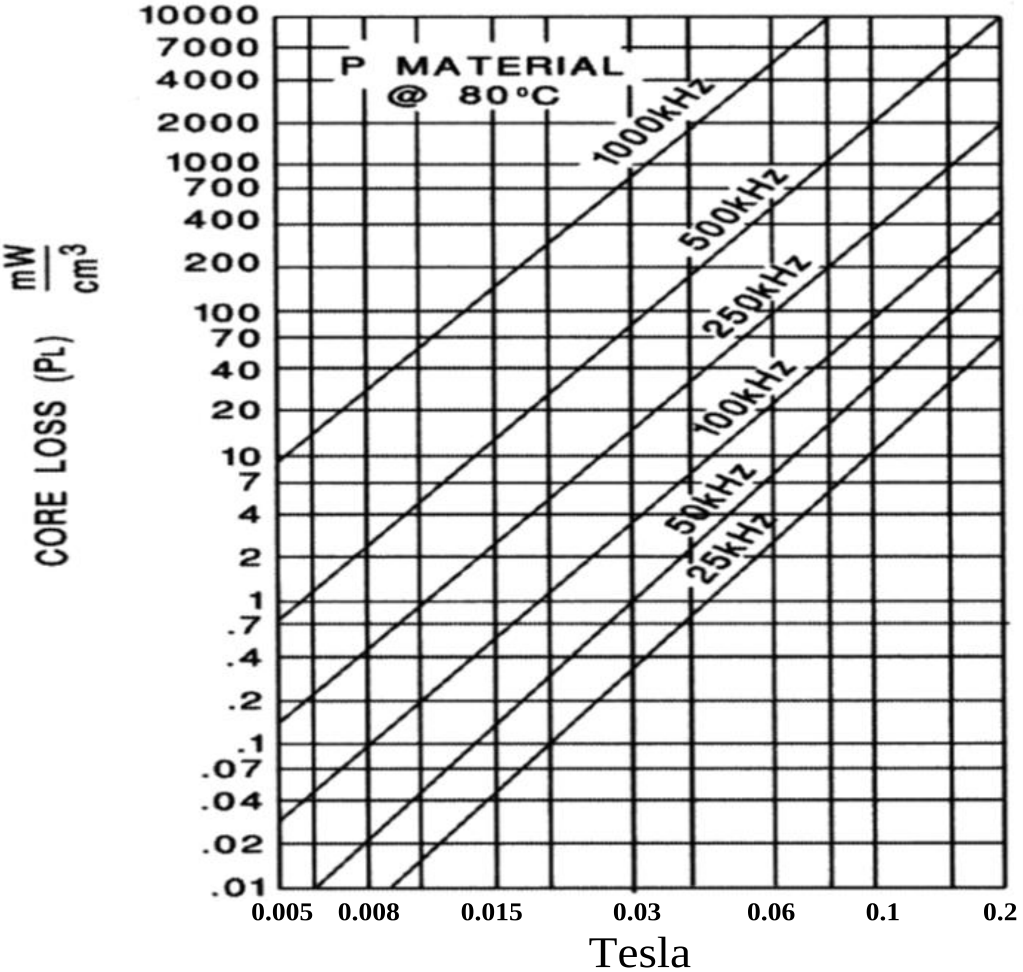

Figure A.2 Core loss versus flux density curve for Ferrite core.

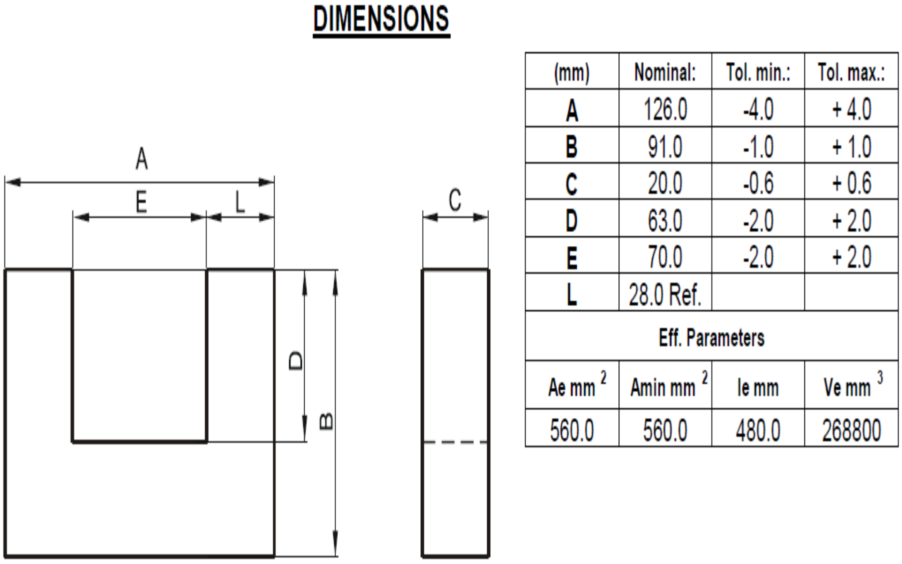

(mm)	Nominal:	Tol. min.:	Tol. max.:
A	126.0	-4.0	+ 4.0
B	91.0	-1.0	+ 1.0
C	20.0	-0.6	+ 0.6
D	63.0	-2.0	+ 2.0
E	70.0	-2.0	+ 2.0
L	28.0 Ref.		

Eff. Parameters

Ae mm ^{2}	Amin mm ^{2}	le mm	Ve mm ^{3}
560.0	560.0	480.0	268800

Figure A.3 U26 core dimensions.

A.2 DC filtering inductor design

i. Core selection

The dc filtering inductor is used in the output LC filter to reduce current ripple levels. The inductor design must meet the energy storage (inductance) requirement as well as requirements for total loss, space, cost, EMI, fault-tolerance, temperature performance, and reliability. For the dc filtering inductor, the core is saturation limited since the core loss caused by the peak-peak flux density swing is limited by the current ripple. Power inductors require an air gap within the core structure. The air gap is used to store the energy and prevent the core from saturating with high current. Air gaps may be discrete or distributed. Discrete gaps are most commonly used in ferrite cores. The main performance advantage of ferrite is low ac core loss at high frequency, due to the high resistivity of the ceramic material, when compared with metal alloys. Ferrites have low saturation flux density, which reduces significantly with increasing temperature. The discrete gap structure results in an inductor that reaches a sharp saturation point, which must be allowed for in the design. Also, inductors with discrete gaps are vulnerable to eddy current losses in the coil due to fringing. The nature of powder core materials, such as MPP, High Flux, Kool Mu, and Iron powder, is that they have distributed air gaps throughout the material. Powder cores with distributed gaps can eliminate the disadvantages of the discrete gap structure, such as sharp saturation, fringing loss, and EMI. Each of the aforementioned powder materials has its own advantages and disadvantages. The properties of these materials are summarised in Table A.2:

Table A.2 Properties of various core materials.

	MPP	High Flux	Kool Mu	XFlux
Permeability	14-550	14-160	26-125	60
Core Loss	Lowest	Moderate	Low	Moderate
Permeability versus dc bias	Better	Best	Good	Best
Saturation (B_{sat})	7.5 Kilogauss	15 Kilogauss	10.5 Kilogauss	16 Kilogauss
Nickel Content	80%	50%	0%	0%
Relative Cost	High	Medium	Low	Low

For the dc inductor, the Kool Mu material is a suitable choice, having low core loss, excellent performance over a wide temperature range and low cost. Table A.3 shows the dc inductor specification for the output filter of the converter.

Table A.3 DC inductor specification.

Inductance	4mH
Full load current	5A
Max ripple current	0.5A
Switching frequency	40kHz
Cooling Method	Natural convection

ii. Core size and winding turns

Core size can be determined by the product of LI^2, where L is inductance required with dc bias (millihenrys) and I is dc current.

A U6527 type core was available. From the Core Selector Table shown in Figure A., it can be seen that this is compatible with the LI^2 value calculated using the data shown in Table A.3.

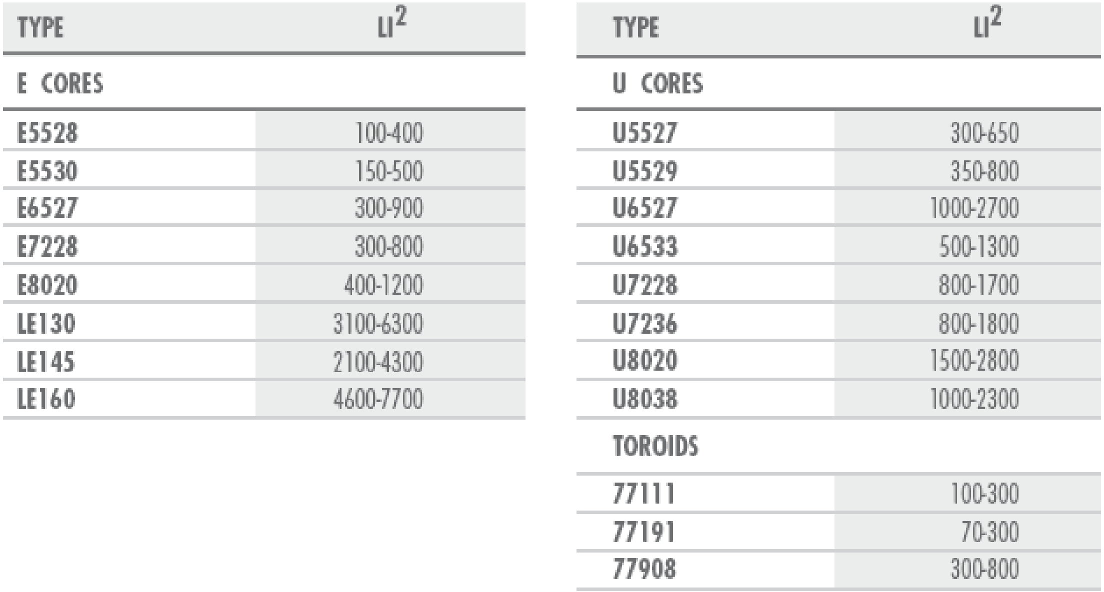

TYPE	LI²
E CORES	
E5528	100-400
E5530	150-500
E6527	300-900
E7228	300-800
E8020	400-1200
LE130	3100-6300
LE145	2100-4300
LE160	4600-7700

TYPE	LI²
U CORES	
U5527	300-650
U5529	350-800
U6527	1000-2700
U6533	500-1300
U7228	800-1700
U7236	800-1800
U8020	1500-2800
U8038	1000-2300
TOROIDS	
77111	100-300
77191	70-300
77908	300-800

Figure A.4 Core Selector Table.

The nominal inductance (A_L=*89 nH/T*^{2}) for core type 6527 is obtained from the core data sheet. The minimum nominal inductance (A_{LMIN}=81.88 *nH/T*^{2}) is determined using the worst-case negative tolerance (-8%). With this information, the number of turns corresponding to the required inductance (in *mH*) is calculated from equation (A.17).

$$N = (L \times 10^6/A_L)^{1/2} = (4.7 \times 10^6/81.88)^{1/2} = 240\ turns \qquad \text{(A.17)}$$

The bias in At/m is calculated from:

$$H = \frac{1000NI}{l_e} = \frac{1000 \times 240 \times 5}{219} = 5779\ \ At/m \qquad \text{(A.18)}$$

The reduction in core permeability is related to the dc bias. Figure A. shows the initial permeability versus dc magnetizing force curve.

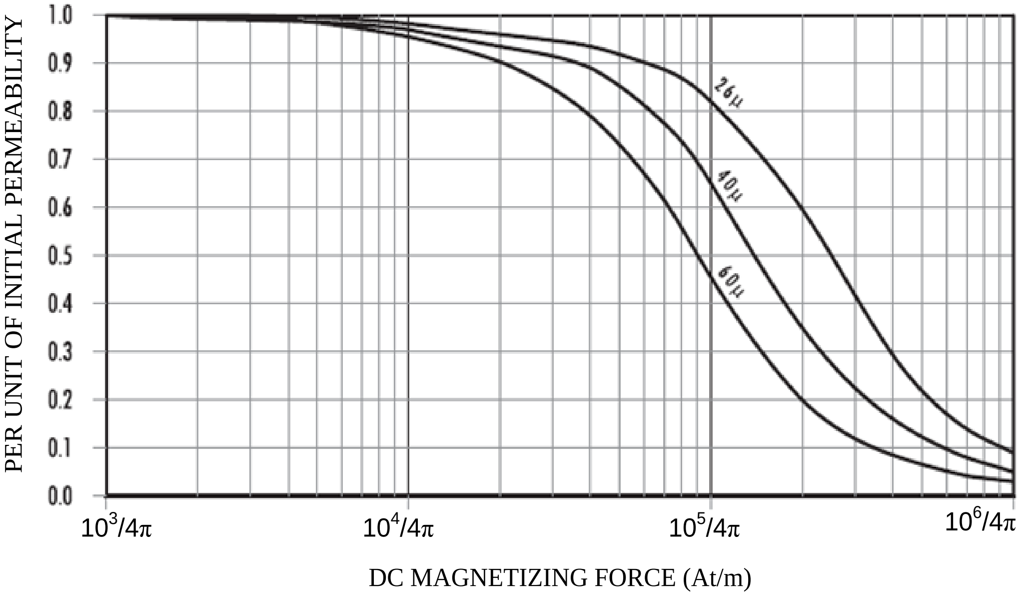

Figure A.5 DC bias roll-off curve for Kool Mu.

From Figure A., the roll-off in per unit initial permeability for the calculated bias level is determined. Figure A.5 shows 88% of initial permeability at 5779 At/m for ‘26μ’ material. Multiplying the minimum nominal inductance of 81.88 nH/T^2 by 0.88 yields 72.1 nH/T^2. Using this revised value of minimum nominal inductance, the number of turns is recalculated according to equation (A.17). This yields an inductance close to the required value.

iii. Loss and temperature rise

Core loss can be obtained according to the corresponding core loss curve, using the appropriate values of peak flux density and operating frequency. The wire size, ac and dc winding losses, and temperature rise are obtained using the same process as for the ac inductor, as described in Section A.1.

A.3 Power transformer design

The function of a power transformer in a switched mode power supply is to transfer power efficiently and instantaneously from an electrical source to a load. Ideally, the power transformer stores no energy. The transformer can also be used to meet the requirements of different input and output voltage levels by using an appropriate primary-to-secondary turns ratio, and may be used to provide galvanic isolation, which is an important safety consideration. Table A.4 shows the power transformer specification for the dc/dc converter.

Table A.4 Power transformer specification.

Primary Voltage	380V
Primary Current	6A
Secondary Voltage	563V
Secondary Current	4A
Transformer turns ratio	1:1.5
Switching frequency	40kHz
Max Temperature Rise	80 ℃
Cooling method	natural convection

i. Core selection for transformer

Several core materials may be used to realise a power transformers, including power ferrites, metal alloy cores, NANOPERM, etc. Power ferrite materials have higher resistivity at higher frequency, and hence lower eddy current losses. Permeability is, however, generally lower (saturation permeability 0.3T), resulting in more winding turns and greater magnetizing current, which must be controlled using snubbers and clamps. Metal alloy cores also have high resistivity at higher frequency, and require very thin laminations. Although saturation flux density is much greater than with ferrite materials, this is usually irrelevant since flux swing is severely limited by eddy current losses. NANOPERM is a rapidly-quenched iron-based alloy with a fine crystalline microstructure: typical grain size is 10 nm. Nanocrystalline materials have higher saturation flux density, which can be 1.2T, and lower eddy current losses. Table A.5 shows the material properties (nominal values) of NANOPERM which is used for the power transformer core.

Table A.5 Material properties of NANOPERM (nominal values)

Saturation flux density(B_{sat})	1.2	T
Saturation magnetostriction	≤0.5	ppm
Specific electrical resistivity	115	mΩ cm
Density	7.35	g cm^{-3}
Curie temperature T_c	600	℃

For safety, the working flux density B_m should be smaller than saturation flux density. Here, B_m is chosen as 0.9T.

ii. Core size and winding turns

The required area product of the power transformer can be calculated using equation (5.24). According to the calculated area product of the core, an approximate core size is selected from the product catalogue. Core type NANOPERM M-049-02 U7 (oval) is used.

The number of primary turns N_p can be expressed using Faraday's Law:

$$N_P = \frac{V_p}{K_f A_e B_{ac} f} = \frac{380}{4\times0.8\times10^{-4}\times0.9\times38\times10^3} = 35\ turns \qquad \text{(A.19)}$$

where K_f =4 for a square voltage wave and 4.44 for a sinusoidal wave.

A_e is the core cross sectional area

B_{ac} is flux density and

f is the switching frequency

The required primary and secondary transformer voltages are shown in Table A.4. Having calculated N_p=35 turns, the number of secondary turns is therefore found to be N_s=53 turns.

iii. Loss and temperature calculation

The nanocrystalline core loss can be calculated as:

$$P_{fe} = P_0 \times \left(\frac{F}{F_0}\right)^x \times \left(\frac{f}{f_0}\right)^y \times \left(\frac{B}{B_0}\right)^z$$

$$= 80 \times \left(\frac{1}{1.11}\right)^{1.6} \times \left(\frac{40}{100}\right)^{1.8} \times \left(\frac{0.877}{0.3}\right)^2$$

$$= 111\mathrm{W/kg} \qquad \text{(A.20)}$$

where P_0=80W/kg

F=1 for a square voltage wave and 1.11 for a sinusoidal wave, F_0=1.11, x=1.6

F is switching frequency (kHz), f_0=100kHz, y=1.8 and

B is flux density, B_0=0.3T, z=2.

For the power transformer, wire size, ac and dc winding losses, and temperature rise are obtained in the same way as for the inductors designed in Sections A.1 and A.2.

Appendix B Test rig structure

B.1 Test rig

The multi-terminal dc WECS test rig is based on two PMSG wind turbine units. One wind turbine uses a serial-parallel resonant converter and the other uses a hard-switched full bridge converter. The test rig is used to verify the performance of the WECS.

i. WECS with serial-parallel resonant converter

The hardware system shown in Figure B.1 details the topology of the resonant converter based WECS, which is comprised of the following components:

- 2.5kW induction machine
- Unidrive SP machine drive
- Torque transducer
- 2kW 5-phase permanent magnet synchronous generator
- TriCore 1796B digital signal processor
- Interface circuits for DSP
- Microchip DSPIC 30F2020
- Gate drive circuits
- Voltage and current measurement circuits
- Serial-parallel LCC resonant converter circuits
- Current source inverter emulator
- DC chopper

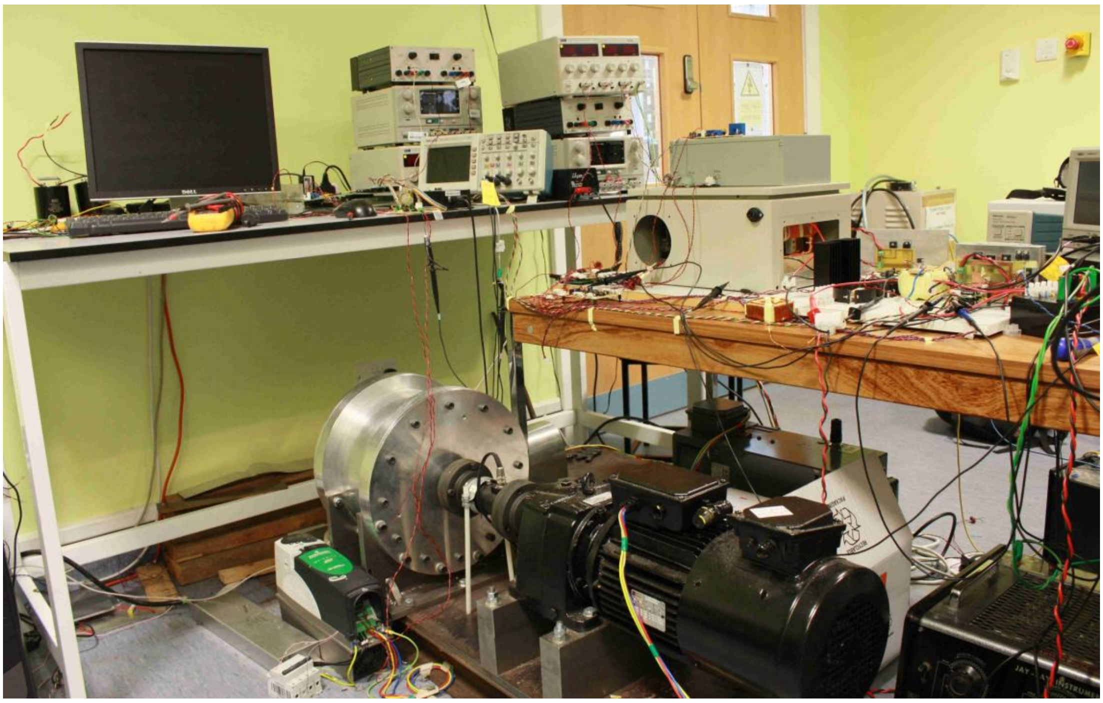

Figure B.1 Photograph of resonant converter based WECS.

ii. WECS with hard-switched converter

The topology of the hard-switched converter based WECS is shown in Figure B.2. It includes the following main components:

- 2.5kW induction machine
- Unidrive SP machine drive
- 2kW 3-phase permanent magnet synchronous generator
- TriCore 1796B digital signal processor
- Interface circuits for DSP
- Microchip DSPIC 30F2020
- Gate drive circuits
- Voltage and current measurement circuits
- Hard-switched full bridge converter
- DC chopper

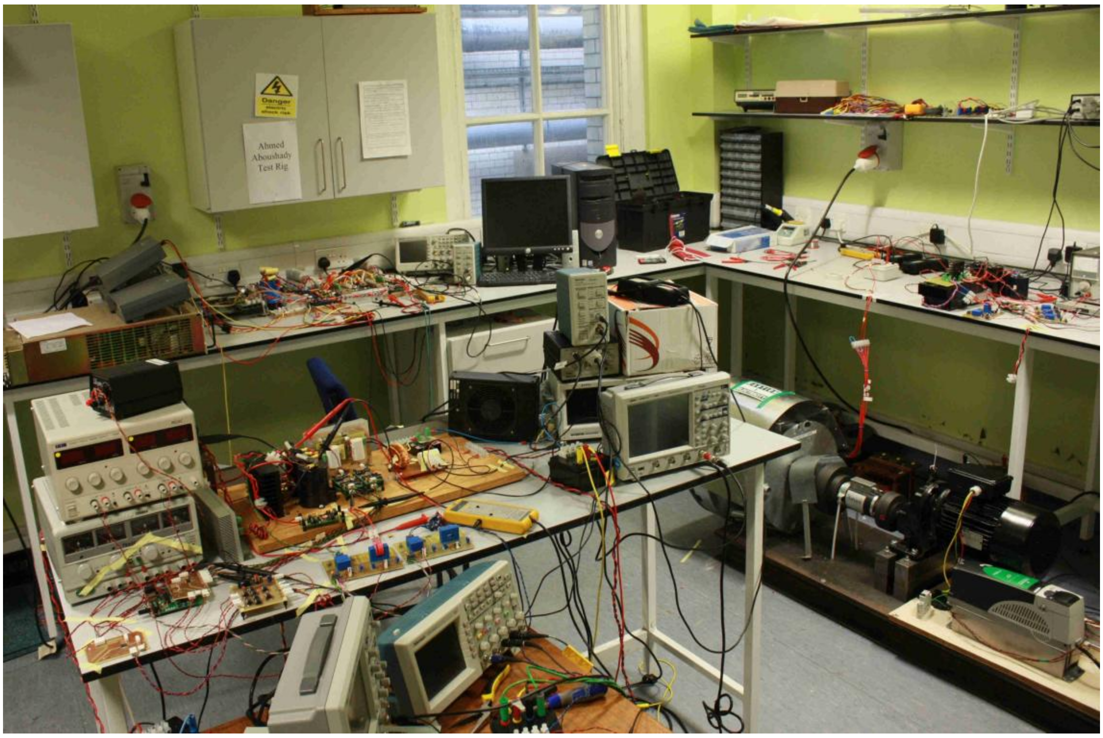

Figure B.2 Photograph of hard-switched converter based WECS.

B.2 Test rig components

This section introduces the main test rig components.

i. Digital signal processor (TriCore 1796B)

The digital signal processor (DSP) is used to sense the analogue feedback signal (rotor speed) and to generate the required control signal (torque). Desirable features include high processor speed, large memory, ease of programming and interface ability. The 32-bit TriCore 1796B DSP shown in Figure B.3 is employed as the controller for the wind turbine emulator. Its main features are:

- High performance 32-bit super-scalar *TriCoreTM* V1.3 CPU with 4 stage pipeline, offering
  - Superior real-time performance
  - Strong bit handling
  - Fully integrated DSP capabilities
  - Single precision floating point unit (FPU)
  - 150 MHz processor speed over the full automotive temperature range
- 32-bit Peripheral Control Processor with single cycle instruction (PCP2)

- Memory
    - 2 MByte embedded program flash with ECC
    - 128 kByte data flash
    - 192 kByte on chip SRAM
    - 16 kByte instruction cache
- 16-channel DMA controller
- 32-bit external bus interface unit with synchronous burst flash access capability
- Sophisticated interrupt system with 2×255 hardware priority arbitration levels serviced by CPU and PCP2
- High performing triple bus structure
    - 64-bit local memory buses to internal flash and data memory
    - 32-bit system peripheral bus for interconnections of on-chip peripherals and further functional units
    - 32-bit remote peripheral bus serving the requirements of high-speed peripherals
- Two general purpose timer array modules plus separate LTC array with a digital signal filtering and timer functionality to realize autonomous and complex I/O management
- Two asynchronous/synchronous serial channels with baud rate generator, parity, framing and overrun error detection (ASC)
- Two high-speed synchronous serial channels with programmable data length and shift direction (SSC)
- 4-channel fast analogue-to-digital converter unit (FADC) with 10-bit resolution
- Two 16-channel analogue-to-digital converter units (ADC) with 8-bit, 10-bit or 12-bit resolution
- 123 general purpose digital I/O lines and 4 input lines with 3.3 V capability
- Power management system and full automotive temperature range -40 ° to +125 ℃

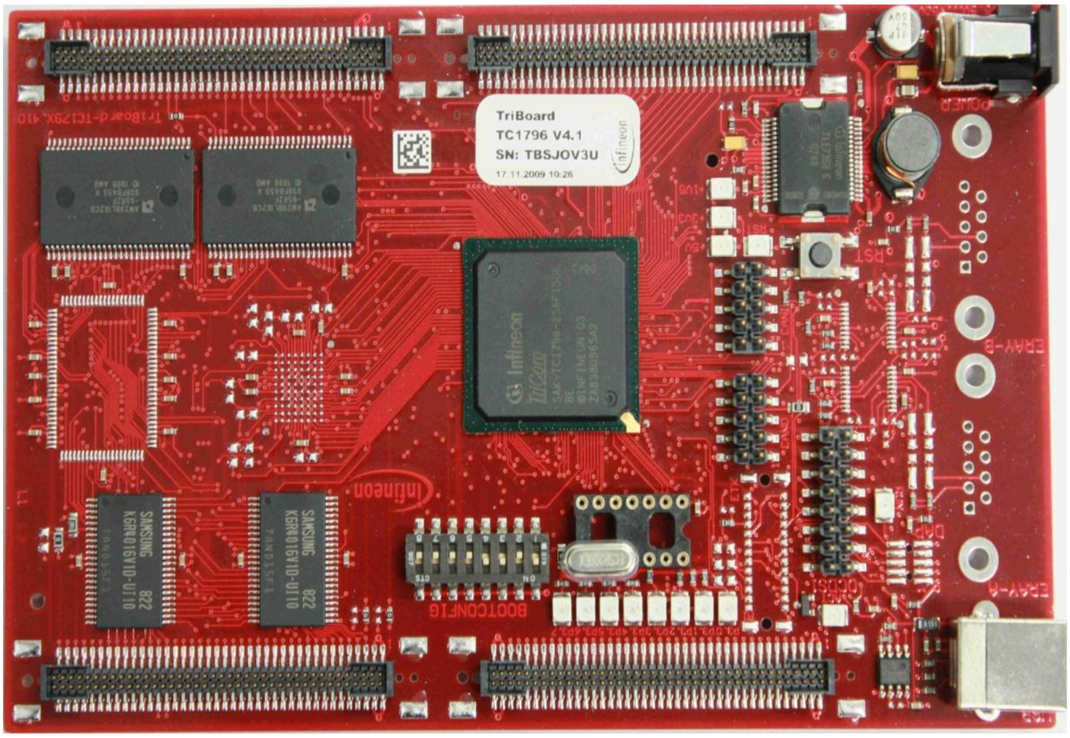

Figure B.3 DSP: 32-bit *TriCore*1796B.

ii. Interface circuits

It is important that the DSP is protected from possible electrical damage which may prevent it from carrying out the safety-critical role of controlling the power conversion system. Two interface boards were therfore used to electrically isolate the DSP from external circuits. The first interface board isolates the DSP PWM output channels from the gate drive circuits used to drive the power electronic devices, whilst the second interface board isolates the DSP ADC channels from the transducers used to monitor voltage and current in the power stage. The interface boards are shown in Figure B.4, and Figure B.6 and Figure B.7 show schematics of the gate drive and ADC interfaces respectively.

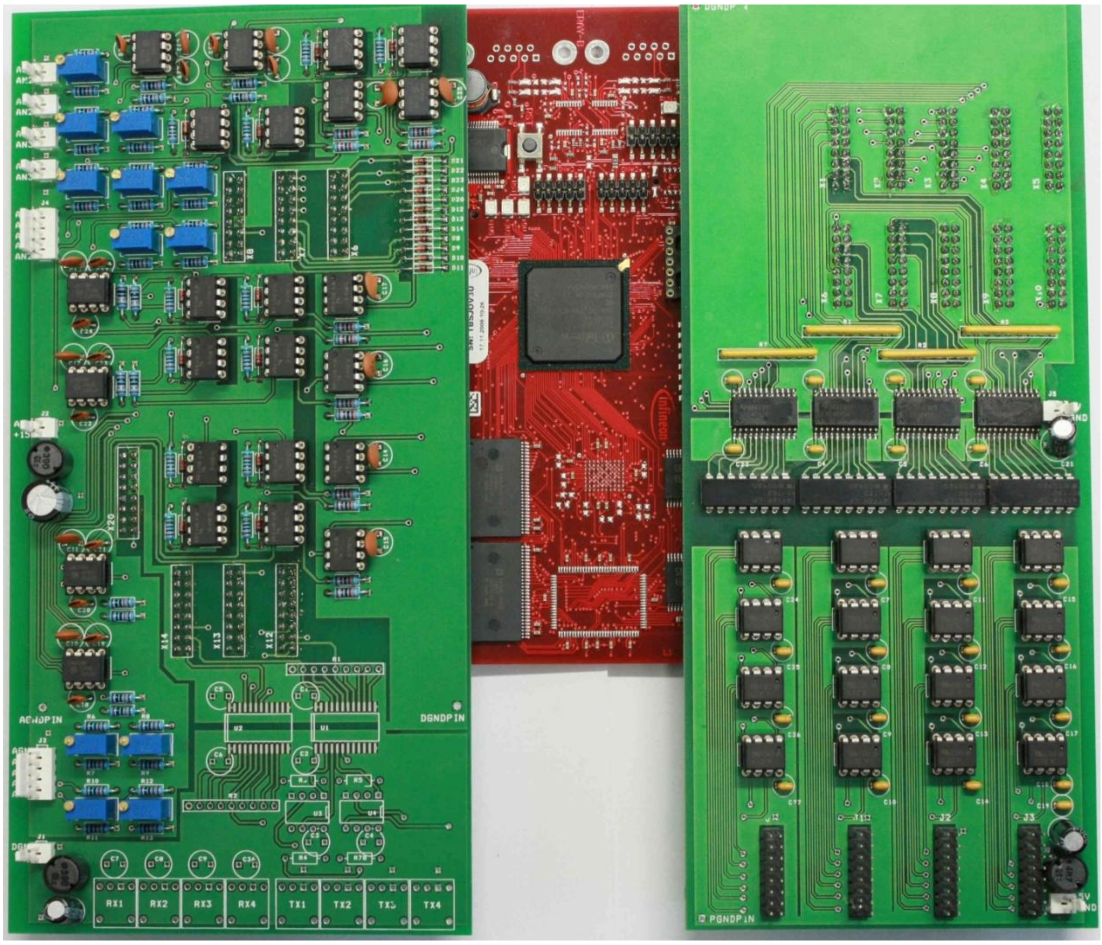

Figure B.4 Interface boards for DSP TriCore1796B.

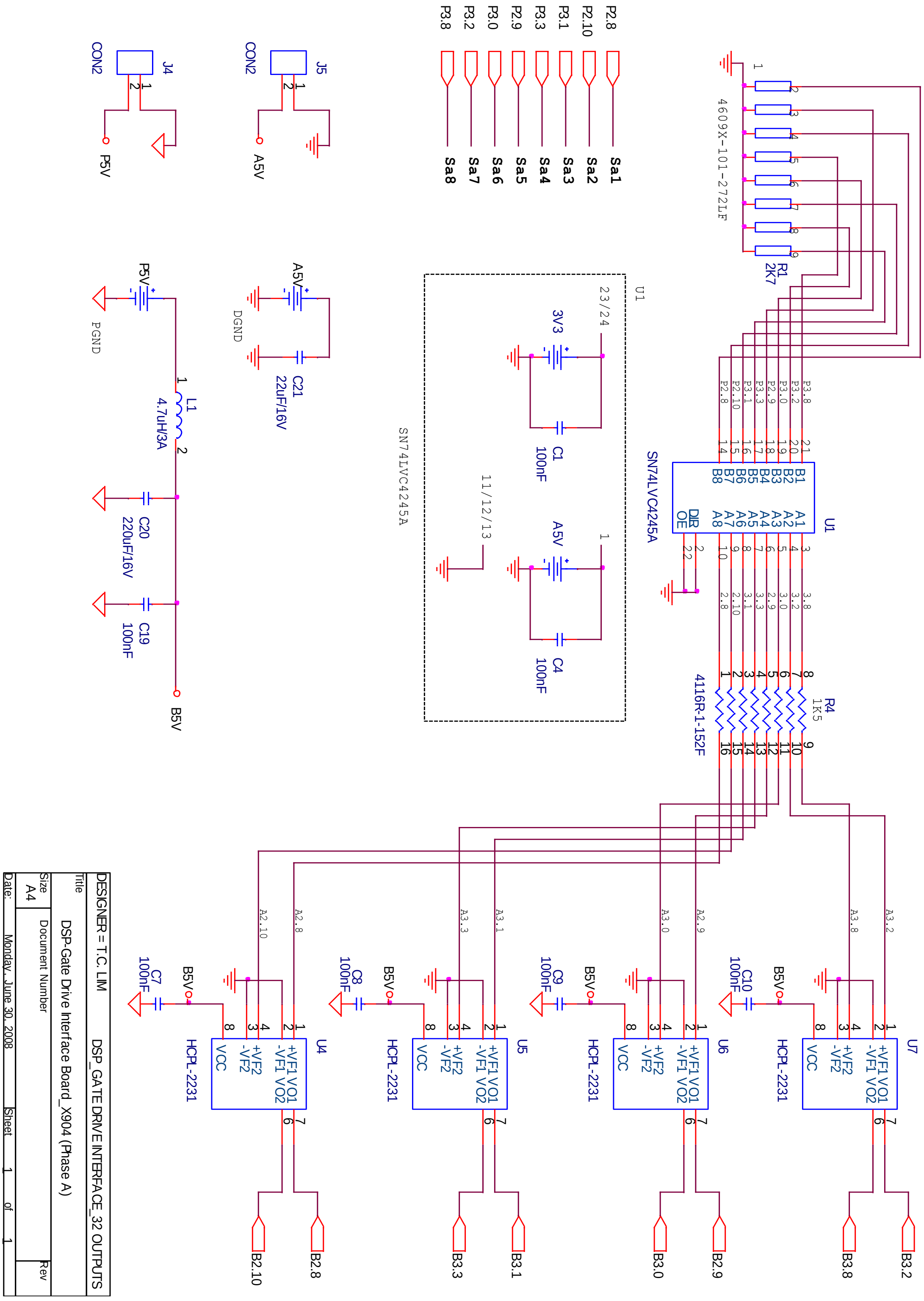

Figure B.5 Interface circuit schematic for PWM channels.

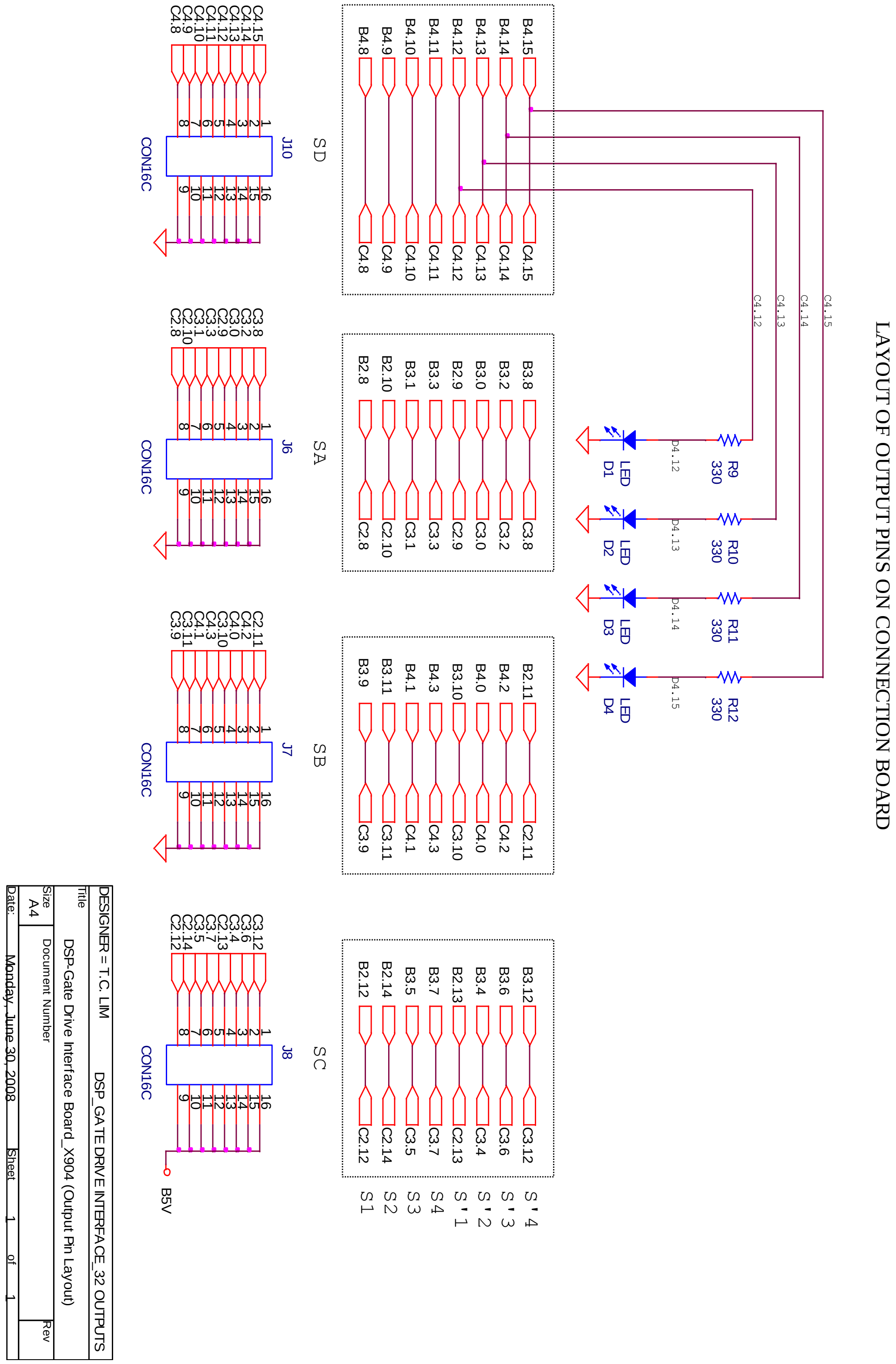

Figure B.6 (cont/…) Interface circuit schematic for PWM channels.

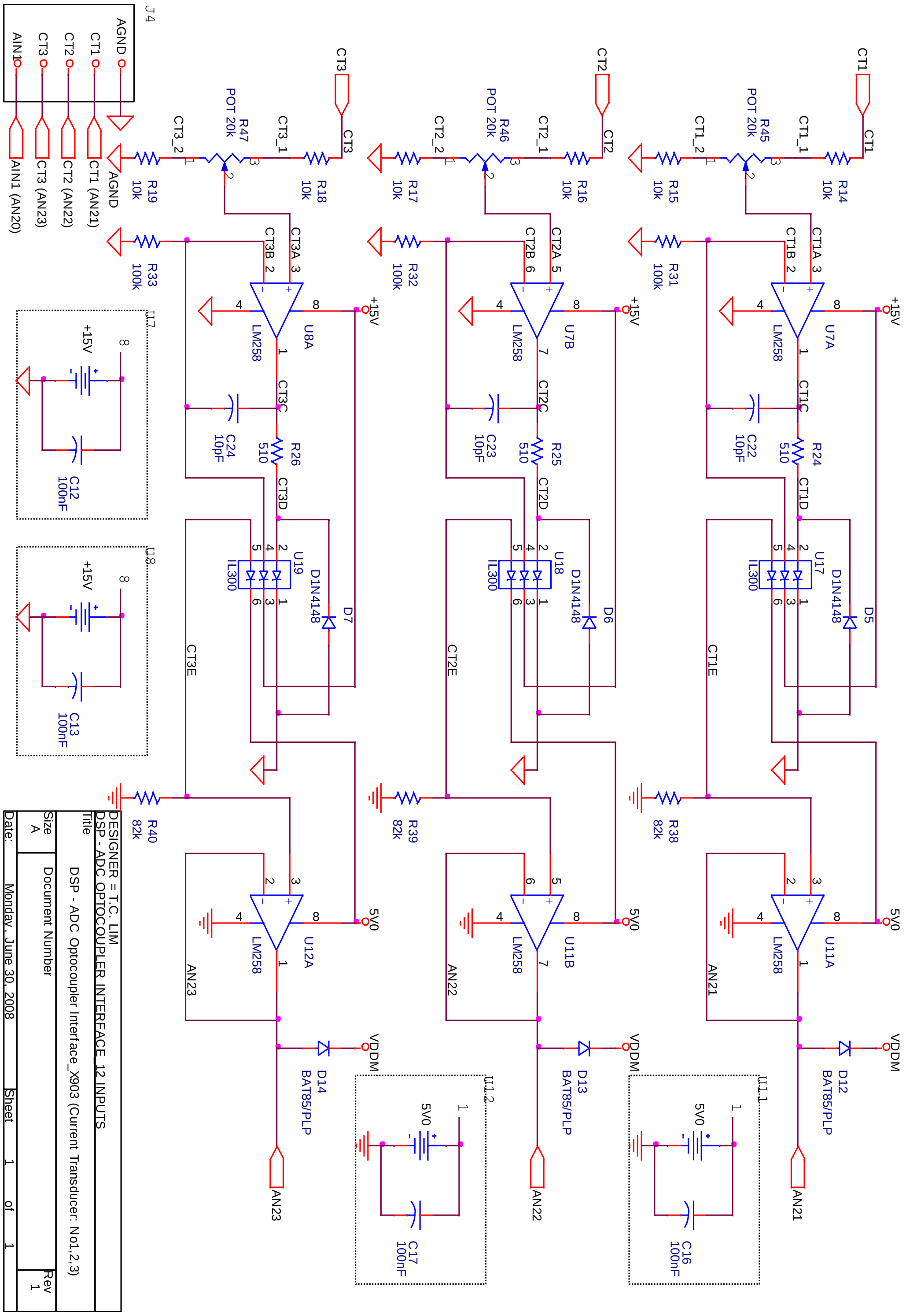

Figure B.7 Interface circuit schematic for ADC channels.

iii. Microchip dsPIC 30F2020

The basic function of the Microchip dsPIC 30F2020 is similar to that of the DSP. It is used to control a dc/dc converter to track the maximum power and to maintain a constant dc link. Figure B.8 shows the dsPIC 30F2020 based development board hardware. The features of the Microchip dsPIC 30F2020 are summarized as:

High-Performance Modified RISC CPU:

- Modified Harvard architecture
- 83 base instructions with flexible addressing modes
- 24-bit wide instructions, 16-bit wide data path
- 12 kByte on-chip Flash program space
- 512 Bytes on-chip data RAM
- 16×16-bit working register array
- Up to 30 MIPS operation:
    - Dual internal RC
      9.7 and 14.55 MHz (±1%) industrial Temp
      6.4 and 9.7 MHz ((±1%) extended Temp
      32× PLL with 480 MHz VCO
    - PLL input ±3%
    - External EC clock 6.0 to 14.55 MHz
    - HS Crystal mode 6.0 to14.55 MHz
- 32 interrupt sources
- 3 external interrupt sources
- 8 user-selectable priority levels for each interrupt
- 4 processor exceptions and software traps

Power supply PWM Module Features:

- Four PWM generators with 8 outputs
- Each PWM generator has independent time base and duty cycle
- Duty cycle resolution of 1.1 ns at 30 MIPS

- PWM modes supported:
    - Complementary
    - Push-pull
    - Multi-Phase
    - Variable Phase
    - Current Reset
    - Current-Limit

ADC module Features:

- 10-bit resolution
- 2000 ksps conversion rate
- Up to 12 input channels
- Interrupt hardware supports up to 1M interrupts per second.

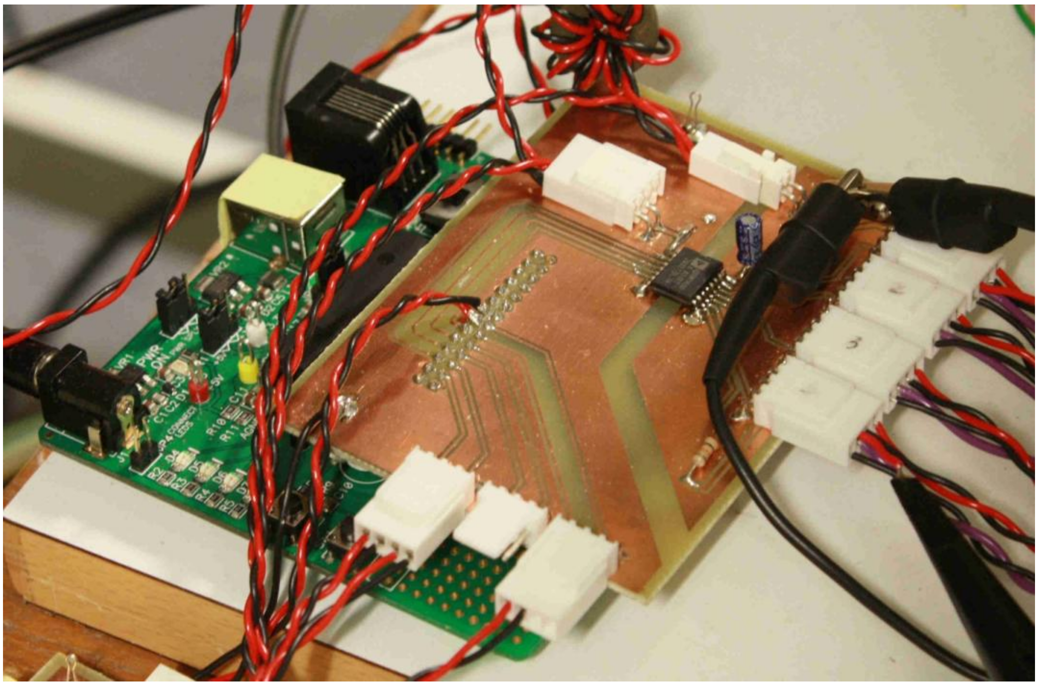

Figure B.8 dsPIC 30F2020 based development board hardware.

iv. Gate drive circuit

The gate drive circuit is required to supply sufficient gate drive voltage and current to the semiconductor switching devices. The drive circuit transformer provides the necessary galvanic isolation between the controller common ground and the common points of each of the inverter switches. Figure B.9 shows the gate drive circuit and Figure B.10 shows the circuit schematic.

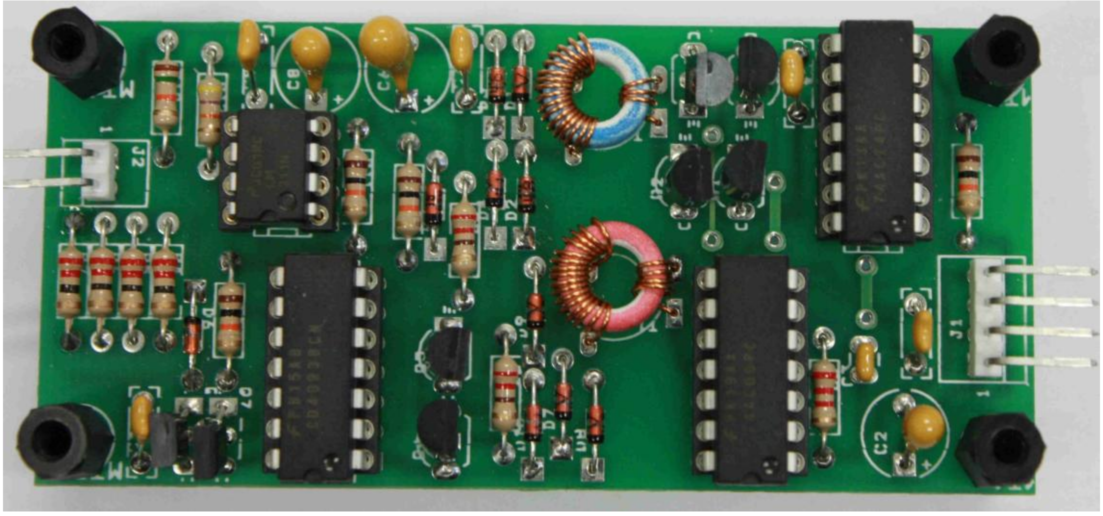

Figure B.9 Gate drive circuit

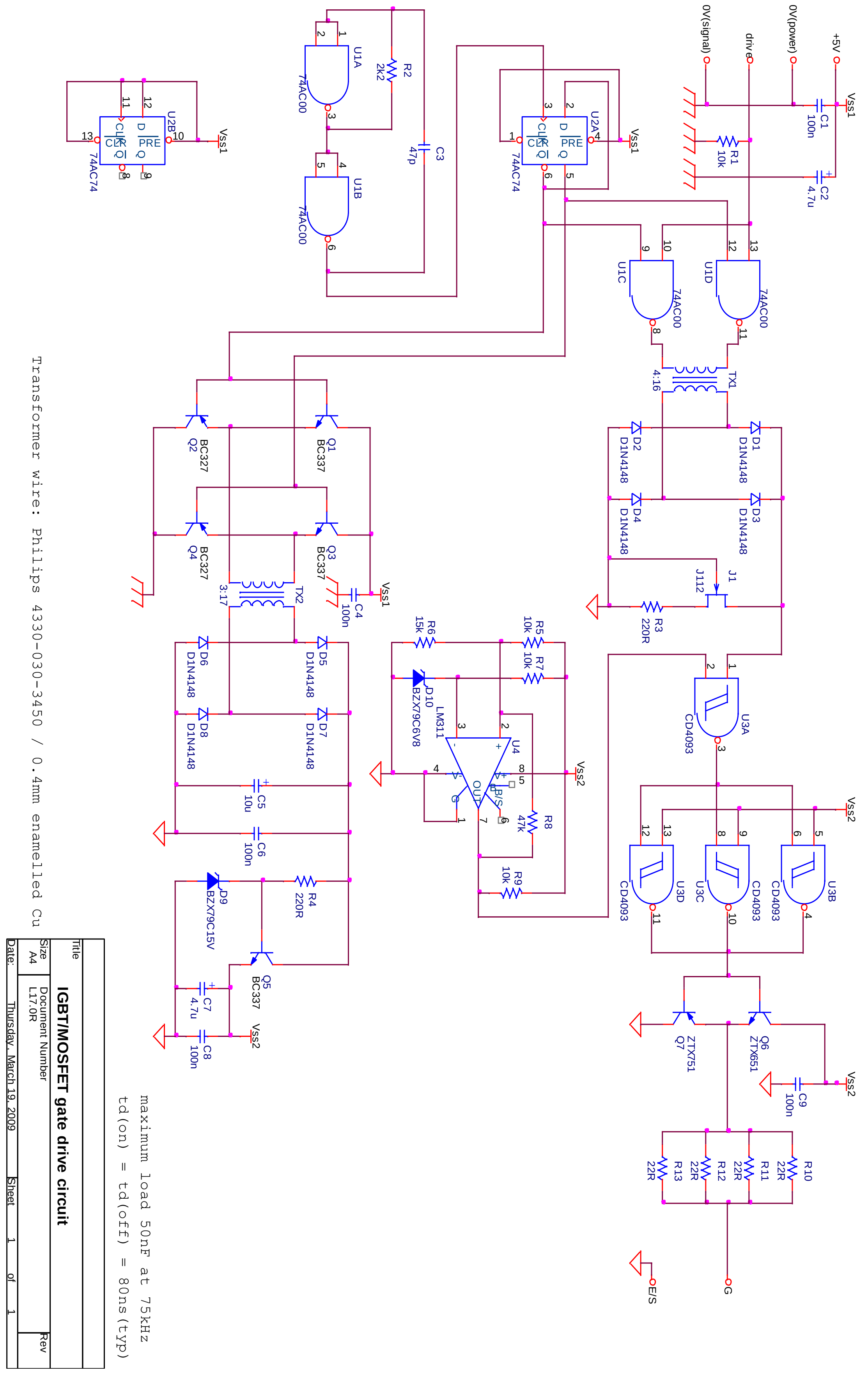

Transformer wire: Philips 4330-030-3450 / 0.4mm enamelled Cu

maximum load 50nF at 75kHz
td(on) = td(off) = 80ns(typ)

Figure B.10 Gate drive circuit schematic.

v. Current and voltage transducer circuit

Current and voltage transducer circuits are used to measure current and voltage in the power stage and to provide signals to the controller. The schematic of the voltage sensing circuit, based on an LEM LV25-P Hall-effect voltage transducer, is shown in Figure B.11. The current sensing circuit, based on an LEM LA55-P Hall-effect current transducer, which has high accuracy, good linearity and optimized response time, is shown in Figure B.11.

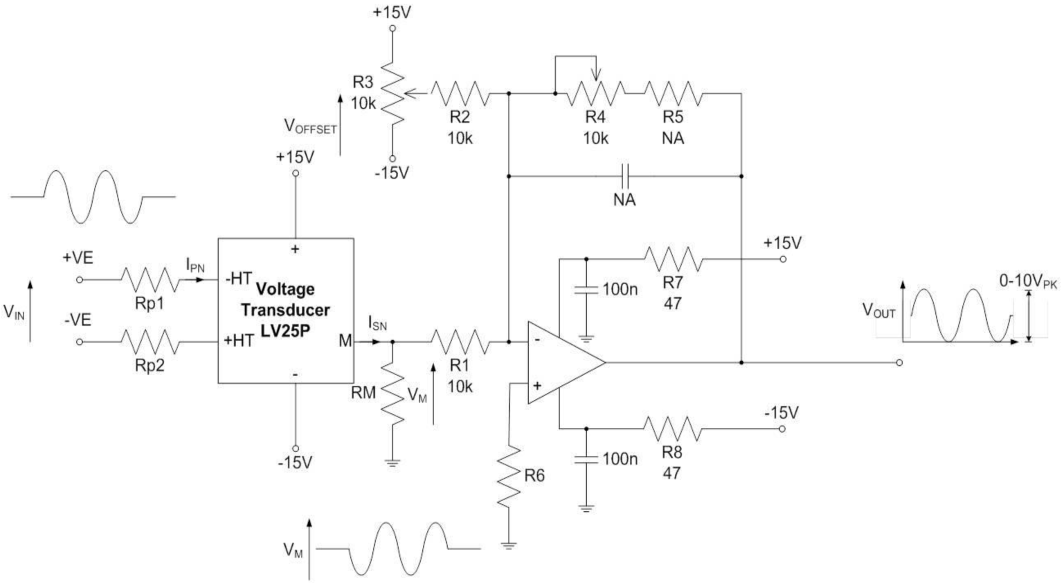

Figure B.11 Voltage transducer circuit schematic.

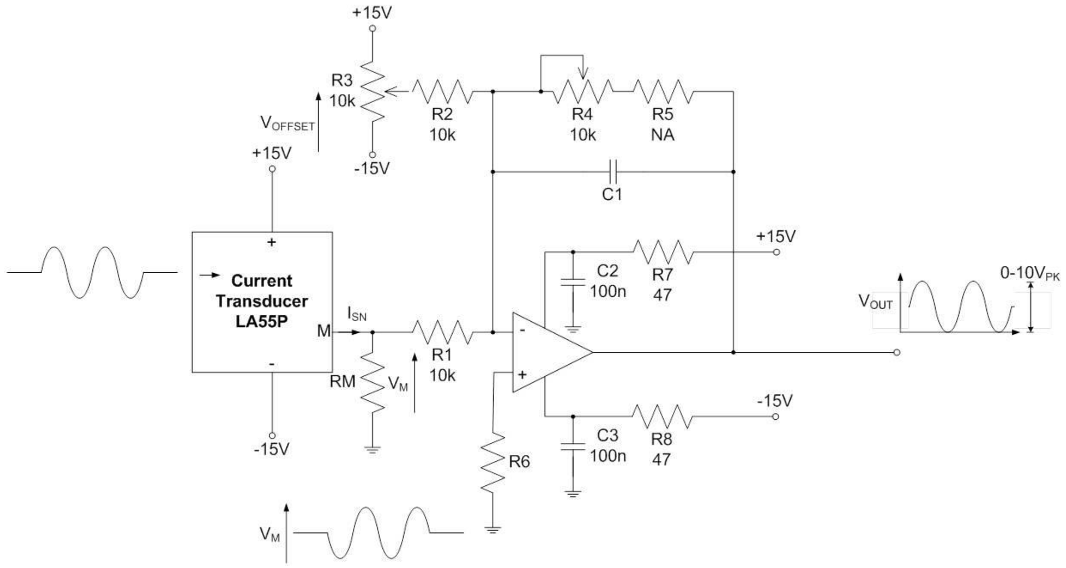

Figure B.12 Current transducer circuit schematic.

Figure B.13 shows the actual transducer circuitry.

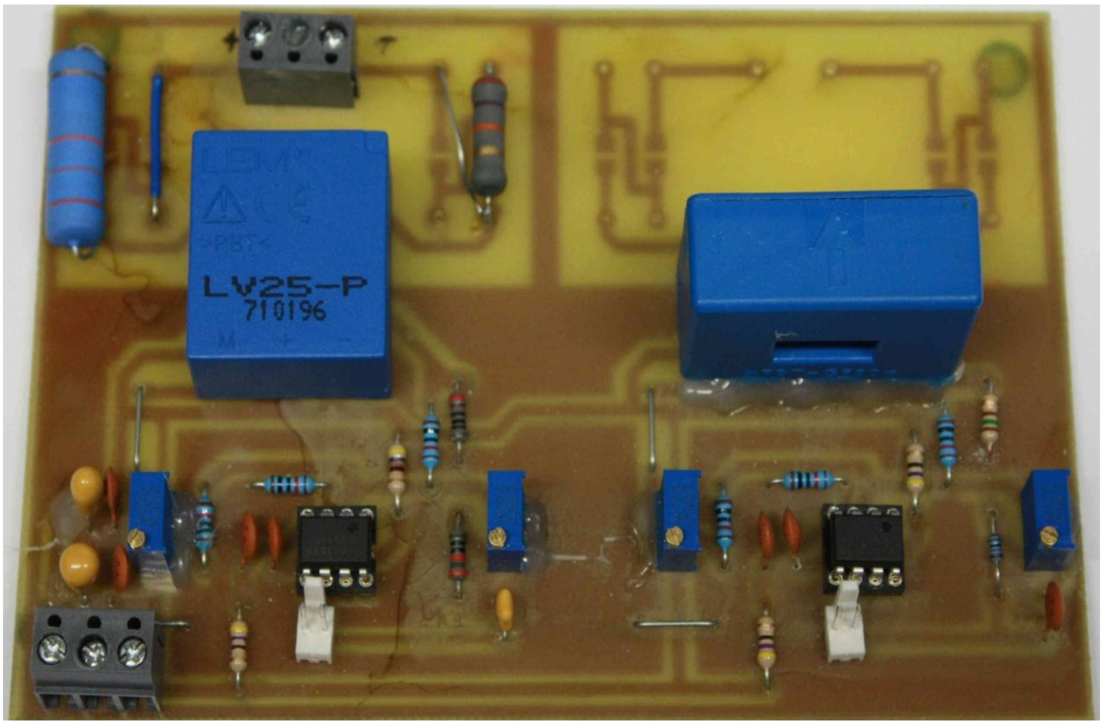

Figure B.13 Voltage and current transducers.

The data sheets for the voltage and current transducers are shown in Figure B.13 and B.14 respectively.

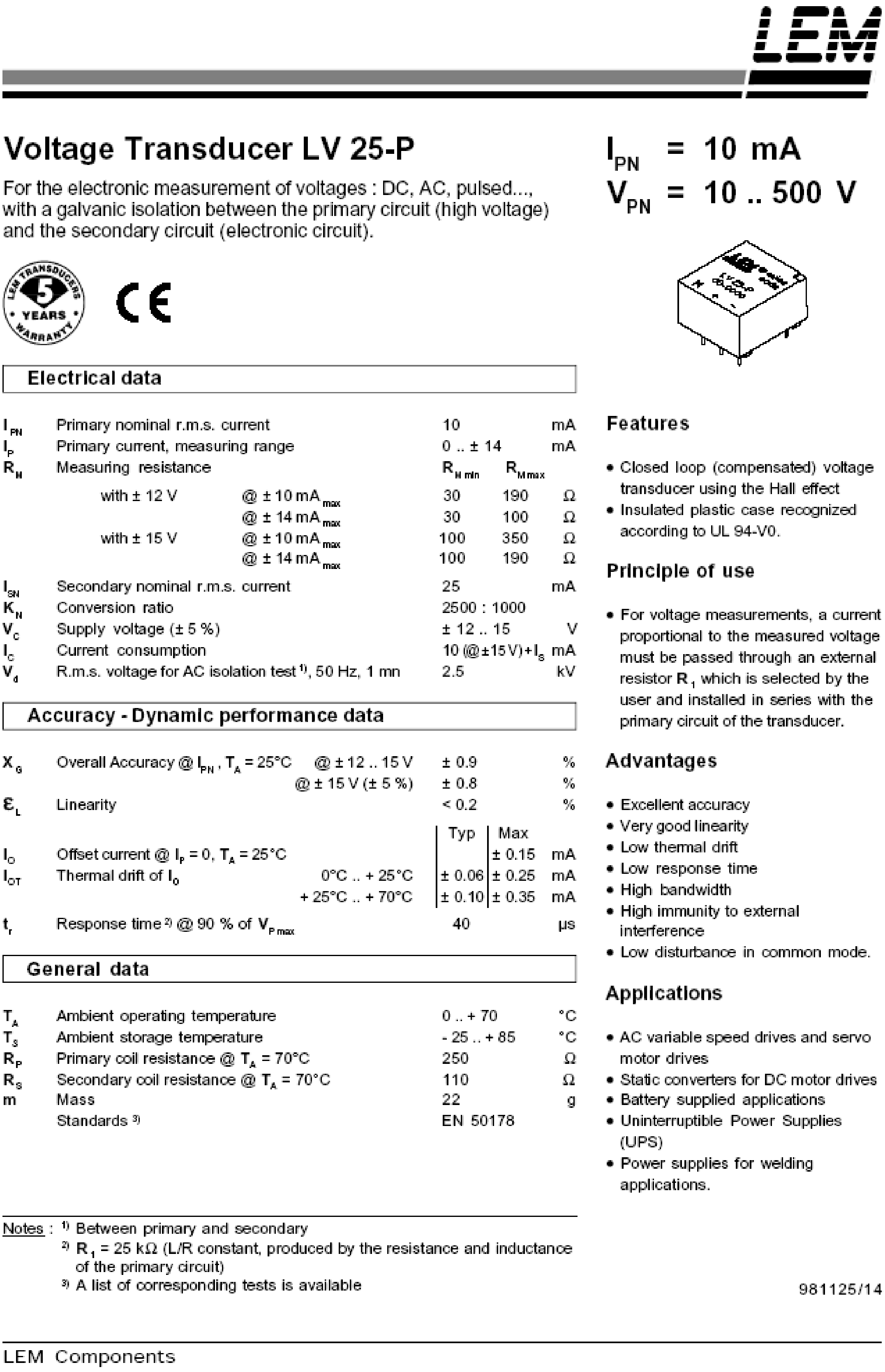

LEM

Voltage Transducer LV 25-P

I_{PN} = 10 mA
V_{PN} = 10 .. 500 V

For the electronic measurement of voltages : DC, AC, pulsed..., with a galvanic isolation between the primary circuit (high voltage) and the secondary circuit (electronic circuit).

LEM TRANSDUCERS 5 YEARS WARRANTY

CE

Electrical data

I_{PN}	Primary nominal r.m.s. current		10		mA
I_P	Primary current, measuring range		0 .. ± 14		mA
R_M	Measuring resistance		$R_{M\,min}$	$R_{M\,max}$	
	with ± 12 V	@ ± 10 mA_{max}	30	190	Ω
		@ ± 14 mA_{max}	30	100	Ω
	with ± 15 V	@ ± 10 mA_{max}	100	350	Ω
		@ ± 14 mA_{max}	100	190	Ω
I_{SN}	Secondary nominal r.m.s. current		25		mA
K_N	Conversion ratio		2500 : 1000		
V_C	Supply voltage (± 5 %)		± 12 .. 15		V
I_C	Current consumption		10 (@±15 V)+I_S		mA
V_d	R.m.s. voltage for AC isolation test [1], 50 Hz, 1 mn		2.5		kV

Accuracy - Dynamic performance data

X_G	Overall Accuracy @ I_{PN}, T_A = 25°C	@ ± 12 .. 15 V	± 0.9		%
		@ ± 15 V (± 5 %)	± 0.8		%
ε_L	Linearity		< 0.2		%
			Typ	Max	
I_O	Offset current @ I_P = 0, T_A = 25°C			± 0.15	mA
I_{OT}	Thermal drift of I_O	0°C .. + 25°C	± 0.06	± 0.25	mA
		+ 25°C .. + 70°C	± 0.10	± 0.35	mA
t_r	Response time [2] @ 90 % of $V_{P\,max}$		40		μs

General data

T_A	Ambient operating temperature	0 .. + 70	°C
T_S	Ambient storage temperature	- 25 .. + 85	°C
R_P	Primary coil resistance @ T_A = 70°C	250	Ω
R_S	Secondary coil resistance @ T_A = 70°C	110	Ω
m	Mass	22	g
	Standards [3]	EN 50178	

Features

- Closed loop (compensated) voltage transducer using the Hall effect
- Insulated plastic case recognized according to UL 94-V0.

Principle of use

- For voltage measurements, a current proportional to the measured voltage must be passed through an external resistor R_1 which is selected by the user and installed in series with the primary circuit of the transducer.

Advantages

- Excellent accuracy
- Very good linearity
- Low thermal drift
- Low response time
- High bandwidth
- High immunity to external interference
- Low disturbance in common mode.

Applications

- AC variable speed drives and servo motor drives
- Static converters for DC motor drives
- Battery supplied applications
- Uninterruptible Power Supplies (UPS)
- Power supplies for welding applications.

Notes :
[1] Between primary and secondary
[2] R_1 = 25 kΩ (L/R constant, produced by the resistance and inductance of the primary circuit)
[3] A list of corresponding tests is available

981125/14

LEM Components

Figure B.13 LV 25-P voltage transducer data sheet

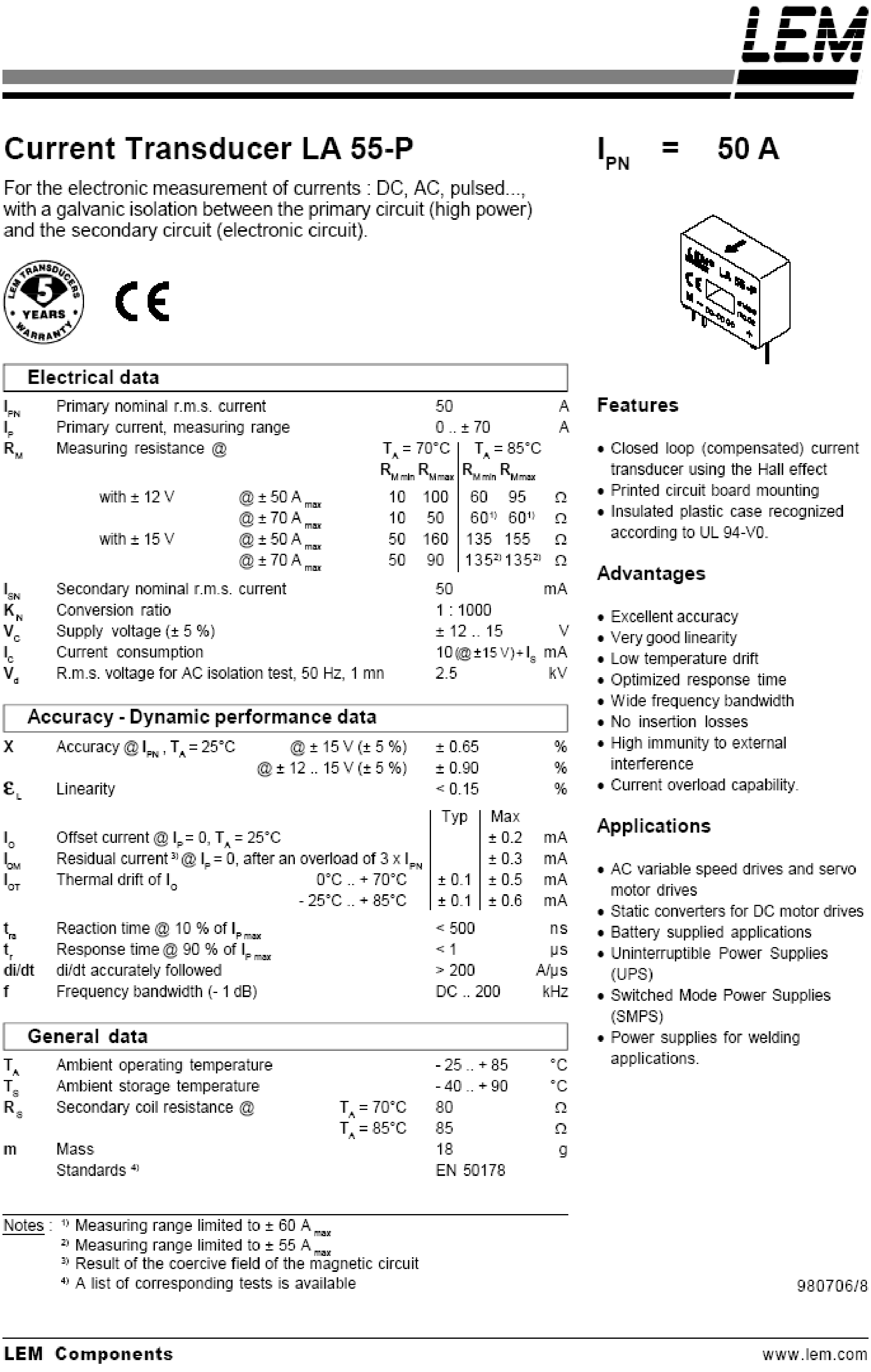

Current Transducer LA 55-P

I_{PN} = 50 A

For the electronic measurement of currents : DC, AC, pulsed..., with a galvanic isolation between the primary circuit (high power) and the secondary circuit (electronic circuit).

Electrical data

I_{PN}	Primary nominal r.m.s. current			50				A
I_P	Primary current, measuring range			0 .. ± 70				A
R_M	Measuring resistance @			T_A = 70°C		T_A = 85°C		
				$R_{M\,min}$	$R_{M\,max}$	$R_{M\,min}$	$R_{M\,max}$	
		with ± 12 V	@ ± 50 A_{max}	10	100	60	95	Ω
			@ ± 70 A_{max}	10	50	60[1]	60[1]	Ω
		with ± 15 V	@ ± 50 A_{max}	50	160	135	155	Ω
			@ ± 70 A_{max}	50	90	135[2]	135[2]	Ω
I_{SN}	Secondary nominal r.m.s. current			50				mA
K_N	Conversion ratio			1 : 1000				
V_C	Supply voltage (± 5 %)			± 12 .. 15				V
I_C	Current consumption			10 (@ ±15 V) + I_S				mA
V_d	R.m.s. voltage for AC isolation test, 50 Hz, 1 mn			2.5				kV

Accuracy - Dynamic performance data

X	Accuracy @ I_{PN}, T_A = 25°C	@ ± 15 V (± 5 %)	± 0.65		%
		@ ± 12 .. 15 V (± 5 %)	± 0.90		%
ε_L	Linearity		< 0.15		%
			Typ	Max	
I_O	Offset current @ I_P = 0, T_A = 25°C			± 0.2	mA
I_{OM}	Residual current[3] @ I_P = 0, after an overload of 3 x I_{PN}			± 0.3	mA
I_{OT}	Thermal drift of I_O	0°C .. + 70°C	± 0.1	± 0.5	mA
		- 25°C .. + 85°C	± 0.1	± 0.6	mA
t_{ra}	Reaction time @ 10 % of $I_{P\,max}$		< 500		ns
t_r	Response time @ 90 % of $I_{P\,max}$		< 1		µs
di/dt	di/dt accurately followed		> 200		A/µs
f	Frequency bandwidth (- 1 dB)		DC .. 200		kHz

General data

T_A	Ambient operating temperature		- 25 .. + 85	°C
T_S	Ambient storage temperature		- 40 .. + 90	°C
R_S	Secondary coil resistance @	T_A = 70°C	80	Ω
		T_A = 85°C	85	Ω
m	Mass		18	g
	Standards[4]		EN 50178	

Features

- Closed loop (compensated) current transducer using the Hall effect
- Printed circuit board mounting
- Insulated plastic case recognized according to UL 94-V0.

Advantages

- Excellent accuracy
- Very good linearity
- Low temperature drift
- Optimized response time
- Wide frequency bandwidth
- No insertion losses
- High immunity to external interference
- Current overload capability.

Applications

- AC variable speed drives and servo motor drives
- Static converters for DC motor drives
- Battery supplied applications
- Uninterruptible Power Supplies (UPS)
- Switched Mode Power Supplies (SMPS)
- Power supplies for welding applications.

Notes : [1] Measuring range limited to ± 60 A_{max}
[2] Measuring range limited to ± 55 A_{max}
[3] Result of the coercive field of the magnetic circuit
[4] A list of corresponding tests is available

980706/8

LEM Components www.lem.com

Figure B.14 LA 55-P current transducer data sheet

vi. Machine drive

In the test rig, an Emerson Control Techniques Unidrive SP industrial drive, shown in Figure B.14, is used to control a permanent magnetic synchronous generator (PMSG) to act as a ‘real’ wind turbine. Rotor speed derived from a shaft-mounted tachometer and a torque command obtained from the DSP are input to the drive, which controls the PMSG to follow the torque-speed curve of a typical wind turbine.

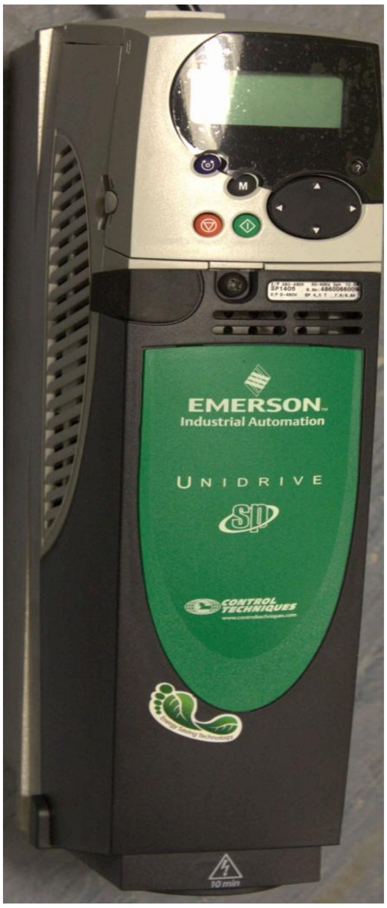

Figure B.14 Emerson Control Techniques Unidrive SP industrial drive

The high-performance machine drive offers flexible operational modes, such as:

- Open-loop V/Hz AC drive
- Open-loop Vector AC drive
- Closed-loop Vector AC drive
- AC servo amplifier for rotary and linear motors
- Regenerative (active) power supply

Appendix C Programme code

C.1 LCC MPPT tracking and DC link voltage control

```
#include "p30f2020.h"
#include "dsp.h"
#include <stdlib.h>
_FOSC(CSW_FSCM_OFF & OSC2_CLKO & HS); //enable clock switching; fail
safe monitor are disabled; CLKO output signal active on the OSCO pin;
_FPOR(PWRT_OFF)                    //turn off the power-up timers
_FWDT(FWDTEN_OFF)                    //turn off watchdog
_FOSCSEL(PRIOSC_PLL)                    //enable Primary Oscillator (HS,EC) with
PLL module, PLL is selectable for 32 only for 30F2020
_FGS(CODE_PROT_OFF)                    //Disable Code Protection
_FBS(BSS_NO_FLASH)                 //No boot program Flash segment
#define max_phase_shift  8250
#define max_duty_cycle   15520   //15220
#define min_duty_cycle  Q15(0.45)
#define opvoltage  496.0//682.0  //inter register value corresponding to Max 0-1024
0-314V
#define opcurrent  360  //1024   360//inter register value corresponding to max 0-
1024  0-5.49A
tPID fooPID;
fractional abcCoefficient[3] __attribute__ ((section(".xbss, bss, xmemory")));
fractional controlHistory[3] __attribute__ ((section(".ybss, bss, ymemory")));
fractional kCoeffs[] = {0,0,0};
tPID fooPID1;
fractional abcCoefficient1[3] __attribute__ ((section(".xbss, bss, xmemory")));
fractional controlHistory1[3] __attribute__ ((section(".ybss, bss, ymemory")));
fractional kCoeffs1[] = {0,0,0};
unsigned int Voltage=0;
unsigned int Current=0;
unsigned int DC_Voltage=0;
unsigned int Aver_Voltage=0;
unsigned int Aver_Current=0;
unsigned int Aver_DC_Voltage=0;
unsigned int i=0;
float Reference;
unsigned int Phase_shift=8250;
unsigned int duty_cycle=15520;
void init_PWM(void)                    // initial Pwm REGISTER
{
IOCON1bits.PENH = 1;                // PWM1H is controlled by PWM module
IOCON1bits.PENL = 1;                // PWM1L is controlled by PWM module
IOCON1bits.PMOD = 0;                // select complementary PWM mode
```

```
IOCON1bits.POLL=0;
IOCON1bits.POLH=0;
PWMCON1bits.TRGSTAT = 0;        /* Clear PWM Trigger Interrupt flag */
PWMCON1bits.TRGIEN = 0;              /* Disable pwm Trigger Interrupt, Coz the
interrupt is enabled by ADC module */
PTPER=16500; //PTPER is primary time base register.sets the counting period for
PTMR(primary time base)
DTR1=640;                         //dead time register //1us
ALTDTR1=640;                          //dead time register //1us
PHASE1=0x0;                       //PWM PHASE-SHIFT REGISTER
PDC1=8250;                         //Duty cycle register
IOCON2bits.PENH = 1;                   // PWM1H is controlled by PWM module
IOCON2bits.PENL = 1;                   // PWM1L is controlled by PWM module
IOCON2bits.PMOD = 0;                   // select complementary PWM mode
IOCON2bits.POLL=0;
IOCON2bits.POLH=0;
DTR2=640;                         //dead time register 1us
ALTDTR2=640;                          //dead time register 1us
PHASE2=4250;                       //PWM PHASE-SHIFT REGISTER
PDC2=8250;                         //Duty cycle register
IOCON3bits.PENH = 1;   /* PWM3H is controlled by PWM module */
IOCON3bits.PENL = 1;   /* PWM3L is controlled by PWM module */
IOCON3bits.PMOD= 0;   /* Select Complementary Output PWM mode */
PWMCON3bits.DTC=1;    /* Negative dead time applied get overlap */
DTR3= 640;              /* Deadtime setting */
ALTDTR3 = 640;              /* Deadtime setting */
PHASE3 = 0;              /* approximately 250 nsec phase shift */
PDC3 =15520;              /* Duty Cycle = PDC1*1.5625nsec = 25usec */
PTCONbits.PTEN = 1;                          // enable PWM module
}
void init_adc(void)
{
ADCONbits.ADSIDL = 0;             // operate in idle mode
ADCONbits.FORM = 0;                  // output in integer format
ADCONbits.EIE = 0;            // generate interrupt after Second conversion
ADCONbits.ORDER = 0;                 // even analogue channel is converted first
ADCONbits.SEQSAMP = 0;             // sample at the start of second conversion
ADCONbits.ADCS = 2;               // Fadc/8
ADPCFG = 0xFFEC;            // AN0 and AN1,AN4 set to analogue inputs
ADCPC0bits.IRQEN0 = 1;               // enable interrupt after AN0 and AN1 complete
ADCPC0bits.SWTRG0 = 1;              // start conversion of AN0 and AN1
ADCPC1bits.SWTRG2 = 1;              // start conversion of AN4 and AN5
ADCPC0bits.TRGSRC0 = 0x4;          //  Trigger conversion on PWM#1 Trigger */
ADCPC1bits.TRGSRC2 = 0x4;          //  Trigger conversion on PWM#1 Trigger */
TRGCON1bits.TRGDIV = 0;          /* Trigger on evry event */
TRGCON1bits.TRGSTRT     = 0;     /* Start the counting at the start */
TRIG1 = 8000;     /* Trigger event at  0.214 usec from start of the PWM cycle */
IFS0bits.ADIF = 0;                        // clear ADC conversion interrupt flag status
```

```
IEC0bits.ADIE = 1;                    // enable ADC conversion complete interrupt
ADCONbits.ADON = 1;                          // turn on the ADC module
}
void __attribute__((interrupt, no_auto_psv)) _ADCInterrupt() // Interrupt function
{
IFS0bits.ADIF = 0;                    // Clear ADC Interrupt Flag
i++;
if (i<10)
{
Voltage=ADCBUF0+Voltage;
Current=ADCBUF1+Current;
DC_Voltage=ADCBUF4+DC_Voltage;
ADSTATbits.P0RDY = 0;    // Clear the ADSTAT bits, set when data ready in buffer
ADSTATbits.P2RDY = 0;    // Clear the ADSTAT bits, set when data ready in buffer
}
else
{
Aver_Voltage=(Voltage+ADCBUF0)/10.0;
Aver_Current=(Current+ADCBUF1)/10.0;
Aver_DC_Voltage=(DC_Voltage+ADCBUF4)/10.0;
Reference=opcurrent*(Aver_Voltage/opvoltage)*(Aver_Voltage/opvoltage);
fooPID.controlReference =Float2Fract (Reference/1024.0);
fooPID.measuredOutput = Aver_Current<< 5;  // Scale measured output to fractional
format
fooPID1.measuredOutput =Aver_DC_Voltage<<5; // Scale measured output to
fractional format
ADSTATbits.P0RDY = 0;    // Clear the ADSTAT bits, set when data ready in buffer
ADSTATbits.P2RDY = 0;    // Clear the ADSTAT bits, set when data ready in buffer
PID(&fooPID);
PID(&fooPID1);           //Call the PID controller using the new measured input
if( fooPID.controlOutput > Q15(0) )
{
Phase_shift = __builtin_mulsu(fooPID.controlOutput, max_phase_shift) >> 15;
}
else
{
Phase_shift = 0;
}
PHASE2=Phase_shift;
if( fooPID1.controlOutput > Q15(0.45) )
{
duty_cycle= __builtin_mulsu(fooPID1.controlOutput, max_duty_cycle) >> 15;
}
else
{
duty_cycle = __builtin_mulsu(min_duty_cycle, max_duty_cycle) >> 15;
}
PDC3=duty_cycle;
```

```
Voltage=0;
Current=0;
DC_Voltage=0;
i=0;
}
}
int main (void)                    //MAIN FUCTION
{
fooPID.abcCoefficients = &abcCoefficient[0];
fooPID.controlHistory = &controlHistory[0];
fooPID1.abcCoefficients = &abcCoefficient1[0];
fooPID1.controlHistory = &controlHistory1[0];
PIDInit(&fooPID);
PIDInit(&fooPID1);
kCoeffs[0] = Q15(0.00001);//0.00001
kCoeffs[1] = Q15(0.022);   //0.022
kCoeffs[2] = Q15(0);
kCoeffs1[0] = Q15(0.001);   //(big capacitor)0.01//0.000001
kCoeffs1[1] = Q15(0.01);   //(big capacitor)0.15//0.01
kCoeffs1[2] = Q15(0);
PIDCoeffCalc(&kCoeffs[0], &fooPID);
PIDCoeffCalc(&kCoeffs1[0], &fooPID1);
fooPID1.controlReference = Q15(0.55);
init_PWM();
ADCBUF0=0;
ADCBUF1=0;
ADCBUF4=0;
__delay32(20000000);  //1sec
init_adc();
while(1)
{
}
}
```

C.2 LCC voltage control and DC chopper control

```
#include "p30f2020.h"
#include "dsp.h"
#include <stdlib.h>
_FOSC(CSW_FSCM_OFF & OSC2_CLKO & HS); //enable clock switching;fail
safe monitor are disabled;CLKO output signal active on the OSCO pin;//
_FPOR(PWRT_OFF)                    //turn off the power-up timers
_FWDT(FWDTEN_OFF)                  //turn off watchdog
_FOSCSEL(PRIOSC_PLL)        //enable Primary Oscillator (HS,EC) with PLL
module, PLL is selectable for 32 only for 30F2020
_FGS(CODE_PROT_OFF)                //Disable Code Protection
_FBS(BSS_NO_FLASH)          //No boot program Flash segment
#define max_phase_shift  8250
#define max_duty_cycle   15420   //15220
```

```
#define min_duty_cycle  Q15(0.007)
#define opvoltage  496.0//682.0  //inter register value corresponding to Max 0-1024
0-314V
#define opcurrent  360  //1024   360//inter register value corresponding to max 0-
1024  0-5.49A
#define Limited_Voltage Q15(0.621)  //0.55-163v  0.573-170
tPID fooPID;  //Mppt control
fractional abcCoefficient[3] __attribute__ ((section(".xbss, bss, xmemory")));
fractional controlHistory[3] __attribute__ ((section(".ybss, bss, ymemory")));
fractional kCoeffs[] = {0,0,0};
tPID fooPID1; //DC_Link control
fractional abcCoefficient1[3] __attribute__ ((section(".xbss, bss, xmemory")));
fractional controlHistory1[3] __attribute__ ((section(".ybss, bss, ymemory")));
fractional kCoeffs1[] = {0,0,0};
tPID fooPID2; //DC_chopper control
fractional abcCoefficient2[3] __attribute__ ((section(".xbss, bss, xmemory")));
fractional controlHistory2[3] __attribute__ ((section(".ybss, bss, ymemory")));
fractional kCoeffs2[] = {0,0,0};
fractional Reference_DC=Q15(0);
unsigned int Voltage=0;
unsigned int Current=0;
unsigned int DC_Voltage=0;
unsigned int Aver_Voltage=0;
unsigned int Aver_Current=0;
unsigned int Aver_DC_Voltage=0;
unsigned int i=0;
unsigned int j=0;
float Reference;
unsigned int Phase_shift=8250;
unsigned int duty_cycle=100;
void init_PWM(void)                    // initial Pwm REGISTER
{
IOCON1bits.PENH = 1;// PWM1H is controlled by PWM module
IOCON1bits.PENL = 1;// PWM1L is controlled by PWM module
IOCON1bits.PMOD = 0;// select complementary PWM mode
IOCON1bits.POLL=0;
IOCON1bits.POLH=0;
PWMCON1bits.TRGSTAT = 0;       /* Clear PWM Trigger Interrupt flag */
PWMCON1bits.TRGIEN = 0;           /* Disable pwm Trigger Interrupt, Coz the
interrupt is enabled by ADC module */
PTPER=16500;              //PTPER is primary time base register.sets the counting
period for PTMR(primary time base)
DTR1=640;                        //dead time register //1us
ALTDTR1=640;                        //dead time register //1us
PHASE1=0x0;                        //PWM PHASE-SHIFT REGISTER
PDC1=8250;                        //Duty cycle register
IOCON2bits.PENH = 1;// PWM1H is controlled by PWM module
IOCON2bits.PENL = 1;// PWM1L is controlled by PWM module
```

```
IOCON2bits.PMOD = 0;// select complementary PWM mode
IOCON2bits.POLL=0;
IOCON2bits.POLH=0;
DTR2=640;                          //dead time register 1us
ALTDTR2=640;                          //dead time register 1us
PHASE2=4250;                     //PWM PHASE-SHIFT REGISTER
PDC2=8250;                          //Duty cycle register
IOCON3bits.PENH      = 1;   /* PWM3H is controlled by PWM module */
IOCON3bits.PENL      = 1;   /* PWM3L is controlled by PWM module */
IOCON3bits.PMOD      = 1;   /* Select independent Output PWM mode */
PWMCON3bits.DTC      =1;    /* Negative dead time applied get overlap */
DTR3    = 640;              /* Deadtime setting */
ALTDTR3 = 640;              /* Deadtime setting */
PHASE3 = 0;              /* approximately 250 nsec phase shift */
PDC3 =100;               /* Duty Cycle = PDC1*1.5625nsec = 25usec */
PTCONbits.PTEN = 1;                              // enable PWM module
}
void init_adc(void)
{
ADCONbits.ADSIDL = 0;               // operate in idle mode
ADCONbits.FORM = 0;                 // output in integer format
ADCONbits.EIE = 0;            // generate interrupt after Second conversion
ADCONbits.ORDER = 0;                // even analogue channel is converted first
ADCONbits.SEQSAMP = 0;              // sample at the start of second conversion
ADCONbits.ADCS = 2;               // Fadc/8
ADPCFG = 0xFFEC;            // AN0 and AN1,AN4 set to analogue inputs
ADCPC0bits.IRQEN0 = 1;              // enable interrupt after AN0 and AN1 complete
ADCPC0bits.SWTRG0 = 1;              // start conversion of AN0 and AN1
ADCPC1bits.SWTRG2 = 1;              // start conversion of AN4 and AN5
ADCPC0bits.TRGSRC0 = 0x4;        //  Trigger conversion on PWM#1 Trigger */
ADCPC1bits.TRGSRC2 = 0x4;        //  Trigger conversion on PWM#1 Trigger */
TRGCON1bits.TRGDIV = 0;        /* Trigger on evry event */
TRGCON1bits.TRGSTRT     = 0;     /* Start the counting at the start */
TRIG1 = 8000;    /* Trigger event at  0.214 usec from start of the PWM cycle */
IFS0bits.ADIF = 0;                  // clear ADC conversion interrupt flag status
IEC0bits.ADIE = 1;                  // enable ADC conversion complete interrupt
ADCONbits.ADON = 1;                           // turn on the ADC module
T1CONbits.TON = 1;                  // turn on timer1
}
void __attribute__((interrupt, no_auto_psv)) _ADCInterrupt() // Interrupt function
{
IFS0bits.ADIF = 0;                       // Clear ADC Interrupt Flag
i++;
if (i<10)
{Voltage=ADCBUF0+Voltage;
Current=ADCBUF1+Current;
DC_Voltage=ADCBUF4+DC_Voltage;
ADSTATbits.P0RDY = 0;    // Clear the ADSTAT bits, set when data ready in buffer
```

```
ADSTATbits.P2RDY = 0;   // Clear the ADSTAT bits, set when data ready in buffer
}
else
{
Aver_Voltage=(Voltage+ADCBUF0)/10.0;
Aver_Current=(Current+ADCBUF1)/10.0;
Aver_DC_Voltage=(DC_Voltage+ADCBUF4)/10.0;
fooPID.measuredOutput = Aver_Current<< 5;  // Scale measured output to fractional
format
fooPID1.measuredOutput =Aver_DC_Voltage<<5;   // Scale measured output to
fractional format
fooPID2.measuredOutput =Aver_Voltage<<5;  // Scale measured output to fractional
format
if (Aver_Voltage<<5>Limited_Voltage &j==0 )      //DC Chopper control
{
PID(&fooPID2);
if( fooPID2.controlOutput < 0)
{
duty_cycle= __builtin_mulsu(min_duty_cycle, max_duty_cycle) >> 15;
}
PDC3=duty_cycle;
j=5;
}
if (j==5)
{
PID(&fooPID2);
if( fooPID2.controlOutput > -min_duty_cycle )
{
duty_cycle= __builtin_mulsu(min_duty_cycle, max_duty_cycle) >> 15;
}
else
{
duty_cycle = __builtin_mulsu(fooPID2.controlOutput, max_duty_cycle) >> 15;
duty_cycle=-duty_cycle;
}
PDC3=duty_cycle;
}
PID(&fooPID1);              //DC_LINK voltage control
if(
fooPID1.controlOutput <Q15(0))
{
Reference_DC=fooPID1.controlOutput;
}
else
{
Reference_DC= 0;
}
Reference=opcurrent*(Aver_Voltage/opvoltage)*(Aver_Voltage/opvoltage);
```

```
fooPID.controlReference=Float2Fract
(Reference/1024.0+Fract2Float(Reference_DC)/(Reference/1024.0)*2);  //1.5（？ ）
ADSTATbits.P0RDY = 0;   // Clear the ADSTAT bits, set when data ready in buffer
ADSTATbits.P2RDY = 0;   // Clear the ADSTAT bits, set when data ready in buffer
PID(&fooPID);           //Call the PID controller using the new measured input
if( fooPID.controlOutput > Q15(0) )
{
Phase_shift = __builtin_mulsu(fooPID.controlOutput, max_phase_shift) >> 15;
}
else
{
Phase_shift = 0;
}
PHASE2=Phase_shift;
Voltage=0;
Current=0;
DC_Voltage=0;
i=0;
}
}
int main (void)                         //MAIN FUCTION
{fooPID.abcCoefficients = &abcCoefficient[0];
fooPID.controlHistory = &controlHistory[0];
fooPID1.abcCoefficients = &abcCoefficient1[0];
fooPID1.controlHistory = &controlHistory1[0];
fooPID2.abcCoefficients = &abcCoefficient2[0];
fooPID2.controlHistory = &controlHistory2[0];
PIDInit(&fooPID);
PIDInit(&fooPID1);
PIDInit(&fooPID2);
kCoeffs[0] = Q15(0.0000005);//0.00001//GOOD  0.0000005
kCoeffs[1] = Q15(0.012);   //0.022  //GOOD  0.0012
kCoeffs[2] = Q15(0);
kCoeffs1[0] = Q15(0.000001);   //(big capacitor)0.01//0.000001
kCoeffs1[1] = Q15(0.01);   //(big capacitor)0.15//0.01
kCoeffs1[2] = Q15(0);
kCoeffs2[0] = Q15(0.001);//0.00001//0.00005//good real0.001
kCoeffs2[1] = Q15(0.01);   //0.012//0.002//0.01
kCoeffs2[2] = Q15(0);
PIDCoeffCalc(&kCoeffs[0], &fooPID);
PIDCoeffCalc(&kCoeffs1[0], &fooPID1);
PIDCoeffCalc(&kCoeffs2[0], &fooPID2);
fooPID1.controlReference = Q15(0.5); //Q15(0.25)=120v DC link voltage reference
fooPID2.controlReference = Limited_Voltage;// input voltage reference
init_PWM();
ADCBUF0=0;
ADCBUF1=0;
ADCBUF4=0;
```

```
__delay32(20000000);  //1sec
init_adc();
while(1)
{
}
}
```

C.3 Wind turbine control and pitch control

```
Wspeed=(Wspeed_reg/4096.0)*730;//1460.0; // 50HZ-1460-4096, 38HZ-
1110-4096 25HZ-730-4096 22HZ-642.4-4096 20HZ-584-4096 18HZ-525.6-4096
16HZ-467.2-4096
Wm=Wspeed*2*pi/60.0/GR/1.35; // 1.35 is the calibration coefficienct;actual shaft
speed,amximum speed of drive is 1460rpm;
TSR=Wm*r/Vw;
if (t>60)   // activated the pitch angle control
{
PI_controller_pitchcontrol (Wspeed_reference, Wspeed, &PI_I_pitchcontrol,
&pitch_angle, &pitch_angle_before);
}
beta=1/(1/(TSR+0.08*pitch_angle)-0.035/(pitch_angle*pitch_angle*pitch_angle+1));
Cp=0.22*(116/beta-0.4*pitch_angle-5)*exp(-12.5/beta);
if (Cp<=0)
Cp=0;
Pm=0.5*Air*pi*r*r*Cp*Vw*Vw*Vw;
Te=Pm/Wm/GR;
if (Te<0)
Te=0;
else if (Te>26.2)
Te=26.2;
Tec=(Te/26.2)*128+128;// torque command, convetered to 128+ see D/A formular
Ted=(int)Tec;// convert to integer for digital output;
if (Ted>=255)
Ted=255;   // maximum output; 8 digits
if (t<15)           //when i=1,means it take 0.05*e-6*515=25.75e-6 Second
{
P3_OUT=160;   //175
}
else
{
P3_OUT=Ted;
}
if (t>120)
{
GPTA0_LTCXR02=0x00000195;
GPTA0_LTCXR04=0x0000014;
GPTA0_LTCXR05=0x00000181;
}
else
```

```
{
GPTA0_LTCXR02=0x00000100;
GPTA0_LTCXR04=0x0000014;
GPTA0_LTCXR05=0x00000EC;
}

void PI_controller_pitchcontrol (double Wspeed_reference, double Wspeed, double
*PI_I_pitchcontrol, double *pitch_angle, double *pitch_angle_before)
{
double PI_P_coefficient = 0.000001;
double PI_I_coefficient = 0.000001;
double PI_result = 0;
PI_result = PI_P_coefficient * (Wspeed-Wspeed_reference);
*PI_I_pitchcontrol=*PI_I_pitchcontrol+PI_I_coefficient*(Wspeed-
Wspeed_reference);
if (*PI_I_pitchcontrol>27)
{
*PI_I_pitchcontrol=27;
}
if (*PI_I_pitchcontrol<0)
{
*PI_I_pitchcontrol=0;
}
PI_result = PI_result + *PI_I_pitchcontrol;
if(PI_result>27)
{
PI_result=27;
}
if(PI_result<=0)
{
PI_result=0;
}
*pitch_angle =PI_result;
if((*pitch_angle)>(1*(1/40000)+(*pitch_angle_before)))
{
*pitch_angle=1*(1.0/40000)+*pitch_angle_before;
}
if((*pitch_angle)<(-1*(1/40000)+(*pitch_angle_before)))
{
*pitch_angle=-1*(1.0/40000)+*pitch_angle_before;
}
*pitch_angle_before=*pitch_angle;
}
```

Appendix D List of tables and figures

D.1 List of figures

Figure 1.1 Top 10 cumulative installed wind capacity December 2010 3
Figure 1.2 The capital cost breakdown of a typical 5 MW onshore project 4
Figure 1.3 UK installed wind power capacity 1990-2011 (operational) 6
Figure 2.1 Scheme of fixed speed WECS. 19
Figure 2.2 Scheme of limited speed WECS. 19
Figure 2.3 Variable SCIG WECS. 20
Figure 2.4 Scheme of variable DFIG WECS. 22
Figure 2.5 Scheme of variable PMSG WECS. 23
Figure 2.6 The schematic diagram of PMSG block. 25
Figure 2.7 the power converter configuration for grid connection (a) ac/dc-dc/ac (b) ac/dc-dc/dc-dc/ac. 25
Figure 2.8 The wind energy conversion system configuration used in this research. 27
Figure 2.9 Three-phase diode bridge rectifier. 27
Figure 2.10 The boost converter topology. 28
Figure 2.11 The current output full-bridge isolated converter. 29
Figure 2.12 Series parallel resonant LCC converter. 29
Figure 2.13 A simplified configuration of the grid converter. 30
Figure 2.14 Inner loop design for the VSI system. 31
Figure 2.15 Outer loop design for VSI system. 32
Figure 2.16 CSI topologies based on IGBTs and GTO (IGCT): (a) IGBT based (b) GTO (IGCT) based. 33
Figure 2.17 Equivalent circuit of the CSI system. 33
Figure 2.18 Outer loop design for CSI system. 34
Figure 2.19 Inner loop design for the CSI system. 35
Figure 3.1 Power coefficient versus tip speed ratio. 41
Figure 3.2 Block diagram of TSR control. 42
Figure 3.3 Block diagram of PSF control. 42

Figure 3.4 P&O control MPPT process flow chart. 43
Figure 3.5 The flowchart for the optimized OPP algorithm. 46
Figure 3.6 Block diagram of the proposed system. 48
Figure 3.7 Comparison of OPP and Optimized OPP operation during linear changes of wind speed. (a) OPP operation. (b) Optimized OPP operation. 51
Figure 3.8 Compared power coefficient for OPP and optimized OPP control with linear wind profiles. 53
Figure 3.9 Compared extracted energy for OPP and optimized OPP control with linear wind profiles. 53
Figure 3.10 Comparison of OPP and Optimized OPP operation with realistic wind profiles (a) OPP operation. (b) Optimized OPP operation. 55
Figure 3.11 Compared power coefficient for OPP and optimized OPP control with realistic wind profiles. 56
Figure 3.12 Compared extracted energy for OPP and optimized OPP control with realistic wind profiles. 56
Figure 4.1 Hard-switched FB topology. 62
Figure 4.2 Single active bridge converter. 62
Figure 4.3 Current output HSFB. 62
Figure 4.4 Hardware structure of the wind turbine emulator system. 63
Figure 4.5 Power coefficient C_p versus tip speed ratio relation in turbine simulator. 64
Figure 4.6 Wind turbine power characteristic with different wind speed for pitch angle β=0°. 65
Figure 4.7 Control flow for the wind turbine emulator system. 66
Figure 4.8 Input current and input voltage to the HF transformer (a) Full duty cycle (b) Partial duty cycle. 68
Figure 4.9 Average input current of boost converter and H-bridge versus rotor speed (pu) at different wind speeds. 72
Figure 4.10 Compared average switch currents for boost converter and H-Bridge converter (a) at different wind speed (b) at maximum power point. 75
Figure 4.11 Compared peak switch currents for boost converter and H-Bridge converter (a) at different wind speed (b) at maximum power point. 75
Figure 4.12 Control diagram of modified OPP control. 77

Figure 4.13 Schematic of the WECS. 78
Figure 4.14 Simulation results of mechanical system dynamical response. 79
Figure 4.15 Practical results of mechanical system dynamical response.................. 80
Figure 4.16 Dynamic response of electrical system... 80
Figure 5.1 Circuit diagram of a series resonant converter. 89
Figure 5.2 Derivation of the equivalent ac resistance. 89
Figure 5.3 Ac equivalent circuit for series resonant converter. 90
Figure 5.4 DC gain characteristic of series resonant converter. 91
Figure 5.5 The circuit diagram of a parallel resonant converter. 92
Figure 5.6 Derivation of the equivalent ac resistance for the parallel resonant converter.. 92
Figure 5.7 The ac equivalent circuit of parallel resonant converter........................... 93
Figure 5.8 DC gain characteristic of the parallel resonant converter......................... 94
Figure 5.9 The circuit diagram of a series-parallel resonant converter...................... 95
Figure 5.10 AC equivalent circuit of series-parallel resonant converter. 95
Figure 5.11 DC gain versus f_s/f_0 and Q_L with different A=C_p/C_s. (a) f_s/f_0 and (b) Q_L. 96
Figure 5.12 Duty cycle of LCC resonant converter (at full load Q_F=4) and H-bridge at the MPPT. 100
Figure 5.13 Converter measured efficiency at the MPP with different wind speeds. 100
Figure 5.14 The 3D plot of dc gain at different switching frequencies and Q_L. 103
Figure 5.15 Schematic of the wind energy conversion system. 106
Figure 5.16 Test rig. 107
Figure 5.17 Dynamic response of the mechanical system for wind speed changes: 108
Figure 5.18 Dynamic response of the electrical system for wind speed changes: ... 108
Figure 5.19 Dynamic response of the mechanical system for wind speed changes: 109
Figure 5.20 Dynamic response of the electrical system for wind speed changes: ... 110
Figure 5.21 Zoom-in waveform of input three-phase rectifier current. 110
Figure 5.22 Voltage across the CSI at wind speed: (a) 3.5m/s and (b) 4.2m/s. 111
Figure 6.1 Series connection wind farm topology. 119
Figure 6.2 DC wind farm parallel connection with switchgear configuration (a) Star collection (b) String collection. 120

Figure 6.3 Proposed current source converter based multi-terminal dc wind farm configuration 122
Figure 6.4 Test rig schematic. 123
Figure 6.5 CSI test rig. 124
Figure 6.6 Practical results with active power change: (a) inverter output power,.. 125
Figure 6.7 Dynamic response of mechanical system of WT1. 126
Figure 6.8 Dynamic response of mechanical system of WT2. 127
Figure 6.9 Dynamic response of the electrical system (a) WT1 (b) WT2. 127
Figure 6.10 Dynamic response of mechanical system of WT2. 128
Figure 6.11 Dynamic response of the electrical system (a) WT1 (b) WT2. 129
Figure 6.12 Dynamic response of mechanical system of WT1. 130
Figure 6.13 Dynamic response of mechanical system of WT2. 130
Figure 6.14 Dynamic response of the electrical system (a) WT1 (b) WT2. 131
Figure 6.15 Practical dynamic response of the mechanical system of WT1. 132
Figure 6.16 Practical dynamic response of the mechanical system of WT2. 132
Figure 6.17 Practical dynamic response of the electrical system (a) WT1 (b) WT2. 133
Figure 6.18 Practical dynamic response of the mechanical system of WT1. 134
Figure 6.19 Practical dynamic response of the mechanical system of WT2. 134
Figure 6.20 Practical dynamic response of electrical system of WT1. 135
Figure 6.21 Practical dynamic response of electrical system of WT2. 135
Figure 6.22 Practical dynamic response of the mechanical system of WT1. 136
Figure 6.23 Practical dynamic response of the mechanical system of WT2. 136
Figure 6.24 Practical dynamic response of the electrical systems of WT1 and WT2. 137
Figure 7.1 Wind turbine operation possibility during de-loading process. 142
Figure 7.2 Multi-terminal dc transmission WECS configuration. 143
Figure 7.3 The proposed de-loading control scheme flow chart. 145
Figure 7.4 The wind turbine characteristics in pu with different pitch angle β 146
Figure 7.5 Pitch controller in a variable speed wind turbine. 146
Figure 7.6 Pitch controller in fixed speed wind turbine. 147
Figure 7.7 DC/DC converter control block diagram. 148

Figure 7.8 DC dumping chopper topology. 148
Figure 7.9 Control schematics for dc dumping chopper. 149
Figure 7.10 Dynamic response of WT1 without the proposed control. 150
Figure 7.11 Dynamic response of WT2 without the proposed control. 151
Figure 7.12 DC link voltage and wind turbine output dc voltage without the proposed control (a) WT1 (b) WT2. 151
Figure 7.13 Dynamic response of WT1 with dc/dc converter voltage control. 152
Figure 7.14 Dynamic response of WT2 with dc/dc converter voltage control. 153
Figure 7.15 DC link voltage and wind turbine output dc voltage with dc/dc converter voltage control (a) WT1 and (b) WT2. 153
Figure 7.16 Dynamic response of WT1 with the proposed coordinated control. 154
Figure 7.17 Dynamic response of WT2 without the proposed control. 155
Figure 7.18 DC link voltage and wind turbine output dc voltage with the proposed coordinated control (a) WT1 (b) WT2. 155
Figure 7.19 Practical dynamic response of WT1 without the proposed control. 156
Figure 7.20 Practical dynamic response of WT2 without the proposed control. 157
Figure 7.21 Practical dc link voltage and wind turbine output dc voltage without the proposed control. 157
Figure 7.22 Practical dynamic response of WT1 with dc/dc converter voltage control. 158
Figure 7.23 Practical dynamic response of WT2 with dc/dc converter voltage control. 159
Figure 7.24 Comparison of dc link voltage and wind turbine output dc voltage with and without dc/dc converter voltage control. 160
Figure 7.25 Practical dynamic response of WT1 with the proposed control. 161
Figure 7.26 Practical dynamic response of WT2 with the proposed coordinated control. 162
Figure 7.27 Compared dc link voltage and wind turbine output dc voltage with dc/dc converter voltage control and with the proposed control. 163

D.2 List of tables

Table 1.1 Operational wind farms statistics in the UK 6
Table 3.1 Wind turbine specifications. 49
Table 3.2 Control parameters. 49
Table 4.1 Proven 2.5 kW PMSG specifications. 67
Table 4.2 Wind turbine parameter. 67
Table 4.3 Electrical system parameters. 78
Table 5.1 The parameters for the five-phase PMSG. 87
Table 5.2 HSFB and LCC resonant converter comparative results. 99
Table 5.3 LCC resonant converter parameters. 107
Table 5.4 Specification of AC inductor. 111
Table 5.5 Specification of DC filtering inductor. 111
Table 5.6 Specification of power transformer. 112
Table 6.1 CSI test rig parameters. 124

Appendix E Summary of relevant published work by the author

[1] F. Shixiong, J. E. Fletcher, Z. Huibin, S. J. Finney, and B. W. Williams, "Optimization of One-Power-Point operation for variable speed wind turbine with synchronous generators," in *IECON 2010 - 36th Annual Conference on IEEE Industrial Electronics Society*, 2010, pp. 2874-2879.

Abstract

This paper presents an optimized One-Power-Point method for maximum power tracking in a variable speed wind energy conversion system that uses a boost converter. For low-cost implementations, One-Power-Point maximum power tracking is preferable due to its ease of implementation and fast tracking ability. Its drawback is that power coefficient C_p deteriorates during wind speed drops. This means the wind turbine speed cannot track rapid wind speed changes. The rate of rotation speed is determined not only by the system inertia, but also the difference between the mechanical power and electromagnetic power. An optimization method based on One-Power-Point operation is developed to improve the system performance and energy conversion efficiency. There is no additional equipment, mechanical sensors or measurements. Simulation results confirm the functionality and feasibility of the method.

[2] S. Fan, T. Lim, H. Zhang, S. Finney, and B. Williams, "Design and control of wind energy conversion system based on resonant DC/DC converter," in *Renewable Power Generation (RPG 2011), IET Conference on*, 2011, pp. 1-6.

Abstract

Nowadays, wind energy is developing rapidly all around the world. There are many options of wind power generation and collection system configuration. DC wind farm collection grid is preferable due to its small size of passive components and better efficiency with high switching frequency. This paper studies the design and control of wind energy conversion system based on serial parallel LCC current output resonant DC/DC converter. LCC resonant converter has combined the advantages of the series resonant converter (SRC) and parallel resonant converter (PRC). It is found to be the suitable choice for multi-terminal DC micro-grid power transmission to interface multiple wind turbines. Design procedure for the LCC converter is explained and the analysis is verified with simulation results. Experimental work based on wind simulator is presented to verify the feasibility of the wind energy conversion system.

[3] S. Fan, T. Lim, H. Zhang, S. Finney, and B. Williams, "Design and control of wind energy conversion system based on resonant DC/DC converter," *Renewable Power Generation, IET*, submitted

Abstract

Recent wind energy harvesting technology development has focused on using a DC collection and a possible smaller passive grid due to its high energy efficient components in the converter system. This paper evaluates and compares the hard-switched H-bridge DC-DC converter and the series-parallel LCC resonant DC-DC converter, both suitable for wind energy conversion systems. Experimental results substantiate their merits and drawbacks in variable wind speed conditions. The unique, previously unexploited feature of the LCC resonant converter is increased gain at low output power, low speed, and low input voltage. A hardware wind turbine simulator emulating an actual wind turbine is used. Its design and control are briefly highlighted. This paper demonstrates the feasibility of utilizing an LCC resonant converter for wind energy conversion systems through simulation and experimental results both at the same power level.